

Quantifying Atherosclerosis: IVUS Imaging For Lumen Border Detection And Plaque Characterization

Amin Katouzian

Submitted in partial fulfillment of requirements for
the degree of Doctor of Philosophy
in the Graduate School of Arts and Sciences

COLUMBIA UNIVERSITY

2011

© 2011

Amin Katouzian

All Rights Reserved

ABSTRACT

Quantifying Atherosclerosis: IVUS Imaging For Lumen Border Detection And Plaque Characterization

Amin Katouzian

The importance of atherosclerotic disease in coronary artery has been a subject of study for many researchers in the past decade. In brief, the aim is to understand progression of such a disease, detect plaques at risks (vulnerable plaques), and treat them selectively to prevent mortality and immobility. Consequently, several imaging modalities have been developed and among them intravascular ultrasound (IVUS) has been of particular interest since it provides useful information about tissues microstructures and images with sufficient penetration as well as resolution. In general, the ultimate goal is to provide interventional cardiologists with reliable clinical tools so they can identify vulnerable plaques, make decisions confidently, choose the most appropriate drugs or implant devices (*i.e.* stent), and stabilize them during catheterization procedures with minimal risk.

In this work, we review existing atherosclerotic tissue characterization algorithms including the state-of-the-art virtual histology (VH) framework, which has been implemented in the Volcano (Rancho Cordova, CA) IVUS clinical scanners using 64-elements 20 MHz phased-array transducer. Initially, we intended to extend this technique for data acquired with 40 MHz single-element transducers. For this reason, we started acquiring *in vitro* IVUS data and studied involved challenges from specimen preparation toward classification. We observed inconsistency among extracted features along with transducer's spectral parameters (*i.e.* bandwidth, center frequency). This, in addition to infeasibility of construction of reliable training dataset due to heterogeneity of atherosclerotic tissues motivated us to develop an unsupervised texture-based atherosclerotic tissue characterization algorithm.

We proposed a two-dimensional multiscale wavelet-based algorithm to expand IVUS backscattered signals and/or grayscale images onto orthogonal symmetric quadrature mirror filters (QMF) such as Lemarie-Battle. At the bottom of decomposition tree, we employed ISODATA to cluster enveloped detected features in an unsupervised fashion and classify atherosclerotic plaque constitutes into fibrotic, lipidic, calcified, and no tissues. For the first time, we studied numbers of factors that were necessary for extension of *in vitro* derived classifier for *in vivo* applications such as reliability of classified tissues behind arc of calcified plaques and effects of pressure changes as well as flowing blood on constructed tissue color maps, called prognosis histology (PH) images.

The second half of this dissertation is devoted to automatic detection of lumen borders in IVUS grayscale images acquired with high frequency (40 MHz up) transducers where more scattering exhibited within lumen area that makes the problem of interest more challenging. We established our framework on three-dimensional expansion of IVUS sub-volumes onto orthonormal brushlet basis function. The rational behind our framework was presence of incoherent (*i.e.* blood) versus coherent (*i.e.* plaque, surrounding fat) textural patterns along pullback direction, which was motivated by what an interventional cardiologist does to locate the lumen border visually by going back and forth among IVUS frames. We studied the feasibility of brushlet analysis through filtering blood speckles and supervised classification of blood versus non-blood regions. Our preliminary study confirmed that the most informative features reside in the innermost cubes, representing low-frequency components in transformed domain. Finally, we explored that tissue responses to IVUS signals are proportionally preserved in brushlet coefficients and it enabled us to classify blood regions in complex brushlet space. Subsequently, we employed surface function actives (SFA) to estimate the lumen borders after regularization. In a comparison study, we quantified our results with two of existing algorithms, employing IVUS grayscale images acquired with 40 MHz and 45 MHz single-element transducers. Overall, our proposed algorithm outperformed and the resulting automated detected borders showed good correlation with manually traced borders by an expert.

Contents

Contents	i
List of Tables	iv
List of Figures	vi
Acknowledgement	xxvi

1. Chapter One: INTRODUCTION.....	1
1.1. Medical Background	1
1.1.1. Coronary Atherosclerosis.....	2
1.1.2. Endothelial Dysfunction.....	4
1.1.3. Vulnerable Plaque.....	6
1.1.4. Stabilization of Vulnerable Plaque.....	9
1.2. Identification of Vulnerable Plaques.....	10
1.2.1. Non-Invasive Techniques.....	11
1.2.2. Invasive Techniques.....	13
1.3. Problem Statement	19
1.4. Specific Aims of The Thesis.....	21
2. Chapter Two: INTRAVASCULAR ULTRASOUND (IVUS).....	23
2.1. Why IVUS?	23
2.2. Technical Principles of IVUS.....	25
2.2.1. Basic Physics of Ultrasound.....	25
2.2.2. IVUS Acquisition System Specifications	26
2.3. IVUS Image Formation and Display	29
2.3.1. Appearance of Atherosclerotic Tissues, Vessel Wall, and Lumen Borders in IVUS Images	32
2.3.2. IVUS Image Artifacts	36
3. Chapter Three: EXISTING ATHEROSCLEROTIC PLAQUE CHARACTERIZATION ALGORITHMS	37
3.1. Introduction	37
3.2. IVUS Data Collection Specification	38
3.2.1. In Vivo Acquisition.....	38
3.2.2. In Vitro Acquisition and Histology Preparation	39
3.2.3. Cardiovascular Histopathology.....	43
3.3. RF- and Spectrum-Based Plaque Characterization Algorithms.....	44
3.3.1. IVUS-Virtual Histology (IVUS-VH)	45
3.3.2. IVUS-Integrated Backscatter (IVUS-IB)	48
3.3.3. IVUS Elastography (IVE).....	51
3.4. Texture-Based Tissue Characterization and Vulnerable Plaque Detection Algorithms	52
3.4.1. IVUS-Error Correcting Output Codes (IVUS-ECOC).....	53

3.4.2.	<i>IVUS-Image Based Histology (IVUS-IBH)</i>	56
3.4.3.	<i>IVUS-Vasa Vasorum (IVUS-VV) Imaging</i>	58
3.5.	Summary and Conclusion.....	60
4.	Chapter Four: CHALLENGES IN ATHEROSCLEROTIC PLAQUE CHARACTERIZATION ALGORITHMS WITH IVUS.....	62
4.1.	Introduction	63
4.2.	Methodological Challenges.....	64
4.2.1.	<i>Variability of Tissue Signatures</i>	64
4.2.2.	<i>Ground Truth</i>	68
4.3.	Eight-Spectral-Feature Extraction Algorithm.....	69
4.3.1.	<i>IVUS Data Normalization</i>	70
4.3.2.	<i>Linear Regression Analysis and Eight-Spectral-Feature Computation</i>	76
4.3.3.	<i>Experimental Results</i>	78
4.4.	Full-Spectrum Analysis and Algorithmic Challenges.....	80
4.4.1.	<i>Full-Spectrum Analysis Algorithm</i>	80
4.4.2.	<i>Complexity of Algorithm and Sufficiency of Data</i>	84
4.5.	Summary and Conclusion.....	87
5.	Chapter Five: UNSUPERVISED ATHEROSCLEROTIC PLAQUE CHARACTERIZATION IN IVUS IMAGES VIA MULTISCALE WAVELET PACKET ANALYSIS	90
5.1.	Introduction	91
5.2.	Methods	92
5.2.1.	<i>Multi-Channel Wavelet Analysis</i>	92
5.2.2.	<i>Filter Selection and Specification</i>	95
5.2.3.	<i>Feature Extraction</i>	96
5.2.4.	<i>Classification</i>	98
5.3.	Experimental Results and Quantification Analysis.....	99
5.3.1.	<i>Atherosclerotic Plaque Characterization</i>	99
5.3.2.	<i>Reliability of Extracted Features</i>	104
5.4.	Summary and Conclusion.....	111
6.	Chapter Six: AUTOMATIC DETECTION OF LUMINAL BORDER IN IVUS IMAGES: PRELIMINARY STUDY.....	113
6.1.	Background	115
6.1.1.	<i>Rational Behind the Use of Brushlet Basis Function in IVUS Image Analysis</i>	115
6.1.2.	<i>Brushlet Analysis</i>	117
6.2.	Lumen Border Detection via Thresholding of Brushlet Coefficients	124
6.2.1.	<i>Frequency Tiling and Overcomplete Representation</i>	125
6.2.2.	<i>Thresholding for Removal of Blood Speckle</i>	125
6.2.3.	<i>Segmentation Framework and Detection of Lumen Border</i>	126
6.2.4.	<i>Results and Discussion</i>	128
6.2.5.	<i>Summary</i>	131
6.3.	Distribution of Brushlet Coefficients.....	132
6.4.	Classification of Blood Regions in IVUS Images Using 3D Brushlet Expansions	138
6.4.1.	<i>Feature Extraction Methodology</i>	138
6.4.2.	<i>Classification</i>	140
6.4.3.	<i>Experimental Results</i>	140
6.4.4.	<i>Discussion and Conclusion</i>	144
6.5.	Visualization of Brushlet Coefficients	145

6.5.1. Arithmetic Manipulation of Brushlet Coefficients in Transformed Domain	148
6.6. Incremental/Decremental Expansion and Reconstruction of IVUS Sub-Volumes	152
6.6.1. Iterative Expansion and Reconstruction	156
6.7. Summary and Discussion	163
7. Chapter Seven: AUTOMATIC DETECTION OF LUMINAL BORDERS IN IVUS IMAGES BY MAGNITUDE-PHASE HISTOGRAMS OF COMPLEX BRUSHLET COEFFICIENTS	165
7.1. A Brief Review on Existing IVUS Lumen Border Detection Algorithms	166
7.2. Methodology	170
7.2.1. Motivations	170
7.2.2. IVUS Signal Modeling in Fourier Domain and Sources Assumptions	171
7.2.3. Construction of 2.5-D Magnitude-Phase Histogram in Brushlet Space	172
7.2.4. Segmentation of Coefficients and Recovery of Regional Peak Correspondences	176
7.2.5. Spatial Regularization and Detection of Lumen Border via Surface Function Actives (SFA)	177
7.3. Experimental Results	180
7.3.1. Evaluation of Proposed Framework Using Phantom Data	181
7.3.2. Evaluation of Proposed Framework Using In Vivo Data	182
7.3.3. Comparison of Our Proposed Algorithm with Existing Techniques	188
7.4.1. Registered Versus Unregistered Data	196
7.4.2. Effects of Tiling Resolution on Constructed Magnitude-Phase Histogram	198
7.4.3. Multiple-Frame Magnitude-Phase Histogram	204
8. Chapter Eight: SUMMARY, CONCLUSION, AND FUTURE WORK	205
8.1. Atherosclerotic Plaque Characterization	205
8.1.1. Refinement of Proposed Algorithm and Future Work	206
8.2. Automatic Detection of Luminal Borders In IVUS Images	209
8.2.1. Refinement of Supervised Classification of Blood Versus Non-Blood Regions	211
8.2.2. Quantitative Measurement for Energy Localization in Incremental/Decremental Decomposition Frameworks	212
8.2.3. Decreasing Processing Time by Adaptive Selection of Numbers of Frames per Blocks of Analysis	213
8.2.4. Dual-Modal Brushlet-Based Lumen Border Detection Technique with Cross Refinement	213
Appendix	215
A. List of Abbreviations	215
B. Bibliography	218

List of Tables

- Table 4.1.** Statistical variations of catheters' spectral parameters. Page 73
- Table 5.1.** Percentage of correct classification as well as misclassification for each tissue type. Page 102
- Table 6.1.** Tanimoto coefficient statistics and correlation between automated and manually traced borders in 233 frames collected from three distinct cases. Page 131
- Table 6.2.** Classification results using neural networks with different topologies: N-M-1; N and M are the number of neurons in the input and hidden layers, respectively. Also shown are results using different numbers of features. Correct classification (CC) rate, sensitivity (SE), specificity (SP) and correct segmentation (S) rate are reported. The better results are highlighted in yellow. The best performance was achieved using 34 features (N) and network topology of N-34-1 (green). Page 141
- Table 6.3.** Classification results and comparison between manual and optimal automated lumen border, generated from a thresholded blood map with an optimized threshold value through linear regression analysis and computation of Tanimoto Coefficients (η). The best performance was achieved using threshold value of 0.45 (green). Page 143
- Table 7.1.** List of some of existing border detection algorithms in IVUS images and their specifications. Page 167

Table 7.2. Quantification of automated detected borders with corresponding manual ones for images acquired with single-element 45MHz transducers.	Page 185
Table 7.3. Quantification of automated detected borders with corresponding manual ones for images acquired with single-element 40MHz transducers.	Page 187
Table 7.4. Quantification of automated detected borders through three different methods with corresponding manual ones for images acquired with single-element 45MHz transducers. The first, second, and third outperforming methods have been highlighted with green, orange, and red colors, respectively.	Page 190
Table 7.5. Quantification of automated detected borders through three different methods with corresponding manual ones for images acquired with single-element 40MHz transducers. The first, second, third, and forth outperforming methods have been highlighted with green, orange, red, and yellow colors, respectively.	Page 192
Table 8.1. Existing atherosclerotic tissue characterization algorithms.	Page 207

List of Figures

Figure 1.1. Schematic of a normal artery (a) and its diseased (narrowed) counterpart (b) along with corresponding cross sections. (Reference: <http://www.nhlbi.nih.gov>).

Page 3

Figure 1.2. Endothelium dysfunction. Normal artery with structural layers (a), atherosclerotic plaque builds up in the endothelial layer (intima) that may lead to unstable plaque (b). It becomes stable if thick fibrotic cap is constructed on top of the lipid core (c) or ruptures (d) that may result in ACS (e) or sudden death (f) depending on sized of blood clot occlusion. (Reference: <http://www.americanheart.org>).

Page 5

Figure 1.3. Different types of vulnerable plaques introduced by Naghavi *et al.* [19]. Rupture-prone plaque with large lipid core and thin fibrous cap infiltrated by macrophages (A). Ruptured plaque with subocclusive thrombus and early organization (B). Erosion-prone plaque with proteoglycan matrix in a smooth muscle cell-rich plaque (C). Eroded plaque with subocclusive thrombus (D). Intraplaque hemorrhage secondary to leaking vasa vasorum (E). Calcific nodule protruding into the vessel lumen (F). Chronically stenotic plaque with severe calcification, old thrombus, and eccentric lumen (G). Correlation between degree of stenosis (green bar), frequency of plaques (yellow bar), and risk of complication per plaque (red bar) as a function of plaque progression.

Page 7

Figure 1.4. A vulnerable plaque before (a) and after (b) rupture. Degree of vulnerability significantly decreases if the fibrotic cap becomes thicker, which turns an

unstable plaque (a) to a stable plaque (c). Histology image (d) corresponding to the stable plaque. Page 8

Figure 1.5. Transaxial view of a contrast-enhanced CTA (a) and corresponding angiogram (b). Yellow arrows point to site of occlusion. Page 11

Figure 1.6. A typical angiogram (a). Different projections may lead to under- or over estimation of plaque burden (b). Red arrows point to the site of occlusion. Page 14

Figure 1.7. [39] Rotary OCT image acquired with 500µm wavelength (a) corresponding transverse image (b) and Movat pentachrome histology (c). Page 17

Figure 1.8. Pullback pathway of IVUS catheter on angiogram (top row) and IVUS grayscale images (bottom row) at three distinct locations (A,B,C). (Reference: Cleveland clinic core lab). Page 19

Figure 2.1. Schematic of transmission of ultrasound wave through two different mediums and resulting reflected-attenuated, refracted, and scattered signals. The reflected-attenuated signals, received by the transducer, are depicted in voltages and grayscale intensities. Page 25

Figure 2.2. Schematic of four different types of imaging catheters. A catheter without guide wire rail (A), a catheter with guide wire rail designed at the side (B), a catheter with guide wire rail designed at its center (C), a catheter with guide wire rail at its center, inflatable balloon and stent (D). (Reference: http://ee.isikun.edu.tr/research.asp-page=projects_files). Page 27

Figure 2.3. Single-element mechanically rotating focused IVUS transducer and its beam width (a), multi-elements phased-array IVUS transducer and its beam width (b). Page 27

- Figure 2.4.** Catheter pullback apparatus. (Reference: <http://img.medscape.com>). Page 29
- Figure 2.5.** An IVUS scanner console (Volcano $s5^{\text{TM}}$ imaging system). Page 30
- Figure 2.6.** Schematic of an artery, catheter, atherosclerotic plaque, and IVUS image cross-section (a) (Reference: <http://www.bmj.com>), cross-sectional anatomy of arterial wall (b), four distinct IVUS frames acquired with 20 MHz (c), 30 MHz (d), 40 MHz (e), and 45 MHz (f) transducers. Red and green borders represent vessel wall and lumen borders, respectively. The yellow dashed line depicts trajectory of transducer scan lines. Page 31
- Figure 2.7.** An IVUS grayscale image in polar (r, θ) (a) and (x, y) Cartesian (b) domains along with longitudinal display (c) along an arbitrary planar cut (yellow line). Page 32
- Figure 2.8.** An IVUS grayscale image acquired *in vitro* (a), corresponding Movat Pentachrome histology image with manually traced tissues (b), constructed tissue color map (c), and imposed tissue color map on original IVUS grayscale image (d). Yellow, magenta, white, and cyan colors represent fibrotic, lipidic, calcified and necrotic core tissues, respectively. Page 33
- Figure 2.9.** An IVUS grayscale image without (a) and with (b) TGC adjustment. Page 35
- Figure 2.10.** An IVUS grayscale image with manually traced vessel wall (green) and lumen (red) borders (a), zoomed in region with anatomical structures of the artery such as lumen, intima (I) or plaque, media (M) and adventitia (A) (b), histology image of artery anatomical structures (c). Page 35

Figure 2.11. IVUS image artifacts. Guide wire artifact (a), discontinuity artifact at 0° (a), Ring-down artifact (b,c), reverberation artifact (c), NURD artifact (d).

Page 36

Figure 3.1. The heart and coronary arteries. Illustration of advanced schematic catheter (red) into LAD (a) LCX (b) and RCA (c).

Page 38

Figure 3.2. Marking ROIs on LAD of a transplant heart; Two needles (pointed with white arrows) are placed into surrounding fat (a) at the tip of the IVUS catheter visualized under fluoroscopic guidance (b). The third needle is passed through the crossed point and a suture is done to mark the ROI (c). The first two needles are removed and the procedure is repeated for each ROI (d).

Page 40

Figure 3.3. Taking three sections at each ROI with 500 micrometer intervals, which corresponds to 30 frames. Marked ROI with reflection of the needle (white arrow) and side branch (*) with corresponding histology (a). Two IVUS frames with 500 micrometer intervals and corresponding histology sections (b,c).

Page 41

Figure 3.4. Tissue cage fixture (a), *in vitro* experiment set-up (b). (Courtesy of Jennifer Liskauskas at InfrareDx (Burlington, MA)).

Page 42

Figure 3.5. Dissimilarity among four tissue spectra, calcium, necrotic core, fibrofatty, and fibrotic measured in sample size of 64 collected from one cross section of interest (CSI).

Page 44

Figure 3.6. Linear regression fit to normalized tissue's spectrum and extracted features; intercept, slope, mid-band-fit (MBF), and minimum and maximum powers and their corresponding frequencies. Slopes (decibels per megahertz) of

regression line and integrated backscatter coefficient have not been shown. The corresponding IVUS data has been collected with 40 MHz unfocused transducer.

Page 46

Figure 3.7. [64] Original IVUS grayscale image acquired in vitro (a), histological validation showing a fibroatheroma with a thick fibrotic cap (b), pathologist's pencil sketch showing the four major tissue types present in the lesion using the IVUS-VH color-coded classification: dark green codes for fibrotic tissue; light green, fibrofatty tissue; red, necrotic core. Micro calcifications are here marked with small dark points (c), IVUS-VH coding with calcium here coded in white (d).

Page 47

Figure 3.8. IVUS-VH *in vivo* results. Four IVUS grayscale images (top row) acquired with 20 MHz 64-elements phased array transducer from distal (left) to proximal (right) and their corresponding VH results (bottom row). Dark green, light green, white, and red represent fibrotic, fibrofatty, calcified, and necrotic core, respectively.

Page 47

Figure 3.9. [69] Color-coded maps of coronary arterial plaques constructed by IB-IVUS and histology, coronary angiography, or angioscopy. **A**, Autopsy study of coronary arterial plaque. A₁, Histological finding with fibrosis, mixed lesion, calcification, and large (right) and small (left) lipid cores (*) stained with Masson's trichrome. Bar=1 mm. A₂, Conventional IVUS image of same segment as A₁. A₃, Color-coded map of intima of A₁ constructed by IB-IVUS. **B**, In vivo study of coronary arterial plaque. B₁, Angiography of left coronary artery. Arrow indicates a segment with 60% diameter stenosis.

B₂, Conventional IVUS image of same segment as shown by arrow in B₁. B₃, Color-coded map of intima of B₁ constructed by IB-IVUS. B₄, Angioscopic finding of plaque at right in B₃. Note that white plaque is related to fibrous tissue. C, In vivo study of coronary arterial plaque. C₁, Angiography of right coronary artery. Arrow indicates a segment with 40% diameter stenosis. C₂, Conventional IVUS image of same segment as shown by arrow in C₁. C₃, Color-coded map of intima in C₁ constructed by IB-IVUS. Note large lipid core (*) with fibrous cap (arrowhead). C₄, Angioscopic finding of plaque at top in C₃. Note that yellow plaque is related to thin fibrous cap. Red and yellow contours represent traced lumen and vessel wall borders, respectively.

Page 49

Figure 3.10. [71] Comparison between IVUS-IB results with corresponding IVUS-VH.

Histological image (Masson's trichrome staining) (top row). * depicts lipid pool region, corresponding color-coded maps constructed by the IVUS-IB technique (middle row), red, yellow, green and blue colors represent calcification, dense fibrosis, fibrosis and lipid pool, respectively. Corresponding IVUS-VH images (bottom row).

Page 50

Figure 3.11. [41] Two *in vitro* IVUS grayscale images acquired at two different levels of pressures (85 mmHg and 90 mmHg) and resulting elastogram along with corresponding histopathological images, Picro-sirus red (a), Alpha-actin (b). The IVUS image reveals an eccentric plaque between 2 and 11 o'clock. The elastogram shows that the plaque can be divided into two parts: a low-strain part (0.2%) between 4 and 11 o'clock and a high-strain part (1%) between 2

and 4 o'clock, both compared with the moderate strain (0.5%) in the normal vessel wall. The histology reveals that the region between 4 and 11 o'clock is fibrous material and the region between 2 and 4 o'clock is fatty material.

Page 52

Figure 3.12. [77] Left: IVUS data set samples. Right: (top) segmentation by a physician and (down) Automatic classification with texture based features. The white area corresponds to calcium, the light gray area to fibrosis, and the dark gray area to soft plaque.

Page 54

Figure 3.13. [77] Performance results for different sets of features, ECOC designs and base classifiers on the IVUS data set.

Page 56

Figure 3.14. [87] Illustration of enhancement of the longitudinal resolution of atherosclerosis plaque composition characterization of grayscale IVUS using IVUS-IBH method compared to IVUS-VH. In IVUS-IBH approach, the tissue color maps are generated for every frame, similar to IVUS-PH algorithm.

Page 57

Figure 3.15. [87] An in vivo acquired IVUS grayscale image (a), corresponding VH image (b), generated tissue color map through IVUS-IBH approach (c). The red, white, green, and blue colors represent necrotic core, calcified, fibro-fatty, and acoustic shadowing regions, respectively.

Page 58

Figure 3.16. Schematic of different VV formations in coronary artery (a), Visualization of VV and neovascularization of atherosclerotic coronary arteries by cinematography of silicone injection in cleared human hearts [95] (b).

Page 59

Figure 3.17. [94] A grayscale IVUS frame before contrast agent injection (a), enhanced frame before (b) and after thresholding (b), zoomed area (d) corresponding to white rectangle in (a), imposed colored VVs (e). Page 59

Figure 4.1. Normalized spectra of two types of plaque tissues found in one particular frame of data. The bars represent the interquartile range of variation. The unfilled bars represent lipidic tissue and the filled bars, fibrotic tissue. For meaningful comparison, each sample spectrum has been normalized to have unit energy. The N refers to the number of spectra used to compute the statistics. Page 65

Figure 4.2. Normalized spectra of two distinct types of plaque tissue found in four cross-sections of data from two cadaver hearts. As before, the bars represent the interquartile range of variation. The unfilled bars represent lipidic tissue and the filled bars, fibrotic tissue. Page 67

Figure 4.3. Signal reflected from plexiglas wall (a), averaged spectra measured from 12 distinct plexiglas acquisition frames using Fourier analysis (catheter 3 in Table 1) (b). Page 73

Figure 4.4. PSD estimation of plexiglas signal with AR models of order 4, 15, 40, 100 along with Fourier analysis. Page 76

Figure 4.5. Plexiglas spectrum fitted with Gaussian model. Page 77

Figure 4.6. Box whisker plots of confidence level of linear regression analysis in four tissue types, 92 ROIs for NC: necrotic core, 73 ROIs for Ca: calcium, 299 ROIs for FF: fibrofatty, 1234 ROIs for F: fibrotic (a) and three frames (b). Each ROI contains 64 hamming windowed samples. Page 79

Figure 4.7. Variations of two spectral features extracted from four tissue types. Intercept (a) and Slope (b). Necrotic core (NC), calcium (Ca), fibro-fatty (FF) and fibrotic (F). Page 79

Figure 4.8. Pictorial illustration of two full-spectrum based classification methods. Movat Pentachrome histology image (a), IVUS image (b), IVUS tissue map generated by Fisher (c), IVUS tissue map generated by k-NN, k=5 (d). Page 83

Figure 4.9. Realistic estimates of the accuracy attainable by a spectrum based tissue characterization algorithm trained to differentiate between blood filled regions (solid line) and tissue (dashed line) in IVUS image. Page 85

Figure 4.10. ROC curves comparing the linear separability of full spectral features (left) with that of a reduced set of 7 features (right). 1451, 475, 10668 and 382 volumes of 128 samples of fibro-lipidic, lipidic, fibrotic and calcified tissue signals were used, respectively. Page 86

Figure 4.11. Atherosclerotic plaque characterization flowchart from data collection toward algorithm development, classification, and validation. Page 88

Figure 5.1. Tree structure for a discrete wavelet packet frame expansion (DWPF) and its associated multiscale indexes. Page 92

Figure 5.2. Lemarie-Battle filter of order 18 (a), constructed filter bank at level 4 (b). Page 96

Figure 5.3. Manually traced vessel wall (green) and lumen border (red) on IVUS B-mode image (a), resulting PH image generated by the algorithm (Blue, yellow and pink colors represent calcified, fibrotic and fibro-lipidic components) (b), corresponding H&E histology image of cross section of interest (c). The

white star points to lipid rich pool region that could be sign of vulnerable plaque if thin fibrotic layer existed on top of it.

Page 100

Figure 5.4. H&E histology image of CSI with manually segmented ROIs (a), corresponding IVUS grayscale image (b), manually selected regions corresponding to presumably homogenous regions for each tissue type (c), corresponding PH image (d). The bottom row illustrates the magnified version of selected ROI (red square) for fibrotic tissue. The inhomogeneity of atherosclerotic tissues are well reflected in (a,b,d). The white star points to lipid rich pool region that could be a sign of vulnerable plaque if a thin fibrotic layer existed on top of it.

Page 103

Figure 5.5. Five consecutive *in vivo* IVUS grayscale images acquired with a 40MHz single-element Boston Scientific transducer (top row) and corresponding generated PH images (bottom row) (a), Box-Whisker plot of number of pixels for each tissue type in 15 consecutive frames (b).

Page 106

Figure 5.6. Effects of change of pressure on generated PH images. *In vitro* grayscale IVUS images acquired at three different levels of pressures (from 20mmHg to 120 mmHg) for a particular cross section of interest (no pullback) (top row), and corresponding constructed PH images (bottom row). Box-Whisker plot of number of pixels for each tissue type in 30 consecutive frames (b).

Page 107

Figure 5.7. IVUS grayscale image of a cross section of interest using circulating Saline (a) and corresponding constructed PH image (b), IVUS grayscale image of the same cross section acquired with circulating human blood (c) and

corresponding constructed PH image (d), H&E histology image of the same cross section (e). Page 109

Figure 5.8. Sample H&E histology image of a calcified CSI (a), grayscale image of the CSI using Saline (b) and corresponding PH image (c). The tissues behind arc of calcified plaque, marked with white star (7-9 o'clock), have been classified as no tissue. Page 110

Figure 6.1. Four distinct IVUS frames acquired with 20 MHz (a), 30 MHz (b), 40 MHz (c), and 45 MHz (d) transducers. Red border represents lumen border. Page 114

Figure 6.2. Windowing functions $b(x)$ and $v(x)$ (a). The ε parameter controls the localization degree of brushlet function in time and frequency domains. Real part (b) and imaginary part (c) of analysis $u_{n,j}$ brushlet function with $l_n = 32, \varepsilon = 16, j = 8$. Page 118

Figure 6.3. Schematic expansion of IVUS sub-volumes onto brushlet basis, tiling of frequency domain (4x4x2) and selective feature extraction along eight directions corresponding to low-frequency components. Page 119

Figure 6.4. Real (a) and imaginary (b) parts of synthesis function, $w_{j,n}(x)$, corresponding to **Figure 6.2 (b,c)**. Page 120

Figure 6.5. Schematic of reconstruction after thresholding or enhancement of brushlet coefficients. Page 120

Figure 6.6. Indexing convention used after tiling of frequency space. 4x4x3 cubes are used to tile the frequency space, resulting 48 quadrants. Each quadrant is indexed incrementally, starting from the most left-top quadrant in roster

format. An individual quadrant is represented by its index and sub-band numbers $q_{index\#}^{subband\#}$. Page 122

Figure 6.7. First ring of quadrants in the 2nd subband (a), first quadrants' sphere (b), and second quadrants' sphere (c). Page 124

Figure 6.8. Original IVUS frame (a), filtered result with threshold values of T=0.25 (b) and T=0.5 (c). Manual traced borders (red), representing lumen border and blood speckles inside luminal area. Page 126

Figure 6.9. ICM segmentation. 4-classes ICM results for original image in polar (a), Cartesian (b) coordinates, and after dilation (c). 4-classes ICM results for filtered image in polar (e), Cartesian (f) coordinates, and after dilation (g). Page 127

Figure 6.10. Segmentation results at two different layers (red and blue) along with manually traced contour by an expert (yellow) on original (a) and filtered (b) IVUS images. Page 128

Figure 6.11. Evaluation of detected contours at two layers (L1,L2) in 104 IVUS frames within a pullback with two different block sizes. Tanimoto coefficients (a), Regression analysis (b). Page 130

Figure 6.12. Original IVUS frame (a), filtered IVUS frame using tiling of frequency domain with 16x16x8 cubes (b), automated detected contours with elliptical shape constraint at first layer (L1, red), second layer (L2, blue), third layer (L3, green) and forth layer (L4, magenta) along with manually traced lumen (yellow) as well as vessel wall (cyan) borders (c). Page 132

Figure 6.13. IVUS frame in Cartesian (a) and polar (b) coordinates and the real part of brushlet coefficients at two different orientations (cubes) corresponding to low frequency components in 4x4x2 expansion scheme. Page 133

Figure 6.14. Thresholded brushlet coefficients corresponding to **Figure 6.13(c)** (a), and **Figure 6.13(d)** (b), classified denoised image using ICM algorithm and four classes in polar (c) and Cartesian (d) coordinates, filtered image corresponding to **Figure 6.13(a)** and automated detected borders extracted from four classes along with manually traced border (yellow) (e). Page 133

Figure 6.15. Real part (a), imaginary part (b), and magnitude (c) of brushlet coefficients in the four innermost cubes at the first subband in 4x4x2 expansion scheme corresponding to blood and non-blood regions. Page 134

Figure 6.16. Real part (a), imaginary part (b), and magnitude (c) of brushlet coefficients in two cubes (14 and 22) that exhibits the largest separation. Page 134

Figure 6.17. Automated (red (L1), blue (L2), green (L3), and magenta (L4)) detected borders depicted on few denoised IVUS frames along with corresponding manual (yellow) traced borders. The results are achieved from expansion of sub-volume of IVUS frames in 4x4x2 scheme followed by thresholding of coefficients in cubes representing $\pm 45^\circ$. Page 135

Figure 6.18. Validation of automated detected borders within short pullback with respect to manually traced borders. Calculated Tanimoto coefficients and corresponding statistics (a) Linear regression analysis (b). Page 135

Figure 6.19. Automated (red (L1), blue (L2), green (L3), and magenta (L4)) detected borders depicted on few denoised IVUS frames along with corresponding

manual (yellow) traced borders. The results are achieved from expansion of sub-volume of IVUS frames in 4x4x2 scheme followed by thresholding of coefficients in cubes representing $+45^\circ$ and zeroing out coefficients in the rest of innermost cubes using generated binary mask. Page 137

Figure 6.20. Calculated Tanimoto coefficients for a short pullback and corresponding statistics. Page 137

Figure 6.21. IVUS frame in Cartesian (a) and polar (b) coordinates. Binary blood (c) and plaque (d) maps generated from manual tracing by an expert. The radial (c) and angular (d) distances are illustrated in red. Real part (e), imaginary part (f), magnitude (g) and phase (h) of brushlet coefficients computed on the radial image (b) along a single orientation. Page 139

Figure 6.22. Two distinct grayscale IVUS frames. Generated blood maps (left column), superimposed blood maps on original grayscale IVUS images with manually traced lumen borders (yellow) by an expert (middle column), and automated detected lumen border (red) by thresholding the grayscale image resulting from output of neural network. Page 142

Figure 6.23. 3-D synthetic image, exhibiting textures with different orientations. Page 145

Figure 6.24. Magnitude of brushlet coefficients in first sub-band (a), and second sub-band corresponding to of 3-D synthetic data in 4x4x2 expansion scheme. Page 145

Figure 6.25. Real part (a,b), imaginary part (c,d), and magnitude (e,f) of brushlet coefficients in the first sub-band (R_1^1 , left column) and the second sub-band (R_1^2 , right column) in 4x4x2 expansion scheme. Page 147

- Figure 6.26.** Resulting grayscale images from summation of brushlet coefficients (a) in four (top row) and two (bottom row) innermost cubes in 4x4x2 expansion scheme. Enhanced images using $\gamma = 1.6$ (b) and $\gamma = 2.2$ (c). Page 149
- Figure 6.27.** Original grayscale images of brushlet coefficients in 4x4x2 expansion (a,b) and corresponding grayscale images of enhanced coefficients (c,d). Page 150
- Figure 6.28.** Real part (a), imaginary part (b), magnitude (c), angle (d) of summed coefficients in the four innermost cubes in 4x4x2 expansion scheme (top row) and their corresponding counterparts after enhancement $\gamma = 2$ (bottom row). The original image is depicted in **Figure 6.23**. Page 151
- Figure 6.29.** Schematic representation of arbitrary tiling of Fourier space using 2x2x2 cubes (a) 4x4x4 cubes (b) in u_x, u_y, u_z directions. Page 152
- Figure 6.30.** Original IVUS frame (a), reconstructed IVUS frame using brushlet coefficients in (b), (c) and (d) in 4x4x2 expansion scheme. Page 153
- Figure 6.31.** Original IVUS frame (a), reconstructed IVUS frame using brushlet coefficients in (b), (c) and (d) in 6x6x2 expansion scheme. Page 153
- Figure 6.32.** Reconstructed IVUS frame using brushlet coefficients in (a), (b), (c), and in 8x8x2 expansion scheme. Corresponding original IVUS frame is depicted in **Figure 6.30(a)** and **Figure 6.31(a)**. Page 153
- Figure 6.33.** Original IVUS frame (a), reconstructed IVUS frame using coefficients in $R_1^{1,2}(S_1)$ in 32x32x2 (b), 64x64x2 (c), and 128x128x2 (d) expansion schemes. Vessel wall and lumen borders have been traced by green and red colors, respectively. Page 155

Figure 6.34. Original IVUS frame (a), grayscale images of summed brushlet coefficients in s_1 (b) s_2 (c) s_3 using $64 \times 64 \times 2$ expansion scheme and corresponding reconstructed IVUS frames in spatial domain. Page 155

Figure 6.35. Iterative projections of the innermost spheres, corresponding to low frequency components, using $4 \times 4 \times 2$ expansions scheme. Page 157

Figure 6.36. Magnitude of computed brushlet coefficients derived from iterative decomposition of the innermost spheres that preserve low frequency components. Magnitude of coefficients in the first (a) and the second (b) subband after the first decomposition (the first level). Magnitude of coefficients in the first (c) and the second (d) subband after the second decomposition (the second level). Magnitude of coefficients in the first (e) and the second (f) subband after the third decomposition (the third level). Page 158

Figure 6.37. Iterative projections of the innermost spheres, corresponding to low frequency components. Unlike previous approach the resolution of tiling was fixed, here the resolution is increased at each level of decomposition. Page 159

Figure 6.38. Original IVUS frame (a), reconstructed IVUS frame using coefficients in S_1 in $8 \times 8 \times 2$ (b), $16 \times 16 \times 2$ (c), $32 \times 32 \times 2$ (d), $64 \times 64 \times 2$ (e), and $128 \times 128 \times 2$ (f) expansion schemes. Page 160

Figure 6.39. Reconstructed IVUS frame using coefficients in S_1 (top row) and R_1^1 (bottom row) in $8 \times 8 \times 2$ (a) $64 \times 64 \times 2$ (b) and $128 \times 128 \times 2$ (c) expansion schemes. Page 161

Figure 6.40. Original IVUS frame (a), reconstructed frame using coefficients in S_1 in 8x8x2 (b), 8x8x4 (c) and 8x8x8 (d) expansion schemes. Page 161

Figure 6.41. Original IVUS frame (a), reconstructed frame using coefficients in S_2 in 8x8x2 (b), 8x8x4 (c) and 8x8x8 (d) expansion schemes. The highlighted rectangle shows that some border information can be extracted from high frequency cubes (S_2) when u_z is increased. Page 161

Figure 6.42. Reconstructed IVUS frames through direct (top row) and iterative (bottom row) decomposition techniques using coefficients in S_1 , S_2 , and S_3 in 64x64x2 expansion scheme. Page 162

Figure 7.1. Constructed magnitude-phase 2.5-D histogram from summed coefficients in R_1^l after projection of in-vitro IVUS sub-volume using 4x4x2 expansion scheme before (a) and after (b) smoothing. The resolution of both histograms is 200x200. Page 174

Figure 7.2. The effects of parameter p on created histogram. $p = 0.5$ (a), $p = 1$ (b), $p = 2$ (c). Page 175

Figure 7.3. IVUS grayscale image acquired from Plexiglas phantom cylinder with circulating blood mimicking fluid in polar domain (a), constructed 2.5-D magnitude-phase histogram (b), generated binary masks corresponding to each peak (c-e), detected cylinder border (red) imposed on the IVUS grayscale image corresponding to (a) in Cartesian domain (f). Page 182

Figure 7.4. Reconstructed IVUS frame after projection of the frame onto 2-D (a) and 3-D (b) brushlet basis and thresholding the real part of the coefficients, constructed 2.5-D magnitude-phase histogram from coefficients derived

from 4x4 expansion scheme in 2-D case (c), and resulting detected cylinder border (d). Page 183

Figure 7.5. Constructed magnitude-phase histogram (a), generated binary masks (b,c), automated (red) and manual (green) traced borders imposed on original IVUS grayscale image (d). Page 183

Figure 7.6. Resulting automated lumen detected border (red) along with manual traced contour (green) imposed on six distinct IVUS frames. The case specifications have been described in **Table 7.2**. Page 184

Figure 7.7. The Bland-Altman plot for lumen areas derived from automated and manual traced borders. Page 185

Figure 7.8. Resulting automated lumen detected border (red) along with manual traced contour (green) imposed on six distinct IVUS images acquired from six patients using single-element 40MHz transducers. The case specifications have been listed in **Table 7.3**. Page 186

Figure 7.9. The Bland-Altman plot for lumen areas derived from automated and manual traced borders. The plot is for data acquired with single-element 40MHz transducers. Page 187

Figure 7.10. Resulting automated lumen detected border in images acquired with 45MHz single-element transducer through our proposed technique (red), *Method 2* (yellow), and *Method 3* (cyan), along with manual traced contour (green) imposed on six distinct IVUS images acquired from six patients using single-element 45MHz transducers. The case specifications have been listed in **Table 7.2**. Page 189

Figure 7.11. Resulting automated lumen detected border in images acquired with 45MHz single-element transducer through our proposed technique (red), *Method 2* (yellow), and *Method 3* (cyan), along with manual traced contour (green) imposed on six distinct IVUS images acquired from six patients using single-element 45MHz transducers. The case specifications and quantitative results have been listed in **Table 7.3** and **Table 7.4**, respectively.

Page 191

Figure 7.12. Probability distribution ρ_{in} and ρ_{out} derived from images acquired with 20 MHz (a), 40 MHz (b), and 45 MHz (c) transducers. The probability distributions were computed from two datasets (solid and dashed lines) in images acquired with 40 MHz and 45 MHz transducers.

Page 195

Figure 7.13. Constructed magnitude-phase histograms for two cases: 1) a frame within stable (consistent) sub-volume of analysis before (a) and after (b) registration, 2) a frame within unstable (inconsistent) sub-volume of analysis before (c) and after (d) registration.

Page 197

Figure 7.14. Constructed grayscale images from summed coefficients in R_1^2 (a), R_1^1 (b), R_2^2 (c), R_2^1 (d) using 4x4x2 expansion scheme and R_1^1 (e), R_1^2 (f), R_1^3 (g), R_1^4 (h), R_2^1 (i), R_2^2 (j), R_2^3 (k), and R_2^4 (l) using 4x4x4 expansion scheme.

Page 199

Figure 7.15. Magnitude-phase histograms constructed from coefficients depicted in **Figure 7.14**.

Page 201

Figure 7.16. Constructed magnitude-phase histograms from coefficients in S_1 in 4x4x4 expansion scheme for two cases: 1) a frame within stable (consistent) sub-volume of analysis by choosing 8 (a) and 16 (b) frames per block and corresponding detected lumen borders (red) (b,d) along with manually traced borders (green), 2) a frame within unstable (inconsistent) sub-volume of analysis by choosing 8 (a) and 16 (b) frames per block and corresponding detected lumen borders (red) (f,g) along with manually traced borders (green).

Page 202

Figure 7.17. Constructed multi-frame magnitude-phase histograms from coefficients in all cubes in S_1 in 4x4x4 expansion scheme for two cases: 1) a frame within stable (consistent) sub-volume of analysis by choosing 8 (a) and 16 (b) frames per block, 2) a frame within unstable (inconsistent) sub-volume of analysis by choosing 8 (a) and 16 (b) frames per block.

Page 203

Figure 8.1. Two examples where the algorithm fails to correctly identify lumen borders. An eccentric artery with deep shallow (a), repetitive reflection of ultrasound signals (ring-down artifact) from surface of transducer's element (b).

Page 210

Acknowledgment

First and foremost, I would like to express my sincere gratitude to my advisor, Dr. Andrew Laine, who has been of extensive support and encouragement during all these years as his graduate student. He has always been a steadfast patient guide, leading me thorough scientific driven challenges. Beyond academic research, he gave me the opportunity to initiate and engage in collaborations with clinicians, faculties, and industry research groups both on national and international scales. This was in fact a valuable experience that a typical Ph.D. student would not practice during his course of study. Thanks Andrew, for providing me everything that a Ph.D. student can possibly wish for and being a great advisor as well as friend.

I especially wish to thank my first advisor, Dr. Elisa Konofagou who guided me through my first research project and supported my application to the Doctoral program. The joy and enthusiasm she has for her research is truly motivational. I appreciate all her contributions, thoughts, and funding to make my research uninterrupted and productive during tough times in the Ph.D. pursuit.

I would also like to thank Dr. Stephane Carlier as my co-advisor and friend to whom I owe most of my career success. He introduced me to the world of interventional cardiology and always supported me to present my work within clinical community, which built up my confidence. I always enjoyed performing experiments with him, collecting hearts from cadavers or animal catheterizations where a sense of humor and

optimism were in the air at all times. Stephane! I am so proud and honored for being your first graduated Doctoral student.

The lumen border detection studies discussed in this dissertation would not have been possible without Dr. Elsa Angelini and Dr. Bernhard Sturm supports and helps. It has been a real privilege to work with Elsa whose kindness and sharp mind helped me to look at brushlet analysis from different perspective and finally explore its relationship with tissue's response to ultrasound signal. Indeed, her valuable inputs and comments improved the scientific merits of my dissertation. I am also very grateful to Bernhard for his worthy insight to our discussions and brainstorming phone conferences that played an integral role in developing of our algorithm.

I wish to thank other members of my defense committee, Dr. Ioannis Kakadiaris, Dr. Thomas Gustafsson, and Dr. Paul Sajda in particular for their constructive comments. I am so delighted to know Paul who provided me inspiring discussions, stimulating critiques, and the best suggestions during my oral qualifying exam and proposal as well as dissertation defense.

A special thank to Dr. Qi Duan, who has always been immensely generous with his time. After three years of his graduation, students at Heffner Biomedical Imaging Lab still benefit from his codes as well as contributions and so did I. It would be an omission if I did not thank Dr. Gozde Unal for having me at her lab and sharing her code for

comparison study. In this regard, I also thank Dr. Naasir Navab and Dr. Taki for their feedbacks and collaborative study.

I would also like to gratefully acknowledge the funding sources that made my Ph.D. work possible. Thanks to Dr. Anuja Nair and executives of Volcano Corporation (Rancho Cordova, CA) who trusted my knowledge when I demonstrated my results at TCT conference and awarded me a fellowship to work on lumen border detection problem. My initial work on atherosclerotic tissue characterization was also founded by Boston Scientific Corporation (Fremont, CA) and I thank Dr. Sathyanarayana, Dr. Li, Dr. Thomas, and Dr. Tatjin for their supports. My work was supported by Siemens (Princeton, NJ) in partial too.

I wish to thank Dr. James Muller, Dr. Steve Sum, and Jennifer Lisauskas at InfrareDx (Burlington, MA) for their helps in collecting IVUS data along with corresponding histology images. I also would like to thank Dr. Joseph Schmitt and Dr. Chenyang Xu at Lightlab Imaging (Westford, MA) for their collaborations in OCT data acquisition.

Very much I wish to thank Babak Baseri and Alper Selver for their contributions in IVUS-histology matching process and preliminary study of brushlet analysis, respectively. I also would like to thank my fellow graduate students at Heffner Biomedical Imaging Lab: Noah Lee, who always had time for scientific discussions and stimulating conversations, Antonio Albanese, Ilyana Atanasova, Auranuch Lorsakul, Won Hee Lee, and especially Ming Jack Po. I also would like to thank two of my best

friends, Alireza Shirazi and Mohsen Shaaker, who provided me with tremendous support while going through all “adventures” of being a graduate student.

I am forever indebted to my family for their unconditional support throughout my academic career. I am so thankful to my sister who has been constant source of encouragement, strength, and motivation. I would like to thank my brother to whom I would have not come this far without his support especially upon my arrival to the US. To my parents I owe everything and I cannot give enough thanks to them for their love and support. Wherever you are, your pride is my greatest everlasting reward. I am also so grateful to my wife’s family for their love and understanding especially during the final stages of my Ph.D. The joy and excitement of this journey was intensified when I married Tannaz two month prior to my defense. Tannaz! you are the best thing that ever happened to me and I appreciate your loving support, encouragement, and patient to complete the Ph.D.

This work is dedicated to my parents and my beautiful wife.

Amin Katouzian

February 2011

New York

1. Chapter One:

INTRODUCTION

1.1. Medical Background

Heart disease or cardiopathy is the number one killer of human worldwide and is responsible for 25.4% of all deaths in the United States [1,2]. It refers to variety of different diseases affecting the heart, which among them coronary heart disease (CHD) is the most common type of heart disease and takes about 500,000 lives in the United States every year [3]. Although CHD is commonly equated with coronary artery disease (CAD) it may be due to other causes such as coronary vasospasm. Nevertheless, both may correlate with deficiency or failure in coronary circulation and ultimately supplying adequate blood, oxygen, and nutrients to cardiac muscles (myocardium) and surrounding tissues, resulting instable or stable angina pectoris (chest pain or discomfort), myocardial infarction also known as heart attack, and sudden death due to full occlusion of coronary artery when an atherosclerotic plaque ruptures, activating the clotting system and atheroma-clot interaction fills the lumen of the artery to the point of sudden closure. Persons at risk typically have no premonitory symptoms, and angiographic studies of coronary arteries in patients with non-fatal acute coronary syndromes (ACS) showed that most such events are because of rapid progression of mild, hemodynamically insignificant lesions [4-6]. In fact, by the time that heart problems due to CAD are detected, the underlying cause (atherosclerosis) is usually quite advanced. Many forms of heart disease including CAD and cardiovascular disease can be prevented or treated with

healthy lifestyle choices, diet, and exercise. In practice, CAD is treated by cardiologists, interventional radiologists or cardiologists through medication, non-invasive, or invasive procedures. The choice of physical treatment approach depends on severity of extended disease, which could lead to minimally invasive (e.g. angioplasty, stent implantation) or invasive (e.g. bypass, heart transplantation) surgical procedures.

Atherosclerosis was a widely misunderstood disease because of misconception about the nature of the arteries that had been thought of as stiff pipes that progressively become clogged. Now a day, the atherosclerosis disease has been redefined and is recognized as a chronic inflammatory disease that affects arteries functionality. In this revised vision, the arteries viewed as muscular organs that adapt their environment in response to various factors, such as change of pressure, by contraction and expansion. More importantly, a new era has begun to unravel the biochemical processes that trigger atherosclerosis disease and has yet to filter into mainstream medicine. Hence, the most progressive and forward-thinking researchers develop innovative approaches to compensate for the endothelial dysfunction that underlies coronary heart disease.

1.1.1. Coronary Atherosclerosis

The CAD or atherosclerotic heart disease is indeed the leading life taking disease in the world, particularly in developed countries. The word “atherosclerosis” comes from the Greek words “athero” and “sclerosis”, meaning gruel or paste and hardness, respectively. As it is inferred from the name, it is a disease in which atheromatous plaque, consisting of fatty substances (*i.e.* cholesterol), platelets, cellular waste products, and calcium build

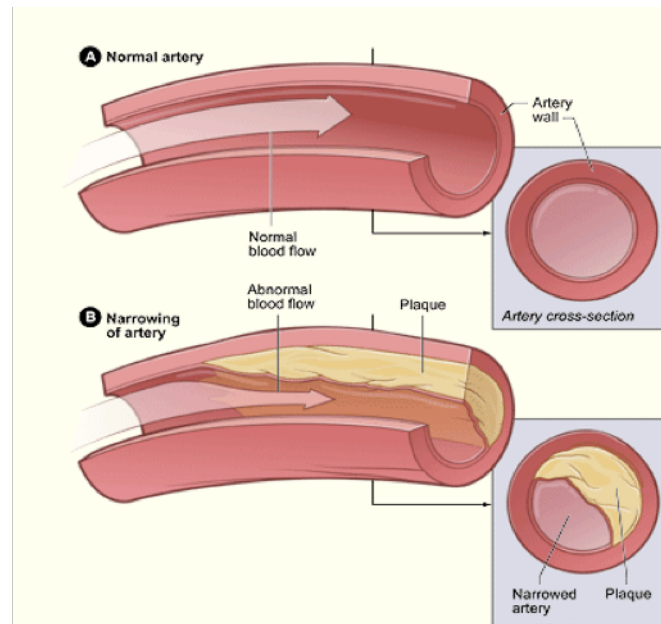


Fig. 1.1. Schematic of a normal artery (a) and its diseased (narrowed) counterpart (b) along with corresponding cross sections. (Reference: <http://www.nhlbi.nih.gov>).

up in the innermost layer of an artery called endothelium. **Figure 1.1** illustrates the schematic of a normal artery in comparison with diseased counterpart and corresponding cross sections. The disease is typically asymptomatic, chronic, slowly progressive, cumulative, and eventually leads to plaque ruptures and therefore clots inside the artery lumen over the ruptures. The clots heal and usually shrink but leave behind stenosis (narrowing) or in worse case scenario complete occlusion of the artery, leading to insufficient blood supply to myocardium tissues and ultimately myocardial infarction (MI). The known risk factors associated with causes of damage to the arterial wall (endothelial cells) include:

- Elevated level of cholesterol and triglyceride in blood.
- High blood pressure.
- Tobacco smoke.
- Diabetes.

Other factors such as advanced age, male sex, hypertension, short sleep duration, and high carbohydrate and trans fat intake may increase the risk as well [7]. Not every person who suffers from atherosclerosis has the risk factors we commonly associated with the disease, such as elevated cholesterol, but every single person with atherosclerosis has endothelial dysfunction.

1.1.2. Endothelial Dysfunction

The arterial wall consists of three layers, intima, media, and adventitia as it appears in Figure 1.2(a). The cause and progression of atherosclerosis are intimately related to the health of the inner arterial wall (intima) that is a smooth with protective surface and consists of a thin layer of endothelial cells, called endothelium. This layer is mainly responsible for adjusting the arterial wall response to any change in blood pressure and preventing toxic as well as blood-borne substances from penetrating to the middle layer (media), which consists of smooth muscles and controls blood flow and pressure by contraction and expansion. Finally, the outer layer (adventitia) is mostly connective tissues and provides structures to the layers beneath.

As we age, the endothelium protective surface becomes leaky, allowing toxins and lipids to infiltrate the middle layer and cause injury. Consequently, the smooth muscle cells congregate at site of injury, resulting loss of flexibility, and endothelium signals white blood cells to immune the wound by damaging free radicals and releasing pro-inflammatory substances such as leukotrienes and prostaglandins. At this point, toxins begin to break into the arterial wall, where low-density lipoprotein (LDL), cholesterol,

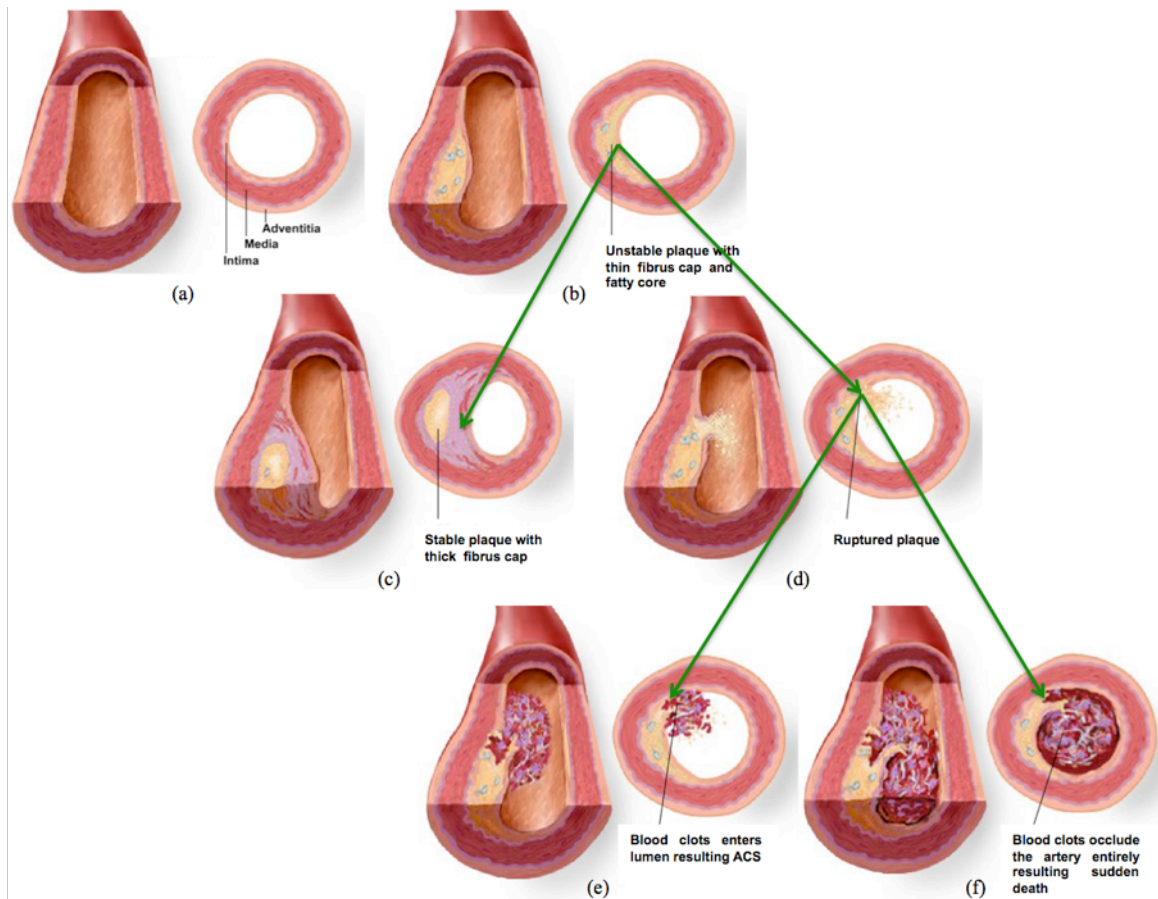


Fig. 1.2. Endothelium dysfunction. Normal artery with structural layers (a), atherosclerotic plaque builds up in the endothelial layer (intima) that may lead to unstable plaque (b). It becomes stable if thick fibrotic cap is constructed on top of the lipid core (c) or ruptures (d) that may result in ACS (e) or sudden death (f) depending on sized of blood clot occlusion. (Reference: <http://www.americanheart.org>).

and triglycerides start accumulating and oxidizing. In response to the oxidized lipids, the body forms an intensive immune response by provoking more white blood cells to attack the fats, which causes more inflammation within the arterial wall. Meanwhile, the smooth muscle cells begin to produce collagen to construct a cap over the site of injury. In fact, the atherosclerotic plaque is a result of the mixture of oxidized lipids, white blood cells, and smooth muscle cells. Over time, calcium is also deposited into the plaque and ensembles a brittle cap. Once the calcified plaque ruptures, a blood clot can form and may result in a heart attack or stroke. All the processes described above, in which the

inner arterial wall is damaged and normal endothelial function is compromised, are collectively referred to as endothelial dysfunction. **Figure 1.2** illustrates endothelium dysfunction and progression of atherosclerotic plaque within endothelial wall that may result in formation of vulnerable plaque and potentially ACS or sudden death. As we can see the risk of complication proportionally increases with percentage of stenosis. Although the average absolute risk of severely stenotic plaques may be higher than the average absolute risk of mildly stenotic plaques, there are more plaques with mild stenosis than plaques with severe stenosis.

1.1.3. Vulnerable Plaque

In 1966, Constantinides [20] examined 17 autopsied cases and for the first time concluded that fissure of thin fibrous cap in atherosclerotic plaque causes thrombosis. This primary study led to further investigations on plaque rupture and its consequences [21-25]. Since then, the term “culprit plaque” widely has been used by interventional cardiologists and cardiovascular pathologists and it refers to a plaque responsible for coronary occlusion and ultimately death regardless of its histopathologic characteristics. In the meantime, prospective evaluations motivated clinicians to define a new term for describing such plaques before *ruptures* or those that were responsible for *acute coronary events*. For the past about 40 years, different terminologies have been introduced and continually updated by scientists such as “unstable plaque”, “dangerous plaque”, “plaque disruption” [10,11], “high-risk plaque” [12], and “vulnerable plaque” [12,13]. Over the past few years, the vulnerable plaque (initially proposed for describing plaques with large lipid pool, thin fibrotic cap, and macrophage-dense inflammation on or beneath its

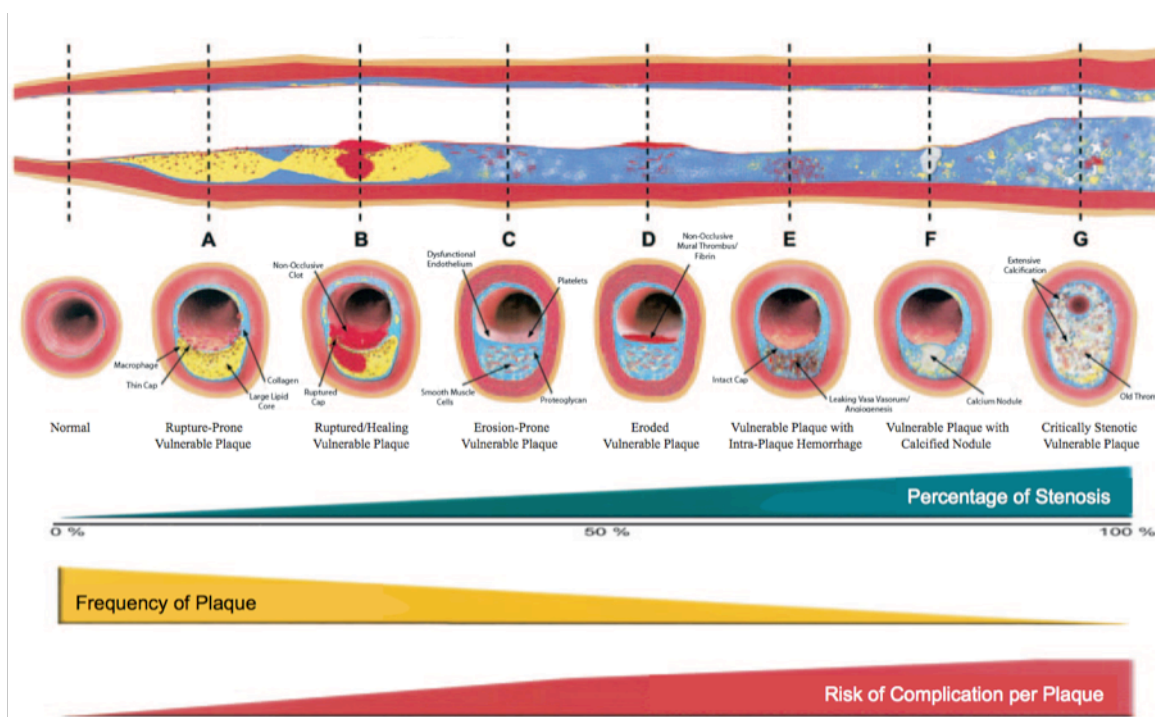


Fig. 1.3. Different types of vulnerable plaques introduced by Naghavi *et al.* [19]. Rupture-prone plaque with large lipid core and thin fibrous cap infiltrated by macrophages (A). Ruptured plaque with subocclusive thrombus and early organization (B). Erosion-prone plaque with proteoglycan matrix in a smooth muscle cell-rich plaque (C). Eroded plaque with subocclusive thrombus (D). Intraplaque hemorrhage secondary to leaking vasa vasorum (E). Calcific nodule protruding into the vessel lumen (F). Chronically stenotic plaque with severe calcification, old thrombus, and eccentric lumen (G). Correlation between degree of stenosis (green bar), frequency of plaques (yellow bar), and risk of complication per plaque (red bar) as a function of plaque progression.

surface, **Figure 1.3(A)**) has been broadly adopted by investigators and clinicians to denote susceptible plaques with different morphological features, **Figure 1.3**, that potentially could lead to ACS or sudden cardiac death.

During these years, there was no consensus on either employed terminologies or definition for vulnerability of plaque [14-18]. Hence, in a comprehensive report, Naghavi *et al.* [19] suggested a uniform language to standardize the terminology and recommended “vulnerable plaque” as a benchmark. Based on their new definition, the rupture-prone plaques are not the only vulnerable plaques and all types of atherosclerotic

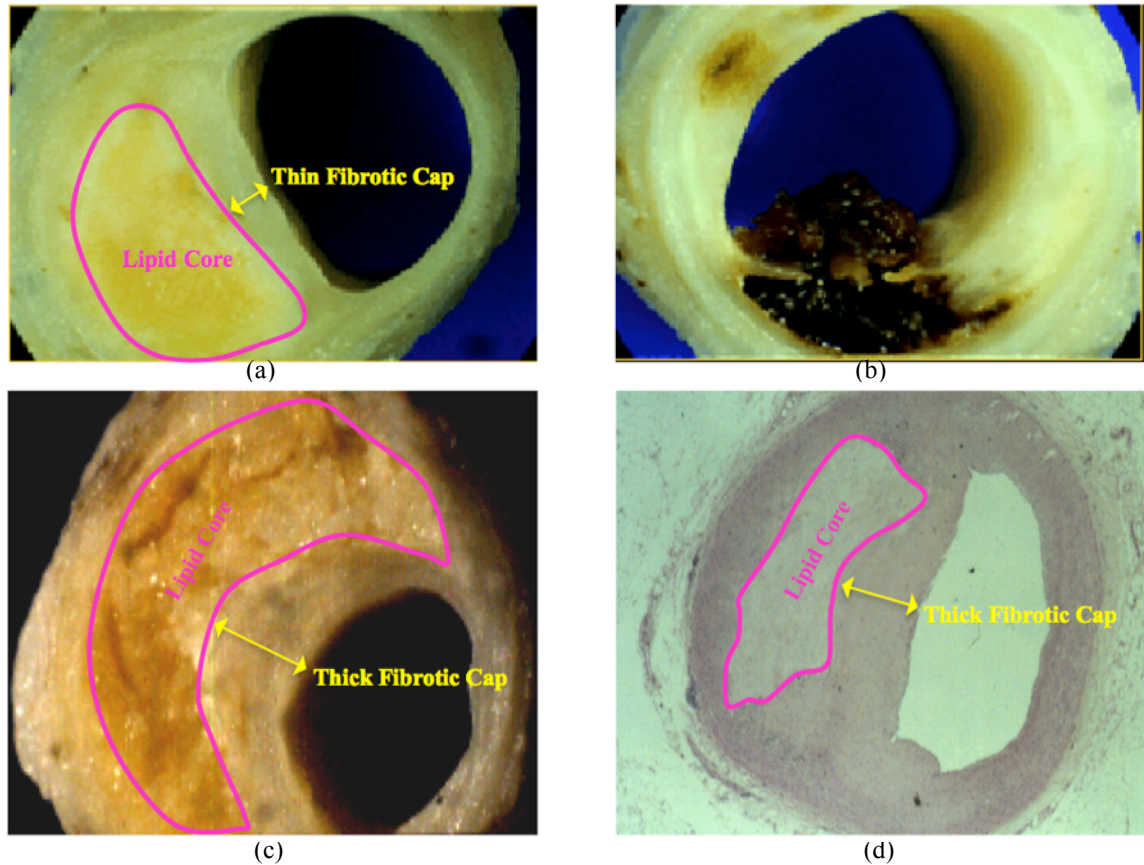


Fig. 1.4. A vulnerable plaque before (a) and after (b) rupture. Degree of vulnerability significantly decreases if the fibrotic cap becomes thicker, which turns an unstable plaque (a) to a stable plaque (c). Histology image (d) corresponding to the stable plaque.

plaques, **Figure 1.3**, with high likelihood of thrombotic complications, rapid progression, and thus becoming culprit plaques must be considered as vulnerable plaques. They further introduced numbers of vulnerability morphological/structural markers based on study of culprit and stenotic plaques such as:

- Cap Thickness.
- Lipid core size.
- Percentage of stenosis (narrowing).
- Mechanical stability (stiffness and elasticity).
- Calcification burden and pattern (nodule vs. scattered, superficial vs. deep, etc).
- Shear stress (flow pattern throughout the artery).

- Remodeling (expansive vs. constrictive).

From mechanical point of view, hemodynamic pulsating expansion during systole and elastic recoil contraction during diastole contribute to a high mechanical stress zone on the fibrous cap of the atheroma, making it prone to rupture. **Figure 1.4(a,b)** demonstrates a vulnerable plaque before and after rupture.

1.1.4. Stabilization of Vulnerable Plaque

Often degree of vulnerability significantly decreases if fibrotic cap becomes thicker, **Figure 1.4(c,d)**. In traditional language, an unstable plaque evolves to a stable plaque by construction of a thick fibrous cap on top of a lipid rich pool. Although this natural process stabilizes the vulnerable plaque it may not be certain for all cases. Therefore, researchers strive to take advantage of different mechanisms at physical, biochemical, and cellular levels to stabilize the vulnerable plaque. Lowering lipid contents of atheromatous plaques and improving endothelial function are two possible alternatives for plaque stabilization. It has been shown that the reduced lipid content is usually accompanied by an increase in collagen concentration that may enhance plaque stiffness and increase stability [26,27]. Among drugs, the lipid-lowering agent such as statin that reduces the LDL cholesterol and increases endothelial functionality is probably the most effective. Another beneficial possibility is the use of gene therapy that requires better understanding of the molecular bases of vulnerable plaque. Needless to say, in the present outcome-oriented era, the future direction of plaque stabilization developments and

therefore atherosclerotic disease management is greatly influenced by new screening modalities that can identify vulnerable plaques with detail characteristics.

1.2. Identification of Vulnerable Plaques

Recent technological advances along with important role of vulnerable plaques in CHDs have drawn investigators' attentions into expansion of physiological, pharmaceutical, and technological approaches in the field of cardiovascular medicine. For the past couple of decades, we have observed changes in life styles, diets, drug therapies, screening modalities, and interventional devices/procedures to prevent progression of atherosclerotic disease in patients. Among all aforementioned alternatives, the imaging technique was the core component that provided interventional cardiologist imperative characteristics of plaques so they could make better decisions during catheterization procedures and validated the effectiveness of new drugs on progression or regression of atherosclerotic plaques in clinical trials. More importantly, the successful treatment of atherosclerosis extremely depends on the stage of the disease so diagnosis systems play a crucial part in correct identification and characterization of the lesions. In this section, we briefly review existing intravascular imaging modalities along with overall advantages, disadvantages, and limitations. Based on interventional cardiologist diagnosis, non-invasive or minimally invasive screening modality might be employed to evaluate the stage of atherosclerosis disease and underlying plaques. Non-imaging approaches are excluded in this study.

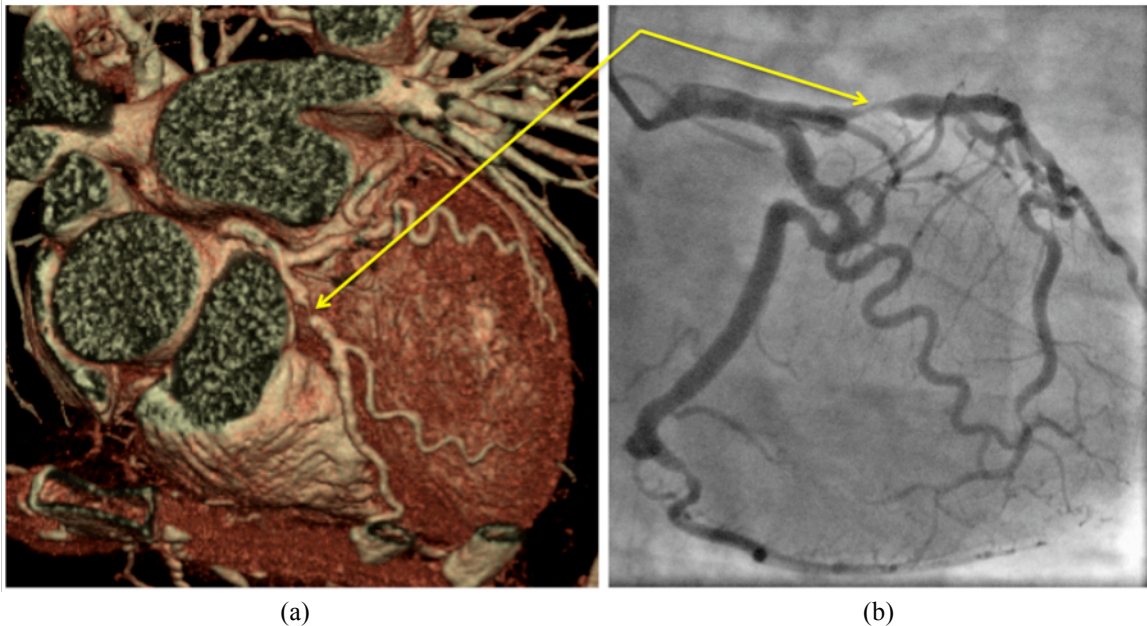


Fig. 1.5. Transaxial view of a contrast-enhanced CTA (a) and corresponding angiogram (b). Yellow arrows point to site of occlusion.

1.2.1. Non-Invasive Techniques

Non-invasive screening techniques are usually recommended for routine check-ups, follow-ups, and for those who have no premonitory symptoms.

1.2.1.1. Computed Tomography Angiography (CTA)

Electron-Beam Computed Tomography (EBCT) is a diagnosis imaging modality that combines the use of X-ray with computerized technology to produce two-dimensional (2D) cross-sectional images (slices) of an organ. In this technique, the X-ray beam circularly moves around the area of interest, allowing different views from the same organ, and interacted X-ray information is characterized by a computer. A newer technology, ultrafast computed tomography (UCT), provides multiple images of the heart

with detailed structures within a single heartbeat. This mechanism is currently being used to quantify the amount of calcium in coronary arteries. **Figure 1.5** illustrates transaxial view of a contrast-enhanced CTA and its corresponding angiogram.

This technique is usually recommended by physicians to diagnose early CHD in people with no symptoms. Although calcification is weighted for CHD its presence might not be correlated with identification of vulnerable plaque. Strictly speaking, the morphological property of a calcified plaque and its interpretation by interventional cardiologist must be taken into account. For example, calcified nodules are sometimes found in vulnerable plaques, **Figure 1.3(F)**, while arc of calcified plaques usually considered as natural stents that make plaques stable. Furthermore, measurement of coronary calcium is not considered relevant in patients, who have already had a heart attack, undergone coronary bypass surgery, or coronary angioplasty. Similarly to all X-ray based diagnosis imaging techniques, exposure of patient to X-rays that are ionizing radiations can be a health hazard.

1.2.1.2. Magnetic Resonance (MR) Based Techniques

MR angiography (MRA) is a MR imaging (MRI) based technique to visualize blood vessels throughout the body. Different methods can be used to generate the images based on flow effects or inherent as well as pharmacologically generated contrast agents. Although MRA has been successful for studying many arteries in the body it has been less successful for studying coronary arteries, comparing with CTA and catheter angiography. The main drawback of MRA is limited spatial resolution, which is a

constraint particularly for delineation of vulnerable plaques. Instead, high-resolution MRI has been employed for detection and classification of atherosclerotic plaques based on biophysical and biochemical characteristics of plaque constituents [28]. The advantage of MR based modalities over CTA and catheter angiography is that the patient is not exposed to any ionizing radiation and contrast agents are less toxic. The disadvantages of this method are lengthier scan time and higher expense. The only limitation associated with these techniques is that patients with pacemakers and metals (i.e. surgical clips) should be excluded due to the presence of high magnetic fields.

1.2.2. Invasive Techniques

These screening techniques are usually deployed when interventional cardiologist is certain about stenosis and aims for balloon angioplasty or stent implantation.

1.2.2.1. Coronary Angiography

It is the most conventional screening technique that enables interventional cardiologists and radiologists to diagnose stenosis inside coronary arteries. Traditionally, a guide wire along with a catheter is advanced from femoral artery toward major coronary arteries in order to administer a radio-opaque contrast agent that absorbs X-rays. Once the contrast agent is injected into the blood at desired location, 2D real-time images are taken at 15-30 frames per second using X-ray based techniques such as fluoroscopy. X-ray images of the transient radio-contrast within flowing blood display the site of occlusion, **Figure 1.6(a)**. Although this technique allows the visualization of the anatomy of the coronary arterial vessels, there are important shortcomings. The angiogram is a 2D presentation of a three-

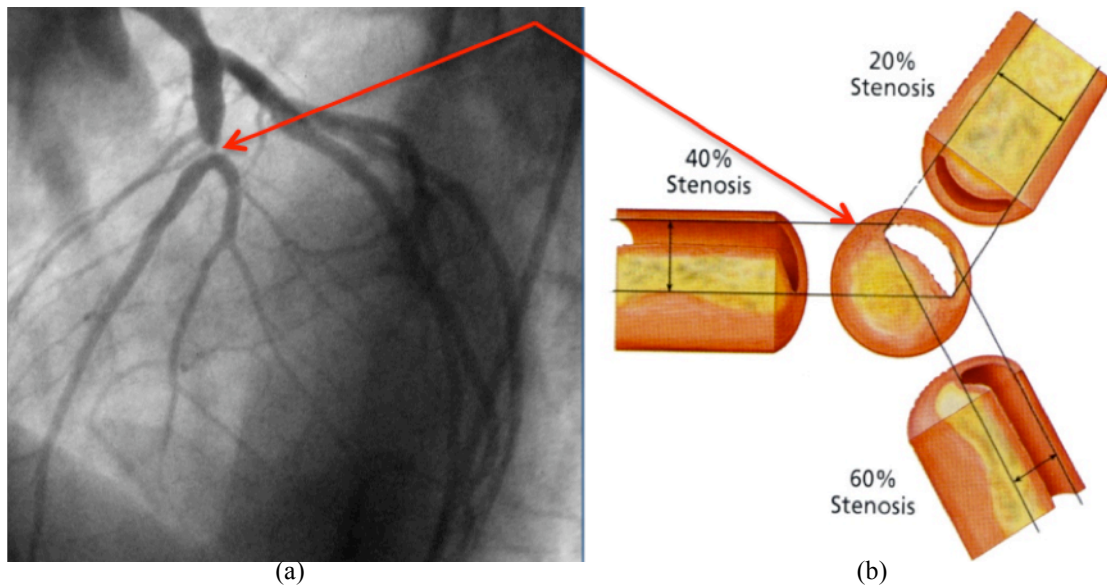


Fig. 1.6. A typical angiogram (a). Different projections may lead to under- or over-estimation of plaque burden (b). Red arrows point to the site of occlusion. (Reference: Cleveland clinic core lab).

dimensional (3D) structure. Stenosis that appears insignificant in one projection can appear severe in other projections, leading to under- or over-estimation of plaque burden, **Figure 1.6(b)**. For this reason, interventional cardiologist needs to take multiple projections during catheterization procedure or employs recently developed 3D angiography systems. With regards to detection of vulnerable plaques, this imaging method fails because it does not provide any information about plaque components. Minor complications associated with this imaging modality are bleeding or bruising at the site where the contrast agent is injected, exposure of patient to ionizing radiation, allergic reaction to the contrast agent, and similar to all catheterization procedures the catheter may damage the blood vessels on the route to the desired location.

1.2.2.2. Angioscopy

Intracoronary angioscopy, recognized as the first intravascular imaging device, is based on fiberoptic transmission of visible light. It facilitates direct visualization of the plaque

surface, color of the luminal surface, presence of thrombus, and macroscopic features of the arterial wall. With this technique, the old thrombus or the normal appearance of the vessel surface, fibrin/erythrocyte-rich thrombus or lipid rich core, and thin fibrous cap appear to be white, red, and yellow, respectively. This technique has several drawbacks. First, size of the device limits access to vessel trees or areas with severe stenosis. Secondly, it does not provide arterial wall structures at different layers. Third, the artery needs to be occluded and remaining blood must be flushed away with saline during examination.

1.2.2.3. Intracoronary Thermography (ICT)

Atherosclerosis is an inflammatory chronic disease, resulting from intensive immune response by white blood cells when damage to endothelial wall is occurred. The measurement of plaque temperature, released by activated inflammatory cells, has been shown to be an indicator for detection of culprit and vulnerable plaques [29-32]. The more inflammatory cells accumulate in plaque, the more heat is generated. The ICT is a catheter-based technique for functional imaging of atherosclerotic plaques and enables the direct measurement of plaque thermal heterogeneity. The local vessel wall temperature can be assessed by thermistor-, thermocouple- or infrared-based measurements. The former technique requires direct contact of either a single or multiple thermal sensors on the end of a catheter tip with the vessel wall, whereas the latter uses an infrared fiber optic catheter to measure temperature without contacting the vessel wall.

The use of ICT catheters appears to be feasible for detection of hot and thus suspected

vulnerable plaques. However, no detailed information about the type of vulnerability and plaque components is provided. The main limitation associated with this technique is that there is no consensus on the amount of temperature heterogeneity. Therefore, identification of vulnerable plaque through this technique becomes subjective. This could be due to several factors such as cooling effect of blood flow, its type as well as velocity, differences in types of thermistors, and use of medication like statin that has been reported to reduce the thermal heterogeneity.

1.2.2.4. Intravascular Optical Coherence Tomography (OCT)

Intravascular OCT is a catheter-based, high-resolution imaging method that provides cross-sectional images of arterial wall and its structures. In this technique, the intensity of reflected light from tissues is measured and compared with a reference. Due to its high resolution, OCT is considered to be the most promising imaging modality for detecting the thin-cap fibroatheroma (TCFA). Moreover, the OCT atherosclerotic tissue characterization has been subject of study for researchers and can be divided into intensity- and optical-derived techniques. In former approach, plaque components are classified by their relative intensities. For example, it has been suggested that fibrous plaques appears as homogeneous signal-rich regions, lipid plaques as signal poor regions with diffuse borders, and calcified plaques as sharply delineated signal-poor regions with islands of signal-rich regions [33,34]. Albeit absence of fundamental physical explanations and formulations, this approach has been utilized for *in vivo* applications [34-37]. On the other hand, optical-derived techniques are established from quantitative measurement of optical properties of atherosclerotic plaques such as scattering

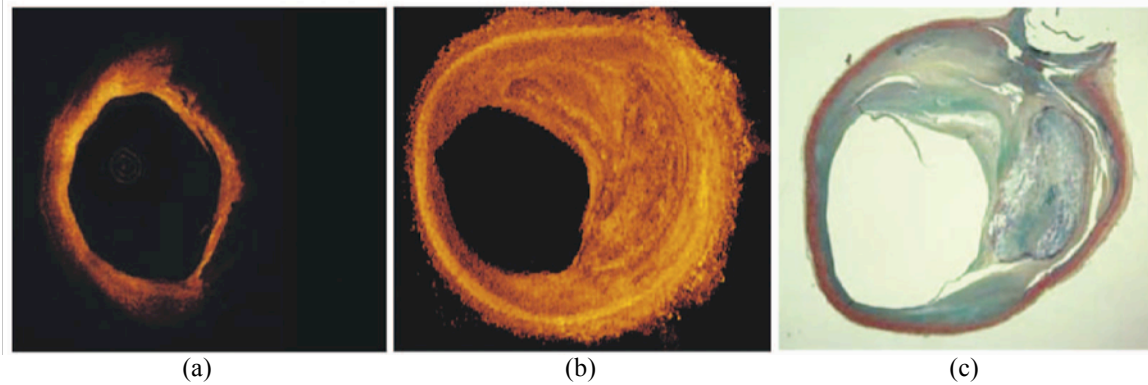


Fig. 1.7. [39] Rotary OCT image acquired with 500 μ m wavelength (a) corresponding transverse image (b) and Movat pentachrome histology (c).

coefficients [38] or combination of backscattering and attenuation properties of each tissue type [39]. The intravascular OCT imaging modality poses a serious limitation particularly for complete characterization and interpretation of atherosclerotic plaques, which is lack of sufficient penetration. As a result, the full radial extend of atherosclerotic plaques cannot be imaged. This can be clearly observed in **Figure 1.7** that shows a rotary OCT image and corresponding transverse image along with its histology.

1.2.2.5. Near Infrared (NIR) Spectroscopy

This technique relies on interactions between organic molecules and photon absorption that varies depending on the wavelength of the incident NIR light. Basically, the absorbance of light by organic molecules and vibrational transitions are measured in the range of NIR (750-2500 nm). The precise identification of subtle chemical differences is achieved through a highly developed mathematical method such as principal component analysis (PCA) that compares the characteristics of equations describing the reflectance spectra. The NIR and Raman spectroscopy have been used for characterization and quantification of chemical components of atherosclerotic plaques [40-44]. Recently, the NIR spectroscopy catheters have been developed to detect and assess the intracoronary

composition of lipid core plaques, which has been one of the indicators for vulnerable plaques. In general, the NIR spectra have low absorptivity and large bandwidths that highly overlap, which strongly influences spectral analysis, particularly in differentiating the precise biochemical components (i.e. cholesterol, lipid).

1.2.2.6. Intravascular Ultrasound (IVUS)

Similar to intravascular OCT and NIR imaging modalities, IVUS is a catheter-based technique but uses high frequency sound waves (20 MHz – 45 MHz) instead of light. In this technique, the catheter is pulled back from distal to proximal segments of an artery with certain speed and sound waves are sent and received by a transducer that has been designed at the tip of a catheter. Subsequently, the echoed signals are converted to grayscale images, **Figure 1.8**. It provides real-time relatively high-resolution cross-sectional images of arterial wall and lumen with sufficient penetration. It offers instant evaluation of morphological information regarding plaque and luminal area particularly in cases where the degree of stenosis is unclear when angiogram is used. Generally, the IVUS is deployed before and after stent implantation to make sure that the stent has been properly placed. Because, if a stent is not expanded flush against the wall of the vessel, turbulent flow may occur between the stent and the arterial wall, which could result in acute thrombosis and restenosis. Without a doubt, IVUS has enabled advances in clinical research providing a more thorough perspective and better behavioral understanding of atherosclerosis process since early 1990. It is also used for pathological interpretation of plaque components and identification of vulnerable plaques. After angiography, IVUS is the only imaging methodology that is widely available in coronary catheterization labs

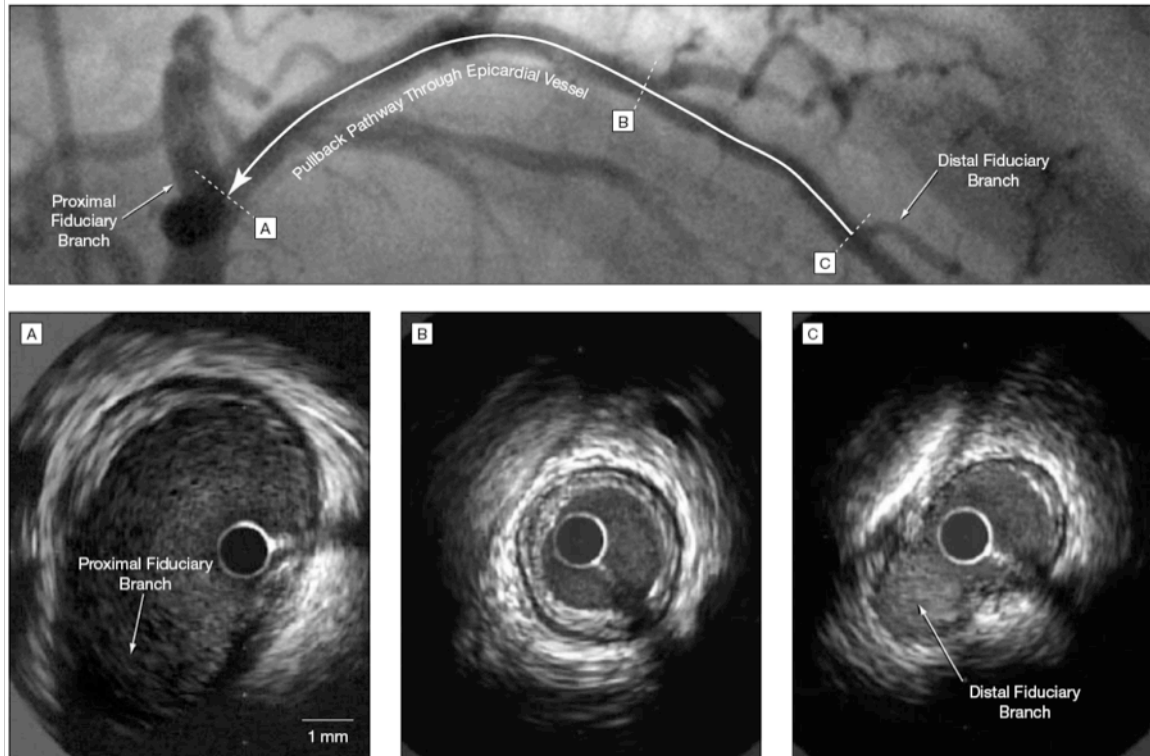


Fig. 1.8. Pullback pathway of IVUS catheter on angiogram (top row) and IVUS grayscale images (bottom row) at three distinct locations (A,B,C).

worldwide and increasingly being used to evaluate newer and evolving strategies for treatment of coronary artery disease. In fact, the IVUS is the only dependable screening method for quantification of novel technical and pharmaceutical approaches. The primary disadvantages of IVUS being used routinely in cathlabs are its expense and additional examination time, which are inherent in all catheter-based imaging methodologies (i.e. OCT, NIR).

1.3. Problem Statement

For many years, the ultimate goal of an interventional cardiologist was to physically expand narrowed artery, using balloon and stent, or create additional blood supply

connections through bypass surgery. With the invention and refinement of new intravascular imaging modalities, today, primary responsibility of an interventional cardiologist is not only to open up the site of occlusion but also to properly cure the atherosclerosis. For example, the United States food and drug administration (FDA) safety panel has suggested that cardiologists take more measures to reduce risks associated with the stents due to troubling headlines about potentially deadly clotting risks in small percentage of them. So far, researchers have mainly focused on the stents themselves and how they are made. But now, attention is turning more toward the way they are being used. There has been a consensus that widespread use of drug-coated stents may increase the risk of deadly clots formation, which has called attentions in the United States and widely reported in the media (*Fox News* report, October 9, 2008 - *The New York Times*, February 13, 2007 – *The Wall Street Journal*, May 7, 2007 - *The Boston Globe*, December 26, 2004) and in many scientific journals [45-49]. The medicine on the stent is released gradually over time to stop the progression of the scar tissue. However, it can also cause the artery to become narrow again, which is known as restenosis.

For chronic disease such as atherosclerosis, which may reoccur after balloon angioplasty, atherectomy, stent deployment, and even bypass surgery, the accurate diagnosis of vulnerable plaques is significantly imperative. In brief, *what make atherosclerosis one of the deadliest diseases is not stenosis alone but failure in detection and proper treatment of vulnerable plaques*. The problem becomes more complicated when we observe that there is no consensus on interpretation of vulnerable plaques from imaging perspectives as well as pathological point of view and it is rather performed in a subjective manner. *Today, more than ever, there is a need for reliable, reproducible, clinically approved*

atherosclerotic plaque characterization algorithms so interventional cardiologists can make confident decisions and choose appropriate devices/drugs during catheterization procedures. Furthermore, they can be used to study the efficacy of different agents coated on drug-eluting stents (DES) and regression of plaques. Undoubtedly, current developments in intravascular coronary imaging systems and atherosclerotic tissue characterization techniques will be a basis for future consistent management and dependable treatment of atherosclerosis. Consequently, more lives will be saved and overwhelming medical expenses burdened on the government and individuals can be considerably reduced.

1.4. Specific Aims of The Thesis

The specific aims of current work are:

1. Atherosclerotic tissue characterization.

- a. We study realistic challenges from tissue preparation toward classification.
- b. We implement the state-of-the-art virtual histology (VH) algorithm for data acquire with 40 MHz single-element transducers.
- c. We develop an unsupervised texture-based tissue characterization technique with proper histology validation. This way, the constructed tissue color maps could be used for tissue labeling as an alternative approach for manual labeling.

- d. For the first time, we investigate the results of effects of blood and pressure change on constructed tissue color maps and reliability of classified tissues behind arc of calcified plaques.

2. *Detection of lumen borders in IVUS images.*

- a. We study the feasibility of brushlet analysis.
- b. We develop an automated lumen border detection technique for images acquire with high frequency (40 MHz) transducers.
- c. We evaluate our proposed algorithm performance in comparison with two of existing techniques and quantify resulting automated detected borders with manually traced borders by an expert.

2. Chapter Two:

INTRAVASCULAR ULTRASOUND (IVUS)

2.1. Why IVUS?

In previous section, we briefly reviewed existing coronary intravascular imaging modalities. Among them, angiography is the only system routinely being used in all percutaneous coronary intervention (PCI) procedures. It provides immediate visualization of stenosis throughout heart vessel trees and guides interventional cardiologist to advance other catheters for imaging and balloon/stent deployment. However, it suffers from lack of adequate geometrical and pathological information regarding plaque burden and its components. Therefore, experts often tend to take advantage of alternative imaging modalities in order to advance their understanding of atherosclerotic process with the goal of development of new therapeutic interventions. So far, the feasibility of IVUS, as the best supplemented imaging modality, has been proven because of the following reasons:

- It provides real-time cross-sectional grayscale images of arterial wall and its morphologic as well as pathologic structures with sufficient resolution and adequate penetration, allowing precise tomographic assessment of lumen area [152].
- IVUS grayscale images and/or backscattered signals can be employed for characterization of plaques and identification of vulnerable ones (see Chapter 3).
- Using IVUS, an interventional cardiologist can determine:

- The need for further treatment (angioplasty, stent implantation, bypass).
- The exact spatial location for angioplasty and stent implantation.
- How well angioplasty and stenting has worked out.
- The need for aggressive management of risk factors prior to onset of symptoms and advanced disease.
- The predictors of transplant coronary artery disease.

Compared with other modalities, the scientific and diagnostic advantages of IVUS are evident. Additionally, IVUS is the primary choice for validation of other competitive imaging modalities (i.e. OCT, NIR) and has been widely used in preliminary and large perspective trials to investigate the efficacy of new endovascular devices/drugs. With respect to detection of vulnerable plaques, the IVUS is capable of becoming the most common and trustworthy technique given a reliable and reproducible plaque characterization algorithm. Recalling vulnerable plaque features, the IVUS could encompass a greater predictive value in detecting vulnerable plaques since the combination of indices (TCFA, lipid core size, calcification patterns) would be detectable and measurable at once, which would not be the case for competitive imaging modalities such as NIR and OCT.

2.2. Technical Principles of IVUS

2.2.1. Basic Physics of Ultrasound

Ultrasound technology has been employed as a diagnostic tool in modern medicine for the past 50 years. The ultrasound is pressure generated sound wave with frequency greater than audible range of human (2kHz – 20kHz). In IVUS applications, the frequency, f , may vary from 10MHz to 45MHz. The ultrasound technology has been established upon transmission of ultrasound signals into a medium and interpretation of echoes that carry signatures corresponding to the medium. The final interpreted result is usually represented in a grayscale image format. The speed of sound, c , in a medium is calculated as follows:

$$c = \sqrt{\frac{1}{K\rho}} = \lambda f \quad (2.1)$$

where, λ , ρ , and K , are wavelength of ultrasound signal, density, and compressibility of medium, respectively. The speed of sound does not depend on its frequency but the characteristics of medium in which it passes through. In IVUS systems, the average speed of sound in atherosclerotic tissues is customarily set to $1.5625 \text{ mm}/\mu\text{sec}$.

A transducer, which converts electrical signals to ultrasound counterparts, is used to transmit ultrasound waves into a medium. When the ultrasound signals travel through a medium and interact with tissues, three different phenomena may occur; reflection, refraction and scattering, **Figure 2.1**. The scattering happens when the size of particle is less than the wavelength of ultrasound wave. The same transducer is used to receive

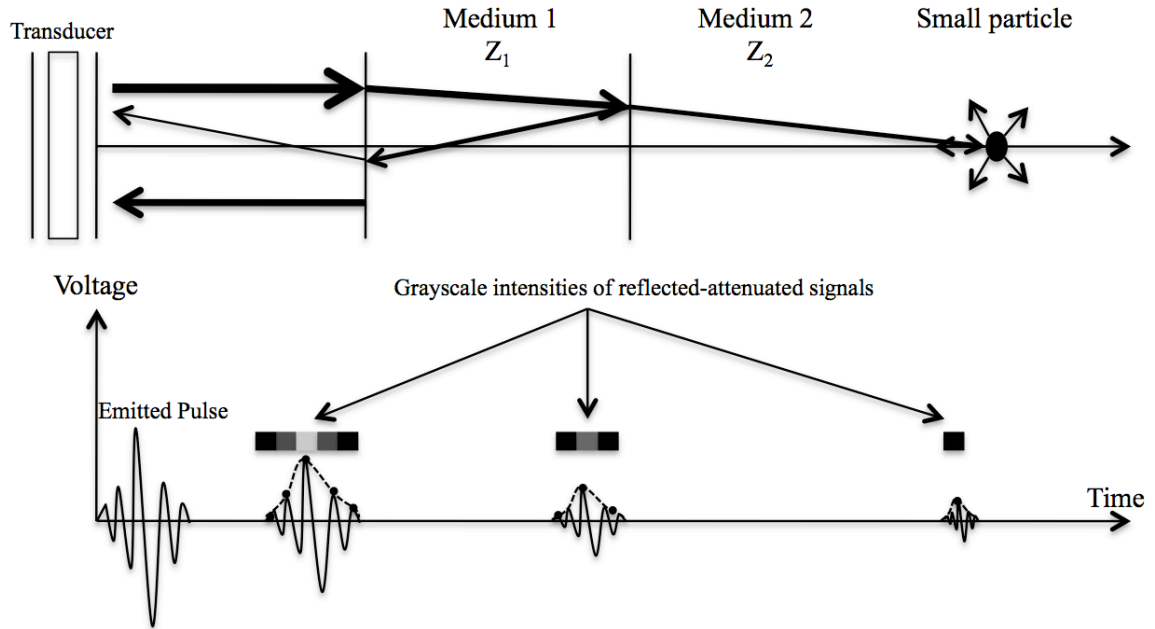


Fig. 2.1. Schematic of transmission of ultrasound wave through two different mediums and resulting reflected-attenuated, refracted, and scattered signals. The reflected-attenuated signals, received by the transducer, are depicted in voltages and grayscale intensities after envelope detection and quantization.

reflected-attenuated (backscattered) signals from tissues that are proportional to the acoustic impedance mismatch, $Z = \rho c$, between two boundaries (mediums). These signals are digitized, stored, and analyzed by a computer to construct typical grayscale images from medium and its structures.

2.2.2. IVUS Acquisition System Specifications

The IVUS is relatively inexpensive imaging modality and could be used in minimally invasive catheterization procedures. The acquisition system consists of a catheter, pullback device, and scanner console. The scanner console carries a computer, keyboard, and screening monitor. We briefly describe the functionality of each part.

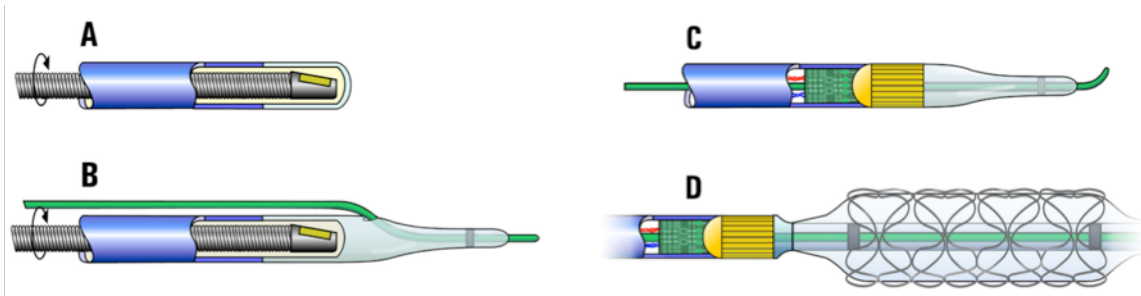


Fig. 2.2. Schematic of four different types of imaging catheters. A catheter without guide wire rail (A), a catheter with guide wire rail designed at the side (B), a catheter with guide wire rail designed at its center (C), a catheter with guide wire rail at its center, inflatable balloon and stent (D). (Reference: http://ee.isikun.edu.tr/research.asp-page=projects_files).

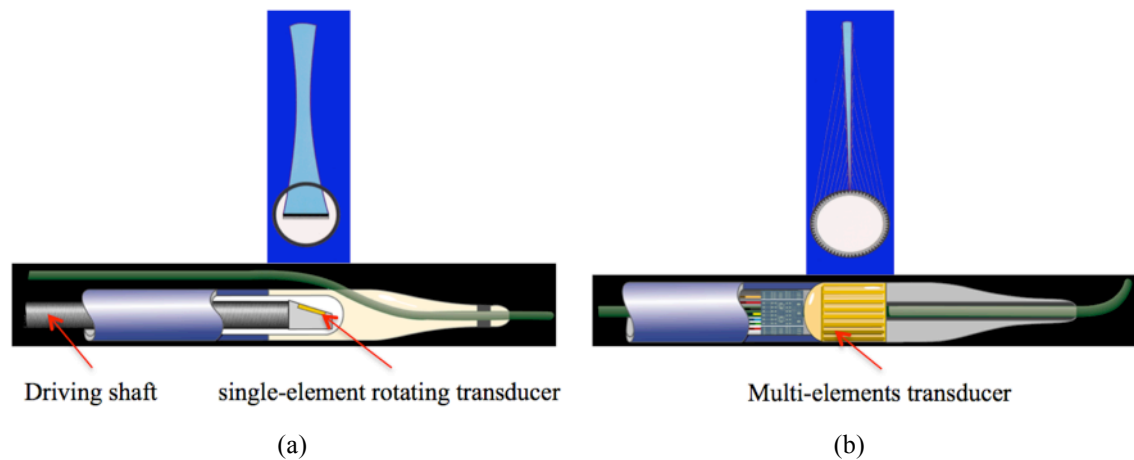


Fig. 2.3. Single-element mechanically rotating focused IVUS transducer and its beam width (a), multi-elements phased-array IVUS transducer and its beam width (b).

2.2.2.1. IVUS Catheter

Catheter is a device that carries a transducer or inflatable balloon with or without stent for imaging purposes and/or expansion of narrowed area, **Figure 2.2**. It is typically advanced from femoral artery toward coronary arteries under angiogram guidance. The tip of the catheter is visible in angiogram so cardiologist can maneuver it with, **Figure 2.2 (B,C)**, or without, **Figure 2.2 (A)**, help of a guide wire depending on type of the catheter. A guide wire rail can be designed next to the catheter plastic sheath **Figure 2.2 (B)** or at its center, **Figure 2.2 (C)**. The advantage of the latter design is that there is no guide wire

artifact in constructed grayscale images. Usually, this type of catheter is stiffer, thicker, and harder for maneuvering.

2.2.2.2. IVUS Transducer

Currently, there are two types of IVUS transducers commercially available in market regardless of their nominal center frequencies. The main difference is in the way that they transmit and receive IVUS signals. **Figure 2.3(A)** shows a single-element mechanically rotating focused IVUS transducer (*i.e.* Atlantis[®] Boston Scientific imaging catheter) that rotates at approximately 1800 revolutions per minutes and its beam width. For a 40 MHz transducer, the axial and lateral resolutions are about 80-100mm and 200-250mm, respectively. The transducer sends a signal and receives the backscattered signal. **Figure 2.3(B)** demonstrates a multi-elements phased-array transducer (*i.e.* Eagle Eye Gold[®] Volcano imaging catheter) with its beam width. An electronic board has been designed so a subset of elements sends signals at once and receives the backscattered signals.

2.2.2.3. Catheter Pullback Device

Once interventional cardiologist diagnoses the location of stenosis the catheter is advanced to the distal side of the stenosis and the transducer is pulled backed while taking cross-sectional images. The apparatus that pulls back the transducer is called pullback device and works manually or automatically, **Figure 2.4**. In automatic option, the speed of pullback can set to 0.5mm or 1mm per second. Typically, a syringe is used to flush Saline in the plastic sheath of the catheter to remove airs and obtain better IVUS images.

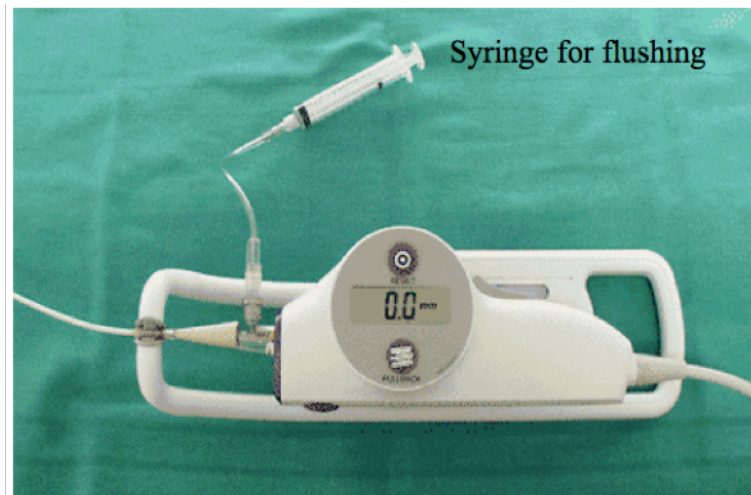


Fig. 2.4. Catheter pullback apparatus. (Reference: <http://img.medscape.com>).

2.2.2.4. IVUS Scanner Console

Figure 2.5 illustrates a portable scanner console for Volcano (Rancho Cordova, CA) s5 imaging system. It carries a computer that is used for post-processing and storing of acquired IVUS data. A cable from end of pullback device is connected to a designed port in computer for data transformation. During catheterization procedure, experts use keyboard and functional buttons to enter patient information, determine percentage of stenosis, and apply image processing and possibly tissue characterization techniques to better understand and evaluate atherosclerotic plaques.

2.3. IVUS Image Formation and Display

Figure 2.6 displays a schematic of an artery, its anatomical structures, catheter and four distinct IVUS frames acquired with transducers with different center frequencies. As we



Fig. 2.5. An IVUS scanner console (Volcano $s5^{\text{TM}}$ imaging system).

can observe, at higher center frequency spatial resolution is improved, at the cost of more scattering from red blood cells inside the lumen. It is worth mentioning that the axial and lateral resolutions depend on transducer center frequency and beam width, respectively.

During acquisition, IVUS backscattered radiofrequency (RF) signals that are continuous-time real-valued and band-limited signals, $x(t)$, are digitized $x(nT_s) = x[n] = x_n$ at periodic time intervals of $T_s = \frac{1}{f_s}$ and stored in hard disk of a computer. The f_s is sampling rate of digitizing board that may vary from one system to another. For example, in Boston Scientific (Fremont, CA) *Galaxy*TM or *iLab*[®] imaging systems, the acquisition boards sample IVUS signals at the rate of $f_s = 400\text{MHz}$ whereas the sampling rate for Volcano $s5^{\text{TM}}$ imaging system is $f_s = 200\text{MHz}$. Once the IVUS backscattered signals are digitized, numbers of steps need to be taken in order to convert digitized signals into typical eyeball IVUS grayscale images. First, the envelope of signal in each acquisition

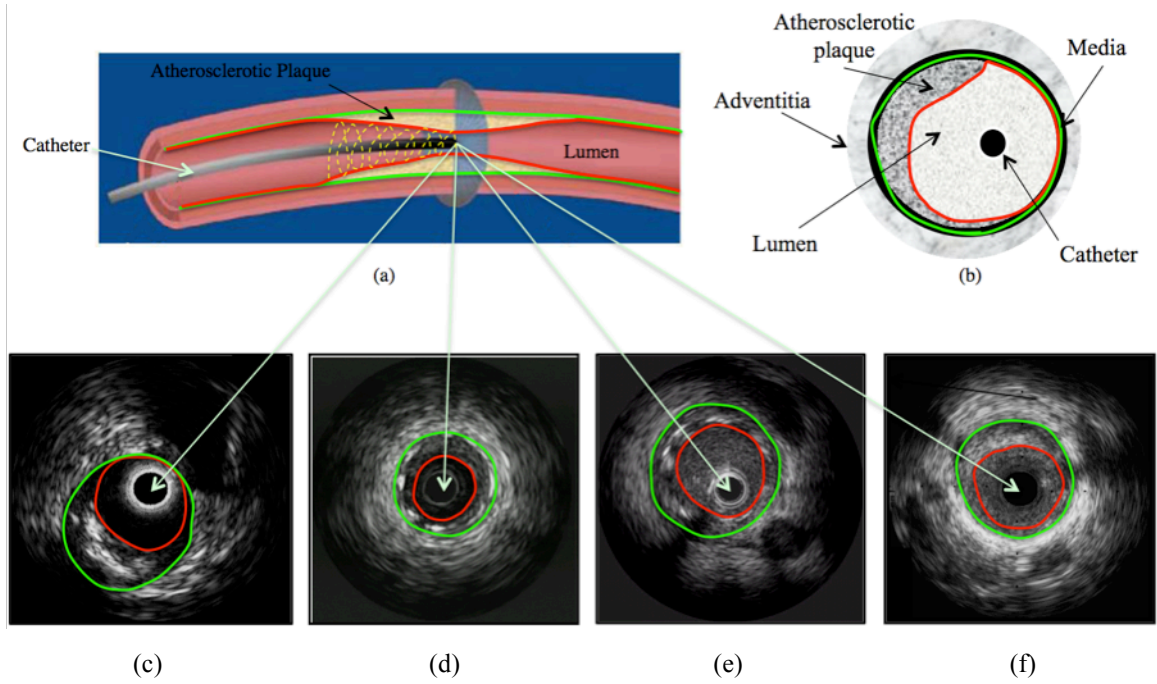


Fig. 2.6. Schematic of an artery, catheter, atherosclerotic plaque, and IVUS image cross-section (a) (Reference: <http://www.bmj.com>), cross-sectional anatomy of arterial wall (b), four distinct IVUS frames acquired with 20 MHz (c), 30 MHz (d), 40 MHz (e), and 45 MHz (f) transducers. Red and green borders represent vessel wall and lumen borders, respectively. The yellow dashed line depicts trajectory of transducer scan lines.

line is computed by corresponding analytical signal [50] followed by decimation and interpolation in axial and lateral directions, respectively. The Log compression is also used to enhance the image quality followed by quantization (ex. 8-bit).

As it is depicted in **Figure 2.6(a)**, the transducer has a spiral trajectory (yellow dashed line) while taking cross-sectional grayscale images with optional rate of 30 frames per second, which can be increased to 60 frames as well. This is due to the fact that the transducer rotates and at the same time is pulled back with speed of 0.5mm/sec that provides IVUS frames of $16.7\mu\text{m}$ thickness. Therefore, the original domain of acquisition is polar (r, θ) and the resulting grayscale image should be transformed to (x, y) Cartesian coordinates to construct a typical IVUS frame. Another advantage of IVUS is that a planar cut through stack of cross-sectional images provides longitudinal

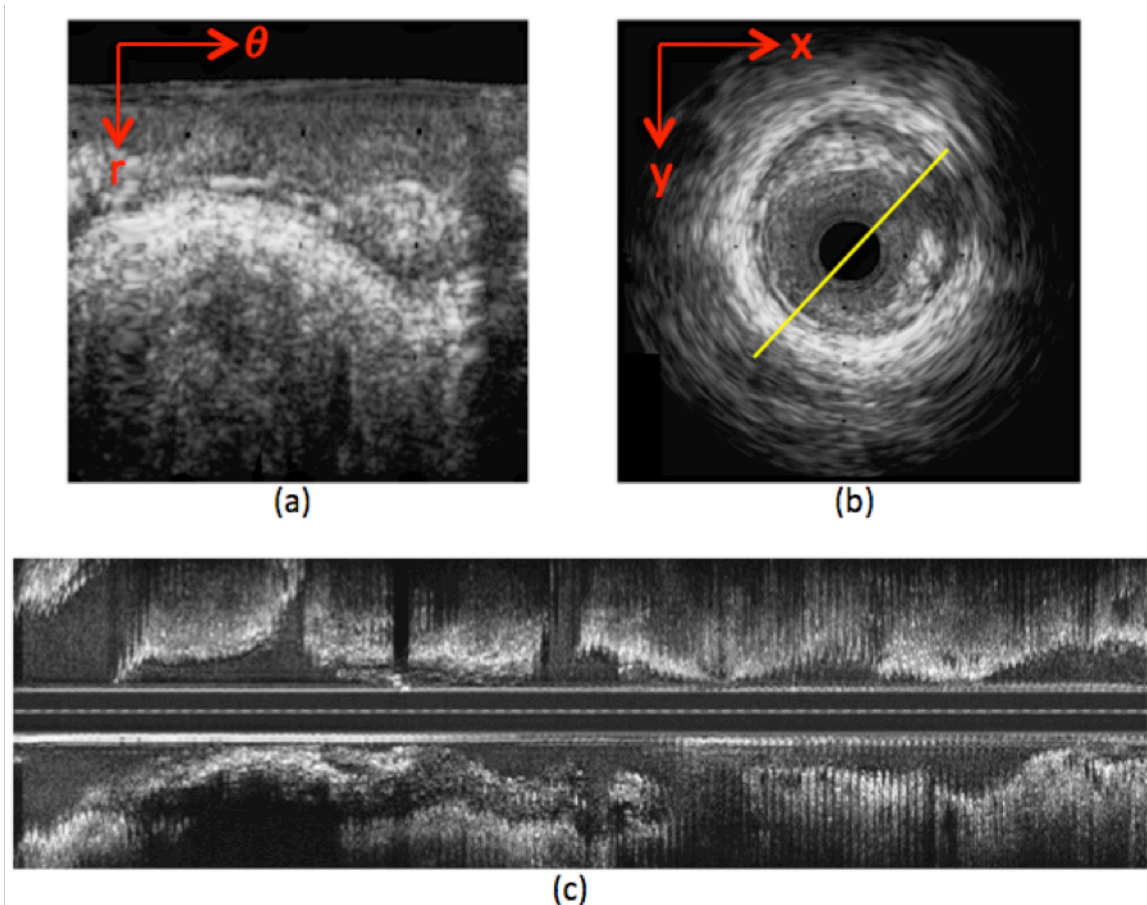


Fig. 2.7. An IVUS grayscale image in polar (r, θ) (a) and (x, y) Cartesian (b) domains along with longitudinal display (c) along an arbitrary planar cut (yellow line).

appearance of an artery. Therefore, interventional cardiologist can assess the length of the artery and distribution of atherosclerotic plaques within pullback direction. **Figure 2.7** illustrates an IVUS grayscale image in polar and Cartesian representations along with an example of longitudinal mode.

2.3.1. Appearance of Atherosclerotic Tissues, Vessel Wall, and Lumen Borders in IVUS Images

Based on pathohistological study of dissected coronary arteries from autopsied or transplanted hearts, there are four types of tissues associated with atherosclerotic plaques:

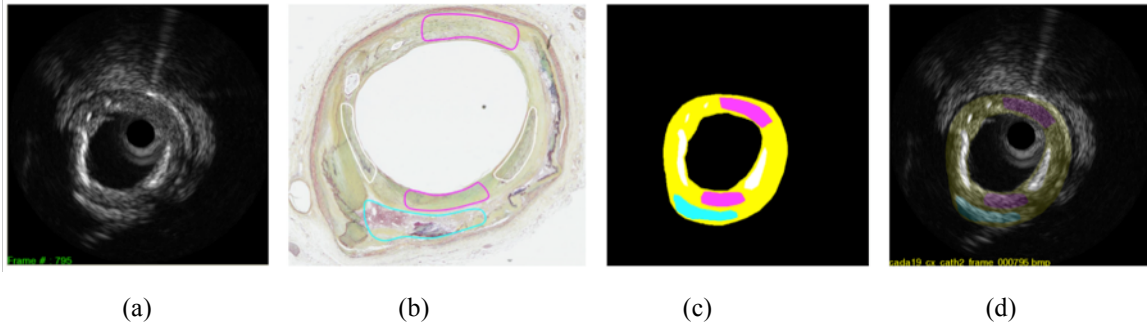


Fig. 2.8. An IVUS grayscale image acquired *in vitro* (a), corresponding Movat-Pentachrome histology image with manually traced tissues (b), constructed tissue color map (c), and imposed tissue color map on original IVUS grayscale image (d). Yellow, magenta, white, and cyan colors represent fibrotic, lipidic, calcified and necrotic core tissues, respectively.

fibrotic, lipidic, calcified, and necrotic core. However, the interpretation of histology images can often vary among experts yielding a subjective process. As a result, one may differentiate between the levels of presence of fatty materials and add fibro-lipidic to compromise between fibrotic and lipidic or another may differentiate between early and old necrotic cores. **Figure 2.8** demonstrates an IVUS grayscale image acquired *in vitro*, corresponding Movat-Pentachrome histology image with manually traced tissues, constructed tissue color map, and imposed tissue color map on original IVUS grayscale image.

2.3.1.1. Calcified Tissue

This is the easiest identifiable tissue in atherosclerotic plaque since it is hyperechoic and appears even brighter than adventitia. Calcified tissues can come out as small nodules so called micro-calcification or in an arc outline, **Figure 2.8(a)** from 7-9 o'clock. The arc of calcified plaque is often so dense and obstructs ultrasound signal penetration, resulting acoustic shadowing.

2.3.1.2. Lipidic and Fibrotic Tissues

Majority of atherosclerotic lesion consists of fatty materials such as lipidic and fibrotic tissues. Fibrotic tissues are dense, hyperechoic, and appear relatively bright so sometimes they are misclassified as calcified tissues. On the other hand lipidic tissues are softer, less echogenic, and appear relatively darker. As a rule of thumb, the more fatty material a tissue contains, the softer it becomes, and the less echogenic it comes out. The lipidic tissue is the most frequent tissue in atherosclerotic plaques. Differentiation between fibrotic and lipidic tissues is known to be very challenging in the field [51,52]. Reduced echogenicity may also be due to presence of thrombus, intramural hemorrhage, and necrotic core.

2.3.1.3. Necrotic Core Tissue

It is a rare and the most complex detectable tissue found in atherosclerotic plaques based on pathohistological studies. Generally speaking, it refers to dead tissues. Appearance of this tissue in IVUS images has not been confirmed to date. It may appear as dark or low intensity regions that could be correlated with old and early necrotic core, respectively. Hence, it is the most challenging detectable tissues in atherosclerotic plaques.

2.3.1.4. Lumen and Vessel Wall Borders

During catheterization procedure, two borders are required to be traced in order to evaluate the degree of stenosis and measure the luminal area in which blood flows. The lumen border is a border at the innermost surface of atherosclerotic plaque and appears relatively darker in comparison with plaque (intimal disease) depends on time gain

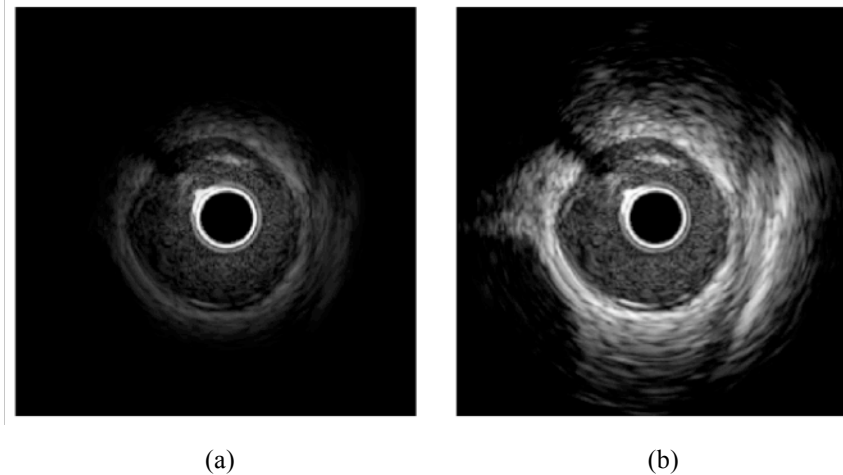


Fig. 2.9. An IVUS grayscale image without (a) and with (b) TGC adjustment.

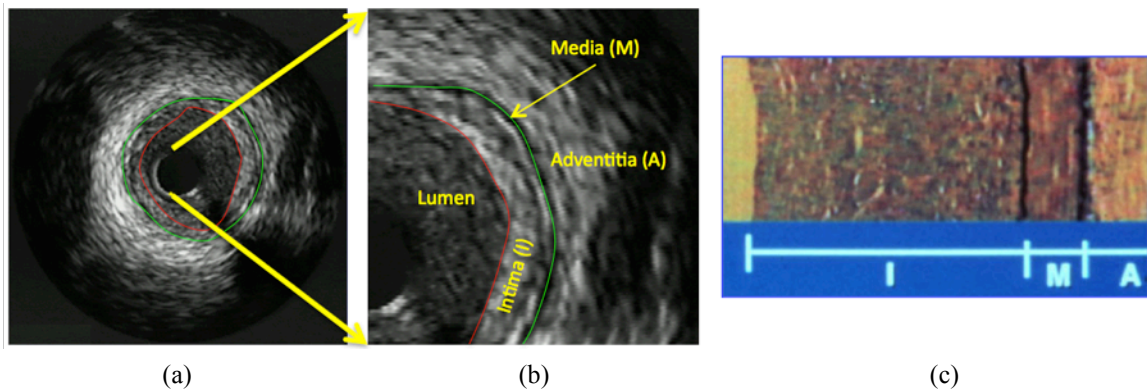


Fig. 2.10. An IVUS grayscale image with manually traced vessel wall (green) and lumen (red) borders (a), zoomed in region with anatomical structures of the artery such as lumen, intima (I) or plaque, media (M) and adventitia (A) (b), histology image of artery anatomical structures (c).

compensation (TGC) setup, type of transducer, and particularly its center frequency. Since signals are progressively weakened with depth, the TGC buttons have been assigned on IVUS console to compensate for attenuated signals at certain depths, **Figure 2.9**. The vessel wall border, also recognized as external elastic membrane (EEM) border, is a contour, which is drawn on media, which is located between intima and adventitia and made of smooth muscle cells. The media does not reflect ultrasound signal and appears as dark regions. Adventitia is the outer layer of an artery contains sheets of that are hyperechogenic and appears as bright regions. **Figure 2.10** demonstrates these

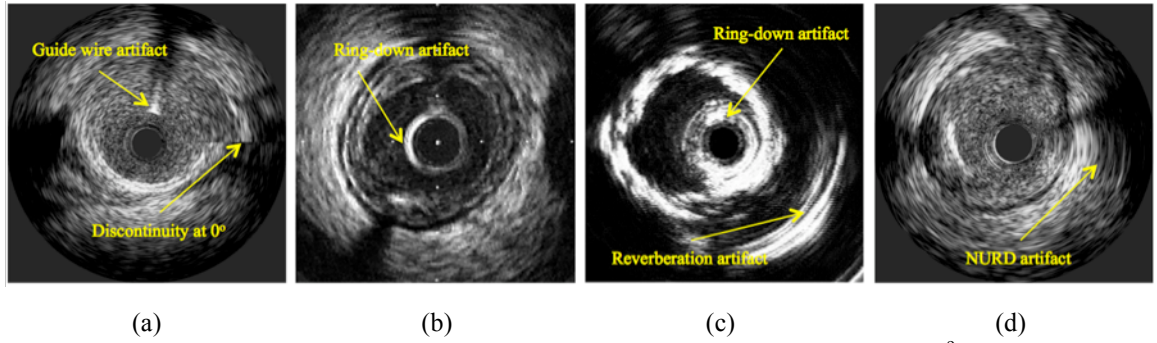


Fig. 2.11. IVUS image artifacts. Guide wire artifact (a), discontinuity artifact at 0° (a), Ring-down artifact (b,c), reverberation artifact (c), NURD artifact (d).

borders and corresponding anatomical structures in an IVUS grayscale image and a histology image.

2.3.2. IVUS Image Artifacts

There are five artifacts associated with IVUS images: guide wire, ring-down, non-uniform rotational distortion (NURD), reverberation, and discontinuity at 0° in Cartesian domain. When a guide wire rail is design along with plastic sheath of a catheter, **Figure 2.2(B)**, it obstructs ultrasound signals, resulting shadowing behind the guide wire, **Figure 2.11(a)**. The second artifact is repetitive reflection of ultrasound signals from surface of transducer because of impedance mismatch, **Figure 2.11(b)**. The NURD artifact is due to mechanical glitch in driving shaft or binding of catheter in arteries curvatures, **Figure 2.11(d)**. The fourth artifact, known as reverberation, is oscillation of ultrasound signals between transducer and arc of calcified plaques, which causes repetitive appearance of calcified arcs, **Figure 2.11(c)**. The last artifact is discontinuity at 0° in Cartesian domain due to abrupt change in tissues textures due to spiral trajectory of transducer as well as severe catheter or heart motions, **Figure 2.11(a)**.

3. Chapter Three:

EXISTING ATHEROSCLEROTIC PLAQUE CHARACTERIZATION ALGORITHMS

3.1. Introduction

In Chapter one, we described the importance of detection of vulnerable plaques and treatment of them selectively before they rupture in order to prevent mortality and morbidity [53]. For this reason, atherosclerotic tissue characterization and detection of vulnerable plaques has been of extensive interest among researchers in the field. In Chapter two, we concluded that the IVUS has been the most favored and clinically approved imaging modality since it is relatively inexpensive and provides adequate spatial resolution along with sufficient penetration while other comparable imaging techniques, such as NIR and OCT with excellent resolution, lack adequate penetration.

Atherosclerotic plaque characterization refers to computer-assisted methods of analyzing IVUS RF signals or images and identifying the component tissue types. The ultimate goal is to deliver information beyond what is possible from a visual reading of unprocessed images or “eyeballing.” As applied to IVUS imaging, tissue characterization methods have the potential to refine the evaluation of the atherosclerotic process and detect rupture-prone plaques. It has been shown that the ultrasound RF signals provide quantitative information on tissue microstructures [54-57]. Consequently, several groups have developed IVUS-based atherosclerotic tissue characterization and vulnerable plaque

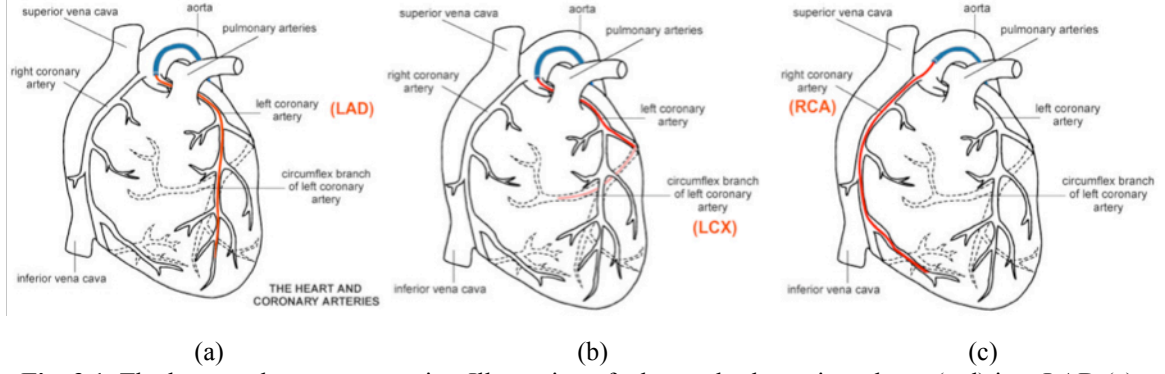


Fig. 3.1. The heart and coronary arteries. Illustration of advanced schematic catheter (red) into LAD (a) LCX (b) and RCA (c).

detection techniques using spectral analysis as an alternative approach to image-based methods.

In this chapter, we review data acquisition as well as staining methodologies and existing IVUS-based atherosclerotic plaque characterization techniques in the context of pathohistological atherosclerotic studies.

3.2. IVUS Data Collection Specification

3.2.1. *In Vivo* Acquisition

Generally, an IVUS catheter is advanced into LAD or RCA and possibly in some side branches on a guide wire coming out of a guiding catheter inserted in the femoral artery, **Figure 3.1.** Acquisition of cross-sectional ultrasound images of right coronary arteries (RCA), left anterior descending (LAD), and left circumflex (LCX) coronary arteries can be performed with rotating single-element or phased array transducers. The catheter pullback speed varies between 0.5-1 mm/sec and the frame rate can be set to 30 or 60 frames/sec. The IVUS RF data and images are acquired as described in Section 2.3.

3.2.2. *In Vitro* Acquisition and Histology Preparation

Sine the overall justification of *in vivo* real-time plaque characterization is made by interventional cardiologists through use of classified tissues, for supervised classification approaches, it is indispensable to train the classifier with the most reliable features. In order to collect a training dataset, the regions of interest (ROIs) on the arteries are marked and relative cross-sectional histology images obtained. The IVUS-histology frame alignment plays a crucial role because the IVUS frames are labeled through the interpretation of the corresponding histology images. Subsequently, the signals are assigned to labeled tissues and desirable features are extracted. The IVUS-histology matching problem becomes more challenging due to the: 1) curvature of arteries, especially in the LCX, 2) registration between an IVUS image and its histology since the IVUS imaging plane and the slicing plane of microtome are somewhat different, 3) the thickness differences in histology slides that is 5μ that is far less than IVUS frames of about 200μ , and 4) shrinkage of the arteries after formalin fixation. Here, we describe two methodologies to prepare specimen and obtain the most precise one-to-one matched IVUS-histology cross-sections.

3.2.2.1. *Local Marking of ROIs*

In this methodology, as we proposed in [58], the arteries are not dissected as the whole heart is examined. Electrocauterization of small distal arteries is performed when necessary to avoid any leakage. A cannula is fixed in the ostium of the left main coronary artery and a circulating system consisting of phosphate buffered saline (PBS) is used to

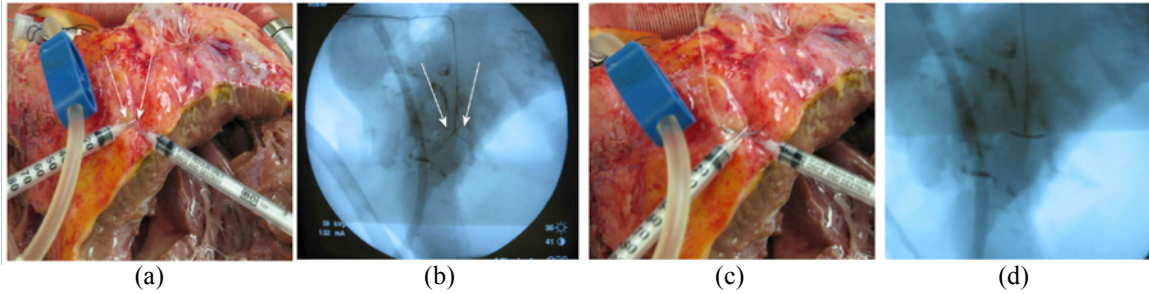


Fig. 3.2. Marking ROIs on LAD of a transplant heart; Two needles (pointed with white arrows) are placed into surrounding fat (a) at the tip of the IVUS catheter visualized under fluoroscopic guidance (b). The third needle is passed through the crossed point and a suture is done to mark the ROI (c). The first two needles are removed and the procedure is repeated for each ROI (d).

ensure a constant pressure (100 mmHg) and flow in order to maintain arteries physiologically opened at 37° Celsius. The IVUS catheter is introduced and advanced on a 0.014” guide wire and manual pullback is performed to search for sites of significant plaques. One of the main challenges in this method is to mark ROIs as precisely as possible to get the best match of IVUS-histology cross-sections. In order to do so, a fluoroscopic X-ray system is deployed to visualize the tip of the IVUS catheter. After stabilizing of catheter at the site of interest, two needles were implanted under fluoroscopic guidance into surrounding fat so that they crossed above the tip of the IVUS catheter. Thereafter, a third needle is passed through the crossing point to mark it by a suture, **Figure 3.2**. The first two needles are then removed. This procedure is repeated for 3-5 different ROIs per artery and the corresponding RF signals are acquired as described in Section 2.3 while complete automatic pullback is taken. Sutures are used to locate the ROIs for slicing and histology processing.

Histology Preparation and Staining

The whole heart is fixed by cannulating coronary arteries to recirculate 10% buffered formaldehyde under 100 mmHg pressure for three hours. In the next step, the arteries are prepared for staining after decalcification. Blocks of 2-3 mm are cut from distal locations

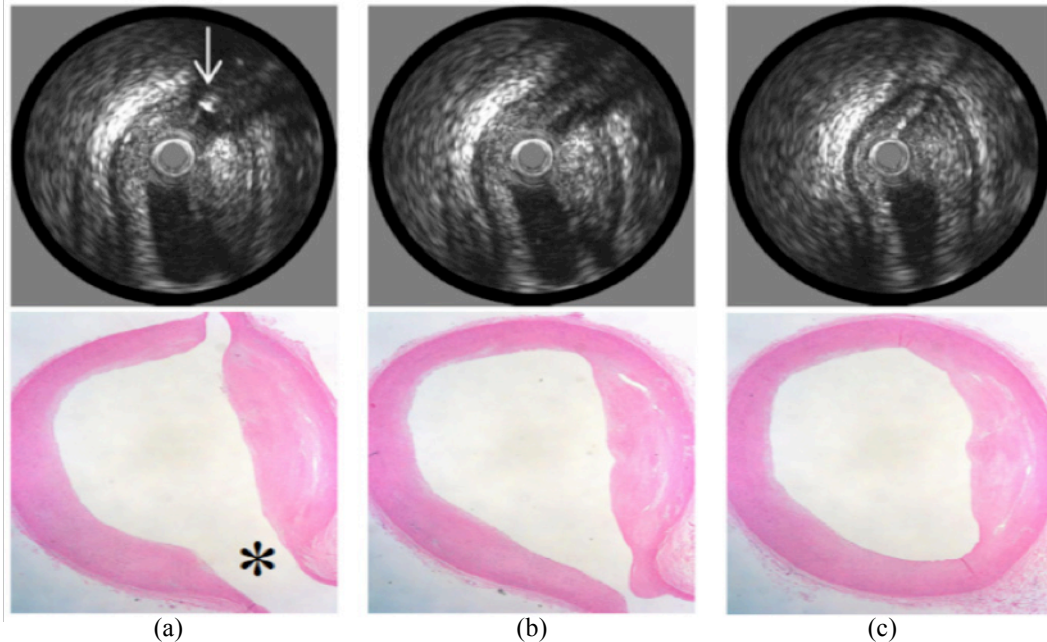


Fig. 3.3. Taking three sections at each ROI with 500 micrometer intervals, which corresponds to 30 frames. Marked ROI with reflection of the needle (white arrow) and side branch (*) with corresponding histology (a). Two IVUS frames with 500 micrometer intervals and corresponding histology sections (b,c).

of the sutures. The proximal end is marked with ink. Histology slices are taken from distal to proximal after arteries are decalcified and embedded in paraffin. In this methodology, for each block, three serial sections are taken at 500 μm intervals, which correspond to 30 frames in IVUS acquisition, **Figure 3.3**. The first two sections are stained with hematoxylin and eosin (H&E) and Movat Pentachrome, and the last section could be kept unstained for future additional staining (e.g., Sirius Red). **Figure 3.3(a)** shows a marked ROI with needle and a side branch as well as corresponding histology image. Taking a complete automatic pullback (or a short pullback along each ROI) and sectioning three slices at intervals of 500 μm allows to find the best possible match between ROI's cross sections and corresponding histology images. Besides reflection of the needle, natural markers such as side branches and small calcified inclusions could be used to improve the IVUS-histology frames correlation accuracy.

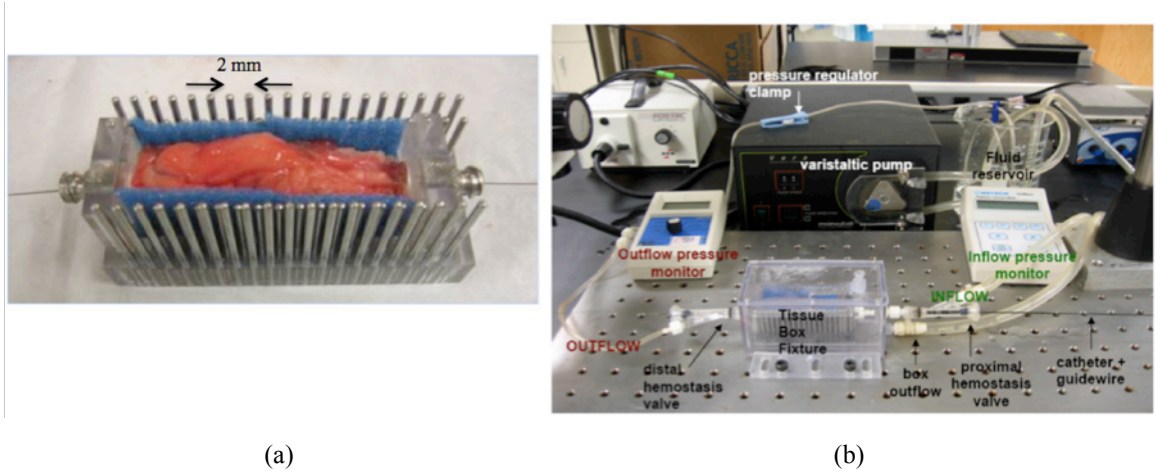


Fig. 3.4. Tissue cage fixture (a), *in vitro* experiment set-up (b). (Courtesy of Jennifer Lisauskas at InfrareDx (Burlington, MA)).

3.2.2.2. Systematic Marking of ROIs

In this methodology, the arteries are dissected from heart, placed in tissue cage fixture, **Figure 3.4(a)**, and attached to a circulating fluid flow system, **Figure 3.4(b)**. Average length of the arterial segments attached to the fluid system could be 50mm. The arterial segments are perfused with saline at body temperature (37°C) with pulsatile flow (60 bpm, 135mL/min) at physiologic pressure (80-120 mmHg). Then, an IVUS catheter is advanced on a 0.014" guide wire and a complete automatic pullback is performed from the distal to the proximal side. The same procedure is repeated using human blood. Prior to the experiment, the blood is agitated by hand for approximately one minute to mix and then stirred at low speed with a magnetic stir bar using a hot/stir plate until the experiments begun. The RF data is collected as described in Section 2.3.

Histology Preparation and Staining

After imaging, the arteries are pressure fixed with 10% buffered formaldehyde followed by decalcification. The histology blocks are prepared every 2mm (corresponding to 120

frames of the IVUS pullback) using the sidebars. All blocks are embedded in paraffin and sectioned for histological staining. Two 5µm thick histologic cross sections are stained with H&E and Russell-Movat Pentachrome. The transplant arteries included a third histologic cross-section, which remained unstained for subsequent staining (e.g., Sirius Red).

This methodology has two main advantages. First, the orientation of artery is not changed throughout the whole procedure. Therefore, more reliable IVUS-histology pairs could be obtained and the number of cross sections of interest (CSIs) per vessel is significantly increased (average of 25 regions) compared to the traditional methods (3-5 regions). Secondly, it allows us to investigate the effect of flowing that is expected to introduce signal changes (i.e. attenuation) and may alter classification results.

3.2.3. Cardiovascular Histopathology

Hematoxylin and eosin are among the most commonly used stains in histopathology. Hematoxylin turns nuclei blue; eosin turns the cytoplasm (mostly composed of proteins arginine and lysine) pink. Another stain, the Russell-Movat pentachrome, colors cytoplasm in red, elastic fibers in black, collagen and reticulum fibers in yellow to greenish and proteoglycans in blue. Clear areas might represent water, carbohydrate, lipid, gas or decalcified areas. Sirius red, on the other hand, has been used exclusively for collagen staining in cardiovascular histopathology. Collagen fibers are stained red and can be distinguished morphologically from other tissue components in the plaque.

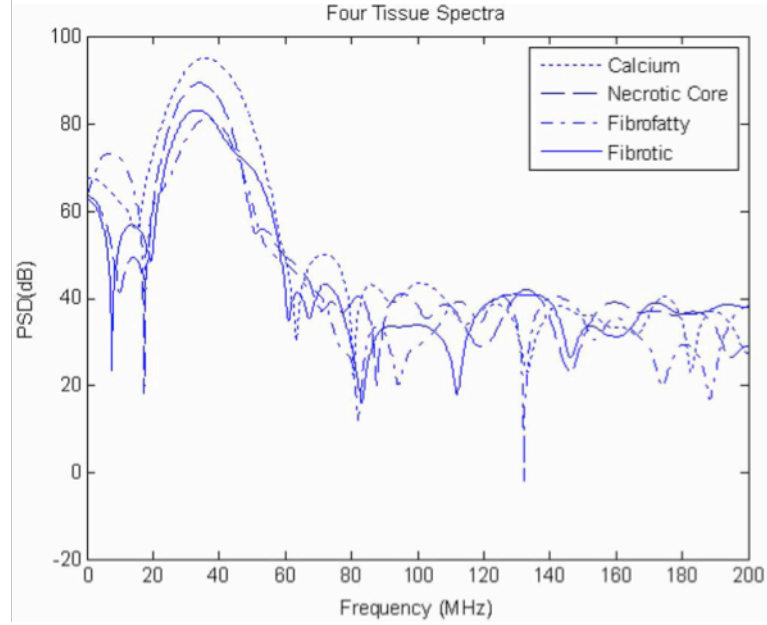


Fig. 3.5. Dissimilarity among four tissue spectra, calcium, necrotic core, fibrofatty, and fibrotic measured in sample size of 64 collected from one cross section of interest (CSI).

3.3. RF- and Spectrum-Based Plaque Characterization

Algorithms

Post-processing of the backscattered RF IVUS signal has been developed in order to better characterize plaque composition. The basic tenet of ultrasound tissue characterization is that different tissue types imprint their distinctive “signatures” on the backscattered echo received by transducer. Hence, spectral analysis of the ultrasound RF signals has been extensively studied and employed in different applications [59-62]. This is because the tissues of interest generate signals that are stochastic (*i.e.* their internal constituents exhibit randomness in size, position, orientation, etc.) and the spectra represent the ensemble properties of the scatterers. If the spatial autocorrelation function describing these factors has a known form, then the theoretical scattering models can be

used with spectral data to estimate two physical scatterer properties: the effective sizes of constituent scatterers and their “acoustic concentration” [61,63]. It is a statistically observable fact that on averaging a large number of spectra obtained from homogenous areas of tissue in carefully controlled *in vitro* experiments, different types of tissue give rise to recognizably different spectra, **Figure 3.5**. In most recent methods of tissue characterization, the spectrum is characterized using a few values (e.g., seven parameters in [64]) to capture its basic attribute.

3.3.1. IVUS-Virtual Histology (IVUS-VH)

In 1983, Lizzi *et al.* presented a sliding-window analysis method to identify tumors in the eye and liver by using two spectral signatures extracted from calibrated tissue spectra [65]. Those parameters were the slope of the regression line fitted to the mid-band portion of calibrated spectrum and intercept of that regression line at zero frequency. They demonstrated that the slope and intercept are indicative of the scatterer size and concentration. Authors in [64] extended Lizzi’s approach and introduced the first commercially available IVUS-based atherosclerotic tissue characterization algorithm known as virtual histology (VH). This methodology has now been implemented in the Volcano (Rancho Cordova, CA) IVUS clinical scanners that offer near real-time tissue characterization *in vivo* using 64-elements 20MHz phased-array transducer.

This approach is based on seven spectral parameters (intercept, slope, mid-band-fit (MBF), and minimum and maximum powers and their corresponding frequencies) extracted from tissue spectra, which were normalized through the spectrum of a Plexiglas

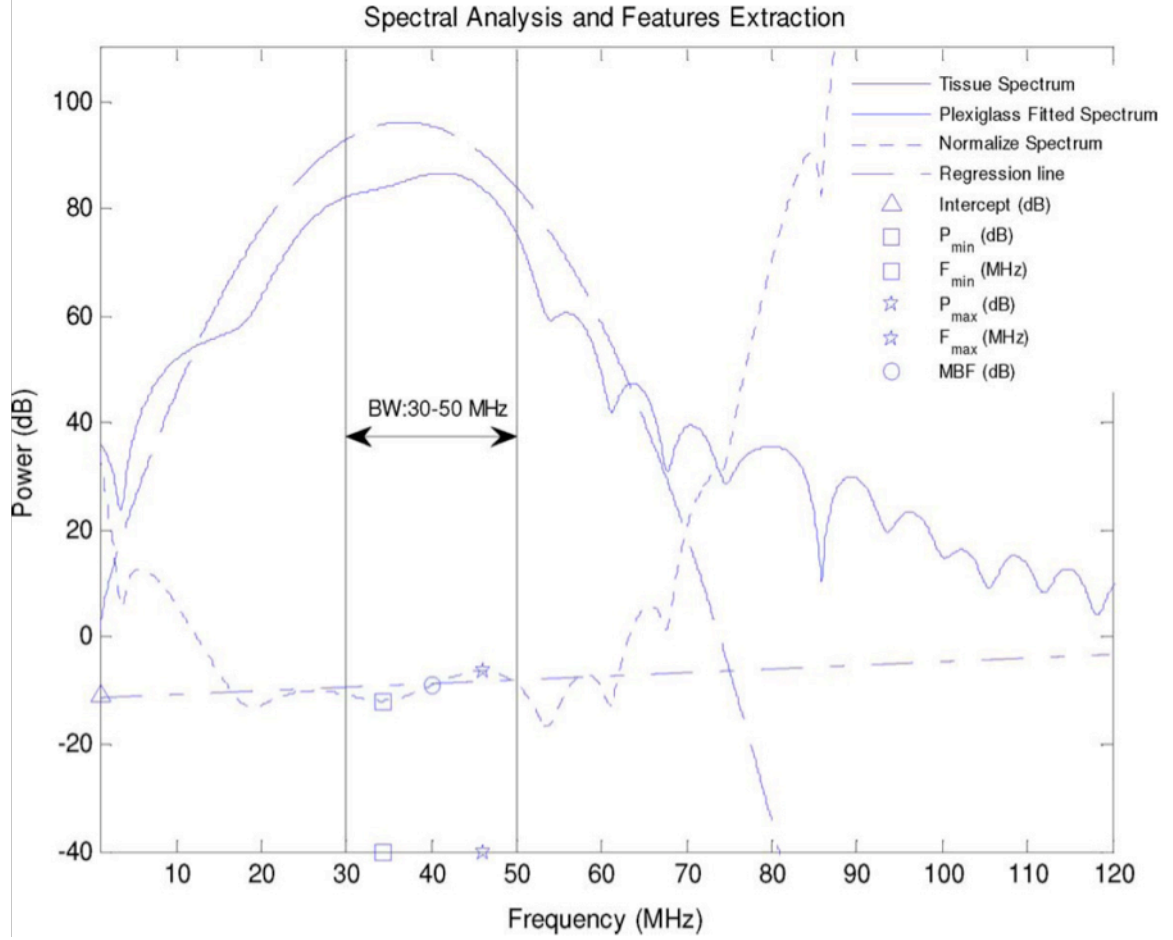


Fig. 3.6. Linear regression fit to normalized tissue's spectrum and extracted features; intercept, slope, mid-band-fit (MBF), and minimum and maximum powers and their corresponding frequencies. Slopes (decibels per megahertz) of regression line and integrated backscatter coefficient have not been shown. The corresponding IVUS data has been collected with 40 MHz unfocused transducer.

reflector. The normalization is necessary in order to eliminate transducer impulse response prior to feature extraction. Basically, a short ultrasonic pulse is transmitted toward perfect reflector and the spectrum of the reflected signal is considered as an estimate of the transducer frequency response. This is not a feasible approach for clinical real-time plaque characterization but has been performed for *in vitro* experiments. The same group deployed blind deconvolution to prevail this problem [66]. They also added integrated backscatter (IB) coefficient as an additional feature [67] and later showed that autoregressive (AR) models were superior to the Fourier technique [68].

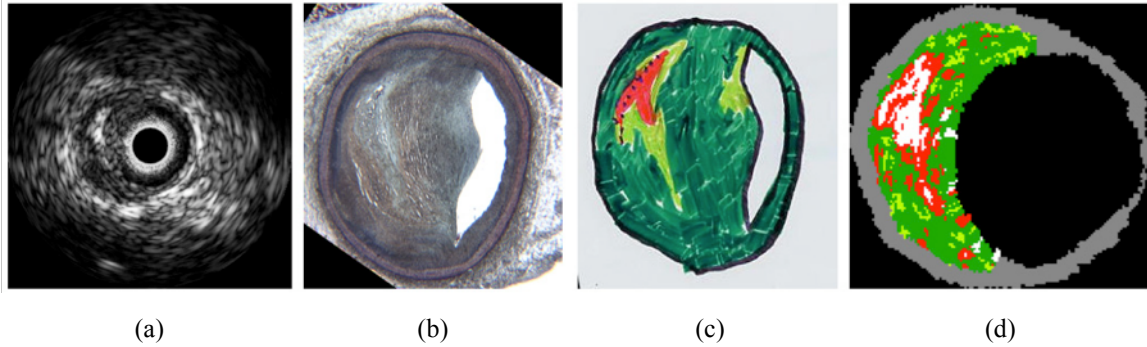


Fig. 3.7. [64] Original IVUS grayscale image acquired in vitro (a), histological validation showing a fibroatheroma with a thick fibrotic cap (b), pathologist's pencil sketch showing the four major tissue types present in the lesion using the IVUS-VH color-coded classification: dark green codes for fibrotic tissue; light green, fibrofatty tissue; red, necrotic core. Micro-calcifications are here marked with small dark points (c), IVUS-VH coding with calcium here coded in white (d).

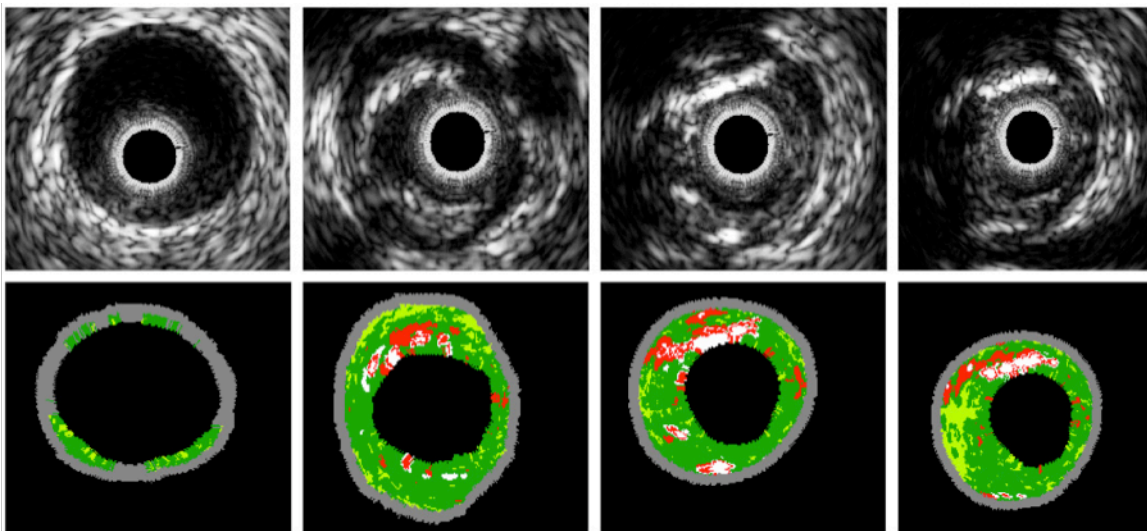


Fig. 3.8. IVUS-VH *in vivo* results. Four IVUS grayscale images (top row) acquired with 20 MHz 64-elements phased array transducer from distal (left) to proximal (right) and their corresponding VH results (bottom row). Dark green, light green, white, and red represent fibrotic, fibrofatty, calcified, and necrotic core, respectively.

Figure 3.6 demonstrates an arbitrary tissue spectrum, averaged Plexiglas spectrum fitted with Gaussian model, normalized spectrum, and extracted features through linear regression fit. Finally, they employed classification tree to differentiate plaque compositions. **Figure 3.7** shows an IVUS cross-section of interest (CSI), corresponding histology image, and VH result. The accuracy of the IVUS-VH technique using AR

analysis in combination with classification tree for IVUS data acquired with 30 MHz single element transducers has been reported as 90.4%, 92.8%, 90.9% and 89.5% in training dataset and 79.7%, 81.2%, 92.8% and 85.5% in the test dataset for fibrotic, fibrofatty, calcified and calcified necrotic regions, respectively. **Figure 3.8** illustrates four grayscale IVUS images acquired *in vivo* with 20 MHz phased array transducer and corresponding VH results. The dark green, light green, red, white, and gray represent fibrotic, fibrofatty, necrotic core, calcium, and media, respectively.

3.3.2. IVUS-Integrated Backscatter (IVUS-IB)

Kawasaki *et al.* introduced an alternative tissue classification scheme based solely on another RF-derived parameter: the integrated backscatter (IB). In this approach, RF signals are windowed and the IB value is computed in frequency domain as follows:

$$IB = \frac{1}{f_{BW_{\max}} - f_{BW_{\min}}} \int_{f_{BW_{\min}}}^{f_{BW_{\max}}} PSD(f) df \quad (3.1)$$

where PSD is estimated power spectral density and $f_{BW_{\min}}$ and $f_{BW_{\max}}$ are the minimum and maximum frequency in the specified bandwidth, respectively. This system is presently distributed only in Japan (YD Co. Ltd, Tokyo) and uses the IVUS catheter from Boston Scientific (Fremont, CA) based on a 40MHz single rotating crystal [69,70]. Color-coded maps of plaques are constructed by use of these IB data, which reflects the plaque histology of autopsied coronary arteries. IVUS-IB values have been divided into five categories to construct color-coded maps: thrombus, intimal hyperplasia or lipid core, fibrous tissue, mixed lesions, and calcification, **Figure 3.9**.

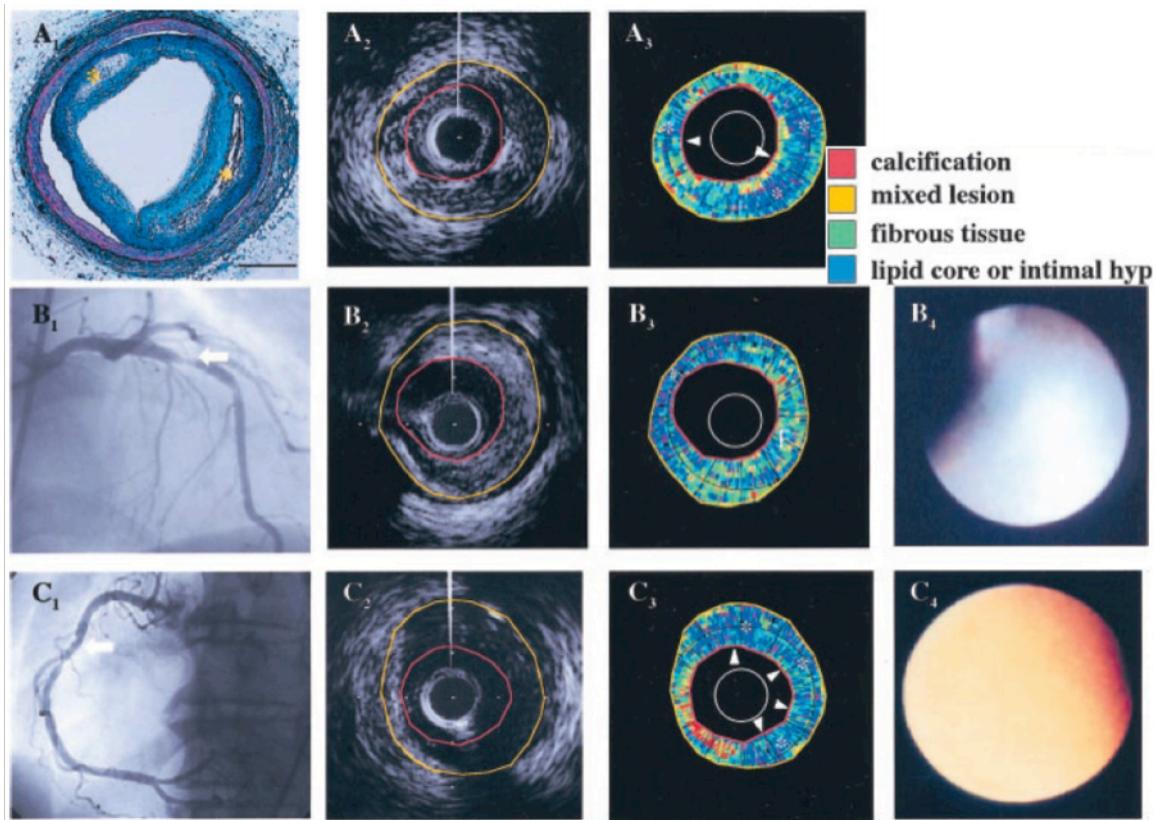


Fig. 3.9. [69] Color-coded maps of coronary arterial plaques constructed by IB-IVUS and histology, coronary angiography, or angioscopy. **A**, Autopsy study of coronary arterial plaque. A₁, Histological finding with fibrosis, mixed lesion, calcification, and large (right) and small (left) lipid cores (*) stained with Masson's trichrome. Bar=1 mm. A₂, Conventional IVUS image of same segment as A₁. A₃, Color-coded map of intima of A₁ constructed by IB-IVUS. **B**, In vivo study of coronary arterial plaque. B₁, Angiography of left coronary artery. Arrow indicates a segment with 60% diameter stenosis. B₂, Conventional IVUS image of same segment as shown by arrow in B₁. B₃, Color-coded map of intima of B₁ constructed by IB-IVUS. B₄, Angioscopic finding of plaque at right in B₃. Note that white plaque is related to fibrous tissue. **C**, In vivo study of coronary arterial plaque. C₁, Angiography of right coronary artery. Arrow indicates a segment with 40% diameter stenosis. C₂, Conventional IVUS image of same segment as shown by arrow in C₁. C₃, Color-coded map of intima in C₁ constructed by IB-IVUS. Note large lipid core (*) with fibrous cap (arrowhead). C₄, Angioscopic finding of plaque at top in C₃. Note that yellow plaque is related to thin fibrous cap. Red and yellow contours represent traced lumen and vessel wall borders, respectively.

Comparisons of IVUS-IB with histopathology demonstrated a high sensitivity for characterizing calcification, fibrosis, and lipid pool (100%, 94%, and 84%, respectively) and a high specificity (99%, 84%, and 97%, respectively). The tissue IB values were calibrated by subtracting the IB values from the IB value of stainless steel placed at a

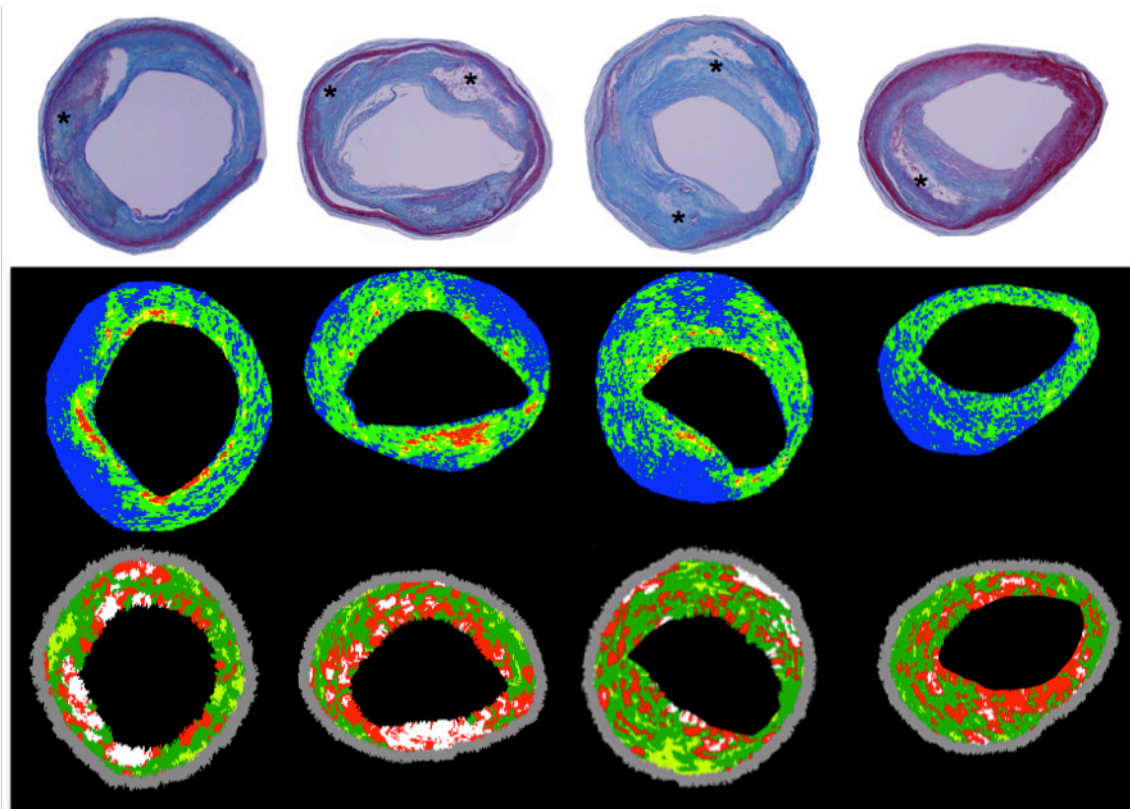


Fig. 3.10. [71] Comparison between IVUS-IB results with corresponding IVUS-VH. Histological image (Masson's trichrome staining) (top row). * depicts lipid pool region, corresponding color-coded maps constructed by the IVUS-IB technique (middle row), red, yellow, green and blue colors represent calcification, dense fibrosis, fibrosis and lipid pool, respectively. Corresponding IVUS-VH images (bottom row).

distance of 1.5 mm from the catheter. In the *ex vivo* studies, each site of each tissue characteristic was placed at a distance of ~ 1.5 mm from the catheter. They further validated their IVUS-IB *in vivo* results with corresponding angioscopy images. The same group recently compared and reported the overall agreement between IVUS-IB and IVUS-VH in the tissue characterization of plaques from the same coronary arterial cross-sections and quantified their results with corresponding histopathological images [71], **Figure 3.10.**

3.3.3. IVUS Elastography (IVE)

The principle of elastography is to study the response of tissue to mechanical excitation (e.g. compression). Several groups have deployed elasticity imaging in order to assess the local mechanical properties of atherosclerotic plaque or vessel wall using different techniques such as envelope based elastography [38], spectral-based strain imaging [39], phase sensitive speckle tracking [40], and cross-correlation based technique between RF signals in consecutive frames [41]. De Korte *et al.* [41] computed the relative local displacements between IVUS images acquired at two different levels of intravascular pressure with a 30 MHz single element mechanically rotating transducer. These displacements were estimated from the time shift between gated radiofrequency echo signals using cross-correlation algorithms with interpolation around the peak. Then, the strain information was presented in an independent complimentary two-dimensional image of the strain called elastogram. Authors demonstrated the feasibility of this technique for intravascular purposes using phantom studies and studies on human arteries both *in vitro* and *in vivo*. The results were further validated with conventional IVUS images, corresponding histology images, and compression modulus values. **Figure 3.11** illustrates two *in vitro* IVUS grayscale images, resulting elastogram, and corresponding histopathological images. The results demonstrate the capability of intravascular elastography to characterize different plaque types and classify tissues based on their mean strain values to fibrous, fibro-fatty and fatty. Additional IVE validation has been reported by authors in [42] that employed the Lagrangian speckle model estimator (LSME) along with the scaling factor estimator (SFE) to compute the radial strain elastograms.

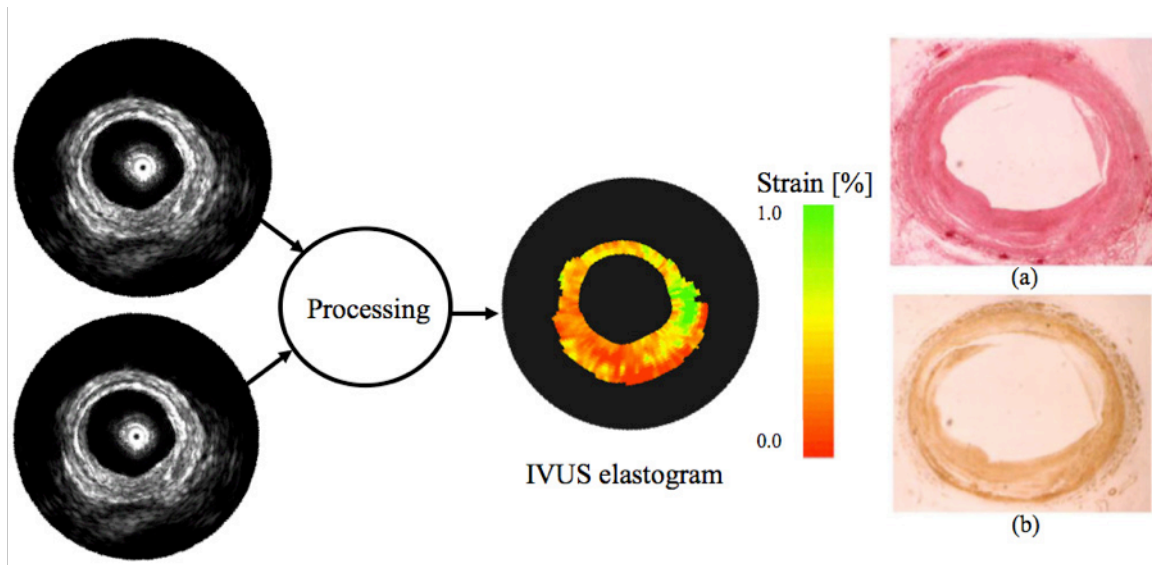


Fig. 3.11. [41] Two *in vitro* IVUS grayscale images acquired at two different levels of pressures (85 mmHg and 90 mmHg) and resulting elastogram along with corresponding histopathological images, Picro-sirus red (a), Alpha-actin (b). The IVUS image reveals an eccentric plaque between 2 and 11 o'clock. The elastogram shows that the plaque can be divided into two parts: a low-strain part (0.2%) between 4 and 11 o'clock and a high-strain part (1%) between 2 and 4 o'clock, both compared with the moderate strain (0.5%) in the normal vessel wall. The histology reveals that the region between 4 and 11 o'clock is fibrous material and the region between 2 and 4 o'clock is fatty material.

3.4. Texture-Based Tissue Characterization and Vulnerable Plaque Detection Algorithms

IVUS findings have shown that the sonographic differences yielded the visual discrimination among plaque constituents [72,73]. In other words, variations of intensities are attributed to the repetitive tissue microstructure patterns. These have motivated researchers to develop texture-based algorithms on IVUS images to differentiate tissue types [74-76]. One of the main differences between texture-derived atherosclerotic plaque characterization algorithms with their spectrum-based counterparts is that no RF signal is needed. This can be advantageous since usually RF signals are not accessible. On the other hand, the appearance of images may vary depends on selected

parameters during acquisition (*i.e.* TGC), normalization, or reconstruction (*i.e.* non-linear transformation) that makes the problem of interest more challenging.

3.4.1. IVUS-Error Correcting Output Codes (IVUS-ECOC)

Authors in [77] introduced a new technique to characterize intravascular ultrasound tissues based on different types of features, such as radial frequency, texture-based features, and combined features. They presented a Sub-class approach of error correcting output codes (ECOC) that splits the tissue classes into different sub-sets according to the applied base classifier. To deal with the classification of multiple tissues, the use of robust multiclass learning techniques is required. In this sense, ECOC shows to robustly combine binary classifiers to solve multi-class problems. Complex IVUS data sets containing overlapping data are solved by splitting the original set of classes into sub-classes, and embedding the binary problems in a problem-dependent ECOC design.

In the proposed technique, three types of features are employed. The first ones obtained from RF signals by computing the energy of A-line and the energy of windowed spectrum. The second ones extracted based on texture-based features from reconstructed images including co occurrence Matrix [78], local binary patterns [79] and Gabor filters [80,81]. Additionally, taking into account that highly non-echogenic plaques produce significant shade in the radial direction of the vessel, a complementary feature that represents the presence of shading in the image, was included in the feature set. Finally, the slope-based features proposed in [64].

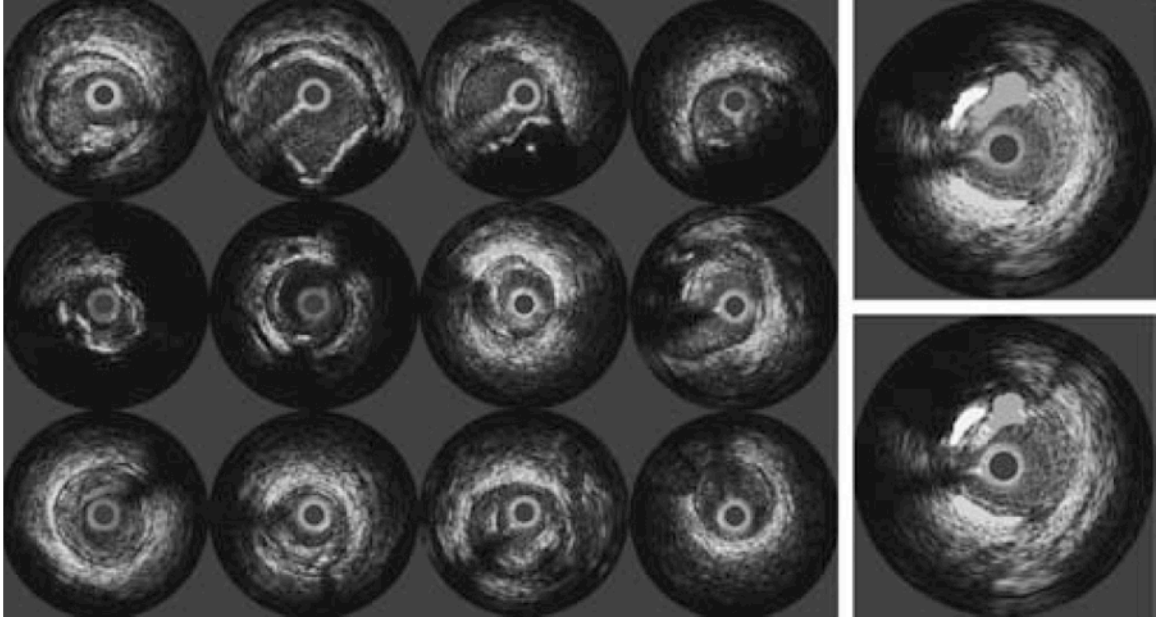


Fig. 3.12. [77] Left: IVUS data set samples. Right: (top) segmentation by a physician and (down) Automatic classification with texture based features. The white area corresponds to calcium, the light gray area to fibrosis, and the dark gray area to soft plaque.

Authors used the RF signals and their reconstructed images from a set of 10 different Patients. To generate the data set on texture features, the intersection between segmented images has been mapped into a feature vector. Then, all collected features were categorized by patient and each of the three possible plaques types. The image features were extracted by using the previous texture descriptors: co-occurrence matrix, local binary patterns, and Gabor filters. Those features were calculated for each pixel and gathered in a feature vector of 68 dimensions. An example of a manual and automatic texture-based segmentation for the same sample is shown in **Figure 3.12**.

To generate the data set of RF features, the RF signals were acquired with single element rotating 40 MHz Boston Scientific catheters using a 12-bit acquisition card with a sampling rate of 200 Mhz. To analyze the RF signals, the sliding window was composed

of 64 samples of depth and 12 radial A-lines, and the displacement was fixed in 16 samples and four A-lines. The power spectrum of the window ranges from 0 to 100 m/s and it was sampled by 100 points. Then, it was complemented with two energy measures yielding a 102 feature vector. We also consider a third data set that concatenates the descriptors from the previous RF and texture based features, obtaining a feature vector of length 170 features.

Authors compared their technique with the state of-the-art ECOC coding designs: one-versus-one [82], one-versus-all [83], dense random [83], sparse random [84], and discriminant ECOC (DECOC) [85]. Three different base classifiers were applied over each ECOC configuration: nearest mean classifier (*NMC*) with the classification decision using the Euclidean distance between the mean of the classes, discrete AdaBoost with 40 iterations of decision stumps [86], and Fisher linear discriminant analysis (*FLDA*). The method automatically characterizes different tissues, showing performance improvements over the state-of-the-art ECOC techniques for *FLDA*, Discrete AdaBoost, and *NMC*. In particular, the results show higher performance when using texture-based features compared with RF signals and slope-based features, and slight improvements when the sets of features are combined, **Figure 3.13**.

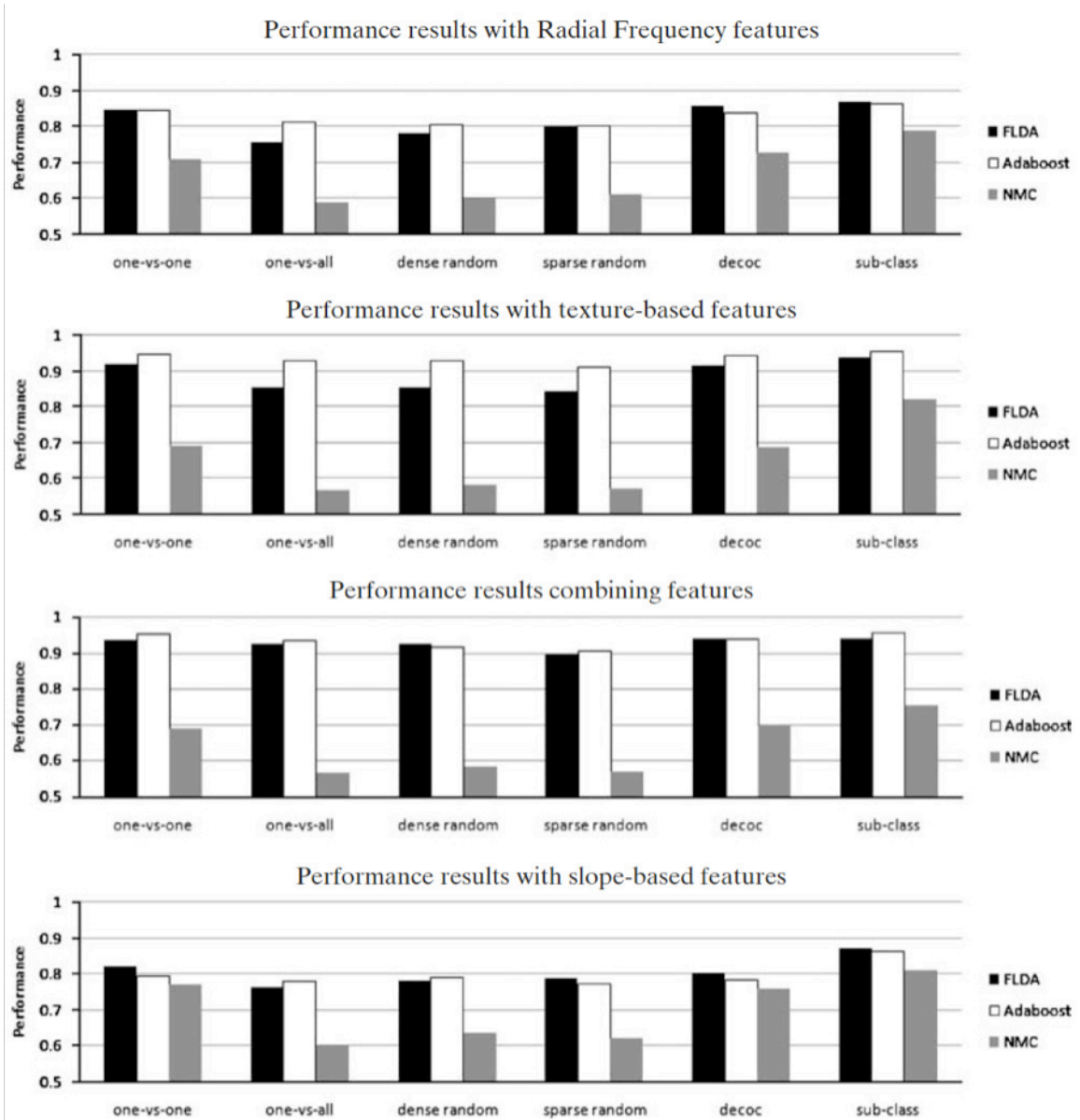


Fig. 3.13. [77] Performance results for different sets of features, ECOC designs and base classifiers on the IVUS data set

3.4.2. IVUS-Image Based Histology (IVUS-IBH)

Authors in [87] developed a technique for characterization of atherosclerotic plaques via textural processing of IVUS images. In this approach, similar to IVUS-PH (See Chapter 4), the generated tissue color maps can be provided for every IVUS frames acquired

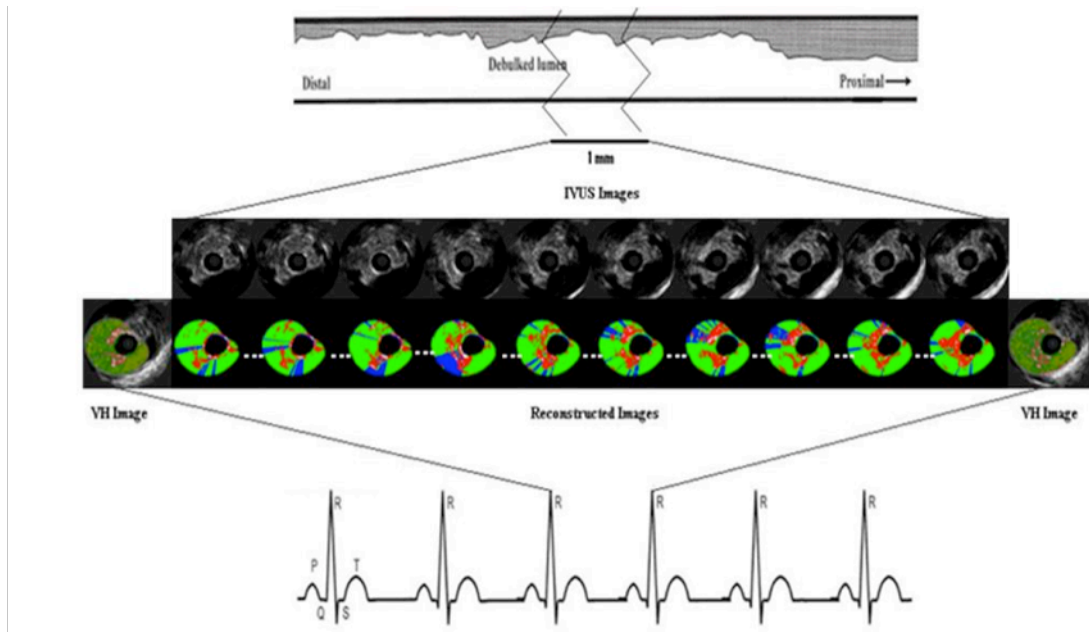


Fig. 3.14. [87] Illustration of enhancement of the longitudinal resolution of atherosclerosis plaque composition characterization of grayscale IVUS using IVUS-IBH method compared to IVUS-VH. In IVUS-IBH approach, the tissue color maps are generated for every frame, similar to IVUS-PH algorithm

during pullback while in IVUS-VH methodology the VH images are generated for every other 30 frames due to ECG-gated protocol, **Figure 3.14**. This would resolve the poor longitudinal resolution in current IVUS-VH technique. What makes this approach different from existing technique is detection of acoustic shadowing behind arc of calcified plaques. These shadow regions which exist and displayed in the plaque area of some IVUS images appears as echo-soft; so, when treated within other parts of plaque area, although they are mostly Calcium and Necrotic Core tissues, normally should be classified to the lipid or Fibrofatty classes [88,89].

Acoustic shadow regions displayed in IVUS grayscale images cannot represent any useful information for plaque component analysis [90], however, IVUS-VH images classifies tissues behind arc of calcified regions in shadow areas. In proposed technique,

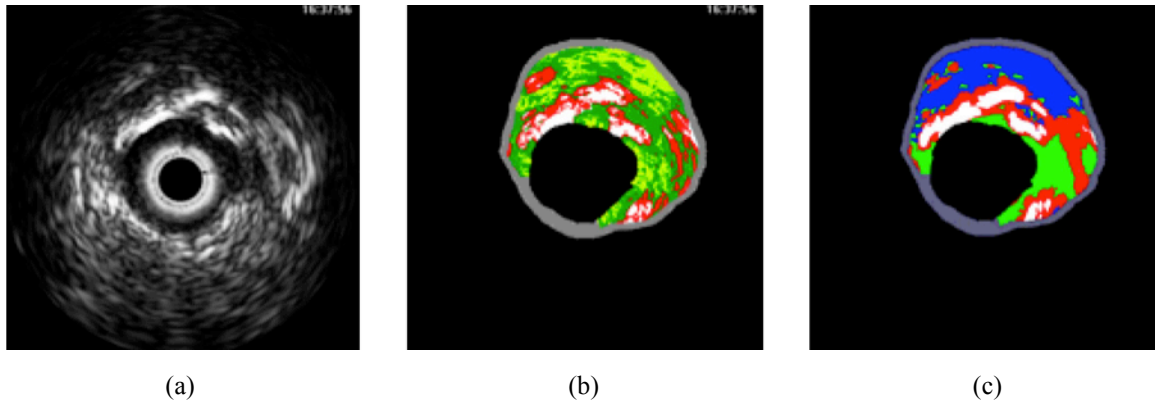


Fig. 3.15. [87] An *in vivo* acquired IVUS grayscale image (a), corresponding VH image (b), generated tissue color map through IVUS-IBH approach (c). The red, white, green, and blue colors represent necrotic core, calcified, fibro-fatty, and acoustic shadowing regions, respectively.

“shadow regions” is detected through two thresholding steps; one thresholding procedure for detecting the high-intensity regions, and another one to identify the existence of the low intensity regions behind the regions detected in the previous step and mark them as “shadow region”. In order to characterize the rest of plaque regions, two feature extraction methods, local binary pattern (LBP) [79] and the run-length method [91] were combined. *In-vivo* and *ex-vivo* results were validated with corresponding IVUS-VH images as gold standard and the overall accuracy for all tissue types found to be 73%. Sensitivities (specificities) were reported 80% (86%) for dense calcium, 80% (92%) for fibro-fatty tissues and 60% (81%) for necrotic core. **Figure 3.15** shows an *in vivo* acquired IVUS frame and generated tissue color map through IBH approach along with corresponding VH image for comparison.

3.4.3. IVUS-Vasa Vasorum (IVUS-VV) Imaging

The vasa vasorum (VV) are microvessels that nourish vessel walls and possibly atherosclerotic plaques **Figure 3.16**. It has been shown that the rich capillary networks of

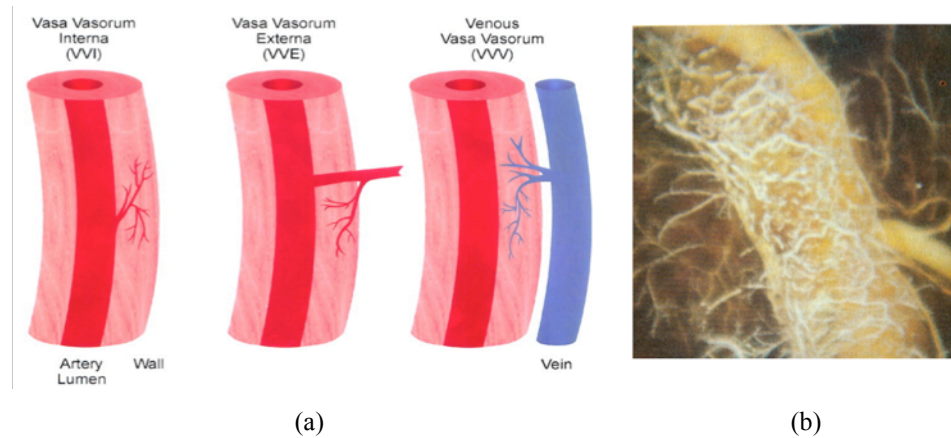


Fig. 3.16. Schematic of different VV formations in coronary artery (a), Visualization of VV and neovascularization of atherosclerotic coronary arteries by cinematography of silicone injection in cleared human hearts [95] (b).

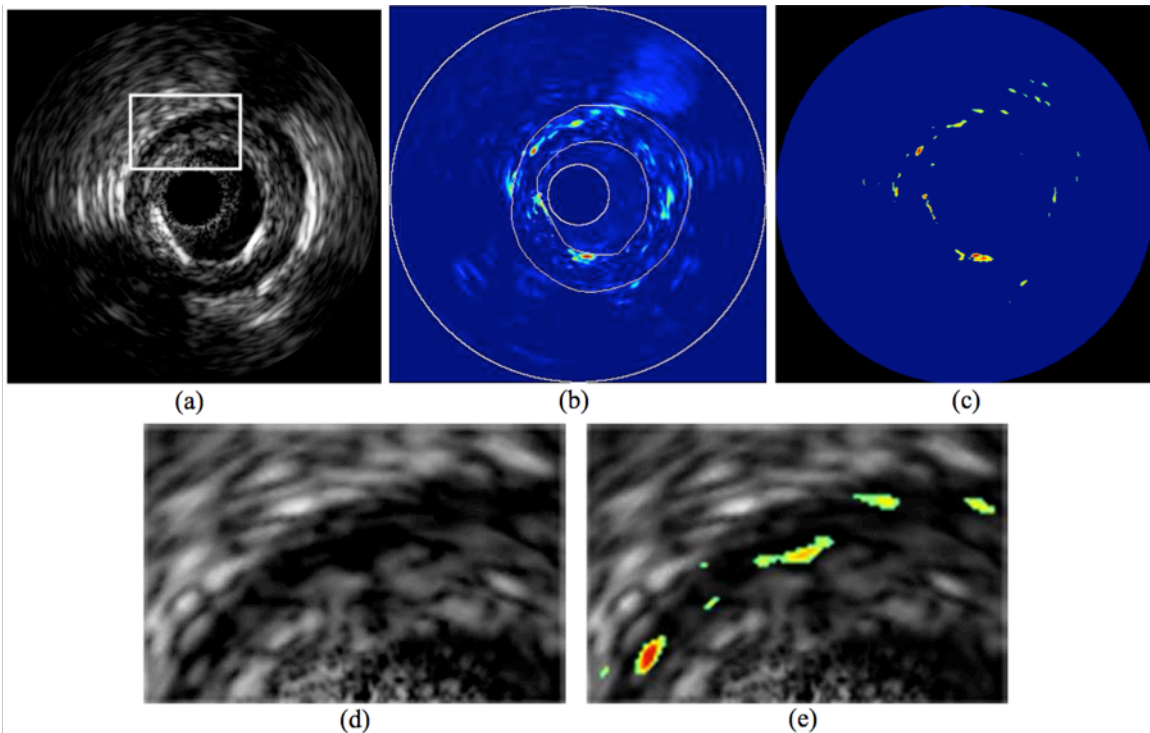


Fig. 3.17. [94] A grayscale IVUS frame before contrast agent injection (a), enhanced frame before (b) and after thresholding (c), zoomed area (d) corresponding to white rectangle in (a), imposed colored VVs (e).

VVs are correlated with vessel wall inflammation and plaque vulnerability [92,93]. Therefore, detection of such neovascularizations is of importance because any disruption in plaque nourishment may lead to regression of atherosclerosis disease. For this reason,

authors in [94] deployed IVUS technology to visualize proliferation of VV neovascularizations for the first time. Their framework relied on two steps: 1) injection of contrast agent (OptisonTM) to increase echogenicity of VVs, 2) registration among collected IVUS frames before and after injections for elimination of vessel and catheter movements, 3) enhancement detection through difference-imaging and statistical techniques. **Figure 3.17** demonstrates a grayscale IVUS frame prior to injection of contrast agent and resulting enhanced image before and after thresholding that show presence of VVs.

3.5. Summary and Conclusion

The numbers of developed IVUS-based frameworks and conducted researches signify the capability of this imaging modality and the importance of better understanding of atherosclerosis disease. It is reasonable to conclude that the ultimate goal of any tissue characterization is the algorithmic detection of all tissue compositions, especially vulnerable plaques, which are ultimately identified by an expert that assesses the classified tissue color maps. In the concept of atherosclerotic plaque characterization, all described methods have their own advantages, however, in their clinical applications, they have been only partially successful due to various reasons including:

- Stringent characteristics of atherosclerotic tissues.
- Variations among extracted tissues features.
- Intrinsic variability among transducer spectral parameters (*i.e.* center frequency, bandwidth).

- Lack of precise, sufficient, and comprehensive matched IVUS-histology datasets (ground truth).
- Extension of *in vitro* trained classifiers for *in vivo* applications without proper validation.

In the next chapter, we consider the realistic challenges from data collection and normalization toward classification. We investigate the possibility of extension of VH algorithm using 40MHz single element transducer.

4. Chapter Four:

CHALLENGES IN ATHEROSCLEROTIC PLAQUE CHARACTERIZATION ALGORITHMS WITH IVUS

In vivo plaque characterization is an important research field in interventional cardiology. We will study the realistic challenges to this goal by deploying 40 MHz single-element, mechanically rotating transducers. In this chapter, the intrinsic variability among the transducers spectral parameters as well as tissue signals will be demonstrated. Subsequently, we will show that global data normalization is not suited for data calibration, due to the aforementioned variations as well as the stringent characteristics of spectral features. We will describe the sensitivity of an existing feature extraction algorithm based on eight spectral signatures (integrated backscatter coefficient, slope, midband-fit (MBF), intercept, and maximum and minimum powers and their relative frequencies) to a number of factors, such as the window size and order of AR model. It will be further demonstrated that the variations in the transducer's spectral parameters (i.e., center frequency and bandwidth) cause inconsistencies among extracted features. In this chapter, two fundamental questions are addressed: 1) what is the *best reliable* way to extract the *most informative* features? and 2) which classification algorithm is the *most appropriate* for this problem? We will present a full-spectrum analysis as an alternative to the eight-feature approach. For the first time, different classification algorithms, such as *k*-nearest neighbors (*k*-NN) and linear Fisher, will be employed and their performances quantified. Finally, we will explore the reliability of the training dataset and the

complexity of the recognition algorithm and illustrate that these two aspects can highly impact the accuracy of the end result, which has not been considered until now.

4.1. Introduction

In [64], the authors presented a spectrum-based technique on the IVUS signals and employed classification tree to differentiate plaque compositions using 30-MHz, unfocused, mechanically rotating transducers. This approach was based on seven spectral parameters (intercept, slope, midband-fit (MBF), and minimum and maximum powers and their corresponding frequencies) extracted from tissue spectra, which were normalized through the spectrum of a Plexiglas reflector. The same group used the IB coefficient as an additional feature and showed that AR models are superior to the Fourier technique [68]. The first two signatures (intercept, slope) were initially introduced by Lizzi *et al.* [65] and extracted through linear regression fit to the calibrated tissue power spectrum. They further quantified their results through analytical tissue models for eye and liver separately [61]. They demonstrated that the slope and intercept are indicative of the scatterer size and concentration. Although the same spectral features were used for both experiments, their interpretations, weights, and variations were studied independently in two distinct databases of examined organs. In addition to the slope and intercept, the IB coefficient has been shown to impart tissue characteristics [70]. The premises of tissue characterization rely upon the principle that any change in the spectrum can reflect tissue attributes. However, due to the: 1) ambiguity in source of perturbation; 2) variations in the transducer spectral parameters (center frequency,

bandwidth); and 3) stringent behavior of closely related tissues (i.e., fibrotic–fibrolipidic or calcified-necrotic core), a reliable feature extraction algorithm, along with a robust classifier, is required.

For the rest of this chapter, we discuss the realistic challenges from preparation of specimens toward classification and review the eight-feature extraction algorithm along with its difficulties supported with experimental results. We describe the complexity of classification algorithm along with full-spectrum analysis. All data was collected *in vitro* as described in Section 3.2.2.2.

4.2. Methodological Challenges

4.2.1. Variability of Tissue Signatures

The basic tenet of ultrasound tissue characterization is that different tissue types imprint their signatures on the backscattered echo received by the transducer. It has been shown that the spectral analysis of ultrasound signals would provide informative features for tissue characterization [61,63]. This is because the tissues of interest generate signals that are stochastic (their internal constituents exhibit randomness in size, position, orientation, etc.) and the spectra represent the ensemble properties of the scatterers. If the spatial autocorrelation function describing these factors has a known form, then the theoretical scattering models can be used with spectral data to estimate two physical scatterer properties: the effective sizes of constituent scatterers and their acoustic concentration.

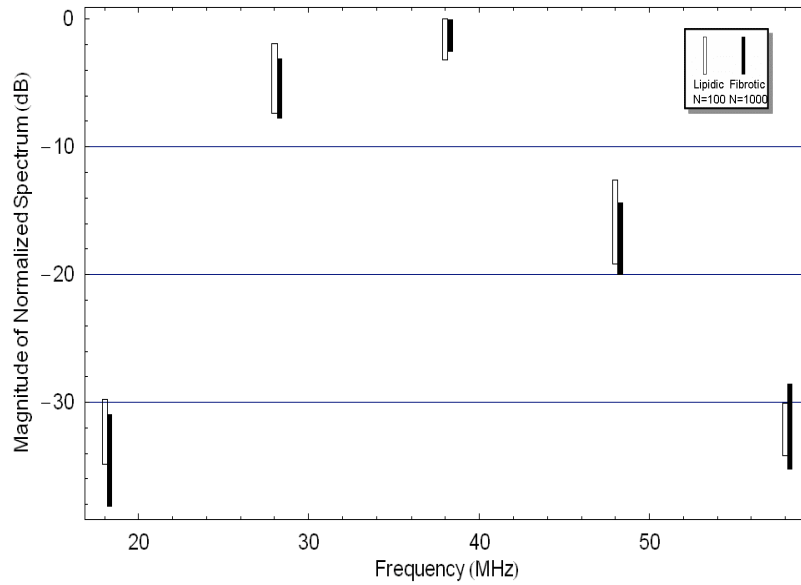


Fig. 4.1. Normalized spectra of two types of plaque tissues found in one particular frame of data. The bars represent the interquartile range of variation. The unfilled bars represent lipidic tissue and the filled bars, fibrotic tissue. For meaningful comparison, each sample spectrum has been normalized to have unit energy. The N refers to the number of spectra used to compute the statistics.

It is a statistically observable fact that on averaging a large number of spectra obtained from homogenous areas of tissue in carefully controlled *in vitro* experiments, different types of tissue give rise to recognizably different spectra, Figure 3.5. The principal challenge in building a tissue characterization system is to develop a proper definition for tissue signatures that maintains their similarity within each tissue type and distinction between tissue types. This is indeed a challenge since the tissue signatures corresponding to a single tissue type can, in general, be shown to vary across different cross-sectional slices even within the same vessel. This is illustrated in **Figure 4.1**, which shows summary statistics of normalized spectra corresponding to two tissue types: lipidic and fibrotic. The normalized spectrum at a point on the IVUS image is computed as follows: a small segment (typically $250 \mu\text{m}$) of the digitized RF signal corresponding to that point

is identified. The windowed Fourier transform of that signal segment is then computed and normalized by scaling so that the total sum of squares is unity. A normalization step is necessary in order to compare the shapes of spectra that might differ significantly in total energy. The bars in **Figure 4.1** were constructed by computing the statistical measures of a number of spectra for each tissue type separately. From the graph, it appears that these two tissue types might be recognizable—albeit with some errors—on the basis of their normalized spectra. It is also clear that increased errors in characterization would be incurred if any single frequency component were used for characterization. A formal pattern recognition algorithm that uses all the spectral information available must be used to achieve the maximum possible accuracy based on the available data.

The source of such variations can be related to: 1) image formation, such as small changes in the angle of incidence of the ultrasound beam or variations in the geometric configuration of scatterers; 2) genuine changes in physical characteristics within the particular tissue type; 3) and variation in transducer properties that confound the recovery of tissue type from tissue signatures. The variability in normalized spectrum across four frames of RF signals acquired from two randomly selected cadaver hearts in **Figure 4.2**. The overlapping spectra visually confirm the difficulty that is involved in characterizing these two tissue types on the basis of their spectral signatures. For example, at 20 MHz, for the third frame analyzed (see filled bar), lipidic tissue seems to be well separated from fibrotic tissue. However, if a classifier were built taking into account the 20 MHz components of the spectra derived from this frame alone, it would be impossible to

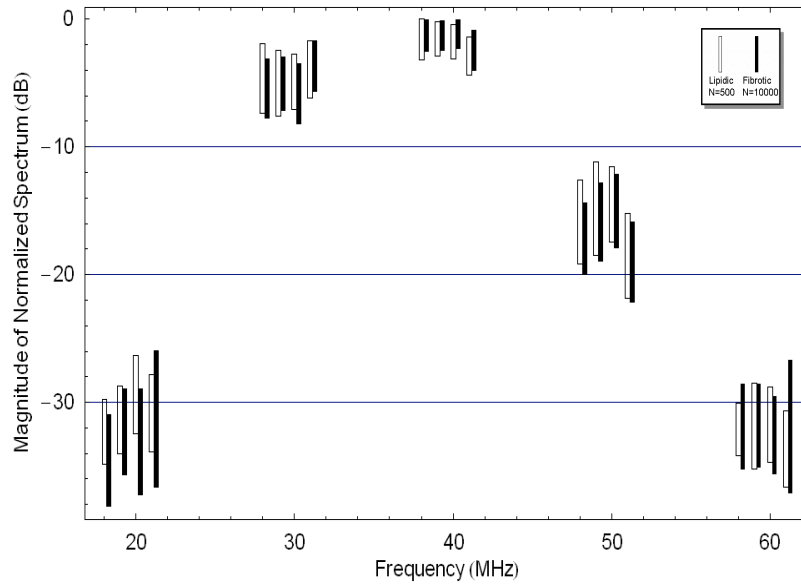


Fig. 4.2. Normalized spectra of two distinct types of plaque tissue found in four cross-sections of data from two cadaver hearts. As before, the bars represent the interquartile range of variation. The unfilled bars represent lipidic tissue and the filled bars, fibrotic tissue.

discriminate between lipidic and fibrotic tissue in another frame (see unfilled bar). In addition to the aforementioned factors, imaging of the plaque through blood, which is difficult to simulate *in vitro*, can be expected to introduce signal changes, e.g., attenuation. Furthermore, tissue fixation might alter the acoustic and structural properties of the tissues. A tissue characterization algorithm developed using *in vitro* data will work on *in vivo* data to the extent that the tissue signatures remain similar. As long as the differences found in the tissue signatures between the *in vitro* and *in vivo* imaging situations are consistent, it may still be possible to empirically retune an *in vitro*-trained algorithm and have it perform well *in vivo*. However, not much is known about the nature of these differences, so they need to be further studied and validated.

Once a database of signatures and the corresponding known tissue types has been built, a pattern recognition algorithm is trained that will take in a signature as the input, carry out

the computations, and arrive at the most likely estimate of tissue type. This method has been established [64,96,97] albeit within limitations due to the variability of tissue signatures.

4.2.2. Ground Truth

The overall justification of *in vivo* real-time plaque characterization is made by interventional cardiologists through the use of classified tissues, therefore, it is indispensable to train the classifier with the most reliable features. In this research, the labeling of IVUS images and validation of color map (classified) tissues are compared with corresponding histology images. Although the histology image is the gold standard, its interpretation can be subjective. Consequently, experts may categorize tissues differently, and as a result, different training datasets may lead to different classification. For example, one can simply categorize tissues as fibrotic, lipid pool, necrotic core and calcium, or one may differentiate between the levels of presence of fatty materials and add fibro-lipid to compromise between fibrotic and lipid. Basically, in order to collect a training dataset, the ROIs in the arteries are marked and relative cross-sectional histology images obtained. The IVUS-histology frame alignment plays a crucial role in this study because the IVUS frames are labeled through the interpretation of the corresponding histology images. Subsequently, the signals are assigned to label tissues and relative features are extracted. The IVUS-histology matching problem becomes more challenging due to the: 1) curvature of arteries, especially in the LCX; 2) registration between an IVUS image and its relative histology since the IVUS imaging plane and the slicing plane of the microtome are somewhat different; and 3) shrinkage of the arteries after formalin

fixation.

The main advantage of presented methodology in Section 3.2.2.2 is that the orientation of the artery is not changed throughout the whole procedure before and after fixation. Therefore, more reliable IVUS–histology pairs can be obtained and the number of CSIs per vessel is significantly increased (average of 25 regions per vessel). In fact, increasing the number of ROIs will help to assemble more comprehensive signature database. It is frequently observed that when tissue characterization algorithms are applied to new data (data that is not part of the training set), unsatisfactory results are obtained [98]. This is explained, at least in part, by the fact that the training database is not comprehensive enough—the pattern recognition algorithm has not seen enough examples to learn to recognize new data with sufficient generality. The sufficiency of the training dataset will be discussed in Section 4.4.2.

4.3. Eight-Spectral-Feature Extraction Algorithm

In 1983, Lizzi *et al.* presented a sliding-window analysis method to identify tumors in the eye and liver by using two spectral signatures extracted from calibrated tissue spectra [65]. Those parameters were the slope of the regression line fitted to the mid-band portion of the calibrated spectrum and the intercept of that regression line at zero frequency. In [64], Nair *et al.* extended Lizzi’s approach for coronary atherosclerotic plaque characterization employing five additional spectral features (MBF, and maximum and minimum power and their relative frequencies). They later added an IB coefficient as

the eighth parameter [67]. Unlike the complementary study by Lizzi on uncertainties associated with the extracted spectral features and the accuracy of spectral estimation for prostate and liver examinations [63,99], no comprehensive statistics regarding the consistency of the eight features or the reliability of linear regression fitting of normalized atherosclerotic tissues spectra using 40-MHz single-element transducers have previously been reported to our knowledge. In fact, the liver and prostate tissues are more homogeneous than the coronary plaques and the preliminary assumption of this windowing technique is that the tissues are homogeneous in the windowed samples. In addition, the ultimate goal in liver, prostate, and ocular examinations is to distinguish between benign and malignant tissues. However, in coronary artery plaque characterization, the tissue spectral features are stringent in which any perturbation in calibrated spectrum may lead to misclassification of one tissue for another.

In the rest of this section, we will describe the normalization techniques and consider the variation among transducer spectral parameters, such as bandwidth and center frequency. We will also take into account the influence of such factors on the eight spectral features and demonstrate the variations of slope and intercept in four tissue types (necrotic core, calcium, fibro-lipid, and fibrotic).

4.3.1. IVUS Data Normalization

Using convolution theory, the measured IVUS signal $x(k)$ which is corrupted by uncorrelated noise signal $n(k)$ can be modeled as:

$$x(k) = h(k) * r(k) + n(k) \quad (4.1)$$

where $*$ denotes the convolution and k is the time index. $h(k)$ and $r(k)$ are the transducer impulse response and tissue acoustic impedance functions, respectively. We assume that the reflected signals are wide sense stationary (WSS) and rewrite **Eq. 4.1** in the frequency domain as:

$$X(f) = H(f) \cdot R(f) + N(f) \quad (4.2)$$

To ease the problem, we will further assume that the noise term is zero. Before we describe the deconvolution algorithms, we need to consider the purpose of performing data calibration in more detail. Prior to feature extraction, the spectra of the tissues are required to be normalized in order to eliminate the transducer frequency response. The contradiction arises when the transfer function of the transducer is considered to be consistent. In this case, according to **Eq. 4.2**, the classification results should be the same with or without doing any data normalization since the extracted features are transformed from one location to another preserving their separability in the feature space. However, due to manufacturing limitations and sensitivity of electronic circuits to noise, the transducer spectral parameters (bandwidth, center frequency, and power) differ not only from transducer to transducer but also during acquisition. The problem becomes more complex when the influence of the transducer position and the incident angle of the ultrasound beam on the spectral features are taken into account [100]. Under these circumstances, the best representation of the spectrum of the transducer remains questionable. Researchers have used global normalization techniques based on the spectrum of a perfect reflector in various applications [64,68,99,101,102]. More recently, a blind deconvolution technique was deployed as an alternative [66]. In the following

sections, we will study a global normalization technique and investigate its limitations as well as effects on coronary artery plaque classification using eight spectral features.

4.3.1.1. *Global Data Calibration Using Plexiglas Spectrum*

According to **Eq. 4.2**, given any spectrum of a transducer $H(f)$, we can simply normalize the data by subtracting its logarithm from the logarithm of the measured IVUS spectrum, $X(f)$ (the noise term is assumed to be zero),

$$20 \log R(f) = 20 \log X(f) - 20 \log H(f) \quad (4.3)$$

Basically, a short ultrasonic pulse is transmitted toward perfect reflector and the spectrum of the reflected signal is considered as an estimate of the transducer frequency response. This is not a feasible approach for clinical real-time plaque characterization but has been performed for *in vitro* experiments. During our *in vitro* experiments, after collecting IVUS data from each specimen, the same catheter was inserted into a plexiglas cylinder of 4 mm in diameter. The transducer must be centered and placed perpendicular to the plexiglas wall. The latter condition might not be exactly met for single-element rotating transducers with 1.41° ($360^\circ/256$) spacing between A-lines unless the rotation of the transducer is halted. We followed a strict protocol to acquire the preeminent plexiglas signals, and studied the variation of center frequency, bandwidth at -6 and -12 dB, of three different transducers. **Figure 4.3(a)** demonstrates a reflected signal from the plexiglas wall with a center frequency of 37.01 MHz. For each Plexiglas frame, the angle with the maximum absolute non-saturated amplitude A_{\max} was found. Then, a Hamming window of sample size 64 was centered at the corresponding time index, t_{\max} and exerted. Subsequently, a 4096-point FFT was performed and the computed spectra were

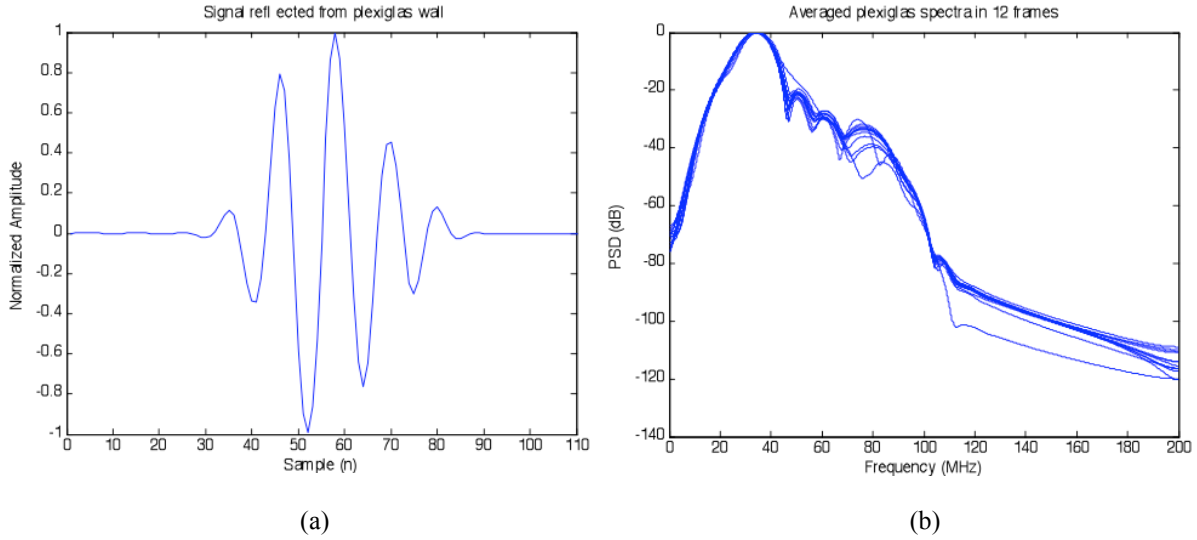


Fig. 4.3. Signal reflected from plexiglas wall (a), averaged spectra measured from 12 distinct plexiglas acquisition frames using Fourier analysis (catheter 3 in **Table 4.1**) (b)

averaged. Our results showed the inter- and intra-frame variations of the aforementioned factors. Inter- and intra-frame variations indicate that the transducer's spectral parameters deviated from line to line in the same frame and among distinct frames. The statistical variations of the center frequency and the bandwidth of 12 averaged spectra measured in 12 distinct frames during pullback have been listed in **Table 4.1** and shown in **Figure 4.3(b)**.

Table 4.1. Statistical variations of catheters' spectral parameters

	Catheter 1	Catheter 2	Catheter 3
Center frequency	34.48 ± 0.14	41.93 ± 0.31	36.46 ± 0.69
Bandwidth (-6dB)	29.31 ± 1.64	37.34 ± 2.28	32.32 ± 2.65
Bandwidth (-12dB)	59.22 ± 2.82	63.68 ± 3.39	66.79 ± 5.36

The transducer center frequency appears to be fairly consistent around a frequency, that is, off from the nominal frequency (40 MHz). This may not directly impact any extracted spectral feature but becomes crucial when the bandwidth is measured. In fact, the

bandwidth is the most important spectral parameter, since the eight features are extracted within a specific bandwidth. It is expected that the variations in the bandwidth increase at lower signal-to-noise ratios (SNRs).

The inter- and intra-frames variations of the spectra of transducers are inevitable and can be the source of (large) perturbations in the tissue spectra, as discussed before. Given these variations, a global normalization technique does not appear suitable to extract the eight spectral features, especially when a statistical classification tree is used for decision-making. In the next sections, we will normalize the spectra of four tissue types within the bandwidth of 30–50 MHz and show overlaps between two spectral features (slope and intercept).

Short-time AR analysis has been employed for ultrasound signals [60,103-105], and shown to be superior to short-time Fourier analysis, depending on the application. However, the accuracy of the estimated power spectral density (PSD) can be influenced by the sampling frequency, order, and window size [106,107], which may not be crucial in other applications but need to be considered in this case due to the stringent characteristics of atherosclerotic tissue spectra. The AR process of order p can be written as:

$$x(k) = \sum_{m=1}^p \alpha_m x(k-m) + n(k) \quad (4.4)$$

where $n(k)$ is the noise term of variance σ^2 . The PSD can be estimated by AR coefficients α_m using the Yule–Walker equations [108,109] as follows:

$$P_{AR} = \frac{\sigma^2}{\left| 1 + \sum_{m=1}^p \alpha_m e^{-j2\pi f_m T_s} \right|} = \sum_{q=-\infty}^{\infty} R_{xx}(q) e^{-j2\pi f_m q T_s} \quad (4.5)$$

where

$$R_{xx}(q) = \begin{cases} -\sum_{m=1}^p \alpha_m R_{xx}(q-m) & ; \quad q > 0 \\ -\sum_{m=1}^p \alpha_m R_{xx}(-m) + \sigma^2 & ; \quad q \geq 0 \end{cases} \quad (4.6)$$

The $T_s = 2.5 \text{ nsec}$ is the sampling interval and the R_{xx} is the autocorrelation function of $x(k)$. **Equation 4.6** can be augmented and expressed in the matrix form in order to incorporate the σ^2 as follows:

$$\begin{bmatrix} R_{xx}(0) & R_{xx}(-1) & \cdots & R_{xx}(-p) \\ R_{xx}(1) & R_{xx}(0) & \cdots & R_{xx}(-(p-1)) \\ \vdots & \vdots & \vdots & \vdots \\ R_{xx}(p) & R_{xx}(p-1) & \cdots & R_{xx}(0) \end{bmatrix} \begin{bmatrix} 1 \\ \alpha_1 \\ \vdots \\ \alpha_p \end{bmatrix} = \begin{bmatrix} \sigma^2 \\ 0 \\ \vdots \\ 0 \end{bmatrix} \quad (4.7)$$

The AR coefficients α_m and σ^2 can be computed by solving the $p+1$ estimated autocorrelation lags and using $R_{xx}(-m) = R_{xx}^*(m)$, where $*$ denotes complex conjugate.

Figure 4.4 shows estimated PSD of reflected signal from the plexiglas wall, **Figure 4.3(a)**, with different AR model orders. The estimated PSD with a low-order (4) AR model has narrower bandwidth, and those with higher orders (15,40) suffer from inconsistencies within the bandwidth that can hinder the normalization accuracy.

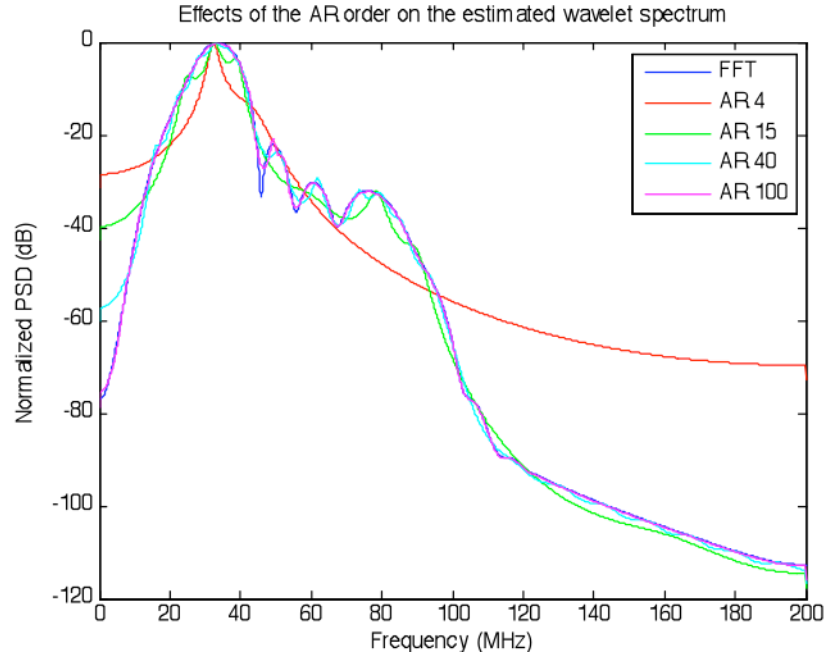


Fig. 4.4. PSD estimation of plexiglas signal with AR models of order 4, 15, 40, 100 along with Fourier analysis.

4.3.2. Linear Regression Analysis and Eight-Spectral-Feature

Computation

In order to extract eight spectral features, the measured IVUS signals reflected from tissues are segmented into short subsequences using overlapped windows. The fundamental assumption is that the tissue is homogeneous in the sampled volume. Subsequently, the spectral Fourier analysis or AR estimate of each piece is performed. The window length is inversely proportional to the main-lobe width of the calculated spectrum, producing a tradeoff on the time–frequency space resolution. After normalization, a linear regression line is fitted to the calibrated spectrum within the specified bandwidth to compute eight spectral features. In order to eliminate any

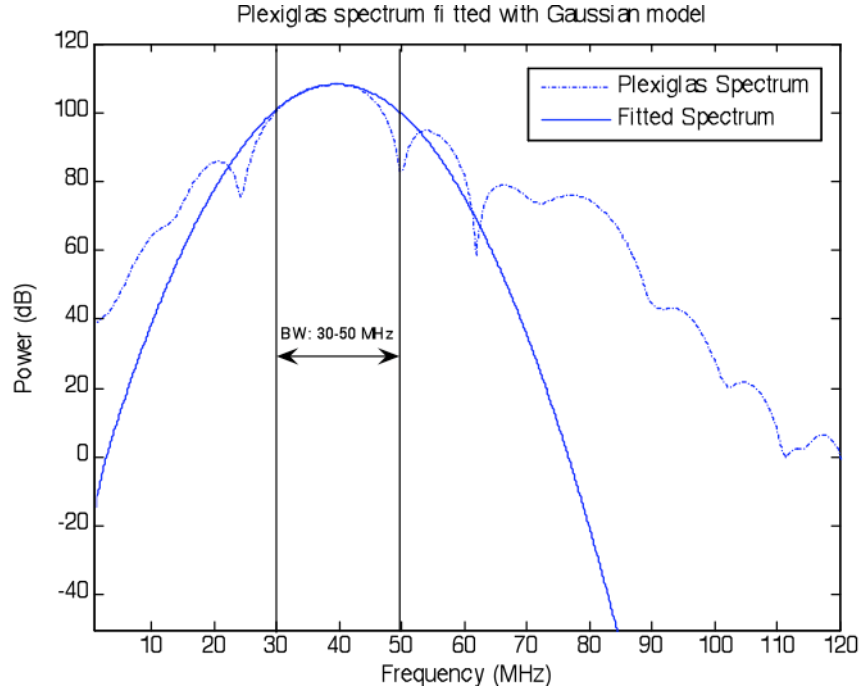


Fig. 4.5. Plexiglas spectrum fitted with Gaussian model within specific range of bandwidth (30-50 MHz \sim -20 dB).

reverberation from the plexiglas wall and obtain more consistent results, the averaged plexiglas spectrum fitted with a Gaussian model was used, **Figure 4.5**.

Seven spectral features are computed through the linear regression fit: 1) the slope of the regression line (in decibels per megahertz); 2) the intercept (in decibels), which is the extrapolation of the regression line at zero frequency; 3) the MBF (in decibels), which is the value of the regression line at the center frequency; 4) the minimum power P_{\min} (in decibels); 5) the relative frequency f_{\min} (in megahertz); 6) the maximum power P_{\max} (in decibels); and 7) the relative frequency f_{\max} (in megahertz). The last feature, IB , is measured as Eq. 3.1.

Figure 3.6 illustrates the extracted features within the bandwidth of 30–50 MHz. Besides the sampled volume, the bandwidth is the other crucial factor that determines on the

statistical accuracy of the spectral estimation and extracted features. Among these spectral features, a linear dependency is deduced from the first three: slope, intercept, and MBF. From the classification point of view, only two of them are informative, since one can be derived from the other two. This has also been noted by Lizzi *et al.* and reported in [110]. They not only used the slope and MBF as independent spectral features for tissue characterization but also pointed out that the intercept could be useful due to its insensitivity to intervening acoustic attenuation. The same dependency can be derived for IB and MBF, since the MBF is the first-order approximation of IB, which has been normalized by the bandwidth [111].

4.3.3. Experimental Results

For illustration, one CSI, **Figure 2.8(a)**, containing four tissue types was chosen from an LCX coronary artery imaged with a 40-MHz single-element Boston Scientific transducer (transducer 2 in Table 4.1). The slope and intercept were extracted from 92, 73, 299, and 1234 ROIs of necrotic core, calcified, fibrolipid, and fibrotic signals, respectively, in three distinct frames with 10-frame interval. Each ROI contained 64 Hamming-windowed samples. For each ROI, the signals were passed through a linear phase bandpass Butterworth filter of order 10 with cutoff frequencies of $f_{c_{\min}} = 10\text{MHz}$ and $f_{c_{\max}} = 80\text{MHz}$. Then, five adjacent line spectra were computed using a 4096-point FFT. In order to get a smoother spectrum, a median filter of size 5×3 was slid on the calculated spectra. The purpose of this experiment was to evaluate the consistency of the intercept and slope along with the reliability of linear regression fitting to the normalized tissue spectra. The bandwidth was chosen to be 30–50 MHz (~ -20 dB) and an average of

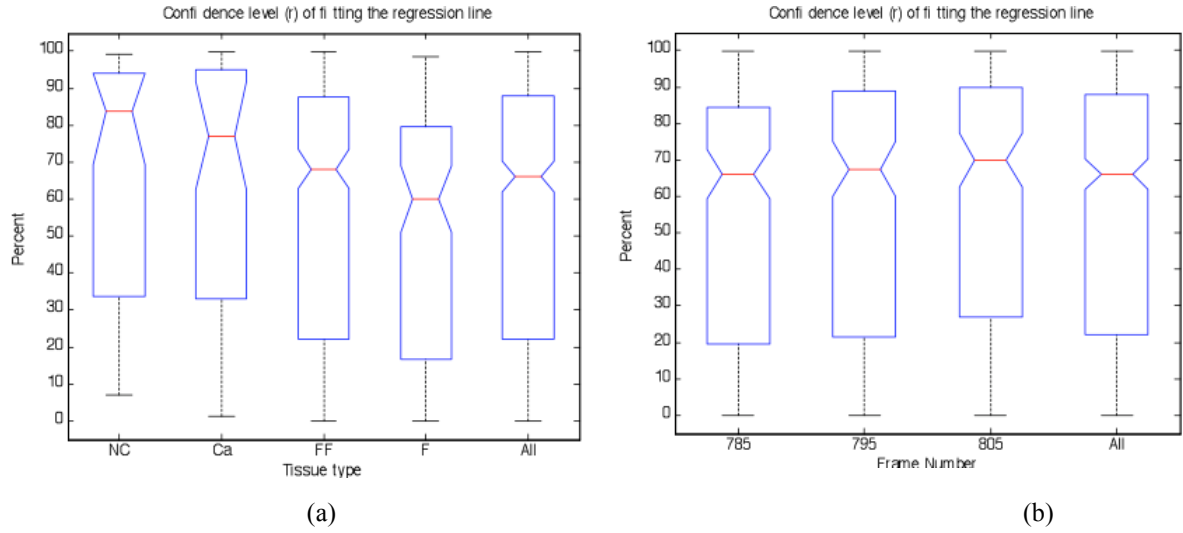


Fig. 4.6. Box whisker plots of confidence level of linear regression analysis in four tissue types, 92 ROIs for NC: necrotic core, 73 ROIs for Ca: calcium, 299 ROIs for FF: fibrofatty, 1234 ROIs for F: fibrotic (a) and three frames (b). Each ROI contains 64 hamming windowed samples.

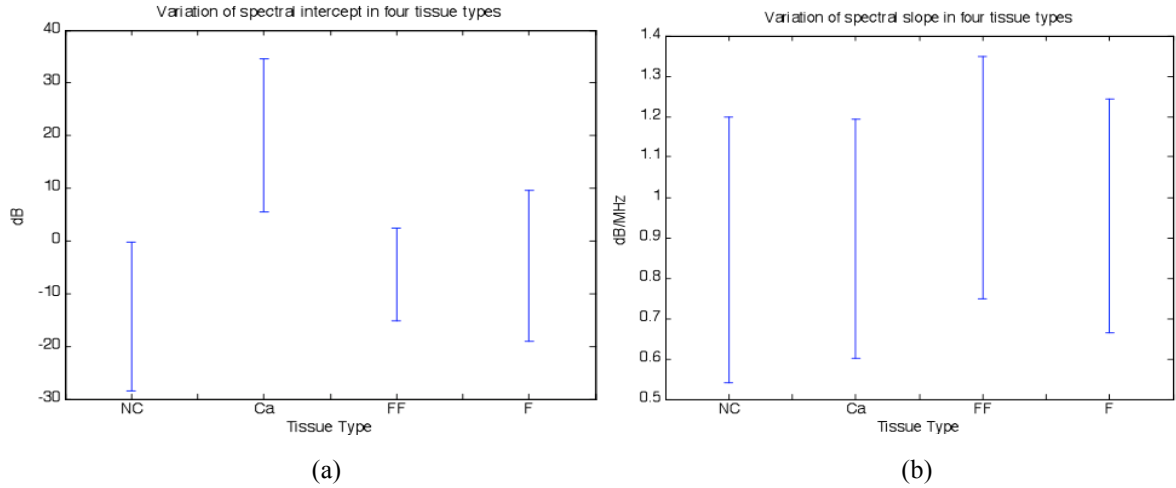


Fig. 4.7. Variations of two spectral features extracted from four tissue types. Intercept (a) and Slope (b). necrotic core (NC), Calcium (Ca), fibro-fatty (FF) and fibrotic (F).

the five plexiglas spectra (measured, as described in Section 4.3.1.1) fitted with a Gaussian model was considered.

Figure 4.6 shows the box-whisker plots of the Pearson's coefficient of correlation (r) of the linear regression analysis for the four tissue types in three frames. The interquartile ranges of boxes demonstrate the high variations in confidence levels. Ignoring the

outliers, we can conclude that the regression lines fitted to the necrotic core and calcified plaque's normalized spectra are more reliable than those of the fibro-lipid and fibrotic. Approximately, the same variations were found in three collected frames. The low confidence levels actually imply that a linear regression of normalized tissue spectra within the selected bandwidth can hardly be achieved. The variations of spectral intercept and slope have been illustrated in **Figure 4.7**. The overlap of the 95% confidence intervals for each parameter (intercept and slope) in the four tissue types suggest the difficulties of classification based on these parameters. Only the calcified region can be easily recognized due to its higher intercept values, but this can also be visually discerned examining the gray-scale final IVUS image.

Variations among spectral features can be expected due to inconsistencies associated with tissue spectra and transducer spectral parameters. Perturbations in extracted features are increased if a broader bandwidth is chosen. Despite these variations and inconsistencies, the plaque characterization in the coronary artery may still be feasible, even through an eight-feature algorithm, if an appropriate classification algorithm is used.

4.4. Full-Spectrum Analysis and Algorithmic Challenges

4.4.1. Full-Spectrum Analysis Algorithm

We showed the perturbations among tissue spectra and pointed out that global normalization could not resolve these variations. However, the atherosclerotic plaque

classification could be achievable if: 1) appropriate features were extracted, with some of them having potential physical and/or biological grounds (*i.e.* intercept that is indicative of acoustic impedance and concentration), and 2) the apposite classification algorithm is deployed. In this section, we will use full-spectrum analysis and extract features in the functional range of the bandwidth of the transducers. For a single-element rotating transducer with nominal 40-MHz center frequency and 100% bandwidth, this range is measured to be 20–60 MHz. The dissimilarities of tissue spectra in this range, **Figure 3.5**, motivated us to use full-spectrum analysis. It can be seen that the most recognizable difference in the backscattered signals spectra is energy. Therefore, we extracted the energy norm E_{norm} as one of the features that could be a measure for the softness or hardness of the tissue structures. For this reason, signals in the regions behind calcified and necrotic core are attenuated sharply and shadows are often visible behind arcs of calcified plaques. The tissue characterization in these regions remains uncertain [38] and needs further study and validation. For a given tissue signal of length l , $\mathbf{x} = [x_1, \dots, x_l]$ the energy norm is calculated as follows:

$$E_{norm} = \|\mathbf{x}\| = \sqrt{\mathbf{x} \cdot \mathbf{x}^T} \quad (4.8)$$

where \cdot and T are vector inner product and transpose notations, respectively. As a second feature, we extract the radial position (r) of the tissue from the center of the transducer in order to incorporate tissue signals attenuations.

In Section 4.2.1, we described the variations among tissue spectra and also illustrated the variations of spectral magnitude at five frequency bins in one and four CSIs for two closely related tissue types (lipidic, fibrotic), **Figure 4.1** and **Figure 4.2** and 5). By

looking at these figures, we will realize that the lipidic tissue spectra have relatively higher mean magnitude compared to fibrotic. Consequently, we opted to extract the spectral magnitudes at every frequency bin within the functional range of bandwidth as supplemental spectral features. For this reason, the IVUS RF signals were windowed followed by taking a N -point FFT. For real-valued time domain signals, we could ignore the negative frequencies as they result in the same estimates as their positive counterparts. Therefore, only $N/2$ frequency bins were required to cover the spectrum up to $f_s/2$, $f_s = 400\text{MHz}$. In order to get smoother spectrum and alleviate perturbations, a 2-D median filter of size $M \times 1$ was applied on the magnitude spectra and $N/2 - M + 1$ spectral features:

$$\mathbf{v} = \left\{ v_i^{\frac{i \cdot f_s}{2}} ; i = 1, \dots, N/2 - M + 1 \right\} \quad (4.9)$$

were extracted (the dc component was ignored). The $v_i^{\frac{i \cdot f_s}{2}}$ is the i -th PSD magnitude corresponding to the frequency at $\frac{i \times f_s}{2}$ Hz. However, due to the narrowband characteristic of IVUS signals, only spectral features within the functional range of transducer bandwidth were considered. In this case, the integer number, i , should be found such that the value of $\frac{i \times f_s}{2}$ approximates the lower and upper frequencies of the bandwidth. Therefore,

$$\begin{cases} i_{\min} \approx \frac{f_{BW_{\min}} \times N}{f_s} \\ i_{\max} \approx \frac{f_{BW_{\max}} \times N}{f_s} \end{cases} \quad (4.10)$$

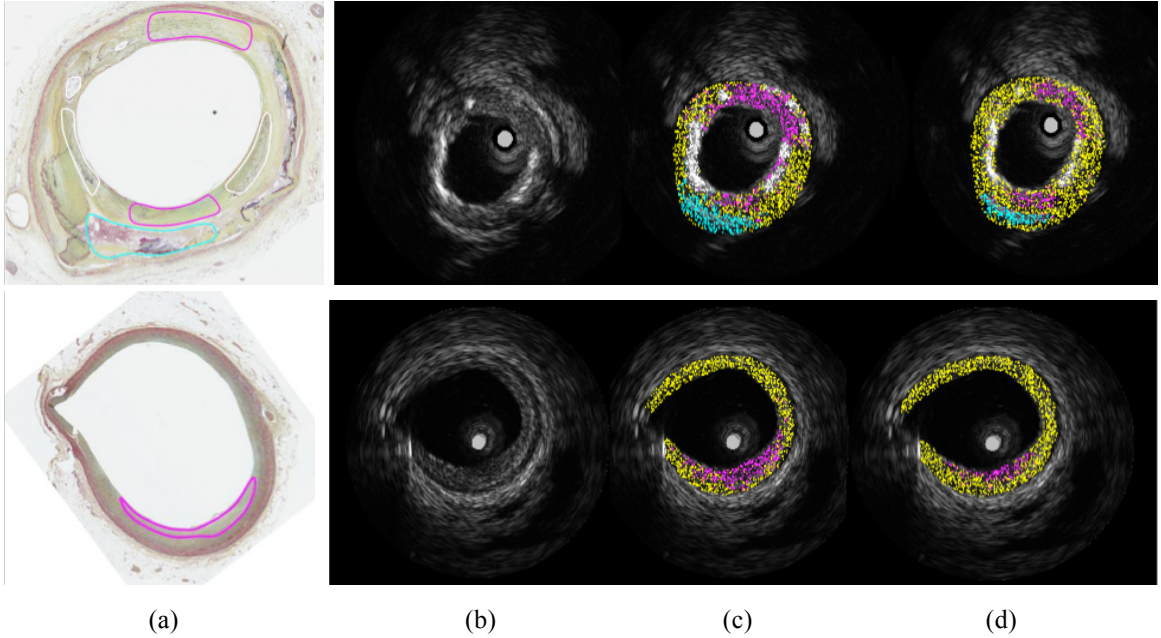


Fig. 4.8. Pictorial illustration of two full-spectrum based classification methods. Movat Pentachrome histology image (a), IVUS image (b), IVUS tissue map generated by Fisher (c), IVUS tissue map generated by k-NN, $k=5$ (d).

Obviously, the resolution of the spectrum is proportional to the number of FFT points. If N is increased, more spectral features can be extracted; however, the training and testing algorithms become more expensive computationally. Finally, the features vector \vec{W} was formed as follows:

$$\vec{W} = \left[\frac{\vec{v}_{BW}}{E_{norm}}, E_{norm}, r \right]$$

$$\vec{v}_{BW} = \left\{ v_j^{\frac{i \cdot f_s}{N}}, j = i_{min}, \dots, i_{max} \right\} \quad (4.11)$$

Figure 4.8 depicts examples of full-spectrum analysis in two CSIs, each collected from different cadavers in the database using the linear Fisher and k -NN classifiers. The parameters were selected as $l = 128$, $N = 512$, $f_{BW_{min}} = 20 MHz$, $f_{BW_{max}} = 60 MHz$, $k = 5$. Only pixels that could be confidently classified were colored. Confidence was related to distance between feature vector and the decision surface. Although both methods show a

good correlation between the corresponding histological regions and the classification color outputs, they should be further investigated with more clinical data in order to assess their efficacy and robustness. In the next section, we shall consider the realistic challenges related to the classification algorithms and training dataset.

4.4.2. Complexity of Algorithm and Sufficiency of Data

The linear Fisher classifier can recognize specific tissue by determining which side of the predetermined hyperplane the features vector \vec{W} is located. The distance between the feature vector and the hyperplane is computed as a measure of reliability. The k -NN classifier recognizes the tissue type by computing distances between the given feature vector and every feature vector in the training set. It determines the most frequently occurring training type among the five nearest neighbors (for $k = 5$). The Fisher classifier is fast and easy to implement but may not be accurate because it does not capture nonlinear separation of spectral regions. On the other hand, the k -NN classifier can capture complex features of the spectral regions but it is computationally expensive.

When assessing the accuracy of a characterization system, one must use a cross-validation approach in which different subsets of the database are, in turn, set aside for testing against an algorithm trained on remaining data. It is important that the test subsets be drawn from separate distributions completely absent in the training data. For IVUS tissue characterization, this translates to drawing test data from cadavers not represented in the training data. Note that this condition is not met by creating a test set by simply drawing a random set of signatures from the entire database. If such procedures that

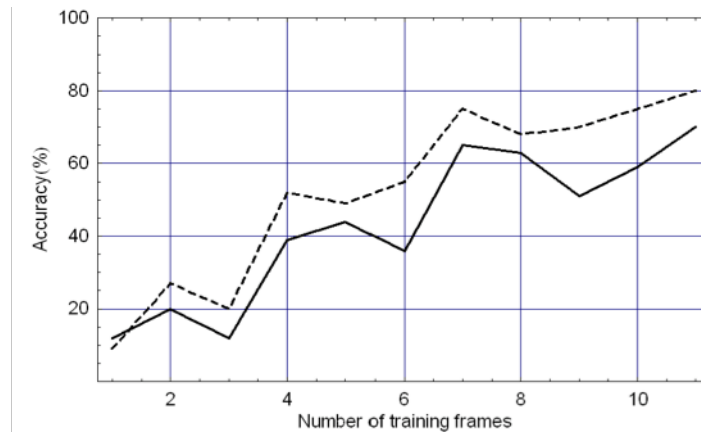


Fig. 4.9. Realistic estimates of the accuracy attainable by a spectrum based tissue characterization algorithm trained to differentiate between blood filled regions (solid line) and tissue (dashed line) in IVUS image.

estimate accuracy are not followed, it might be estimated overly optimistically, especially for small training set sizes. Once the proper method of assessing accuracy is employed, the estimate turns out to be much lower—consistent with what is encountered in clinical evaluations of currently existing algorithms.

In order to appreciate this behavior of pattern recognition algorithms, we show in **Figure 4.9** the estimates of the accuracy of a “tissue characterization” algorithm for lumen detection using *in vivo* data. It is clear that, even for this “simple” problem of discriminating regions of flowing blood (lumen) from regions corresponding to tissue, only modest accuracies are obtained using ten frames even when the very exhaustive k -NN algorithm is deployed. The k -NN algorithm finds the class (“Blood” or “Tissue”) of a given instance of normalized spectrum by searching for the most frequently occurring class among k nearest instances of normalized spectrum found in the training set. In this numerical experiment, the Euclidean metric was used as a measure of nearness and k was set to 5. From this graph, we see that a classifier that is built using data from four frames will correctly detect blood-filled areas in novel frames only 40% of the time. The

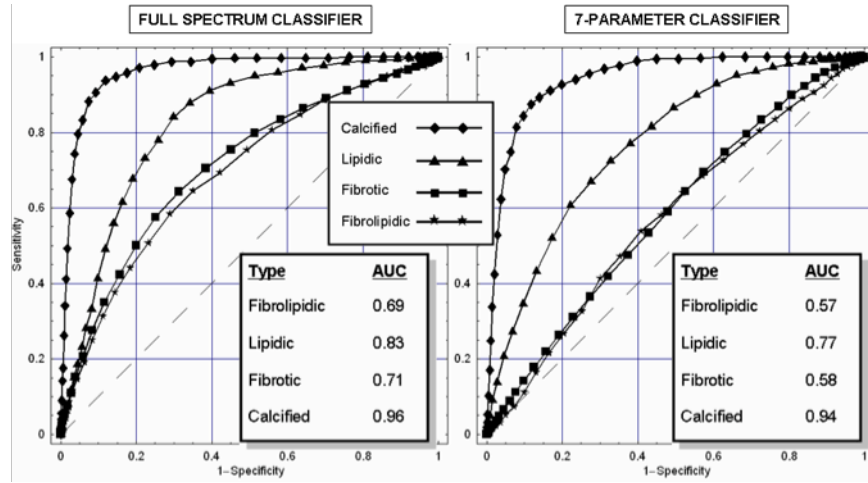


Fig. 4.10. ROC curves comparing the linear separability of full spectral features (left) with that of a reduced set of 7 features (right). 1451, 475, 10668 and 382 volumes of 128 samples of fibro-lipidic, lipidic, fibrotic and calcified tissue signals were used, respectively.

accuracy improves to 70% when 11 frames are used. An examination of the spectra in Figure 4.10 suggests that a simple linear classifier may not be able to satisfactorily discriminate between lipidic and fibrotic tissue because of the large amount of overlap and bracketing seen in each frequency component. However, results obtained using simple linear classifiers are still useful to understand the differences in characterizability of different tissue types. Using simple linear classifiers also helps us establish a standard, against which we can evaluate other characterization schemes.

A useful way to evaluate the accuracy of a classifier is by drawing the receiver-operating-characteristic curve (ROC) that portrays the tradeoff between sensitivity and specificity when the threshold is varied. The area under the ROC curve (AUC) is a metric that can be used to rate different classifiers. We have evaluated the relative ease of characterization of four tissue types (lipidic, fibrotic, fibro-lipidic, and calcified tissue) using the specific definition of tissue signatures suggested previously [64]. As suggested

by the ROC curves shown in **Figure 4.10**, it is empirically evident that the process of summarizing the spectrum by specifying the seven (excluding IB) parameters previously described reduces discrimination in comparison to a full-spectrum analysis.

4.5. Summary and Conclusion

In this chapter, we described the realistic challenges in atherosclerotic plaque characterization including specimen preparation and classification. We intended to implement eight-feature-algorithm and pointed to *in vitro* inter- and intra-frame variations of tissue spectra extracted from data acquired with single-element 40MHz transducer. Spectral slope and intercept were shown to be highly variable and a simple linear regression was not often valid. As a complementary study, these variations can be evaluated using lower frequency transducers in more homogenous media. Among the proposed eight spectral features, we pointed to linear dependency among the slope, intercept, MBF, and IB coefficient. Regardless of the normalization methodology, data calibration cannot be performed precisely and employed due to: 1) variations among tissue and transducer spectra and 2) clinical impracticality.

Full-spectrum analysis algorithm was introduced as an alternative to the eight-feature algorithm and evaluated different classifier performances such as linear Fisher, k-NN. Our hypothesis was that the relative differences in tissue spectra would be held at every frequency bin. In the end we could only partially classify tissues in limited number of CSIs. The extension of full spectrum analysis, as a reliable clinical atherosclerotic plaque

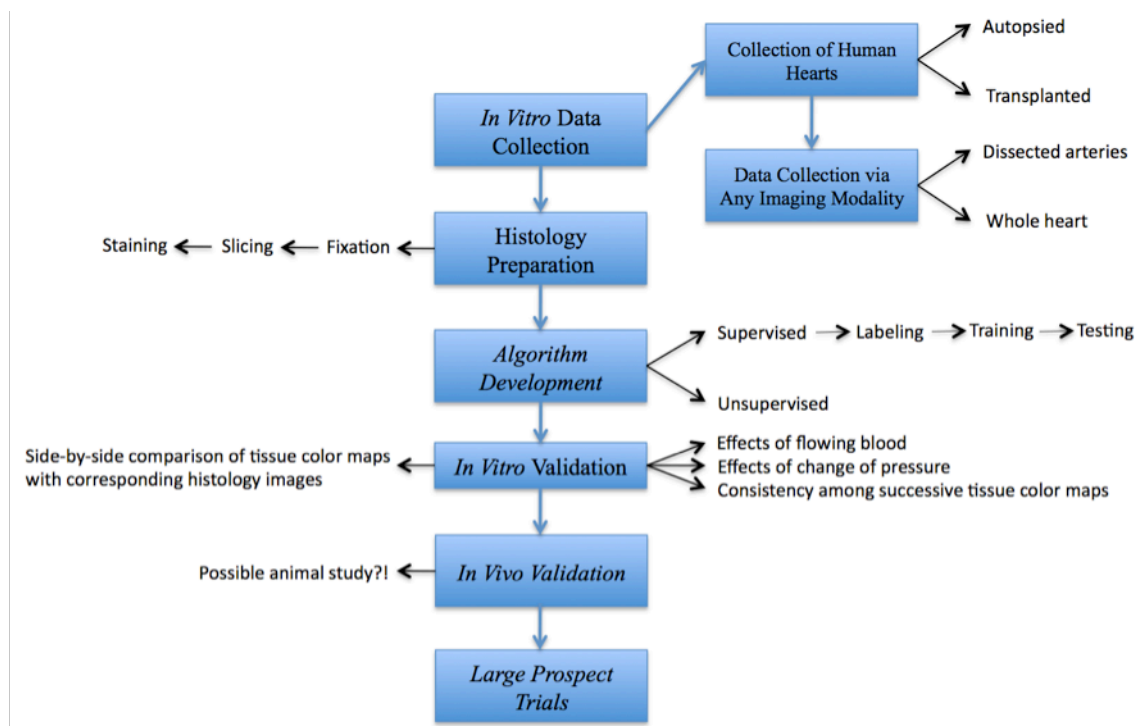


Fig. 4.11. Atherosclerotic plaque characterization flowchart from data collection toward algorithm development, classification, and validation.

characterization tool, needed further refinement and quantification. Like all spectrum-based technique, the full-spectrum analysis algorithm, suffered from inconsistency among tissue spectra.

Comprehensive assessment of advantages and disadvantages of each developed algorithm, expressed in chapters three and four, is beyond the scope of this research. Our findings prompted us to look at atherosclerotic plaque characterization problem from more rigorous perspective by attracting attentions toward essential steps for *in vivo* applications as illustrated in **Figure 4.11**. As we can see, none of reviewed algorithms encompass all necessary steps. For example, IVUS-ECOC and IVUS-IBH lack of proper labeling and validation. IVE and IVUS-VV suffer from miss-registration among

successive frames and complete characterization of plaque constitutes are not possible through these techniques.

To date, the IVUS-VH is the most well recognized atherosclerotic plaque characterization algorithm and the only commercially available platform in the field. Two minor critics on IVUS-VH are: 1) excessive detection of necrotic core particularly at the border of calcified regions, and 2) Characterization of tissues behind arc of calcified plaques. The major critic is extension of this algorithm for *in vivo* applications without considering important factors such as effects of flowing blood and change of pressure on constructed tissue color maps (VH images). In addition, the IVUS-VH provides the VH images for every other 30 frames.

Recently, ultra-high frequency IVUS transducers (40MHz up) have designed to obtain images with higher resolution that are preferred by interventional cardiologists. Consequently, we strived to extend this algorithm for data acquired with single-element 40MHz transducer and found critical difficulties, which made it very challenging if not impossible. In the next chapter, we propose an unsupervised texture based framework as an alternative approach to supervised spectrum based techniques.

5. Chapter Five:

UNSUPERVISED ATHEROSCLEROTIC PLAQUE CHARACTERIZATION IN IVUS IMAGES VIA MULTISCALE WAVELET PACKET ANALYSIS

IVUS is the predominant imaging modality in the field of interventional cardiology that provides high-resolution real time cross-sectional images of coronary arteries and the extent of atherosclerosis. In this chapter, we will present a robust texture-derived atherosclerotic plaque characterization technique as an alternative to existing spectrum-based algorithms. We acquired *ex vivo* IVUS RF signals, using a 40 MHz mechanically rotating single-element Boston Scientific (Fremont, CA) Atlantis transducer, from 32 diseased transplanted and cadaver hearts. For each CSI, we processed its IVUS signals, employing discrete wavelet packet frame (DWPF), and extracted envelope detected signatures. An unsupervised ISODATA classifier was deployed to partition the wavelet packet representations and generate prognosis histology (PH) images. Finally, an independent human observer evaluated the algorithm performance by contrasting the histology images corresponding to PH images. The effects of blood flow and pressure change on the PH images were also studied *in vitro*. This determined whether *in vitro* trained classifiers were reliable for *in vivo* applications, an indispensable validation that has not been considered by other groups to date. For the first time, we verify the reliability of extracted features as well as consistency among constructed PH images. The

main advantages of the proposed algorithm are its use independent of the type as well as frequency of transducer and its application on both RF signals and grayscale images. The main contribution of presented work is that the constructed PH images through our unsupervised classification technique can be reliably used for building training sets from highly heterogeneous regions in atherosclerotic plaques for any supervised classification algorithm.

5.1. Introduction

IVUS findings have shown that sonographic differences yielded visual discrimination among plaque constituents [72,73]. In other words, variations of intensities are attributed to repetitive tissue microstructure patterns. These have motivated researchers to develop texture-based algorithms on IVUS images to differentiate tissue types [74,75,77,87]. However, none of these studies validated their results with histology images *in vitro*, an indispensable validation step that is required before deploying any algorithm for *in vivo* classification. In this chapter, we present an effective texture-derived atherosclerotic tissue characterization algorithm using discrete wavelet packet frame (DWPF) and a 2D envelope detection technique introduced by Laine *et al.* [112] that relies on the Hilbert transform of multiscale representations. The extracted textural features of such expansions are perfectly suited for classification and capture characteristics of the plaque with the highest correlation to histology. This resolves one of the main limitations of the IVUS, which is discrimination between fibrous and fatty tissues [51,52]. The main advantages of our proposed technique are its independence on transducer frequency, and construction of PH images in an unsupervised fashion that requires no labeling. The latter

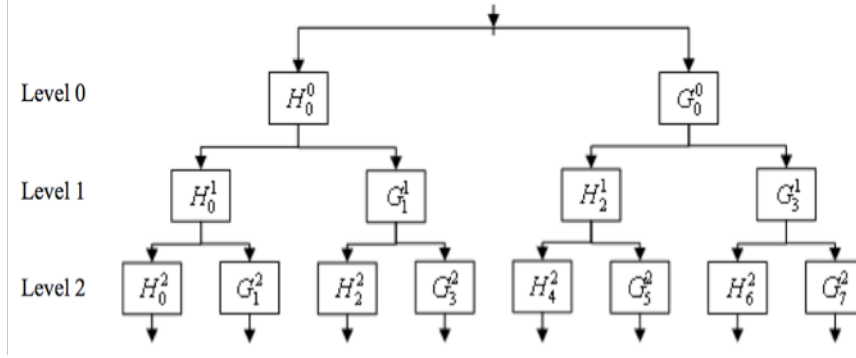


Fig. 5.1. Tree structure for a discrete wavelet packet frame expansion (DWPF) and its associated multiscale indexes.

becomes crucial due to inhomogeneity of atherosclerotic tissues that makes manual labeling so challenging in training of supervised classification approaches. In fact, the generated PH images can be more confidently used as labeled images for training.

5.2. Methods

5.2.1. Multi-Channel Wavelet Analysis

It has been shown that a multi-scale approach for texture discrimination is a compatible analysis to human and mammalian vision processing systems due to its conservation of energy in both spatial and frequency domains [113,114]. We will take advantage of spatial-frequency-localized expansions and their generalization to 2D to discern textural patterns on constructed images from backscattered IVUS signals while geometrically oriented decompositions are provided at this dimension. Unlike the classical discrete wavelet (DWT) [115-117] and discrete wavelet packet transforms (DWPT) [118], we compute decompositions that are translation invariant in a discrete wavelet frame (DWF)

[119] or discrete wavelet packet frame (DWPF) where no decimation (down sampling) occurs between expansion levels, **Figure 5.1**. Although the DWPF seems redundant and insufficient, it has two advantages that benefit texture analysis and multiscale representations; 1) less restriction on filter selection and 2) the variations of the modulus in the transform domain are not corrupted by aliasing.

Wavelet packets are orthonormal in the space of summable-integrable functions $L^2(R)$ [120] and described by a collection of functions $\{\xi_j(x) | j \in Z^+, \langle \xi_p, \xi_q \rangle = 0, p \neq q\}$ obtained from:

$$2^{l/2} \xi_{2k}(2^l x - n) = \sum_{m \in Z} h_{m-2n}^l 2^{\frac{l+1}{2}} \xi_k(2^{l+1} x - m) \quad (5.1)$$

$$2^{l/2} \xi_{2k+1}(2^l x - n) = \sum_{m \in Z} g_{m-2n}^l 2^{\frac{l+1}{2}} \xi_k(2^{l+1} x - m) \quad (5.2)$$

where $l, n, k, \xi_0(x) = \phi(x)$ and $\xi_1(x) = \psi(x)$ are the scale index, translation index, channel index, scaling function and basic wavelet, respectively [116]. We will describe our method and rationale for selection of discrete filters h_n and g_n in more details in the next section. The wavelet packets at different scales can also be found by the inverse relationship as follows:

$$2^{\frac{l+1}{2}} \xi_k(2^{l+1} x - m) = \sum_n h_{m-2n}^l 2^{\frac{l}{2}} \xi_{2k}(2^l x - n) + \sum_n g_{m-2n}^l 2^{\frac{l}{2}} \xi_{2k+1}(2^l x - n) \quad (5.3)$$

Any function $f(x) \in L^2(R)$ can be decomposed onto a wavelet packet basis by computing the inner product $\langle f(x), \xi_k(2^l x - n) \rangle$. Using **Eq. 5.3** we can write:

$$\begin{aligned}
& 2^{\frac{l+1}{2}} \int_{-\infty}^{\infty} f(x) \xi_k(2^{l+1}x - m) dx = \\
& \int_{-\infty}^{\infty} f(x) \left(\sum_n h_{m-2n}^l 2^{\frac{l}{2}} \xi_{2k}(2^l x - n) + \sum_n g_{m-2n}^l 2^{\frac{l}{2}} \xi_{2k+1}(2^l x - n) \right) dx = \\
& \sum_n h_{m-2n}^l 2^{\frac{l}{2}} \int_{-\infty}^{\infty} f(x) \xi_{2k}(2^l x - n) dx + \sum_n g_{m-2n}^l 2^{\frac{l}{2}} \int_{-\infty}^{\infty} f(x) \xi_{2k+1}(2^l x - n) dx
\end{aligned} \tag{5.4}$$

Defining the decomposition coefficients as:

$$\rho_{k,n}^l = 2^{\frac{l}{2}} \int_{-\infty}^{+\infty} f(x) \xi_k(2^l x - n) dx \tag{5.5}$$

Eq. 4 can be rewritten as:

$$\rho_{k,m}^{l+1} = \sum_n h_{m-2n}^l \rho_{2k,n}^l + \sum_n g_{m-2n}^l \rho_{2k+1,n}^l \tag{5.6}$$

Using **Eq. 5.1** and **Eq. 5.2**, the coefficients are calculated by:

$$\rho_{2k,n}^l = \sum_m h_{m-2n}^l \rho_{k,m}^{l+1} \tag{5.7}$$

$$\rho_{2k+1,n}^l = \sum_m g_{m-2n}^l \rho_{k,m}^{l+1} \tag{5.8}$$

In the standard wavelet transform, the index k is restricted to $k=0$ and only two wavelet packets ξ_0 and ξ_1 are used. Consequently, only the leftmost nodes (ρ_0^l) are decomposed into high and low frequency subbands. However, in wavelet packets, the decompositions are performed on both low and high frequency components. Therefore, a tree-structure multiband extension of the standard wavelet transform is constructed, **Figure 5.1**. This can be seen as subband filtering and implemented using iterated constructed highpass and lowpass filters in frequency domain. Taking the Fourier transform of both sides of **Eq. 5.7** and **Eq. 5.8** yields:

$$\Upsilon_{2k}^{l+1}(\omega) = G^l(\omega) \Upsilon_k^l(\omega) \tag{5.9}$$

$$\Upsilon_{2k+1}^{l+1}(\omega) = H^l(\omega) \Upsilon_k^l(\omega) \tag{5.10}$$

where $\Upsilon_k^l(\omega)$ is the Fourier transform of the frame coefficients at channel k and level l . Since the IVUS signals are sampled at the rate of f_s , the original discrete signal is considered as the set of frame coefficients at the first scale $l=0$ for the rest of this chapter.

5.2.2. Filter Selection and Specification

The highpass $G^l(\omega)$ and the lowpass $H^l(\omega)$ filters at each level l can be realized as presented in [117] by: $G^l(\omega) = G^0(2^l\omega)$ and $H^l(\omega) = H^0(2^l\omega)$. Consequently, the multi-channel wavelet schematic in **Figure 5.1** behaves like a filter bank with channel filters $\{F_k^l(\omega) | 0 \leq k \leq 2^l - 1\}$, where $F_k^l(\omega)$ can be derived recursively as follows:

$$F_0^0(\omega) = G^0(\omega), F_1^0(\omega) = H^0(\omega) \quad (5.11)$$

$$F_{2k}^{l+1}(\omega) = G^{l+1}(\omega)F_k^l(\omega) = G^0(2^{l+1}\omega)F_k^l(\omega) \quad (5.12)$$

$$F_{2k+1}^{l+1}(\omega) = H^{l+1}(\omega)F_k^l(\omega) = H^0(2^{l+1}\omega)F_k^l(\omega) \quad (5.13)$$

It has been shown that the selection of the filters $G^0(\omega)$ and $H^0(\omega)$ can have significant impact on texture classification performance [112,118]. The filter candidates must satisfy necessary criteria such as symmetry as well as boundary accuracy and have optimal frequency response. Hence, we selected Lemarie-Battle [116] wavelets that are symmetric (have linear phase response) and satisfy quadrature mirror filter (QMF) criteria. The former property alleviates boundary effects through simple methods of mirror extension. The discrete highpass filter g_n^0 is obtained by $g_n^0 = (-1)^n h_n^0$ or $G^0(\omega) = H^0(\omega + \pi)$ in the frequency domain. **Figure 5.2** illustrates the constructed filter

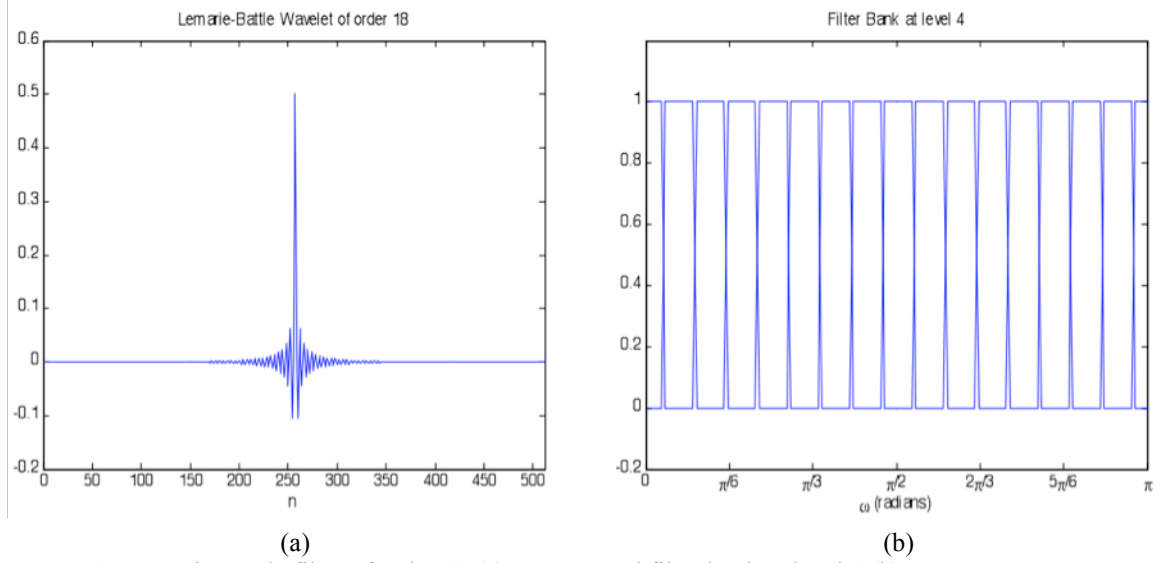


Fig. 5.2. Lemarie-Battle filter of order 18 (a), constructed filter bank at level 4 (b).

bank at level 4 generated by Lemarie-Battle wavelet of order 18. The wavelets using QMF as well as constructed filter bank $\{F_k^l(\omega)\}$ cover exactly the frequency domain and satisfy the property:

$$|G^0(\omega)|^2 + |H^0(\omega)|^2 = |G^0(\omega)| + |H^0(\omega)| = 1 \quad (5.14)$$

$$\sum_{k=0}^{2^l-1} |F_k^l(\omega)|^2 = \sum_{k=0}^{2^l-1} |F_k^l(\omega)| = 1 \quad (5.15)$$

Thus this expansion is pointwise/pixelwise 1:1 (a bi-jection across levels of analysis) and allows for perfect representation (and reconstruction).

5.2.3. Feature Extraction

We processed the IVUS signals from each raw data frame, represented in the (r, θ) domain, which is the original domain of acquisition, containing 256 lines that span over

360 degrees with 2048 samples per line. In order to have an optimal frame size with respect to its computational complexity and textural resolution, we decimated and interpolated (via a spline) the signals in axial and lateral directions, respectively, to generate square $M = 512$ pixels frame. **Figure 2.7(a,b)** demonstrates B-mode images of an IVUS frame in both (r, θ) and (x, y) Cartesian domains. For further information see Section 2.3.

For each frame, a separable tensor product was used, in which channel filters were denoted by $F_{i \times j}^l(\omega_r, \omega_\theta) = F_i^l(\omega_r)F_j^l(\omega_\theta)$. Consequently, such an extension will lead to orientation selectivity in the decomposition tree. Four possible orientations can be considered excluding the root node, which is omnidirectional.

1. The node last filtered by $G^l(\omega_r)H^l(\omega_\theta)$ corresponds to coefficients having a vertical orientation. The highpass filter G^l and lowpass filter H^l are applied in the axial and lateral directions, respectively.
2. The node last filtered by $H^l(\omega_r)G^l(\omega_\theta)$ corresponds to horizontal orientation. The lowpass filter H^l and highpass filter G^l are applied in the axial and lateral directions, respectively.
3. The node last filtered by $G^l(\omega_r)G^l(\omega_\theta)$ is responsive to coefficients in the diagonal orientation. The highpass filter G^l and highpass filter H^l are applied in the axial and lateral directions, respectively.

4. The node last filtered by $H^l(\omega_r)H^l(\omega_\theta)$ has the same orientation as its parent.

The lowpass filter H^l and lowpass filter H^l are applied in the axial and lateral directions, respectively.

Due to narrowband characteristic of IVUS signals, the envelope of output signals from channel filters were computed using the corresponding 2D analytical signals. Finally, the feature matrices were constructed as follows:

$$\mathbf{V}_{i,j}^{l,k} = \{e_{i,j}^{l,k} \mid 0 \leq k \leq (2^l - 1), \quad i, j = 1, \dots, M\} \quad (5.16)$$

where $e_{i,j}^{l,k}$ represents the envelope value of pixel (i, j) for the k -th channel at level l .

5.2.4. Classification

The overall justification of *in vivo* real-time plaque characterization is made by an interventional cardiologist through the use of classified tissues. Traditionally, researchers build training data sets by marking ROIs in arteries and taking corresponding cross-sectional histology images to label the plaque compositions. Once the training data set is developed, a supervised classifier is used to differentiate tissue types. Eventually, the overall performance of such a classifier is evaluated through cross-validation. Due to stringent behavior of closely related tissues (*i.e.* fibrotic, fibro-lipidic), it is crucial to substantiate the validity of extracted features. Although Lizzi *et al.* quantified the extracted spectral parameters (intercept, slope) through analytical tissue models for eye and liver experiments [61], no such validation has previously been performed for atherosclerotic tissue signatures. For this reason, we chose the ISODATA clustering

algorithm in order to generate prognosis histology (PH) images. Our hypothesis was that, in an unsupervised classifier, if extracted signatures represent true characteristics of atherosclerotic tissues, then they could be more reliably used for supervised classification.

For every feature representation matrix, $\mathbf{V}_{M \times M}$, a label was assigned to each pixel by modulo N_c where N_c represented the number of classes. We computed the center of clusters $\{C_\kappa \mid 0 \leq \kappa \leq N_c - 1\}$ by calculating the mean vector for each class. The pixel $\{v_{i,j} \mid i, j = 1, \dots, M\}$ was assigned to the class κ , if the Euclidean distance between the corresponding pixel and the class center C_κ was the closest. The centers of the clusters were updated and possibly merged in an iterative fashion by recomputing the relative mean vectors. The procedure was terminated once no change in labeling occurred.

5.3. Experimental Results and Quantification Analysis

5.3.1. Atherosclerotic Plaque Characterization

Both decomposition and ISODATA algorithms were implemented in C++. All computations were executed on an IBM ThinkStation workstation, 64-bit 3 GHz dual Intel Core2Quad Processors with 32 GBs of RAM. The execution time for each CSI was evaluated to be 20msec.

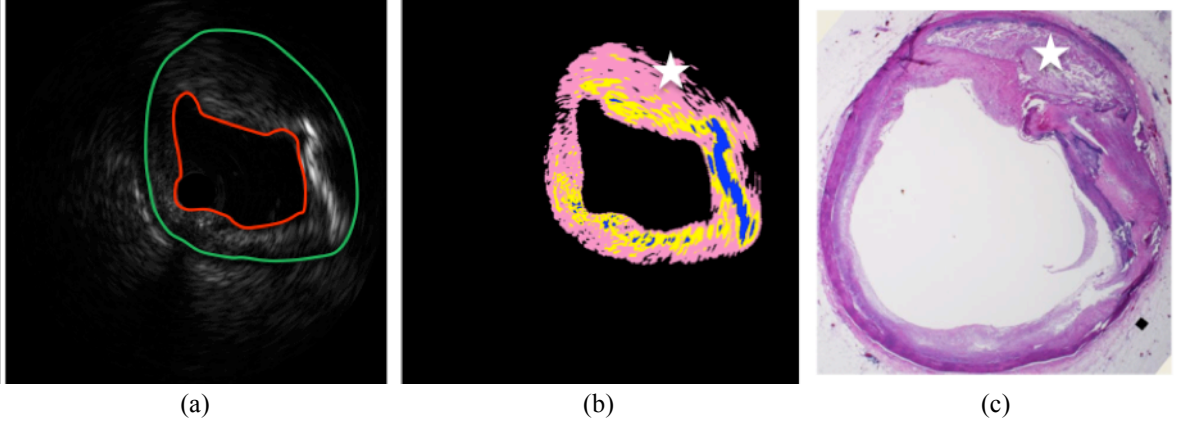


Fig. 5.3. Manually traced vessel wall (green) and lumen border (red) on IVUS B-mode image (a), resulting PH image generated by the algorithm (Blue, yellow and pink colors represent calcified, fibrotic and fibro-lipidic components) (b), corresponding H&E histology image of cross section of interest (c). The white star points to lipid rich pool region that could be sign of vulnerable plaque if thin fibrotic layer existed on top of it.

We acquired IVUS data, as described in Section 3.2.2.2, from Autopsy human hearts ($n=30$) and explanted hearts from transplant surgery ($n=2$) were procured within 24 hours postmortem and transplantation, respectively. Eighty-three CSIs collected from 51 segments of 32 hearts *ex vivo*, including 19 LADs, 16 RCAs and 16 LCXs segments that had more than 30% stenosis were examined. For each frame, an expert manually segmented the plaque by tracing the vessel wall and lumen borders, **Figure 5.3(a)**. We performed our algorithm on 512-by-512 segmented frames that only contains plaque textures and selected Lemarie-Battle filters of order 18, expansion level $l = 2$ and the initial number of classes $N_c = 4$ (Calcified, Fibrotic, Fibro-lipidic, no tissue). The main advantage of ISODATA, over our previously developed framework based on k -means clustering algorithm [121], is that the clusters were merged in the absence of one or two tissues. Finally, the resulting classified images were transformed into the Cartesian coordinates. **Figure 5.3** demonstrates a CSI, corresponding H&E histology image, and

resulting PH image. The blue, yellow and pink colors exhibit calcified, fibrotic and fibro-lipidic plaque components, respectively.

For quantification, histology is the best available version of ground truth for *in vitro* tissue characterization. However, the interpretation of histology images can often vary among experts yielding a subjective process. As a result, plaque constituents can be separated into fibrotic, lipidic, necrotic core and calcified while another may differentiate between the levels of presence of fatty materials and add fibro-lipidic to compromise between fibrotic and lipidic. Generally, in supervised classification techniques, the most homogeneous regions, for each tissue type, are selected on histology images and mapped to the corresponding IVUS images manually, **Figure 5.4(c)**. Subsequently, the features are extracted in order to build the training and testing dataset. **Figure 5.4** demonstrates a CSI, corresponding histology image with manually segmented ROIs by a histopathologist, image containing manually traced labels for each tissue type, and constructed PH image. Traditionally, in order to build the training dataset, experts trace the most homogeneous regions for each tissue type and extracted corresponding features, although the homogeneity assumption may not be completely valid.

As we can observe in histology image and corresponding IVUS as well as PH image, the atherosclerotic plaque consists of heterogeneous tissues that makes manual labeling tedious and possibly infeasible. **Figure 5.4(a,b,d)** clearly demonstrate that the manually segmented ROI (**Figure 5.4(c)**), which presumably should only contain fibrotic tissue, is heterogeneous and contains mixture of fibrotic and lipidic tissues. This may lead to

incorrect classification results if used for training of any supervised classifier. For this reason, we designed our tissue characterization framework based on unsupervised classification to substantiate extracted features. In this way, we confidently used the classification results (PH images) as labeled images for building a training set in any supervised classification algorithm.

Due to the nature of the unsupervised classification approach taken, we evaluated the algorithm performance employing an independent histopathologist, by contrasting the histology images corresponding to PH images. We deployed a scoring approach to quantify the results and asked the histopathologist to score each PH image by eye-balling. For higher accuracy, each histology image was divided into distinguishable regions, Figure 5.4(a). The corresponding PH images were oriented and scaled as the histology image and same divisions were mapped visually. The accuracy of characterization was evaluated for each region separately and averaged for composite rating for each tissue type. **Table 5.1** demonstrates the average values for correct and miss-classified tissues in 83 CSI. For example, the first row shows that 99.70% of calcified tissues in histology images were correctly classified as calcified while 0.32% and 0.07% of them were misclassified as lipidic and fibro-lipidic, respectively. The overall classification performance has been evaluated to be 90.87%, 87.75%, and 99.70% for calcified, fibrotic, and fibro-lipidic tissues, respectively.

Table 5.1. Percentage of correct classification as well as misclassification for each tissue type.

	Calcified	Fibrotic	Fibro-lipidic	No Tissue
Calcified	99.70	0.32	0.07	0.00
Fibrotic	7.17	87.75	5.05	0.00
Fibro-lipidic	1.89	6.50	90.87	0.74

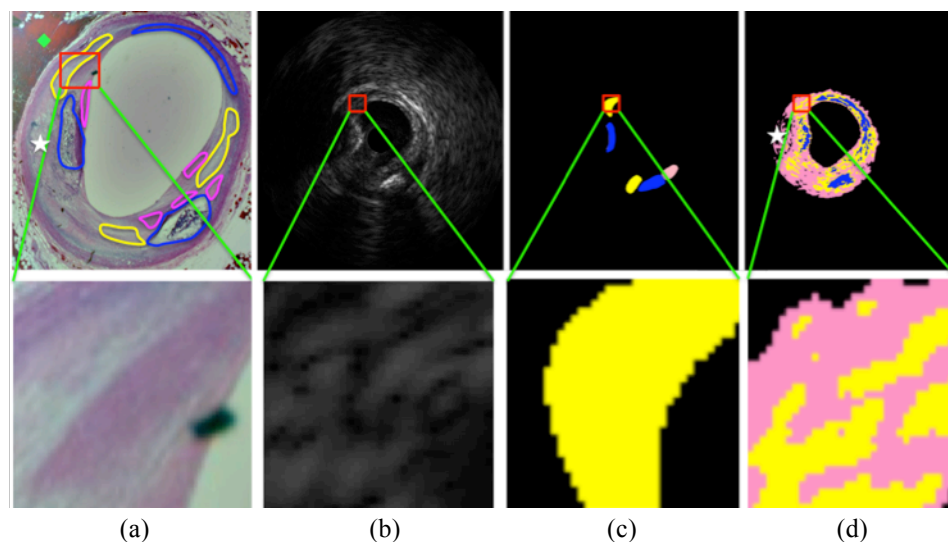


Fig. 5.4. H&E histology image of CSI with manually segmented ROIs (a), corresponding IVUS grayscale image (b), manually selected regions corresponding to presumably homogenous regions for each tissue type (c), corresponding PH image (d). The bottom row illustrates the magnified version of selected ROI (red square) for fibrotic tissue. The inhomogeneity of atherosclerotic tissues are well reflected in (a,b,d). The white star points to lipid rich pool region that could be a sign of vulnerable plaque if a thin fibrotic layer existed on top of it.

In comparison with the spectrum-based classification technique such as IVUS-VH, our texture-derived algorithm performs promising. It has been shown that the IVUS-VH algorithm implemented through AR models of IVUS signals is superior to the windowed Fourier transform [68]. The accuracy of the IVUS-VH technique using AR analysis in combination with classification tree for IVUS data acquired with 30 MHz single element transducers has been reported as 90.4%, 92.8%, 90.9% and 89.5% in training dataset and 79.7%, 81.2%, 92.8% and 85.5% in the test dataset for fibrotic, fibro-lipidic, calcified and calcified necrotic regions, respectively.

In the case of atherosclerotic tissue characterization, the ultimate goal is detection of vulnerable plaques. Pathological and more recent IVUS studies of ruptured plaques have

shown that the underlying lesions present a large plaque burden without always much lumen compromise, positive remodeling, and a thin macrophage-rich fibrotic cap that covers a large necrotic core underneath [122-124] (see Section 1.1.3). Although we cannot detect the necrotic core directly, due to unsupervised classification of tissues, the vulnerability of plaques can still be deduced through appearance of lipid rich pool region with thin layer of fibrotic cap on top of it. In other words, the regions containing necrotic core often correlated with relatively large lipid pools.

Resulting PH images in **Figure 5.3** and **Figure 5.4** demonstrate two vulnerable plaques that contain lipid rich pools (depicted with white stars) along with fibrotic cap on top. Similar approach has also been taken by Okubo *et al.* [71] to show the vulnerability of atherosclerotic plaques. A vulnerable plaque would be characterized by a thin, or absent layer of fibrotic tissue with under a large fibro-lipidic pool.

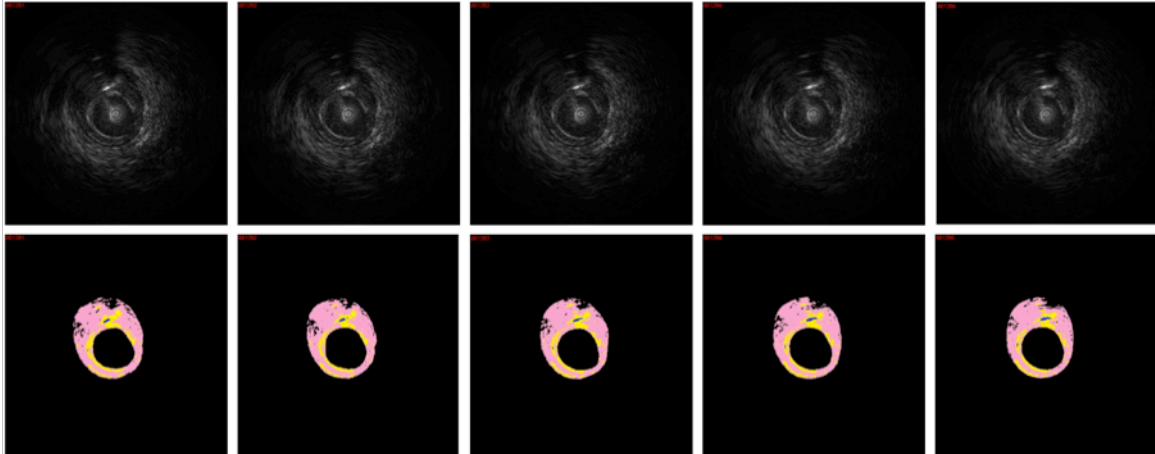
5.3.2. Reliability of Extracted Features

Due to the narrowband characteristic of IVUS signals, the spectral signatures used in IVUS-VH and IB-IVUS must be extracted within the functional range of the transducer's bandwidth. It is evident that any changes in the tissue or calibration spectra within the specified bandwidth would alter the classification results and could misclassify tissues. In Section 4.3, we comprehensively reported on inter- and intra-frame variations of tissues spectra and their effects on two spectral parameters (*i.e.* slope, intercept) employing 40 MHz single element Boston Scientific Atlantis transducers. We also pointed to variations among transducer spectral parameters such as center frequency and bandwidth, which

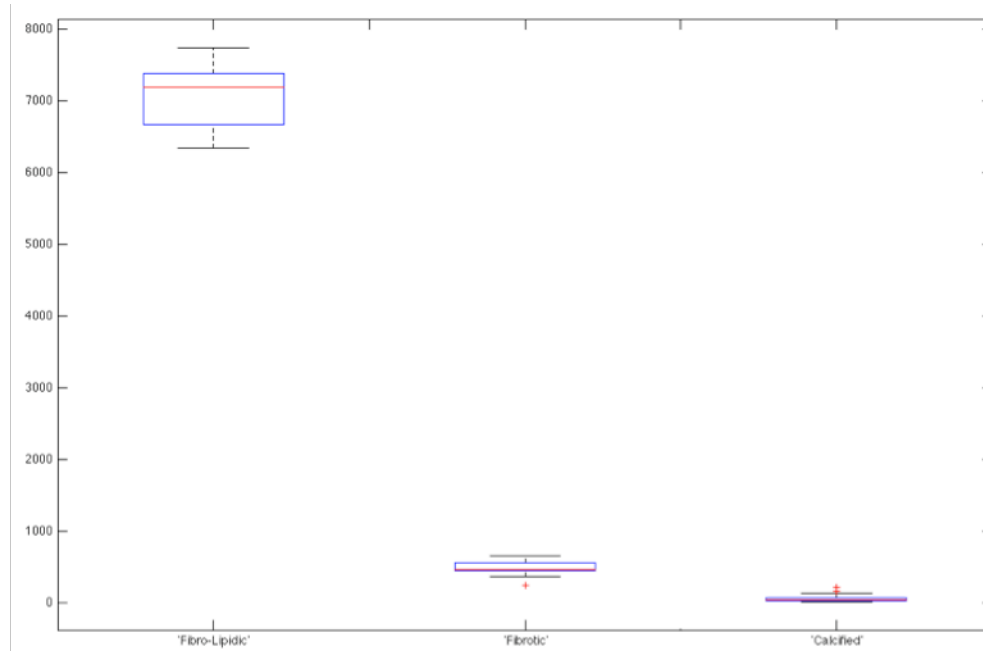
could alter the classification results. Our texture-derived algorithm untangled this limitation and can be deployed independently of the transducer's center frequency and bandwidth. We performed three experiments to investigate the consistency of extracted features and more importantly considered the effects of change of pressure and blood flow on constructed PH images qualitatively for the first time.

5.3.2.1. Consistency Among PH images in Adjacent Frames

The best way to examine the consistency among extracted features for atherosclerotic plaque characterization using IVUS is to examine the PH images in adjacent frames. We know that the local properties of lesions are not changed very much in successive frames taken $16\mu m$ apart. In other words, the plaque characteristics are gradually changed during pullback and abrupt changes among successive tissue color maps are not expected. **Movie 5.1** and **Movie 5.2** demonstrate the grayscale images and corresponding changes in plaque constituents in constructed PH images for 15 consecutive frames where five of them have been shown in **Figure 5.5(a)**. Contrary to IVUS-VH algorithm that deploys gating protocol and provides the VH images for every other 30 frames, our technique generates the PH images for all acquired frames. We counted number of pixels corresponding to every tissue types in each frame and **Figure 5.5(b)** show the Box-Whisker of counted pixels for all 15 frames. Since fibro-lipidic tissue appears in outer boundaries, some of the differences for this tissue are due to manual tracing of luminal borders by expert particularly for the last few frames.



(a)



(b)

Fig. 5.5. Five consecutive *in vivo* IVUS grayscale images acquired with a 40MHz single-element Boston Scientific transducer (top row) and corresponding generated PH images (bottom row) (a), Box-Whisker plot of number of pixels for each tissue type in 15 consecutive frames (b).

5.3.2.2. Stationary Catheter with Change of Pressure

During catheterization procedure, the coronary artery is dilated and relaxed due to pressure changes. The effects of change of pressure on extracted features, especially those derived from normalized spectrum, are unknown and have not been investigated

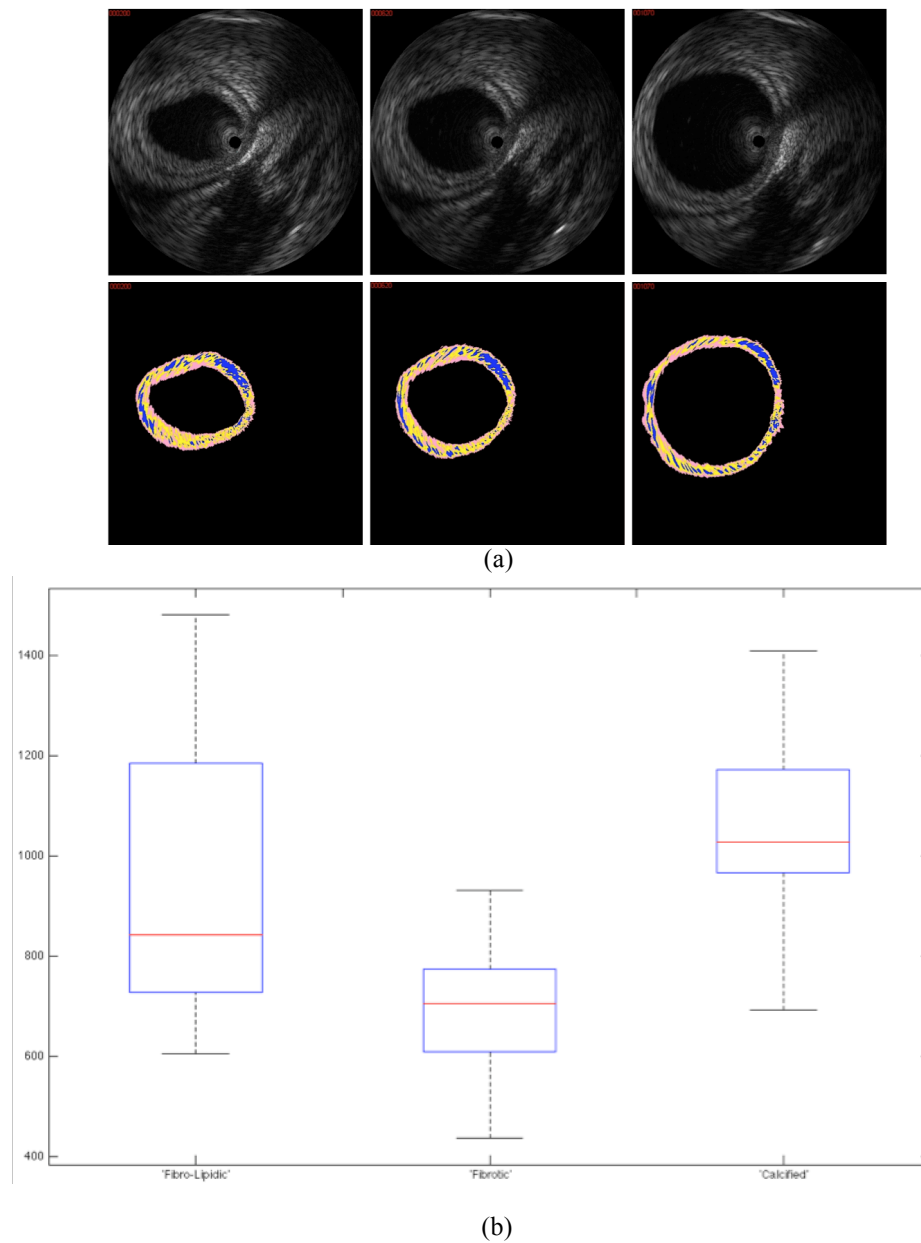


Fig. 5.6. Effects of change of pressure on generated PH images. *In vitro* grayscale IVUS images acquired at three different levels of pressures (from 20mmHg to 120 mmHg) for a particular cross section of interest (no pullback) (top row), and corresponding constructed PH images (bottom row). Box-Whisker plot of number of pixels for each tissue type in 30 consecutive frames (b).

and reported by any group yet. In fact any reliable tissue characterization algorithm must be as less sensitive as possible to any change including pressure and its consistency should be validated. Therefore, we performed an experiment and changed the pressure

while acquiring the IVUS images at a single CSI (no pullback), **Movie 5.3** and **Movie 5.4**. **Figure 5.6(a)** displays the effects of change of pressure on the grayscale IVUS images and constructed PH images at three different levels of pressure, respectively. Similar to previous experiment, we counted the number of pixels for every tissue types in each frame during change of pressure, **Figure 5.6(b)**. Although the morphology of pathological structures are changed, the global interpretations on the PH images remain unvaried, keeping in mind that some of the variations are due to the contractions/expansions of the plaque in 3-D volume as well as manual tracing of the luminal borders by expert.

5.3.2.3. Effects of Flowing Blood

It has not been verified by any group to date whether *in vitro* trained classifier can be used for *in vivo* classification or not. In general, the supervised classifier is trained using *in vitro* derived features deploying PBS while the effects of flowing blood on *in vivo* constructed tissue color maps remained unknown. For this purpose, we acquired the IVUS signals in PBS and human blood solution for each segment. **Figure 5.7** demonstrates the IVUS grayscale images of a cross section of interest acquired using circulating Saline as well as human blood and corresponding constructed PH images along with H&E histology image. As seen, imaging of the plaque in blood introduces some differences although the overall interpretation seems to be very similar. However, not much is known about the nature of these differences, other than that imaging plaque through blood (which is difficult to duplicate *in vitro*) can be expected to introduce some differences and also that tissue fixation through formalin (which situation is absent *in*

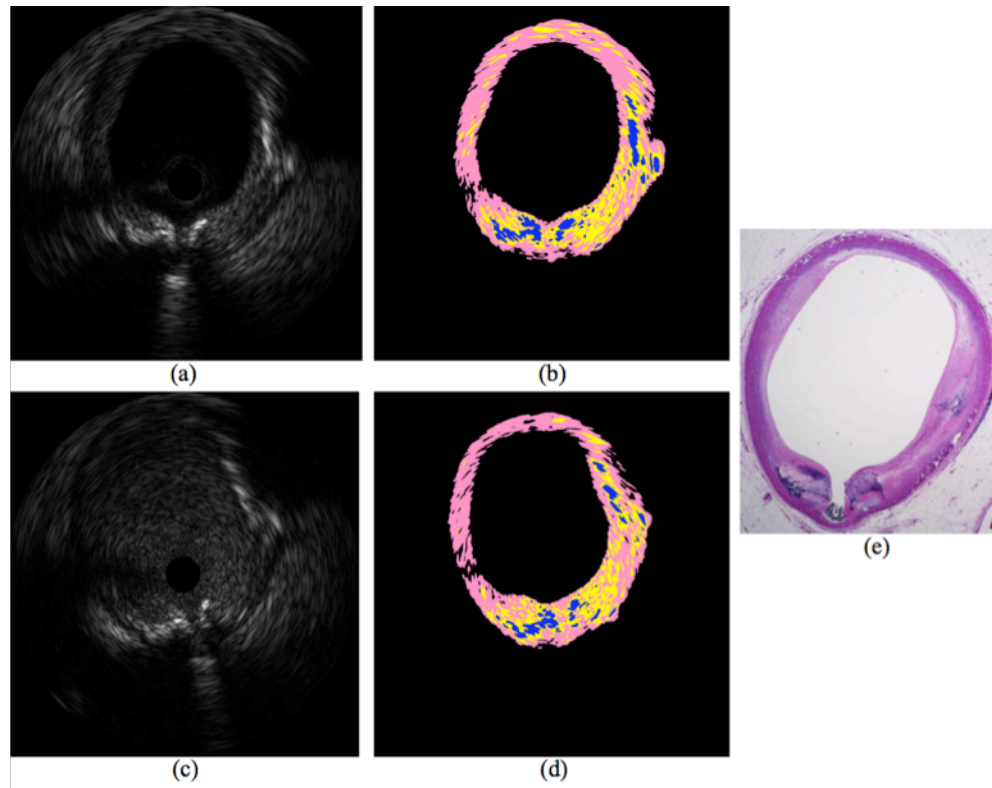


Fig. 5.7. IVUS grayscale image of a cross section of interest using circulating Saline (a) and corresponding constructed PH image (b), IVUS grayscale image of the same cross section acquired with circulating human blood (c) and corresponding constructed PH image (d), H&E histology image of the same cross section (e).

vivo) might alter the tissue response to ultrasound. It is therefore crucial that we explore the nature of these dissimilarities (*i.e.* the attenuation of signals in blood, blood flow rate, *etc.*) since it impacts the *in vivo* classification accuracy using an *in vitro* trained classifier. As long as the differences found in the tissue signatures between the *in vitro* and *in vivo* imaging situations are systematic, it may still be possible to empirically re-tune an *in vitro*-trained algorithm to reliably perform *in vivo*. Since the initial angular position of the transducer element during acquisition for two CSIs were different, the IVUS grayscale images were slightly rotated.

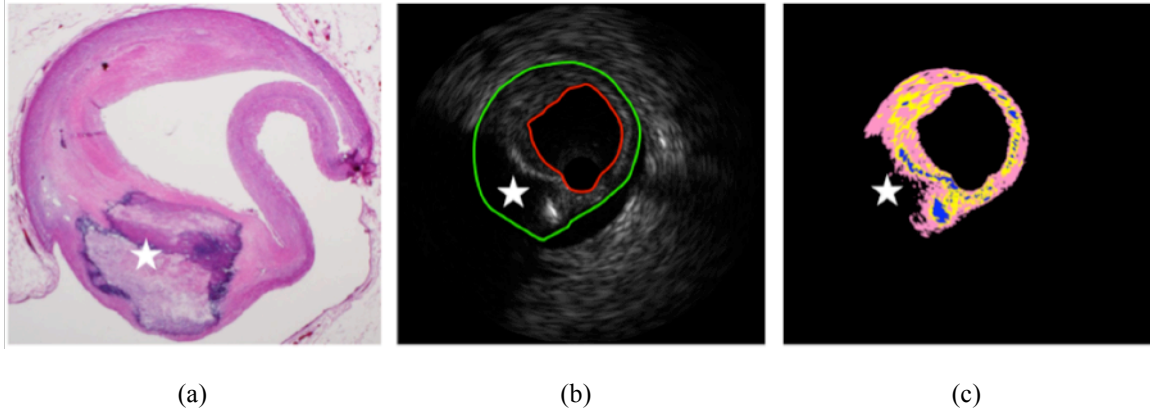


Fig. 5.8. Sample H&E histology image of a calcified CSI (a), grayscale image of the CSI using Saline (b) and corresponding PH image (c). The tissues behind arc of calcified plaque, marked with white star (7-9 o'clock), have been classified as no tissue.

5.3.2.4. Classification of Tissues Behind Arc of Calcified Plaques

We pointed to the unreliability of tissue classification in the regions behind the arc of calcium [90] for the first time. We concluded that the acoustic shadowing in the grayscale IVUS images, caused by attenuation of signals in dense calcified tissues, limited lesion assessment in these regions. We examined the CSIs that contained calcified plaques and confirmed that not enough reliable features existed throughout the regions behind the arc of calcified region extended to the vessel wall. We only had found noise-like signals behind these regions. Consequently, in the ISODATA classifier, we assigned one of the classes to “no tissue” to encompass such limitation into resulting PH images. **Figure 5.8** illustrates a CSI with a large calcified plaque, in which the corresponding region was partially labeled as background or lack of tissue. The reliability of characterization of tissues behind arc of classified plaque later was studied and reported by authors in [125]. In fact, recent developed algorithms have taken this limitation into account and either mark tissues in these regions with “no tissue” [121] or detect them automatically and do not classify them [77,87].

5.4. Summary and Conclusion

In this paper we presented a reliable texture-derived atherosclerotic plaque characterization algorithm as an alternative to spectrum-based approaches like IVUS-VH, and IB-IVUS analysis. We deployed a multi-channel wavelet packet frame representation and extracted textural features along with unsupervised ISODATA classifier to generate PH images. The accuracy of the algorithm was evaluated by an independent histopathologist and reported to be 99.70%, 87.75% and 90.87% for calcified, fibrotic and fibro-lipidic tissues respectively in 83 CSIs collected from 32 hearts *ex vivo*. We presented the qualitative results of fundamental issues that have not been considered by any group previously. We showed that our algorithm could provide fairly reliable results under various conditions such as pressure changes and presence of arc of calcified plaques (a complete study of such variations is a topic of future work). We also demonstrated constructed PH images for same CSIs acquired *in vitro* using circulating saline and human blood and observed that the overall interpretation of PH images were alike. It was important to validate the reliability of an *in vitro* trained classifier for *in vivo* atherosclerotic plaque characterization. Ongoing studies include further analysis and quantification of abovementioned issues.

The most important and practical advantage of this algorithm is that it can be performed on both IVUS RF signals as well as grayscale images and reliably classify tissues independently of the transducer center frequency while inconsistency among the spectral-derived features within the functional range of bandwidth still remains a major challenge. Our results showed a fine differentiation between fibrotic and fibro-lipidic components,

which had been a major challenge in the field. Above all, we showed that constructed PH images through our unsupervised approach could be reliably used for building training sets in any supervised classification approach without any manual labeling in the typically highly heterogeneous media of atherosclerotic plaques.

6. Chapter Six:

AUTOMATIC DETECTION OF LUMINAL BORDER IN IVUS IMAGES: PRELIMINARY STUDY

IVUS image segmentation has been a subject of interest for researchers due to the rapidly growing use of this imaging modality in catheterization procedures for the following two main reasons. First, one important parameter during angioplasty or stent implantation procedure, is the ratio of lumen to artery cross sectional area for stenoses regions. For instance, the interventional cardiologist uses these measurements to select the appropriate type, length and diameter of a stent. Secondly, vessel walls and lumen contours are required to be traced prior to tissue characterization and plaque RF signals extraction. Pullback IVUS data files contain thousands of cross-sectional images, automatic extraction of vessel wall and lumen borders has been the topic of only a few research efforts [126-129] and remains a challenging image processing problem.

Clinical application of automated segmentation methods has seen limited success due to the presence of guide wire, the presence of arc of calcified plaques, the motion of the catheter as well as heart, and appearance of sub branches. Generally speaking, on IVUS image data, detection of the external vessel wall border is relatively easier than internal lumen border. This is due to the fact that media, which consists of smooth muscle cells reflect no signals and usually appears as dark strip so it is used as a marker for vessel wall border detection. Finding such a marker for lumen border is more challenging

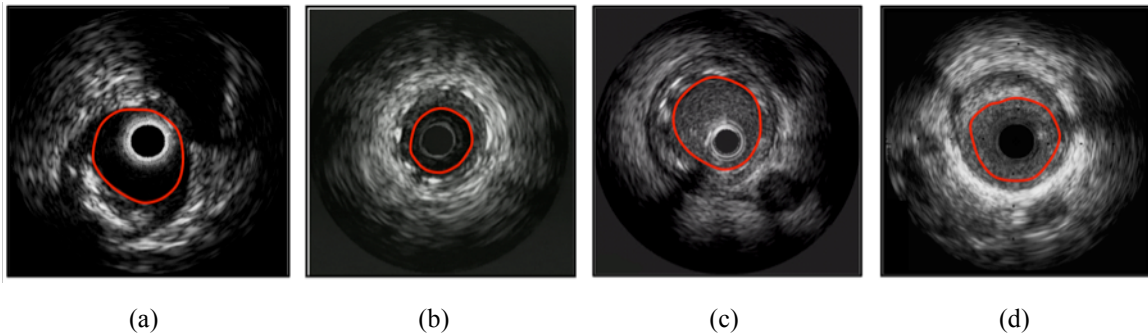


Fig. 6.1. Four distinct IVUS frames acquired with 20 MHz (a), 30 MHz (b), 40 MHz (c), and 45 MHz (d) transducers. Red border represents lumen border.

particularly in images acquired with high frequency transducers (40MHz up). Comparing IVUS ultrasound probes, the lumen border is better depicted in images acquired with a 64-element phased-array 20 MHz transducer in comparison with those acquired with a single element mechanically rotating 45 MHz transducer. **Figure 6.1** illustrates four distinct cross-sectional grayscale IVUS images acquired with 64-elements phased-array 20MHz, as well as a single-element rotating 30 MHz, 40 MHz, and 45MHz transducer. As we can see, at higher center frequency spatial resolution is improved, at the cost of more scattering from red blood cells inside the lumen.

This chapter covers developed multiscale brushlet-based algorithms for IVUS image filtering and segmentation of lumen border resulting form a collaboration study between Heffner Biomedical Imaging Lab (HBIL) at Columbia University (New York, NY) and VOLCANO Corporation (Rancho Cordova, CA) from September 2008 to August 2009.

6.1. Background

We collected IVUS grayscale images from patients, as described in Section 3.2.1, using a single element mechanically rotating 45 MHz Revolution™ transducer and s5™ imaging system manufactured by VOLCANO. The catheter was advanced on top of the guide wire from the femoral artery toward the site of coronary arterial occlusion (*i.e.* RCA, LAD, LCX, Figure 3.1) via aorta. **Figure 2.6** displays a schematic of an artery, its anatomical structures, catheter and four distinct IVUS frames acquired with transducers with different center frequencies including 45MHz.

6.1.1. Rational Behind the Use of Brushlet Basis Function in IVUS

Image Analysis

As we mentioned previously, IVUS provides rich temporal as well as spatial resolution of plaque and arterial wall structures. Due to sufficient temporal resolution ($\sim 0.167\text{mm}$), plaque structures appear to be relatively persistent within limited number of frames (e.g. eight frames) that is defined as *sub-volume*. We hypothesized that projection of IVUS temporal sub-volumes on brushlet basis functions provides complex directional-derived features of both temporal and spatial domains 1) enabling us to characterize coherent plaque textures versus dynamic and incoherent blood speckle noise along the pullback dimension, 2) alleviating variations among extracted features from similar plaque structures depending on a) their orientations with respect to transducer's position in its spiral-like trajectory, b) genuine changes in physical characteristics within particular tissue type, and c) variations in transducer's properties. The inter- and intra-frame

variations in extracted features [130] (*i.e.* the maximum absolute amplitude and maximum power in spatial and spectral domains, respectively) makes tissue characterization (*i.e.* blood versus non-blood) very challenging through global intensity-based thresholding techniques. It is worth mentioning that the strong spatial coherence in the appearance of plaque, arterial wall and surrounding fats within an IVUS sub-volume is better expressed and visualized in polar representations (the original domain of acquisition) of the image data. Hence, we design our framework upon multi-scale analysis of textural features, which is the most compatible analysis to human and mammalian vision processing systems due to its conservation of energy in both spatial and frequency domains [113,114]. We will take advantage of the spatial-frequency-localized expansions such as brushlet analysis and their generalization to 3-D to discern the textural patterns on constructed images from backscattered IVUS signals. One of the major advantages of expansion of IVUS sub-volumes onto orthogonal brushlet basis functions is that it is invariant to intensity so that the extracted brushlet coefficients do not depend on intensity but spatial frequency content of IVUS signals. In addition, the brushlet is a well-localized complex valued function in time and frequency domains that is suitable for analyzing the local frequency content of IVUS signals and offers an orthogonal transform of the Fourier coefficients, which are Hermitian-symmetric so the phase information might also be used in IVUS image filtering and eventually detection of lumen border.

6.1.2. Brushlet Analysis

We are particularly interested in orthogonal localized exponentials basis functions since they enable us to characterize valuable information about the direction of textures at different scales, frequencies, and locations. Brushlet basis was first introduced in [131], as a family of steerable functions, that provide projected coefficients associated with particular brushstrokes (of specific sizes and orientations), analogous to a wavelet scaling function, yielding the characterization of textural features with distinct directions corresponding to specific brushlet functions. The functions divide the real axis into subintervals $[a_n, a_{n+1}]$ of length l_n , and define a brushlet analysis function, as follows:

$$u_{j,n}(x) = b_n\left(x - \frac{l_n}{2}\right)e_{j,n}(x) + v(x - a_n)e_{j,n}(2a_n - x) - v(x - a_{n+1})e_{j,n}(2a_{n+1} - x) \quad (6.1)$$

The $b_n(x)$ and $v(x)$ are two localized window functions, providing the orthogonality property. The complex orthonormal basis function, $u_{j,n}(x)$, can be constructed using these two functions along with the complex exponential function $e_{j,n}(x)$ that is defined as:

$$e_{j,n}(x) = \frac{1}{\sqrt{l_n}} e^{-2i\pi j \frac{(x-a_n)}{l_n}} \quad (6.2)$$

Figure 6.2 illustrates the windowing functions as well as the imaginary and real parts of $u_{j,n}(x)$. Given any one-dimensional signal f in $L^2(R)$, its Fourier transform \hat{f} can be projected onto the brushlet basis as $\hat{f} = \sum_n \sum_j \lambda_{j,n} u_{j,n}$ (6.3), where $\lambda_{j,n}$ are the brushlet coefficients. It has been shown that the projection of \hat{f} onto the brushlet basis

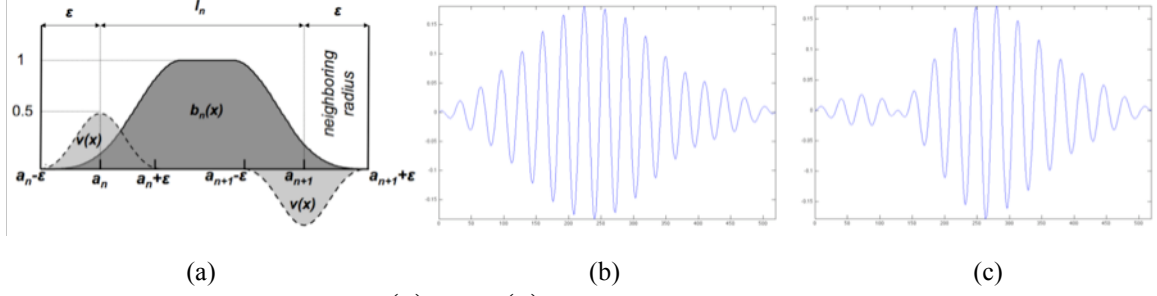


Fig. 6.2. Windowing functions $b(x)$ and $v(x)$ (a). The ϵ parameter controls the localization degree of brushlet function in time and frequency domains. Real part (b) and imaginary part (c) of analysis $u_{n,j}$ brushlet function with $l_n = 32, \epsilon = 16, j = 8$.

can be implemented in an efficient fashion using a folding technique and fast Fourier transform (FFT) [132]. The major advantage of brushlet basis over wavelet packets is the unique well-localized frequency response of each extracted coefficient and also arbitrary tiling of the time-frequency plane. The analysis can also be extended to n-D via separable tensor products. Although the primary application of brushlet analysis, presented in [131], was for image compression authors in [133] introduced an overcomplete representation of brushlet analysis and successfully developed a denoising/enhancing scheme to automatically extract left ventricular (LV) endocardial borders in real-time 3-D (RT3D) (4-D) echocardiograms. **Figure 6.3** demonstrates the schematic of feature extraction procedure (computing brushlet coefficients) and selection of features along arbitrary numbers of directions.

By applying the inverse Fourier transform, we can then compute the decomposition of signal f onto the orthonormal synthesis function $w_{j,n}(x)$ defined as:

$$w_{j,n}(x) = \sqrt{l_n} e^{(2i\pi a_n - l_n/2)} \times \left[(-1)^j \hat{b}_\sigma(l_n x - j) - 2i \sin(\pi l_n x) \hat{v}_\sigma(l_n x + j) \right] \quad (6.4)$$

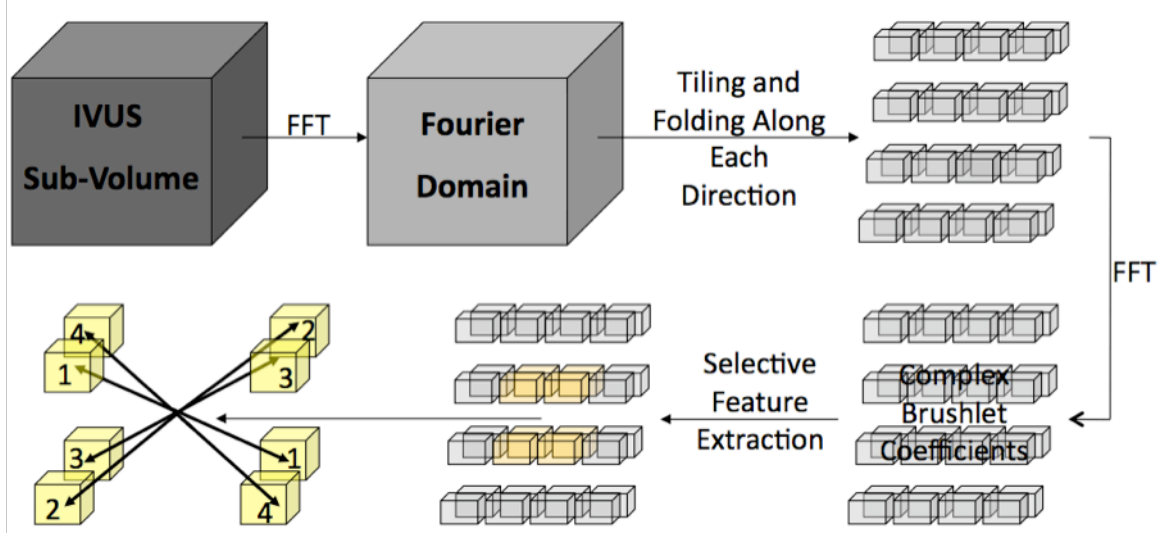


Fig. 6.3. Schematic expansion of IVUS sub-volumes onto brushlet basis, tiling of frequency domain (4x4x2) and selective feature extraction along eight directions corresponding to low-frequency components.

with scaling factor l_n , translation factor j , and steepness factor $\sigma = \frac{\varepsilon}{l_n}$. The parameter ε

controls the degree of localization of brushlet analysis and synthesis functions in time and frequency domains, respectively. Pair of synthesis brushlet functions has been depicted in **Figure 6.4**. The schematic of reconstruction process, after enhancement or thresholding of brushlet coefficients, is also shown in **Figure 6.5**.

In the rest of this chapter, we project 3-D IVUS volumes in polar coordinates with brushlet overcomplete expansion. Our hypothesis is that complex brushlet coefficients in transformed domain provide information regarding plaque and blood regions at different orientations. **Figure 6.3** demonstrates the schematic of feature extraction procedure (computing brushlet coefficients) and selection of features along arbitrary numbers of directions.

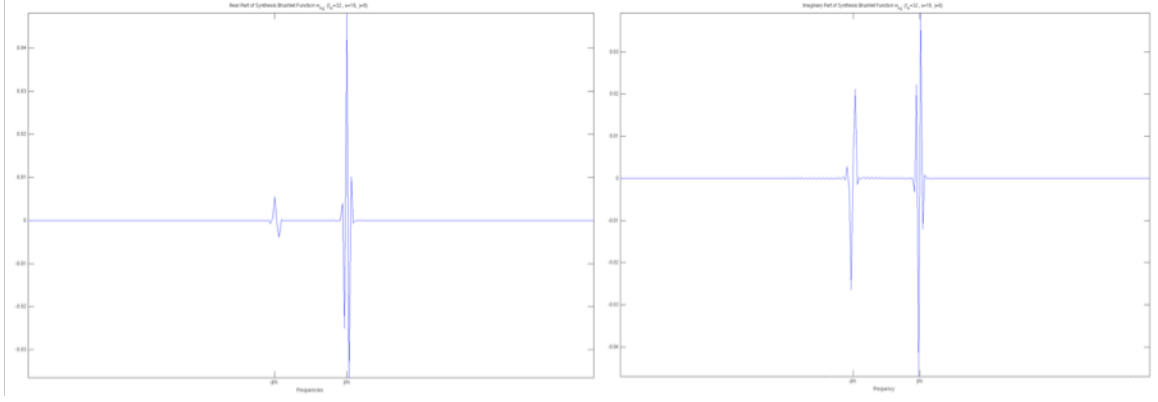


Fig. 6.4. Real (a) and imaginary (b) parts of synthesis function, $w_{j,n}(x)$, corresponding to Figure 6.2 (b,c).

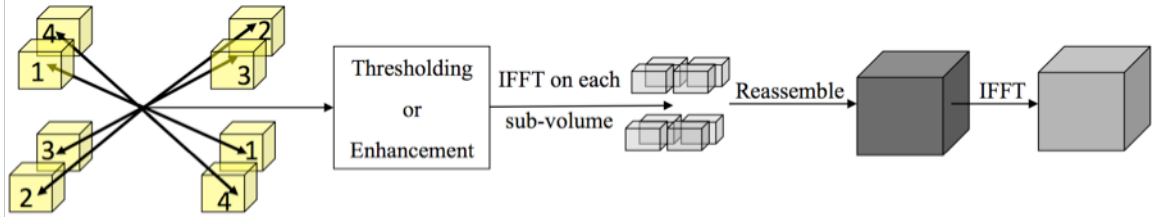


Fig. 6.5. Schematic of reconstruction after thresholding or enhancement of brushlet coefficients.

As we can observe, the more cubes for tiling of frequency domain is used, the more orientations (angular resolution) are obtained. Perhaps, there is a tradeoff between spatial and frequency resolutions and the smaller cubes are employed, the better frequency resolution is achieved at cost of less resolution in spatial domain. As we pointed previously, authors in [131] introduced the brushlet analysis for compression of richly textured images. They further presented an adaptive tiling approach to obtain the most concise and precise representation of an image in terms of oriented textures with all possible directions, frequencies, and locations. Contrary to image compression where the least numbers of coefficients are desirable to be transmitted, we try to preserve as much textural information (coefficients) as possible due to stringent behavior of blood and plaque signals. Thus, over-completeness of the decomposition is advantageous in IVUS

lumen border detection and segmentation. Such redundant representation of the original data in multiscale analysis makes the brushlet analysis shift invariant, which is a suitable for segmentation task. Before we continue, we need to define some terminologies and notations that we will use for the rest of this chapter.

Sub-volume

We processed each acquired IVUS pullback by truncating it into small volumes called sub-volume that contained limited number of frames (e.g. 8 or 16 frames).

Fourier Domain Tiling

Extension of brushlet analysis to n -D ($n \geq 2$) through separable tensor products provides flexibility in partitioning the transform domain known as tiling. The tiling of Fourier domain allows us to analyze signals at specific orientation, frequency, and resolution.

6.1.2.1. Notation Convention for Tiling of Fourier Space

For the sake of clarity, we define our notations so individual or ensemble of cube(s) in Fourier space can be uniquely represented. Given expanded sub-volume of IVUS data of size $X \times Y \times Z$ onto 3-D brushlet basis in an overcomplete fashion, the Fourier space can be tiled with n, m, p cubes in u_x, u_y, u_z directions, respectively, assuming:

1- n, m, p are of power of two.

2- $n = m$.

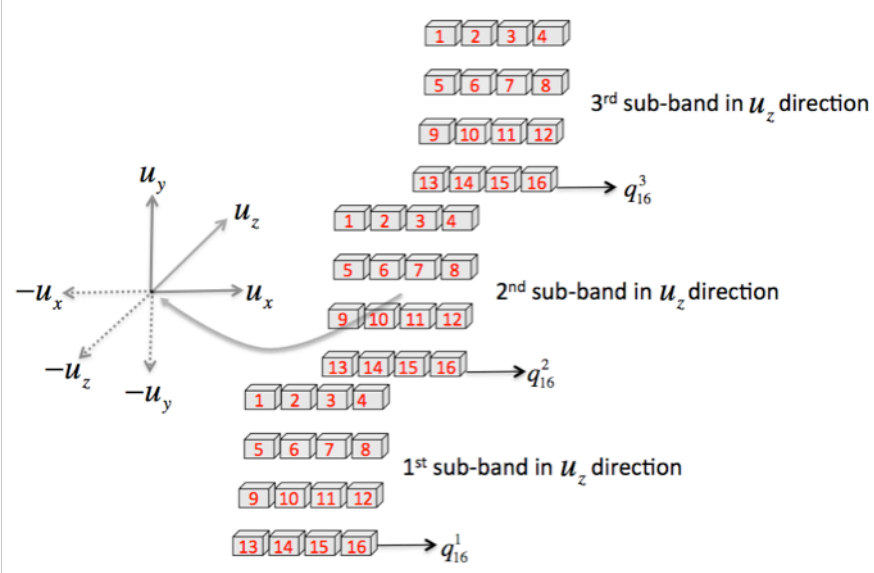


Fig. 6.6. Indexing convention used after tiling of frequency space. $4 \times 4 \times 3$ cubes are used to tile the frequency space, resulting 48 quadrants. Each quadrant is indexed incrementally, starting from the most left-top quadrant in roster format. An individual quadrant is represented by its index and sub-band numbers $q_{\text{index \#}}^{\text{subband \#}}$.

After expansion, each cube is indexed incrementally starting from the most left-top cube in roster format as shown in **Figure 6.6**. We also use two terminologies that refer to ensemble of cubes, defined as follows:

Subband

Refers to frequency space tiling resolution. For example, in Figure 6.6, we used 4, 4, and 3 cubes in u_x , u_y and u_z directions, respectively to tile the frequency space and obtain 4, 4, and 3 sub-bands of cubes in the same directions.

Ring of cubes

Refers to ensemble of symmetric cubes that span 360° in any frequency plane. We mainly focus on constructed rings in (u_x, u_y) plane, **Figure 6.7(a)**. An individual ring can

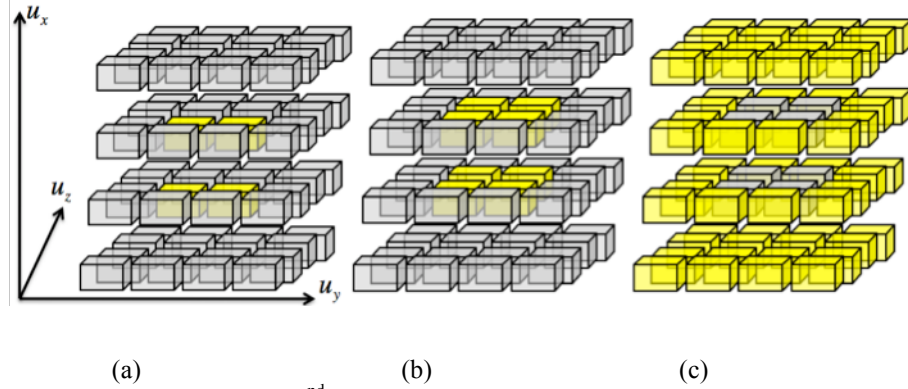


Fig. 6.7. First ring of quadrants in the 2nd subband (a), first quadrants' sphere (b), and second quadrants' sphere (c).

be represented by its index and subband numbers $R_{index\#}^{subband\#}$. For example, the highlighted ring in **Figure 6.7(a)** is denoted by R_1^2 .

Cubes' sphere

Refers to ensemble of cubes that span 360° and encloses the center of the Fourier space $((u_x, u_y, u_z) = (0, 0, 0))$, **Figure 6.7(b,c)**. Each sphere can be represented by its index number $S_{index\#}$. For example the illustrated spheres in **Figure 6.7(b)** and **Figure 6.7(c)** can be denoted by S_1 and S_2 , respectively.

For the rest of this chapter, we will investigate numbers of important factors (*i.e.* tiling of frequency domain, selection of the most informative cubes through visualization of brushlet coefficients, etc) in IVUS 3-D brushlet analysis, and describe developed techniques in details, and demonstrate results along with quantification.

6.2. Lumen Border Detection via Thresholding of Brushlet Coefficients

The presence of blood speckles within the sub-volume of analysis is considered to be dynamic due to blood flow. In other words, the appearance of regions corresponding to plaques, vessel wall and surrounding fat is more stable within successive frames than for the blood pool. Consequently, we can assume that there is a strong spatial coherence in the appearance of plaque, arterial wall and surrounding fats within blocks of the analysis. This coherence is organized in concentric circular layers in Cartesian domain and is better expressed and visualized in polar representations of the image data. Furthermore, in brushlet analysis, tiling of frequency domain and expansion are based on a regular square lattice, which are better correlated with homogeneous textured patterns in polar (r, θ) rather than Cartesian (x, y) image representation. Hence, the analysis is performed in polar domain and final results are mapped back to Cartesian coordinates for visual display. The underlying hypothesis for brushlet filtering via thresholding is that blood speckle can be removed by including the pullback dimension in the textural brushlet analysis in the frequency domain and appeared as high frequency components. Therefore, we apply a 3D (cross-sectional image of arterial content + pullback distance) overcomplete brushlet analysis to sub-volumes of IVUS frames in polar coordinates during each pullback.

6.2.1. Frequency Tilling and Overcomplete Representation

We partitioned the IVUS pullback data into temporal sub-volume of analysis without overlap and project them onto 3-D brushlet basis. The decomposition of IVUS sub-volumes onto the brushlet orthonormal basis provides selectable textural features with different orientations in the Fourier (brushlet) domain, **Figure 6.3**. Since, we deal with volumetric datasets, this can be reliably performed by tilling the Fourier domain into quadrants (cubes), each representing a specific size and orientation of a brushstroke, which is analogous to a wavelet scaling function. We used an overcomplete multiscale representation of the brushlet coefficients for two reasons. First, we avoided aliasing effect and secondly, we intended to preserve as much textural information as possible in the transform domain due to the stringent behavior of blood and plaque signals that makes the lumen border detection very challenging.

6.2.2. Thresholding for Removal of Blood Speckle

The purpose of this study is to offer a reliable filtering algorithm by removing blood speckles, such that the resulting filtered data can be employed as an input for any 2D or 3D segmentation algorithm. We treated dynamic behavior of blood speckles as noise that could emerge as high frequency components in transformed domain. Therefore, we only considered coefficients from different directions corresponding to low frequency components in 3D brushlet domain. We then employed the magnitude of brushlet coefficients as a condition to perform thresholding and zeroed out the coefficients that had values below the selected threshold and finally reconstructed the sub-volume of IVUS data. **Figure 6.8**, Shows the resulting filtered images with two different threshold

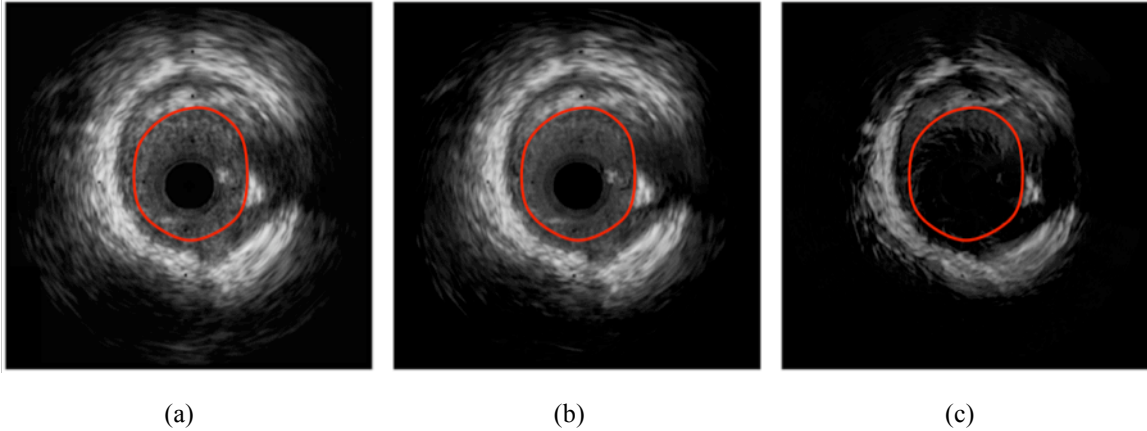


Fig. 6.8. Original IVUS frame (a), filtered result with threshold values of $T=0.25$ (b) and $T=0.5$ (c). Manual traced borders (red), representing lumen border and blood speckles inside luminal area.

values. As we can see, when the threshold value was increased ($T = 0.5$), better result was obtained and we could partially remove blood speckles, **Figure 6.8(c)**. Although we chose the threshold values empirically and results were not perfect (especially for part of the pullback that had registration problem) they showed that brushlet-based denoising approach had a great potential to be used as a preprocessing step for lumen border detection.

6.2.3. Segmentation Framework and Detection of Lumen Border

We used the iterative conditional model (ICM) segmentation framework to segment the IVUS data into 4 regions (layers), characterized by their average gray values. The ICM segmentation framework corresponds to a discrete minimization of the piece-wise Mumford and Shah functional energy [134] replacing curvature constraints with a Markovian regularization of the contours. The Markovian regularization provides a very efficient computational framework to control orthogonal and vertical associations of similar class labels when applied on a regular lattice corresponding to 4-neighbor pixels

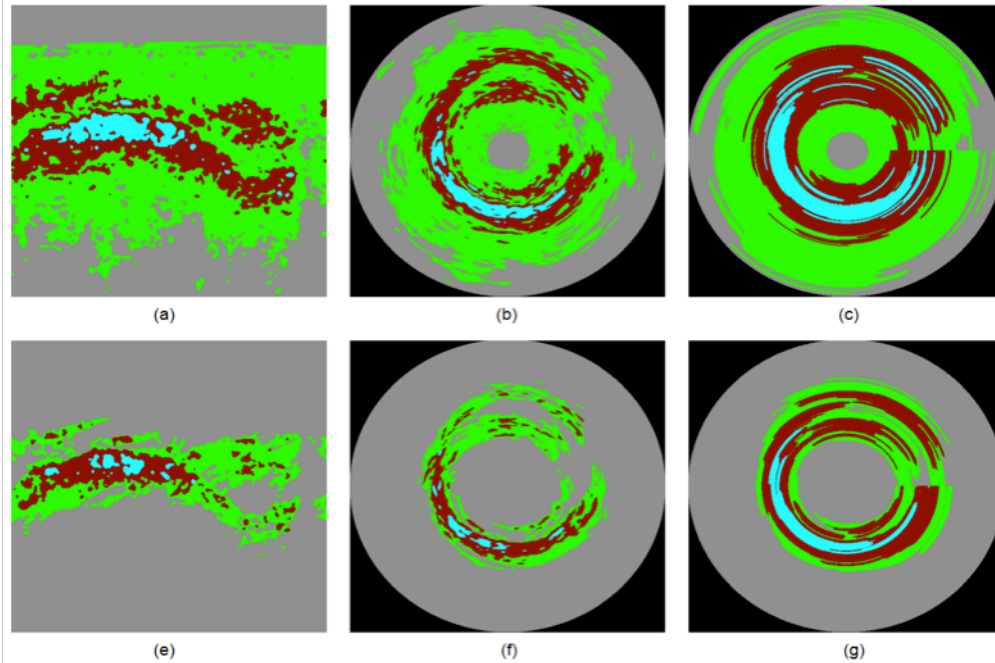


Fig. 6.9. ICM segmentation. 4-classes ICM results for original image in polar (a), Cartesian (b) coordinates, and after dilation (c). 4-classes ICM results for filtered image in polar (e), Cartesian (f) coordinates, and after dilation (g).

in 2D. Such a constraint is ideal for circular patterns such as vessel layers, when displayed in polar coordinates. We therefore applied the ICM on the IVUS original and filtered volumes in polar coordinates. Consequently, classification results were transformed to the Cartesian coordinates for visualization and extraction of the center contours with a standard parametric deformable model applied on thresholded ICM classifications for the four classes and imposing a regular growth of vessel contour areas by iteratively initializing the deformable model with lower-class results. This extraction step was performed after dilation of the ICM classification results with a horizontal line structuring element of 70 pixels, in polar coordinates. This computational step was designed to close the open and unconnected borders to obtain better results from parametric deformable model and estimate the lumen border more precisely, as illustrated in **Figure 6.9**.

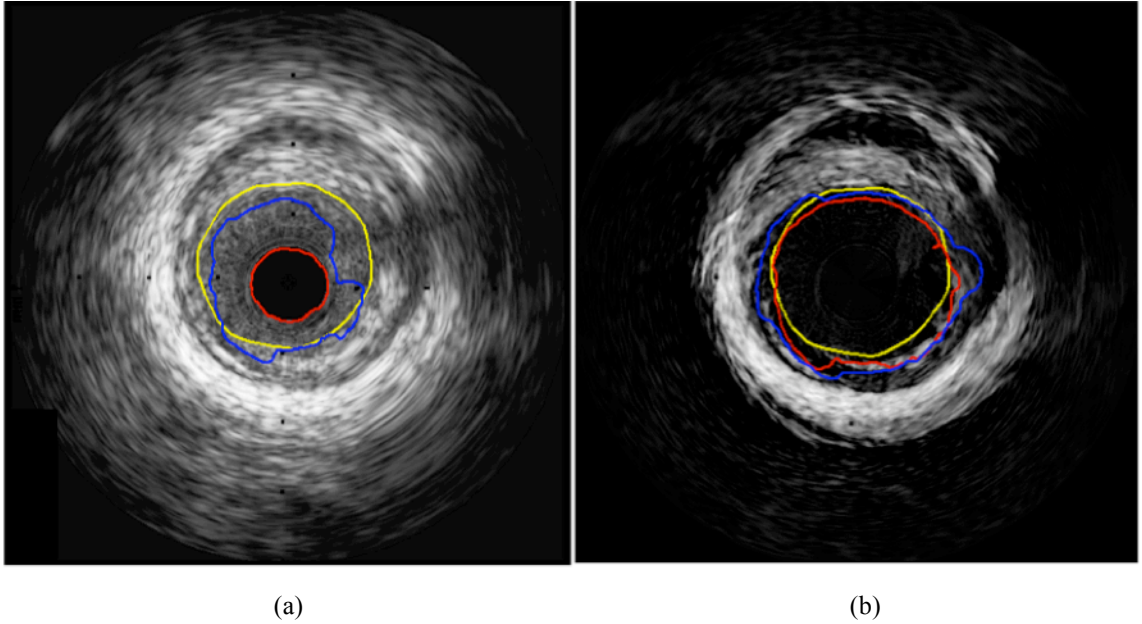


Fig. 6.10. Segmentation results at two different layers (red and blue) along with manually traced contour by an expert (yellow) on original (a) and filtered (b) IVUS images.

6.2.4. Results and Discussion

In the first experiment, we processed IVUS volumes of size $512 \times 512 \times 2$ and the Fourier domain was tiled using four, four and two cubes in x , y and pullback dimension respectively each with overcomplete representation. In this case, the brushstroke orientation was $\pm 90^\circ$, $\pm 90^\circ$ and $\pm 180^\circ$ in x , y and pullback direction, respectively. We repeated the experiment using volumes of size $512 \times 512 \times 8$ to ensure adequate spatial resolution in the pullback dimension (8 slice depth). Higher spatial resolution in this dimension resulted in blurred denoised data due to the effects of the motion of the catheter and heart.

Figure 6.10 illustrates the results of our segmentation algorithm, in the second experiment, on original IVUS image and resulting filtered image using a hard

thresholding operator. For this purpose, the thresholding was performed in each cube empirically for the threshold value of 50% of the maximum value of real part of the coefficients. The resulting filtered coefficients were then classified into four groups with uniform gray level values for ICM initialization. However, we only extracted the contours from the first two layers since they better approximated the true lumen border. As we can see, the segmentation algorithm outperforms on filtered images and the automated borders at two layers (red L1 and blue L2) are well correlated and matched with manually traced lumen border (yellow) traced by an expert cardiologist.

For both experiments the regression analysis was performed to evaluate the agreement between automated and manual traced contours for 104 frames within a pullback, **Figure 6.11(a)**. In addition, we computed the Tanimoto coefficients to see how well the automated and manual contours are matched throughout the pullback, **Figure 6.11(b)**. The Tanimoto coefficient (η) is calculated as follows:

$$\eta = \frac{N_c}{N_a + N_m - N_c} \quad (6.5)$$

where, N_a, N_m are the number of enclosed pixels in automated and manually traced contours respectively and N_c is the number of common pixels in both. The average Tanimoto coefficients for L1 and L2 borders in the first experiment, using block size of $512 \times 512 \times 2$, found to be 41.75 ± 13.46 and 69.16 ± 7.37 , respectively, which were less than the computed Tanimoto coefficients for the second experiment using block size of $512 \times 512 \times 8$ IVUS frames (case #1, **Table 6.1**). The Tanimoto coefficients show the highest agreement in positioning of automated and manually traced borders. According to

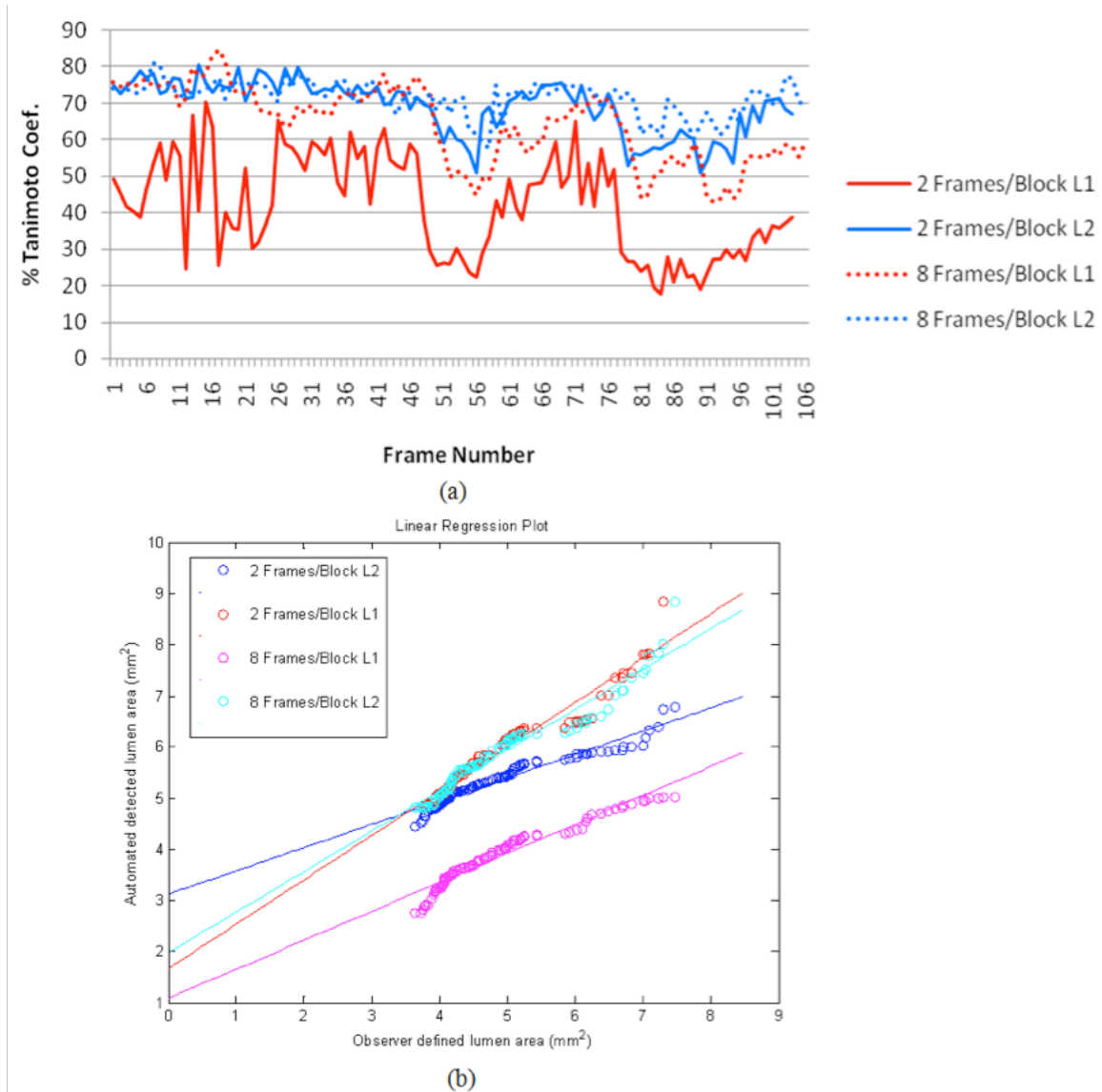


Fig. 6.11. Evaluation of detected contours at two layers (L1,L2) in 104 IVUS frames within a pullback with two different block sizes. Tanimoto coefficients (a), Regression analysis (b).

Figure 6.11(b), the higher Tanimoto coefficients were achieved for the first 50 frames where the pullback was more consistent. Our results show that the incoherent pattern of blood speckle is better captured in longer IVUS volumes although the changes in plaque textures or motion artifacts may be more observed that can degrade the results (frames 51 and 81 in **Figure 6.11(a)**). This suggests an adaptive processing technique in future. **Table 6.1** summarizes the Tanimoto coefficients statistics as well as correlation values

for 233 frames extracted from three distinct cases using block size of $512 \times 512 \times 8$ IVUS frames. Overall, the extracted contour at the second layer (L2) found to have more agreement with manually traced borders.

Table 6.1. Tanimoto coefficient statistics and correlation between automated and manually traced borders in 233 frames collected from three distinct cases.

	<i>Number of Frames</i>	<i>Mean Tanimoto Coefficients</i>	<i>Maximum Tanimoto Coefficients</i>	<i>Minimum Tanimoto Coefficients</i>	<i>Correlation ($p < 0.0001$)</i>
Case # 1	104	$L1 : 64.12 \pm 10.56$ $L2 : 71.34 \pm 4.74$	$L1 : 84.85$ $L2 : 81.02$	$L1 : 42.78$ $L2 : 57.53$	$L1 : 0.79$ $L2 : 0.78$
Case # 2	104	$L1 : 71.10 \pm 9.69$ $L2 : 72.70 \pm 4.05$	$L1 : 84.20$ $L2 : 81.09$	$L1 : 48.33$ $L2 : 60.87$	$L1 : 0.78$ $L2 : 0.80$
Case # 3	25	$L1 : 69.73 \pm 4.22$ $L2 : 77.08 \pm 4.63$	$L1 : 77.69$ $L2 : 86.93$	$L1 : 60.47$ $L2 : 70.14$	$L1 : 0.94$ $L2 : 0.95$

6.2.5. Summary

We presented a 3D filtering technique based on brushlet representations to remove blood speckles in IVUS images acquired with a 45MHz single-element transducer. We further used filtered volumes as input to a 3D multi-region multi-channel segmentation algorithm to estimate the lumen border. We observed that the algorithm performance was encouraging especially in consistent pullback where there is a strong spatial coherence in the appearance of plaque. We mainly tiled the Fourier domain using fixed number of cubes (four, four and two cubes in x , y and pullback dimension, respectively) each with overcomplete representation and extracted the low frequency complex brushlet coefficients. We also considered the tiling of frequency domain using more number of cubes (higher resolution) and studied the effects of such tiling on reconstructed filtered IVUS volumes. The resulting images were more blurred due to spatial-frequency

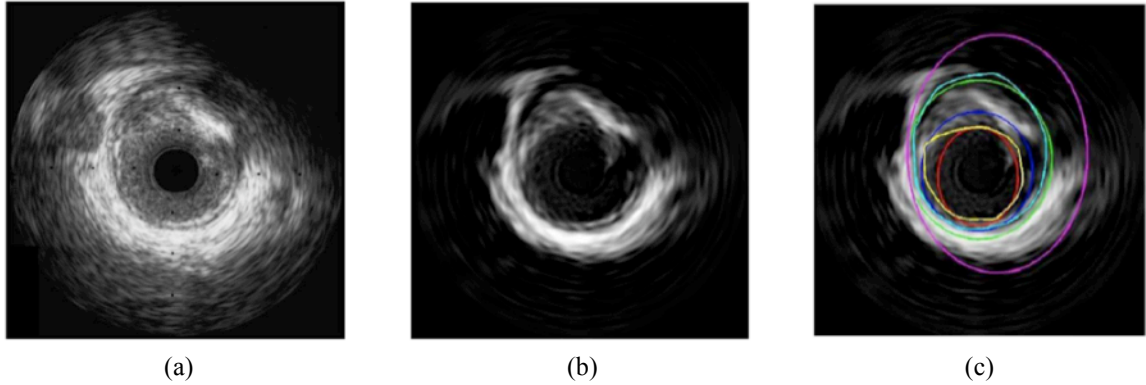


Fig. 6.12. Original IVUS frame (a), filtered IVUS frame using tiling of frequency domain with $16 \times 16 \times 8$ cubes (b), automated detected contours with elliptical shape constraint at first layer (L1, red), second layer (L2, blue), third layer (L3, green) and fourth layer (L4, magenta) along with manually traced lumen (yellow) as well as vessel wall (cyan) borders (c).

resolution trade off similar to Heisenberg uncertainty principle. **Figure 6.12** illustrates a filtered IVUS frames resulting from thresholding of coefficients in cubes corresponding to the low frequency components. The automated detected borders with elliptical shape constraint have been displayed too. It is worth mentioning that the algorithm performance was degraded particularly within those frames that encompassed misregistration due to catheter and heart motions.

6.3. Distribution of Brushlet Coefficients

We look at the distribution of coefficients, assuming the most valuable information resides in cubes corresponding to low frequency components. For this reason the distribution of real and imaginary parts as well as magnitude of coefficients at different orientations were considered. We know that tiling the Fourier domain into specific numbers of cubes, yields cubes that contain more information for differentiation between blood and non-blood regions than the rest. For instance, the real part of brushlet

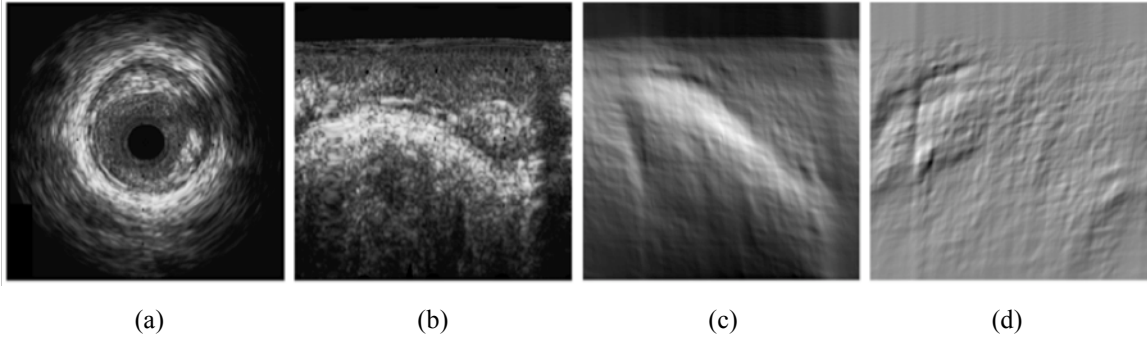


Fig. 6.13. IVUS frame in Cartesian (a) and polar (b) coordinates and the real part of brushlet coefficients at two different orientations (cubes) corresponding to low frequency components in 4x4x2 expansion scheme.

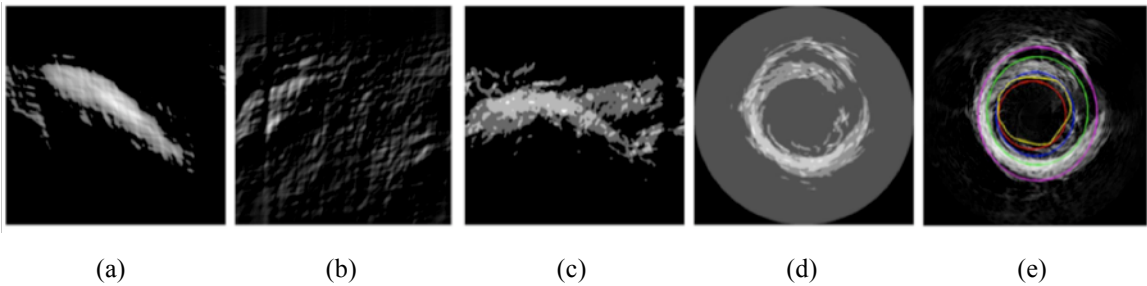


Fig. 6.14. Thresholded brushlet coefficients corresponding to Figure 6.13(c) (a), and Figure 6.13(d) (b), classified denoised image using ICM algorithm and four classes in polar (c) and Cartesian (d) coordinates, filtered image corresponding to Fig. 6.13(a) and automated detected borders extracted from four classes along with manually traced border (yellow) (e).

coefficients in one direction, **Figure 6.13(c)**, provides better delineation between blood and plaque textures compared to another one that is shown in **Figure 6.13(d)**. This can be also seen by looking at the corresponding filtered results after thresholding, **Figure 6.14(a)** and **Figure 6.14(b)**. Therefore, the challenge is to identify the most informative cubes and set proper threshold values in order to eliminate coefficients corresponding to blood textures more efficiently. Considering the distribution of brushlet coefficients within each cube can do this.

We used the manual traced borders to differentiate blood from non-blood regions and mask out corresponding coefficients in each cube. **Figure 6.15** illustrates the 1-D

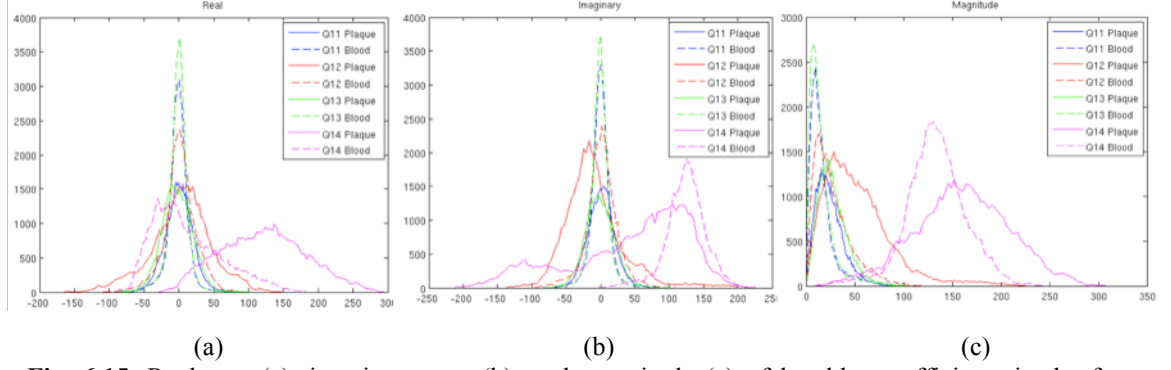


Fig. 6.15. Real part (a), imaginary part (b), and magnitude (c) of brushlet coefficients in the four innermost cubes at the first subband in 4x4x2 expansion scheme corresponding to blood and non-blood regions.

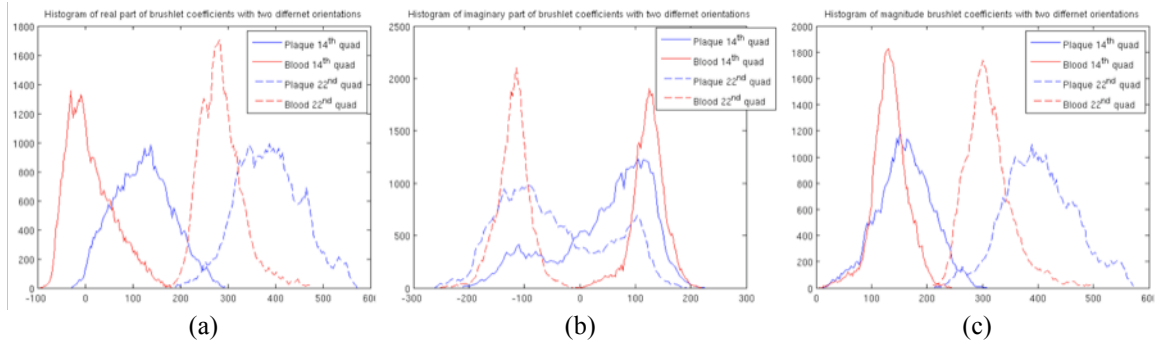


Fig. 6.16. Real part (a), imaginary part (b), and magnitude (c) of brushlet coefficients in two cubes (14 and 22) that exhibits the largest separation.

histograms of real and imaginary parts along with magnitude of brushlet coefficients in the four innermost cubes at the first subband in 4x4x2 expansion scheme. As we can see, the largest separation between blood and non-blood coefficients is derived from cube 14 (+45 direction). Similar distributions were obtained from cubes at the second subband and coefficients in cube 22 (-45 direction) demonstrated the largest separation.

Based on our observations, computed coefficients in cubes that represented expansions along $\pm 45^\circ$ exhibit the most informative features in terms of delineation between blood and non-blood regions. **Figure 6.16** illustrates the histograms of real and imaginary parts of brushlet coefficients as well as their magnitudes at those cubes for both blood and non-

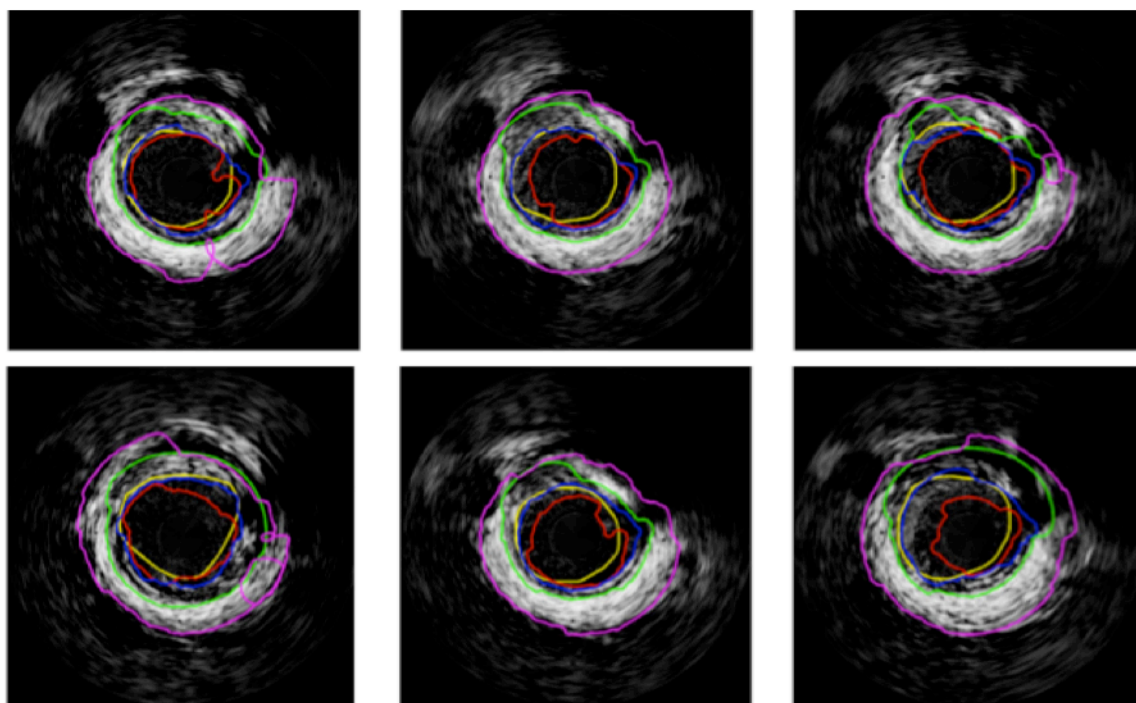


Fig. 6.17. Automated (red (L1), blue (L2), green (L3), and magenta (L4)) detected borders depicted on few denoised IVUS frames along with corresponding manual (yellow) traced borders. The results are achieved from expansion of sub-volume of IVUS frames in 4x4x2 scheme followed by thresholding of coefficients in cubes representing $\pm 45^\circ$.

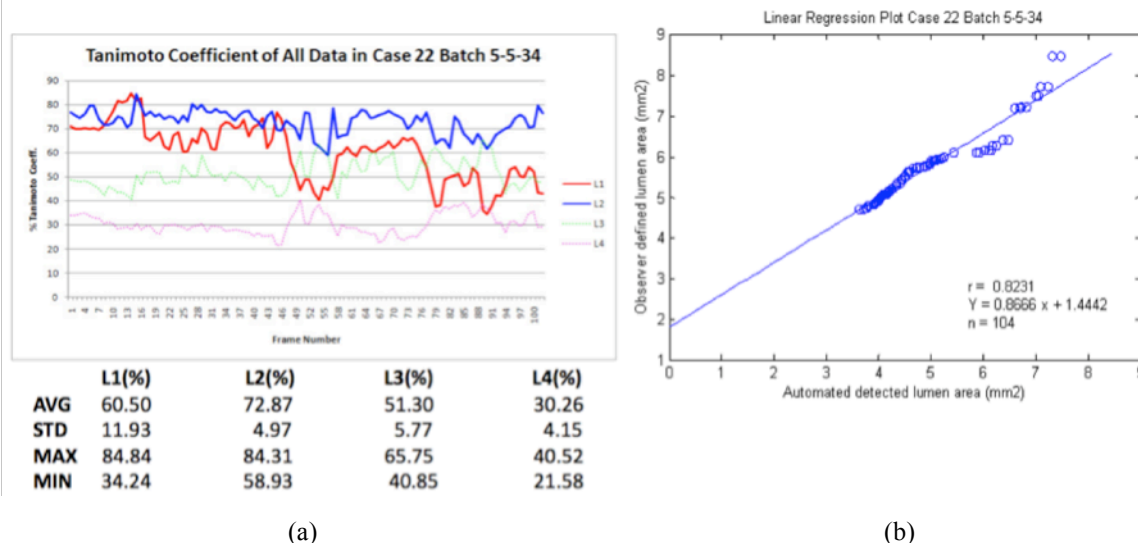


Fig. 6.18. Validation of automated detected borders within short pullback with respect to manually traced borders. Calculated Tanimoto coefficients and corresponding statistics (a) Linear regression analysis (b).

blood cases. These findings motivated us to detect lumen borders by using filtered images reconstructed from thresholding of coefficients in the most informative cubes. **Figure**

6.17 and **Figure 6.18** illustrate automated as well as manual traced borders on few IVUS frames, resulting from thresholding of coefficients in cubes representing $\pm 45^\circ$, and computed correlation along with Tanimoto coefficients, respectively.

By looking at depicted histogram of imaginary part of brushlet coefficients in **Figure 6.16**, we note that brushlet coefficients in cubes 14 and 22 are anti-symmetric and it is because the original IVUS data is real. Hence, we performed another experiments and filtered IVUS sub-volumes by thresholding brushlet coefficients only in cube 14 and generating a binary mask. The binary mask then used to zero out the coefficients in the rest of the innermost cubes. **Figure 6.19** and **Figure 6.20** illustrate automated as well as manual traced borders on few IVUS frames along with computed Tanimoto coefficients and corresponding statistics, respectively.

We detected borders at different layers (classes) that depended on number of classes chosen in ICM classification algorithm. Although the very two borders estimated the lumen border closely we need to find an approach to uniquely select one automatically. One possible solution could be use the average of both detected borders (L1 and L2). Furthermore, the main limitation associated with employed technique was finding the right threshold value. One possible solution is to implement a supervised classification approach using Neural Networks (NN) to distinctively approximate the lumen border.

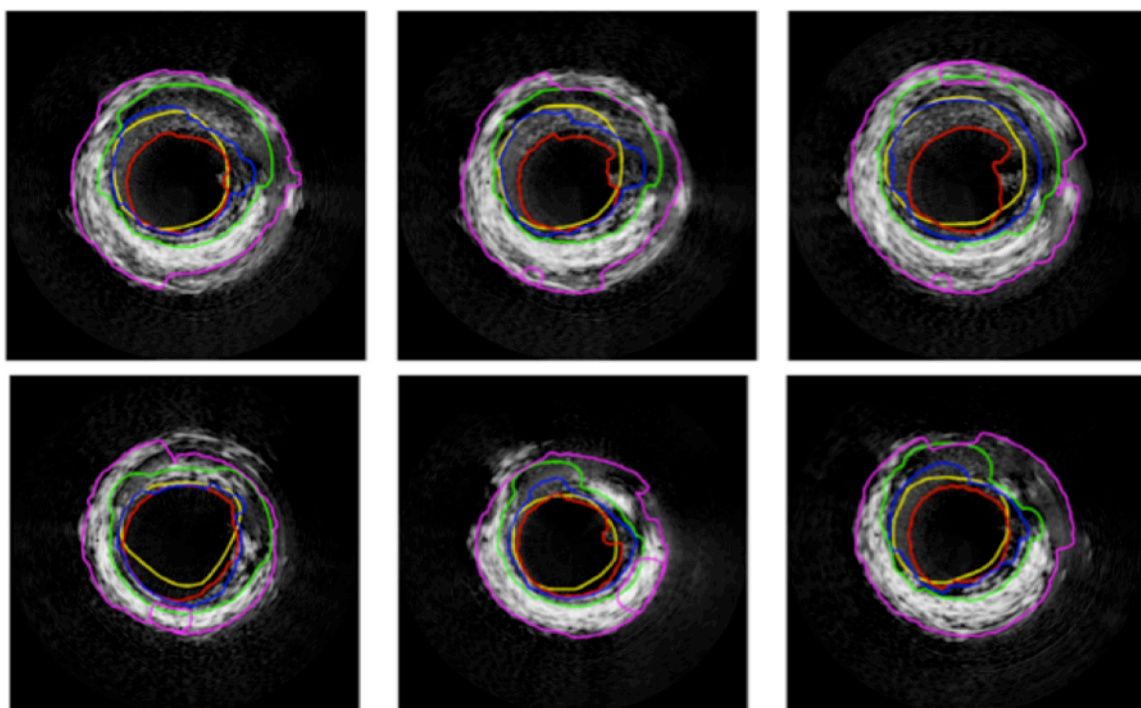


Fig. 6.19. Automated (red (L1), blue (L2), green (L3), and magenta (L4)) detected borders depicted on few denoised IVUS frames along with corresponding manual (yellow) traced borders. The results are achieved from expansion of sub-volume of IVUS frames in 4x4x2 scheme followed by thresholding of coefficients in cubes representing $+45^\circ$ and zeroing out coefficients in the rest of innermost cubes using generated binary mask.

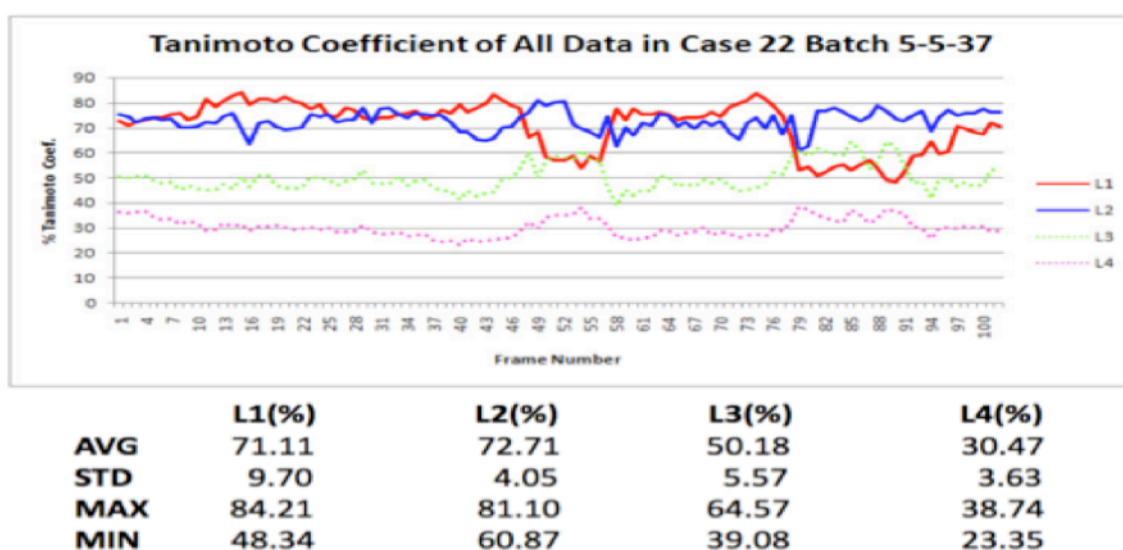


Fig. 6.20. Calculated Tanimoto coefficients for a short pullback and corresponding statistics.

6.4. Classification of Blood Regions in IVUS Images Using 3D Brushlet Expansions

The presence of incoherent blood speckle patterns makes the assessment of lumen size in IVUS images a challenging problem, especially for images acquired with recent high frequency transducers (40MHz up). In the rest of this section, we present a robust 3D feature extraction algorithm based on the expansion of IVUS cross-sectional images and pullback directions onto an orthonormal complex brushlet basis. We select the 3D low-frequency complex brushlet coefficients to train a neural network and generate blood map images. Several features are selected from the projections of low-frequency 3D brushlet coefficients. These representations are used as inputs to a neural network that is trained to classify blood maps on IVUS images. We will evaluate the algorithm performance using repeated randomized experiments on sub-samples to validate the quantification of the blood maps when compared to expert manual tracings of 258 frames collected from three patients. Our results demonstrate that the proposed features extracted in the brushlet domain capture the incoherent structures of blood speckle good enough, enabling identification of blood pools and enhancement of the lumen area.

6.4.1. Feature Extraction Methodology

One of the main advantages of a brushlet expansion is that one can select features along specific directions. Tilling the Fourier domain into numbers of cubes, each representing a specific size and orientation of a brushstroke, can reliably perform this. In order to train and then use a classifier to extract the blood regions on IVUS images, we built a vector of

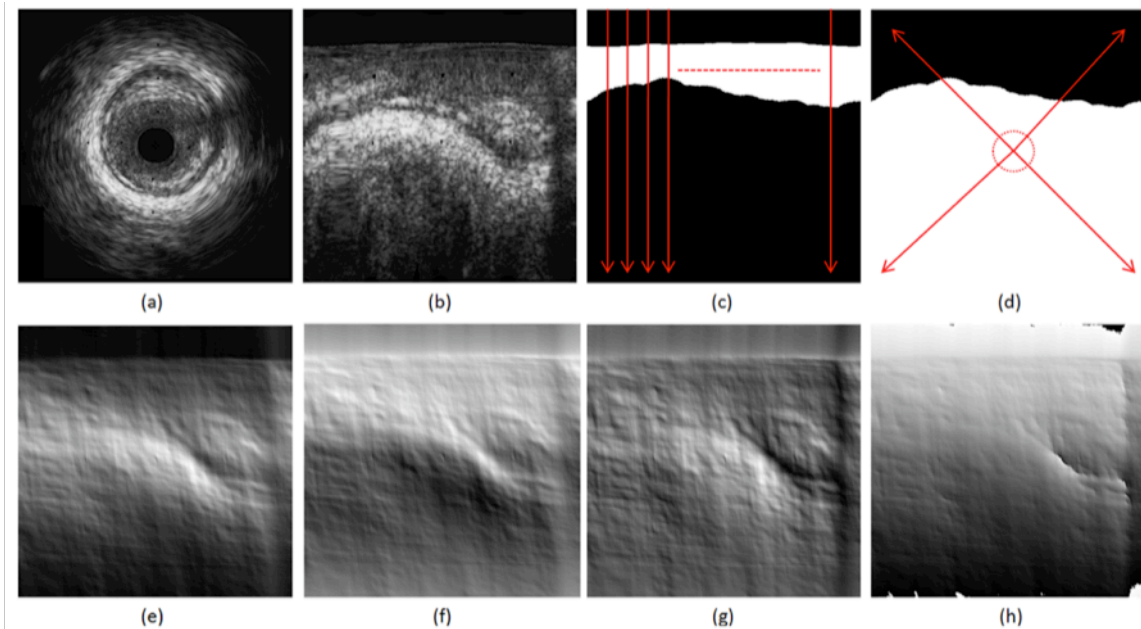


Fig. 6.21. IVUS frame in Cartesian (a) and polar (b) coordinates. Binary blood (c) and plaque (d) maps generated from manual tracing by an expert. The radial (c) and angular (d) distances are illustrated in red. Real part (e), imaginary part (f), magnitude (g) and phase (h) of brushlet coefficients computed on the radial image (b) along a single orientation.

features, combining *image information*, via brushlet expansion, and *geometric constraints*. First, for each quadrant of brushlet coefficients, we combined redundant coefficient value information: (1) magnitude values, which are typically used in spectral-based tissue characterization algorithms [6,70,130], (2) phase values, (3) real and (4) imaginary values. In preliminary experiments, we observed significant improvement of the classifier performance when using redundant coefficient information versus only (real, imaginary) or (magnitude, phase) information.

Geometric constraints were defined using two distance maps: a radial *distance map*, with respect to the transducer surface, computed in polar coordinates (to encode the fact that the blood pool is close to the transducer), and a direct map of individual pixel locations

(angular distance), to encode geometric information in the feature vector, which is built via an arbitrary rasterization of the IVUS data. These two geometric constraints are illustrated in **Figure 6.21**.

6.4.2. Classification

Feature vectors are used as the input of a neural network classifier. More specifically, we employed a Multi Layer Perceptron (MLP) [135], which was trained using Back Propagation (BP) algorithm with adaptive learning rate. The specifications of the MLP design are further explained in the next section.

6.4.3. Experimental Results

We deployed 258 IVUS frames in pullbacks data collected from three patients, consisting of small, medium and large blood pools to accommodate for diversity within patients. For each pullback, the volumetric IVUS data was partitioned into sub-volumes of size $512 \times 512 \times 8$. An overcomplete expansion was performed through tiling of the Fourier domain into four, four and two sub-cubes in x , y and pullback direction that provided adequate spatial-temporal resolution. We only preserved the $[2 \times 2 \times 2]$ low-frequency redundant coefficients, leading to a total of $N=32$ coefficients-based features. Finally, by including the two geometric features, we constructed our feature vector with $N=34$ features. For the sake of simplicity and to enable a fair comparison, we used, in our initial experiments, an MLP topology as previously employed in IVUS related studies for lumen border detection [136] and catheter motion compensation [137]. The MLP had one

Table 6.2. Classification results using neural networks with different topologies: N-M-1; N and M are the number of neurons in the input and hidden layers, respectively. Also shown are results using different numbers of features. Correct classification (CC) rate, sensitivity (SE), specificity (SP) and correct segmentation (S) rate are reported. The better results are highlighted in yellow. The best performance was achieved using 34 features (N) and network topology of N-34-1 (green).

Neural Network Topology (N-M-1)	N=32 Features				N=33 Features				N=34 Features			
	CC	SE	SP	S	CC	SE	SP	S	CC	SE	SP	S
N-3-1	93.31	81.47	92.55	70.21	93.67	83.16	93.02	71.22	94.11	83.42	95.90	71.34
N-5-1	94.15	87.69	95.86	71.66	93.82	84.08	95.98	72.27	94.56	83.10	96.90	72.21
N-10-1	94.51	86.65	97.14	74.31	94.32	85.83	97.04	75.47	94.69	86.75	96.56	76.94
N-15-1	94.85	87.47	96.68	75.20	94.86	78.46	97.10	76.41	95.04	87.88	97.82	78.56
N-20-1	94.27	86.61	96.80	75.07	94.82	77.08	97.98	78.05	95.10	88.20	97.14	78.27
N-34-1	95.12	86.73	96.38	77.23	95.33	77.32	98.10	77.94	95.84	86.80	97.87	79.59

hidden layer and one neuron as output with linear activation functions. The network goal, adaptive learning rate, and maximum number of iterations set to 0.001, 0.01, and 5000 epochs, respectively. For each experiment, the training set was constructed with random selection of 2/3 of the dataset (172 frames) and the remaining 1/3 (86 frames) were used for testing. For this purpose, binary masks for blood and non-blood regions in each frame were generated using manually traced lumen borders by an expert, as illustrated in **Figure 6.21(b,c)**.

First, we repeated the experiments with different numbers of neurons in the hidden layer (20 experiments for each) to find out the optimal setting. In order to evaluate the classification accuracy, the correct classification (CC) and segmentation (S) rates were defined as $(TN+TP)/(TN+TP+FP+FN)$ and $(TP)/(TP+FP+FN)$, respectively, where TP, TN, FP, and FN correspond to true positive, true negative, false positive, and false negative rates. We computed the S value, in addition to traditional CC rate, for fair representation of classification results since the lumen embodied small area compared to the whole IVUS image, causing large TN rates. The sensitivity (SE) and specificity (SP)

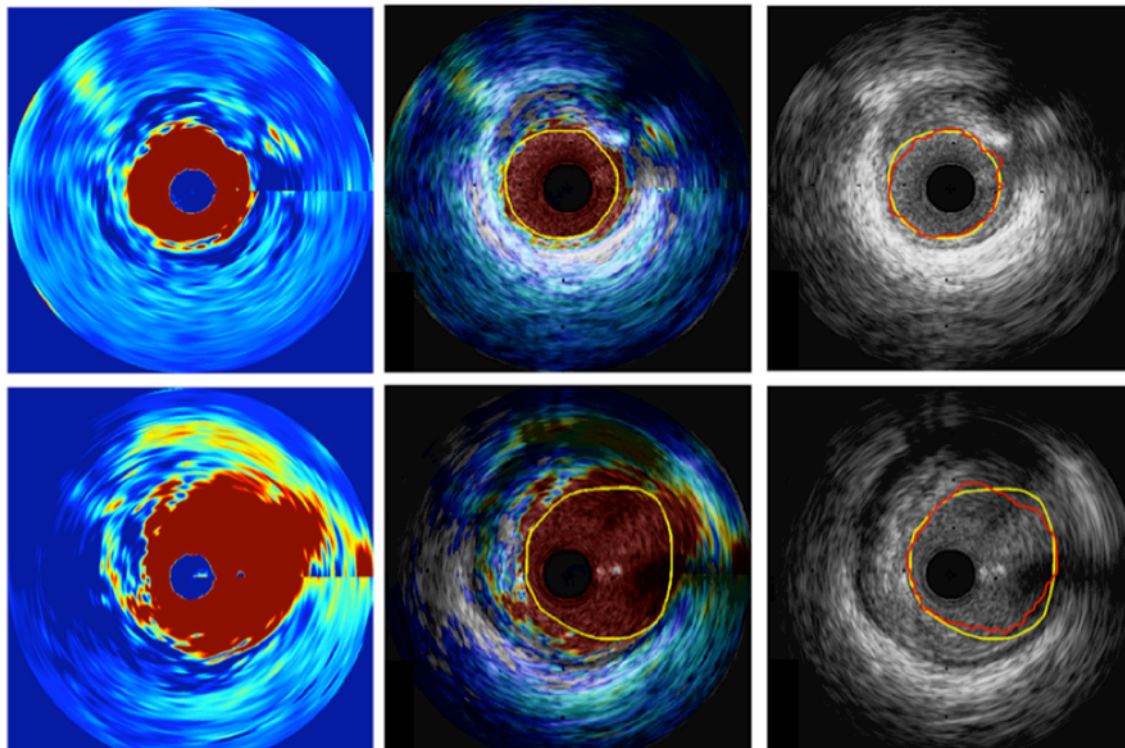


Fig. 6.22. Two distinct grayscale IVUS frames. Generated blood maps (left column), superimposed blood maps on original grayscale IVUS images with manually traced lumen borders (yellow) by an expert (middle column), and automated detected lumen border (red) by thresholding the grayscale image resulting from output of neural network.

rates were also defined as $TP/(TP+FN)$ and $TN/(TN+FP)$, respectively. **Table 6.2** summarizes the results and demonstrates that a hidden layer with more than 15 neurons does not alter the results significantly. The best performance was achieved when both geometric features were used, confirming the influence of such features. We constructed blood maps using the output of linear activation functions and represented the least (blue) as well as the most (red) probable blood regions in color jet spectrum. **Figure 6.22** illustrates a blood map generated by the neural network and corresponding to a relatively small vessel. The constructed blood map provided fair representation of the lumen cavity, confirming that the extracted features were sufficiently reliable.

Table 6.3. Classification results and comparison between manual and optimal automated lumen border, generated from a thresholded blood map with an optimized threshold value through linear regression analysis and computation of Tanimoto Coefficients (η). The best performance was achieved using threshold value of 0.45 (green).

Threshold value	Classification Statistics Case 1, Case 2, Case 3						Comparison Between Manually Traced and Automated Detected Borders									
							Case 1					Case 2				
	CC	FP	FN	SE	SP	S	η_{ave}	η_{max}	η_{min}	η_{std}	Correlation (p<0.0001)	η_{ave}	η_{max}	η_{min}	η_{std}	Correlation (p<0.0001)
0.25	94.42	5.10	4.13	95.86	94.10	75.87	73.97	84.91	65.11	4.97	0.82	76.81	86.97	61.46	5.93	0.85
0.35	95.50	3.38	6.94	93.06	96.05	79.09	78.20	88.97	60.07	6.24	0.82	76.85	89.49	59.62	7.21	0.82
0.4	95.75	2.76	8.75	91.25	96.76	79.71	79.29	88.03	71.05	4.43	0.88	76.60	89.64	58.61	7.41	0.76
0.45	95.86	2.25	10.83	89.17	97.36	79.77	79.94	87.70	74.76	3.97	0.86	76.52	91.37	57.43	7.73	0.75
0.5	95.84	1.81	13.19	86.80	97.87	79.59	78.59	87.80	71.71	4.23	0.88	76.24	90.39	56.11	8.24	0.66
0.55	95.68	1.45	16.07	83.93	93.31	78.02	76.54	88.94	69.81	4.67	0.88	75.50	89.01	54.85	8.58	0.67
0.6	95.39	1.13	19.3	80.70	97.68	76.20	74.23	86.03	68.18	4.27	0.91	73.98	87.51	53.12	8.77	0.63
0.65	94.97	0.87	23.02	76.98	98.99	73.66	71.59	81.42	63.41	4.45	0.93	72.60	86.78	51.93	9.29	0.58
0.75	93.61	0.45	32.59	67.40	99.47	65.87	63.70	72.34	56.76	4.00	0.95	67.64	84.58	48.44	10.07	0.54

Although blood maps offer necessary information on blood regions they are not sufficient for detection of the lumen border, which is a priority for any blood detection algorithm. For this purpose, we used the output of the linear activation function in the last neuron layer of the neural network and constructed 8-bit grayscale images by mapping these values from the range of [0,1] onto [0,255], linearly. Subsequently, we used thresholding followed by edge detection to delineate the lumen border. Although the value of 0.5 (128 in grayscale) seemed to be the appropriate threshold, we experimented with several values to validate this setting. Results are listed in **Table 6.3**. Given a threshold value of 0.5, the classifier slightly overestimated the blood region compared with a threshold value of 0.45. This can be due to the non-linear behavior of the neural network or insufficiency of our current training dataset.

6.4.4. Discussion and Conclusion

We expanded IVUS volumes onto brushlet basis functions in an overcomplete fashion and extracted brushlet-based features from cubes corresponding to low frequency components in combination with geometric features and used a neural network as a classifier. The reconstructed blood maps were compared to blood pools quantified with manually traced lumen borders, confirming that the proposed features were sufficiently representative of blood speckle appearance and localization. We also extracted the lumen border based on reconstructed grayscale images masked with the output of the neural network. We achieved promising results although tracking the lumen border depended on thresholding of generated blood maps and we chose the threshold values empirically. Our results demonstrated that such a supervised classification approach might resolve one of the most challenging problems that were detection of lumen borders in vessels with relatively large blood pools (lumen area). As complementary study a fast forward searching approach could also be a solution for finding the most informative cubes. Things that needed further investigation are:

- Combining brushlet derived features with statistical (mean, standard deviation, kurtosis, entropy, etc) and/or textural (homogeneity, contrast, energy, correlation, etc) features.
- Neural network topology.
- Kernel size for feature extraction.
- Performance of different classification algorithms (i.e. SVM).

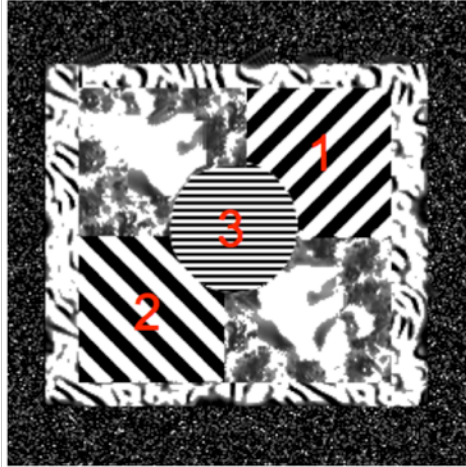


Fig. 6.23. 3-D synthetic image, exhibiting textures with different orientations.

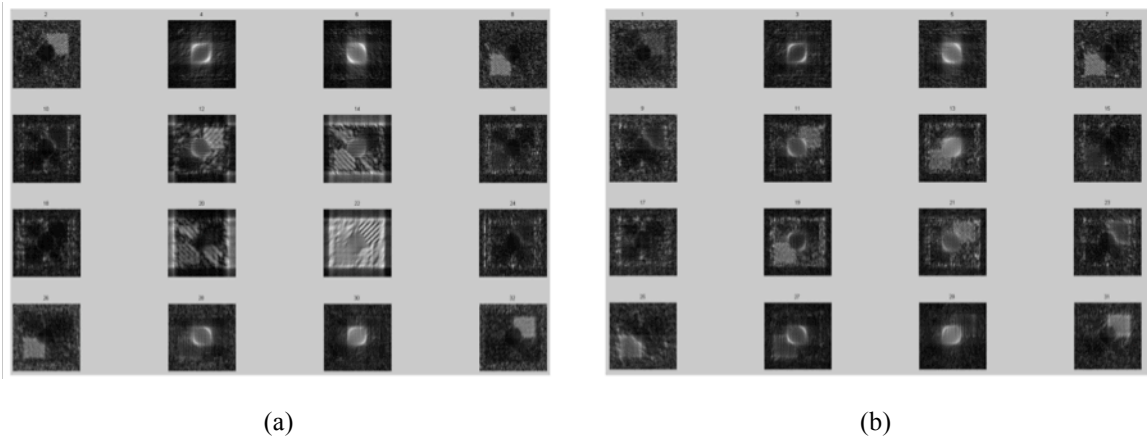


Fig. 6.24. Magnitude of brushlet coefficients in first sub-band (a), and second sub-band corresponding to of 3-D synthetic data in 4x4x2 expansion scheme.

6.5. Visualization of Brushlet Coefficients

In previous performed experiments, there were numbers of factors that needed to be further studied such as tiling the Fourier domain (we mainly employed 4x4x2 expansion scheme), thresholding method (we always selected threshold values empirically), and finding the most informative cubes. In this section, we focus on visualization/enhancement of brushlet coefficients, investigate several textural features extracted from sum and difference histograms computed based on brushlet coefficients.

The basic tenet of volumetric IVUS data expansion onto brushlet basis is that the phase of brushlet analysis function **Eq. 6.1** provides information about the orientation of textural patterns. Given any texture with particular orientation, we can simply expand the data onto brushlet basis and directly extract features from cube(s) that best represent(s) that specific direction. For example, **Figure 6.23** and **Figure 6.24** display a single frame in 3-D synthetic image, exhibiting textures with different orientations, and its magnitude of computed brushlet coefficients in 4x4x2 expansion scheme, respectively. As we can see, features in cubes q_1^1 and q_{16}^1 as well as their correspondence in the second sub-band (higher frequency) q_1^2 and q_{16}^2 explicitly represent patterns corresponding to texture 1. Likewise, features in $q_4^{1,2}$ and $q_{13}^{1,2}$ represent patterns corresponding to texture 2. Although the four inner most cubes (R_1^1 and R_2^1 or $R_{1,2}^1$ or S_1) contain features that represent textures 1 and 2 they also carry out features corresponding to circular patterns in texture 3 and are not as explicit as aforementioned cubes. Therefore, in this particular case, we would extract features from cubes located at higher frequencies.

However, none of structures (plaque, blood, arterial wall, epicardial fat) in IVUS images appear to have unique orientation. Otherwise, we would have expanded the sub-volume of IVUS data and extract features from cubes, representing patterns with orientation of interest. **Figure 6.25** demonstrates real part, imaginary part and magnitude of brushlet coefficients for an arbitrary IVUS frame. The coefficients are anti-symmetric with respect to the origin because IVUS is real valued data.

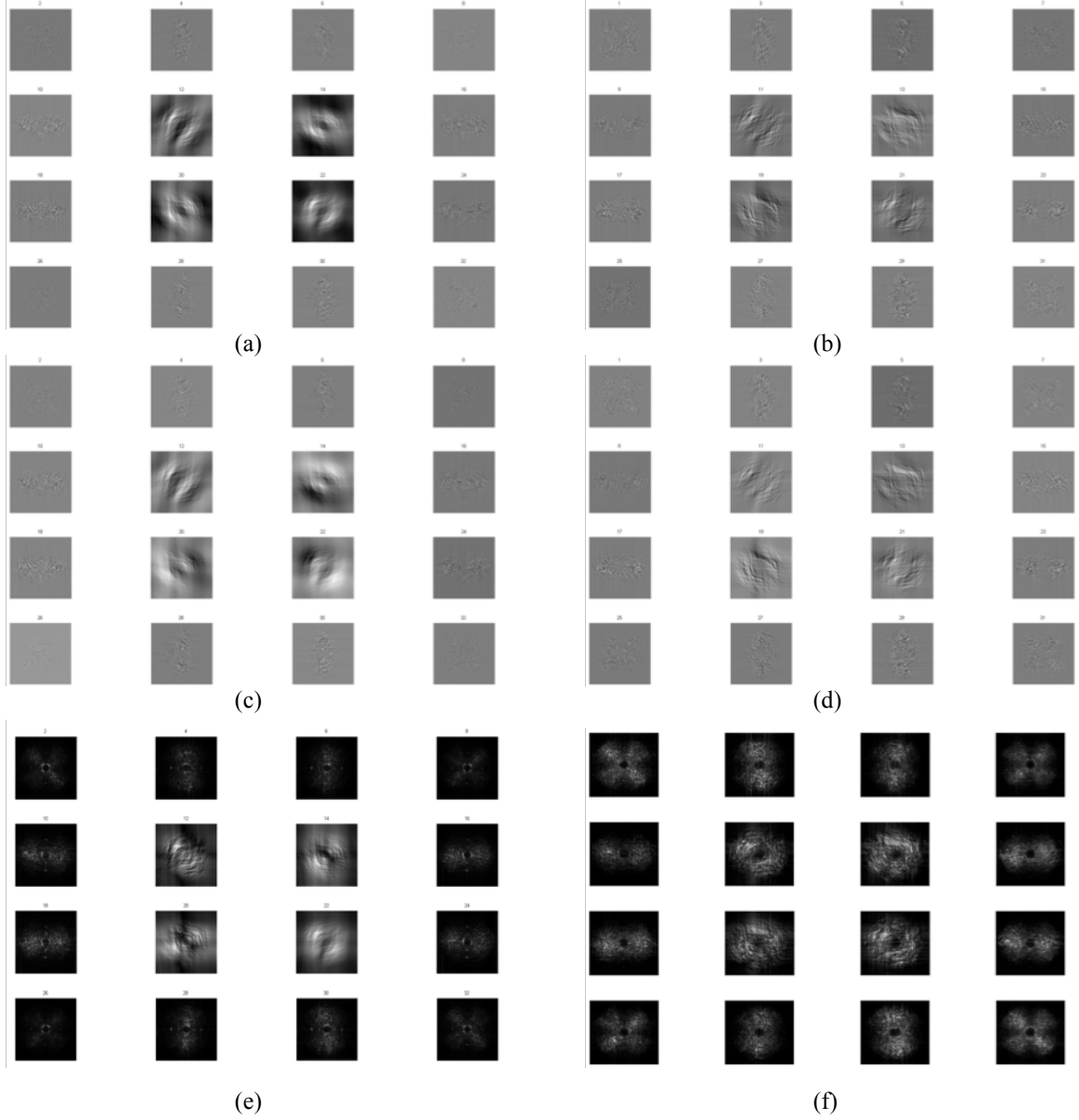


Fig. 6.25. Real part (a,b), imaginary part (c,d), and magnitude (e,f) of brushlet coefficients in the first sub-band (R_1^1 , left column) and the second sub-band (R_1^2 , right column) in 4x4x2 expansion scheme.

Although we may not know precisely which cubes contain the most informative features we can confine our search, presuming that 1) blood speckle is translated to high frequency components in transformed domain due to its noise-like characteristic, 2) the lumen border is smooth and periodic along lateral direction in polar domain. The first presumption implies that the most valuable features might be found in cubes,

representing the low frequency components. The latter suggests a ring of cubes to be searched because they span 360° and enfold all possible orientations so the lumen border can be reconstructed in transformed domain. This can be simply observed by looking at $R_1^{1,2}$ in **Figure 6.25** that displays patterns corresponding to tube's wall or at $q_{2,3,14,15}^{1,2}$ in **Figure 6.24** that represent the circular pattern corresponding to texture 3 in **Figure 6.23**. Precisely speaking, arithmetic manipulation of coefficients might be necessary to reconstruct the feature space of interest, which in this case would be the circular patterns of plaque in Cartesian domain. We will elaborate more on this issue in the next section.

6.5.1. Arithmetic Manipulation of Brushlet Coefficients in Transformed Domain

The ultimate goal of any manipulation of brushlet coefficients is to enrich and suppress plaque and blood textures, respectively. The only constraint is to retain cubes that span 360° so we can preserve all plaque area as well as arterial wall, required for vessel wall border detection, after reconstruction. The linear property of brushlet transform allows us to use arithmetic operations in selected cubes so we can ease the constraint. This can be done by summing up the coefficients in cubes that span 360° . **Figure 6.26** demonstrates the grayscale images resulting from summation of brushlet coefficients, using four and two innermost cubes in $4 \times 4 \times 2$ expansion scheme, along with corresponding enhanced images. The images were acquired from a tube with circulating blood mimicking fluid. We enhanced the coefficients by applying a non-linear operator pixel-wise to the magnitude of each coefficient $I_{enhanced}(x, y, z) = |I(x, y, z)|^\gamma$. We observed that if $\gamma < 1$ and

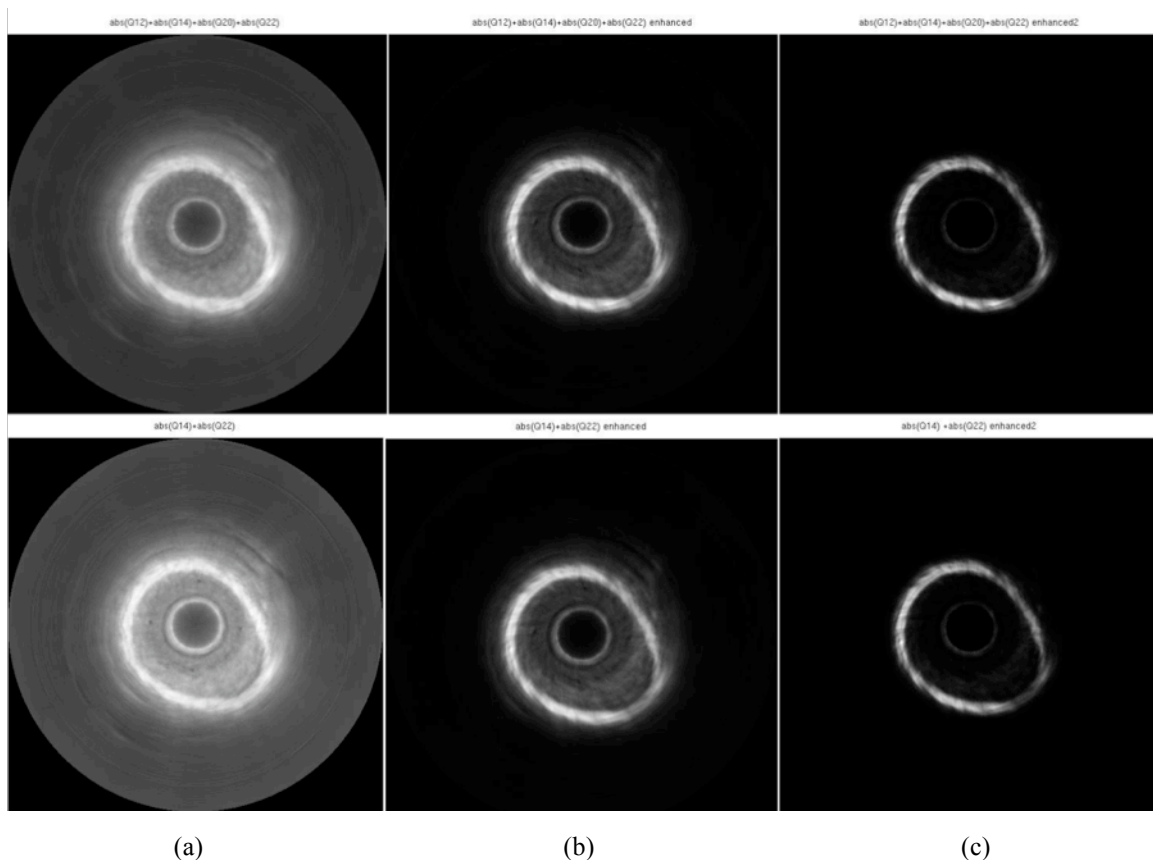


Fig. 6.26. Resulting grayscale images from summation of brushlet coefficients (a) in four (top row) and two (bottom row) innermost cubes in 4x4x2 expansion scheme. Enhanced images using $\gamma = 1.6$ (b) and $\gamma = 2.2$ (c).

$\gamma > 1$ were chosen, textures corresponding to blood speckle were enhanced and suppressed, respectively. As we can see in **Figure 6.26 (b,c)**, the enhancement has been achieved by suppressing blood speckle in simulated lumen area such that the detection of tube's border appears to be easier. Figure 31 also illustrates the enhanced coefficients for all cubes in 4x4x2 expansion scheme corresponding to the original coefficients depicted in **Figure 6.25(e,f)**. **Movie 6.1** demonstrates grayscale images of original *in-vivo* data and corresponding constructed grayscale images of enhanced summed brushlet coefficients in the four innermost cubes in 4x4x2 expansion scheme.

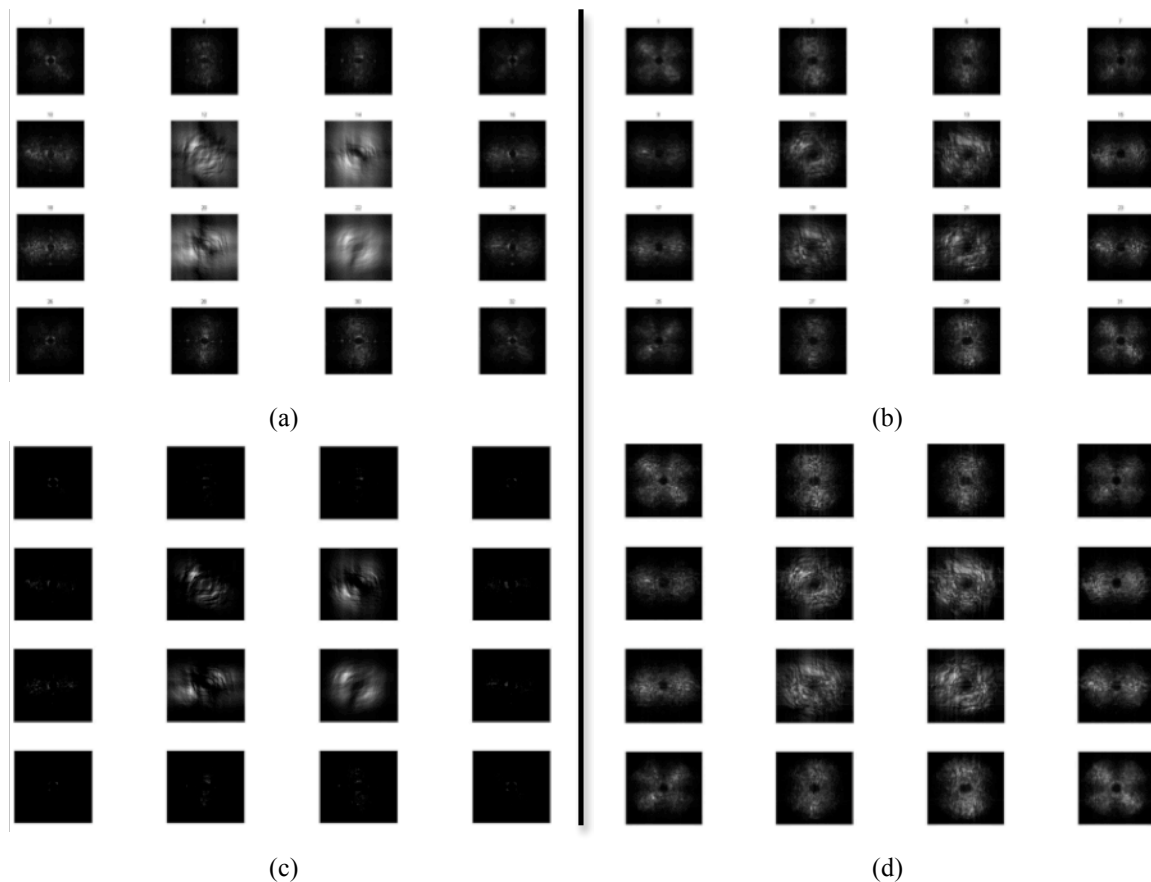
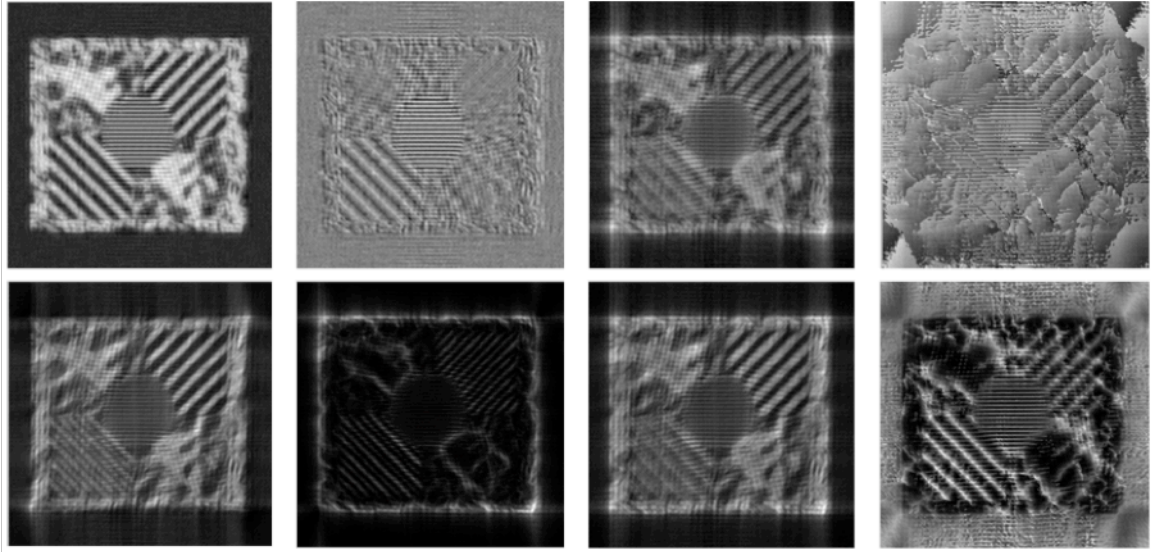


Fig. 6.27. Original grayscale images of brushlet coefficients in $4 \times 4 \times 2$ expansion (a,b) and corresponding grayscale images of enhanced coefficients (c,d).

We also performed the enhancement technique on real part, imaginary part, magnitude and angle of coefficients and the best results were achieved when the magnitude of brushlet coefficients were used, **Figure 6.27**. Such an enhancement seems to be very effective, suppressing blood speckle in lumen area particularly in cubes representing the low frequency components. **Figure 6.28** illustrates the results of the same enhancement technique on real part, imaginary part, magnitude and angle of summed coefficients in the four innermost cubes using synthetic images. As we can see, the enhancement significantly improved the textures particularly when applied on the imaginary part and angle of coefficients.



(a) (b) (c) (d)
Fig. 6.28. Real part (a), imaginary part (b), magnitude (c), angle (d) of summed coefficients in the four innermost cubes in $4 \times 4 \times 2$ expansion scheme (top row) and their corresponding counterparts after enhancement $\gamma = 2$ (bottom row). The original image is depicted in **Figure 6.23**.

As an alternative to the abovementioned non-linear enhancement technique, we also deployed logarithmic transformation on real part, imaginary part, magnitude and angle of coefficients using in-vitro as well as in-vivo data and the results were not of particular interest. Previously, we observed that the best filtering (denoising) results were achieved by thresholding the real part of the brushlet coefficients. Therefore, we decided to employ logarithmic transform and investigate the enhancement results. We made the real part of the brushlet coefficients positive (ignoring the imaginary part), took the magnitude and applied the logarithmic transform but no significant improvement was achieved.

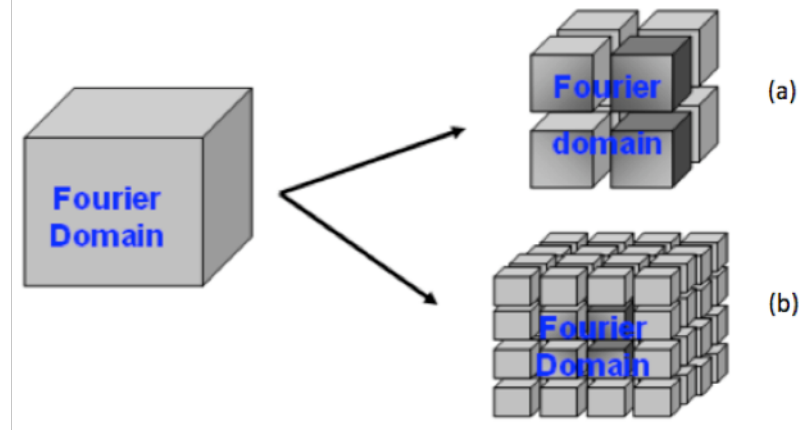


Fig. 6.29. Schematic representation of arbitrary tiling of Fourier space using $2 \times 2 \times 2$ cubes (a) $4 \times 4 \times 4$ cubes (b) in u_x, u_y, u_z directions.

6.6. Incremental/Decremental Expansion and Reconstruction of IVUS Sub-Volumes

So far, we only projected sub-volumes of IVUS data onto brushlet basis using $4 \times 4 \times 2$ expansion scheme. In this section, we study the effects of different tiling schemes, and try to tease out as much information as possible from cubes representing low frequency components. The overcomplete nature of analysis is desirable in isolating blood speckles and detecting lumen border due to stringent behavior of IVUS signals especially when high frequency transducers (40 MHz up) are used. Moreover, we can preserve numbers of coefficients at each level of analysis equal to the original dimension of sub-volume of analysis and ensure the existence of a direct homomorphism between the data and transform domains. Such redundant representation of original data in multiscale analysis makes the analysis shift invariant, which is suitable for segmentation purpose.

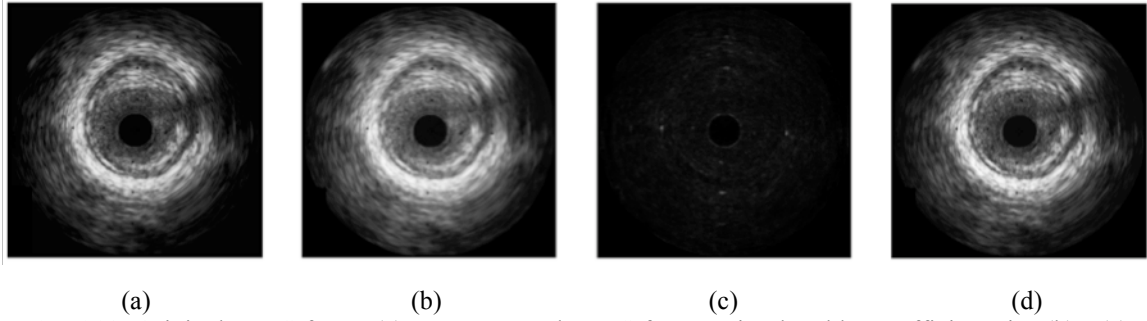


Fig. 6.30. Original IVUS frame (a), reconstructed IVUS frame using brushlet coefficients in (b), (c) and (d) in 4x4x2 expansion scheme.

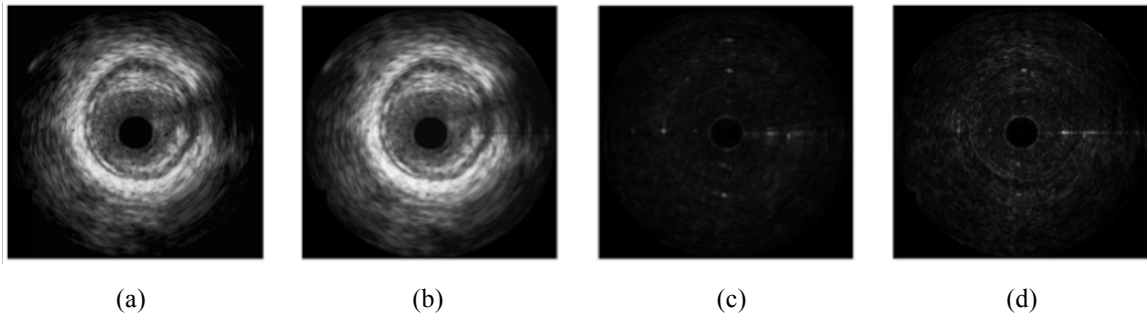


Fig. 6.31. Original IVUS frame (a), reconstructed IVUS frame using brushlet coefficients in (b), (c) and (d) in 6x6x2 expansion scheme.

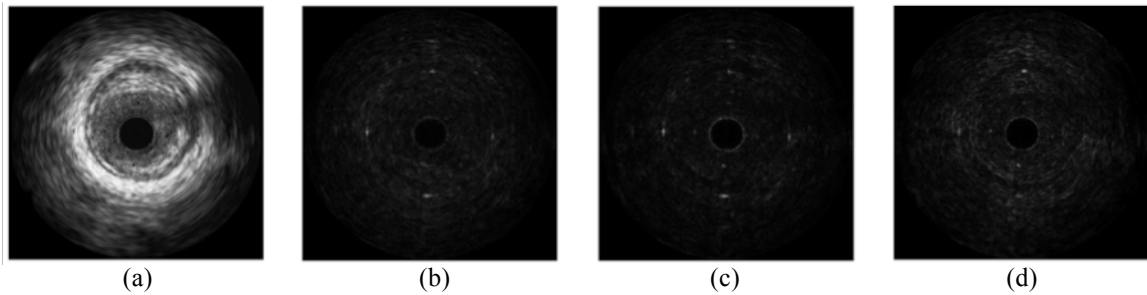


Fig. 6.32. Reconstructed IVUS frame using brushlet coefficients in (a), (b), (c), and in 8x8x2 expansion scheme. Corresponding original IVUS frame is depicted in Figure 6.30(a) and Figure 6.31(a).

Here, we strive to answer to two main questions: 1) what would be the best tiling scheme to analyze IVUS data and remove blood speckle or detect lumen border? and 2) where the most valuable features are located in Fourier space? As shown in **Figure 6.29**, tiling of the Fourier space determines the resolution of analysis in terms of angular directions. More numbers of cubes corresponds to more directions and therefore higher resolution in frequency domain at the costs of lower spatial resolution. Meyer and Coifman [131]

developed an algorithm to find the optimal tiling of the Fourier domain based on some cost function for recursive quadtree decomposition to compromise between spatial and frequency resolutions with respect to the content of the data.

Due to noisy behavior of blood speckles, we had hypothesized that blood textures are translated into high frequency components so we often reconstructed IVUS sub-volumes using thresholded coefficients in cubes that contained low frequency - DC - components. **Figure 6.30** illustrates an individual reconstructed IVUS frame from selected brushlet coefficients in $R_1^{1,2}(S_1)$, $R_2^{1,2}(S_2)$ and $R_{1,2}^{1,2}(S_{1,2})$ without any thresholding. As we can see, a large amount of energy is concentrated in $R_1^{1,2}$ and reconstructed frame using this ring is similar to the original frame except it is somewhat blurred. In this case, brushlet coefficients in $R_2^{1,2}$ do not appear to be of particular interest. However, we need to validate this by processing the IVUS sub-volumes with different expansion schemes of Fourier space with finer tiling of cubes representing low frequency components. **Figure 6.31** and **Figure 6.32** demonstrate the same IVUS frame, reconstructed from coefficients in different rings (spheres) without any thresholding using 6x6x2 and 8x8x2 expansion schemes.

Finer tiling along u_x and u_y directions, resulting lower spatial resolution after reconstruction, **Figure 6.33**. It is also apparent that as we go toward outer spheres (rings), higher frequency components appear and the overall energy decreases. This can be seen in **Figure 6.34**, when the low frequency components are localized in $R_1^{1,2}(S_1)$ using 64x64x2 expansion scheme. Although finer resolution in Fourier space was used the

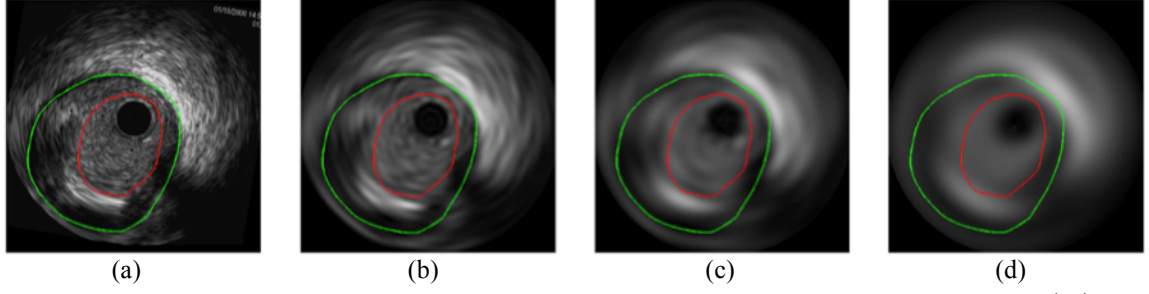


Fig. 6.33. Original IVUS frame (a), reconstructed IVUS frame using coefficients in $R_1^{1,2}(S_1)$ in $32 \times 32 \times 2$ (b), $64 \times 64 \times 2$ (c), and $128 \times 128 \times 2$ (d) expansion schemes. Vessel wall and lumen borders have been traced by green and red colors, respectively.

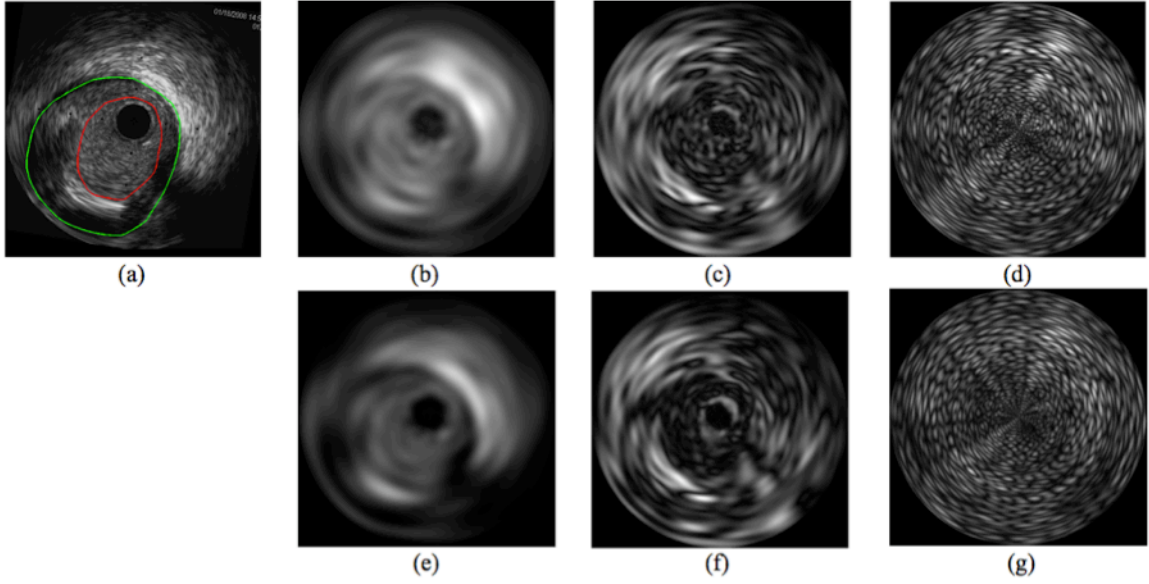


Fig. 6.34. Original IVUS frame (a), grayscale images of summed brushlet coefficients in S_1 (b) S_2 (c) S_3 using $64 \times 64 \times 2$ expansion scheme and corresponding reconstructed IVUS frames in spatial domain.

results demonstrated that the innermost cubes contain majority of energy of IVUS data.

In the rest of this section we introduce a systematic approaches to further investigate the localization of energies in cubes representing low frequency components using incremental and decremental expansions along with reconstruction.

We often observed that reconstructed IVUS sub-volumes using innermost spheres remove some high frequency content. This can be noticed by comparing **Figure 6.34(c)** and **Figure 6.34(f)**. For better delineation of borders, higher degree of expansion is

needed. This is achieved by increasing the resolution along each direction in Fourier domain (n, m, p) . However, this increases computational complexity, causes more distortion in reconstructed volumes and hardens the analysis and observation of coefficients in cubes. In order to prevail these limitations, we implemented an iterative method in order to tease as much information as possible from cubes that preserve low frequency components.

6.6.1. Iterative Expansion and Reconstruction

Experiment #1

Figure 6.35, displays schematic of an iterative method such that sub-volume of IVUS images projected onto brushlet basis and cubes preserving low frequency components are further decomposed iteratively. The purpose of such experiment was to remove high frequency components at each level of decomposition and retrieve features as close as possible to DC components. The algorithm is performed as described below:

1. Apply brushlet transform to the IVUS sub-volume.
2. Reconstruct the IVUS sub-volume using selected cubes (i.e. rings or spheres) particularly those that contain low frequency components (i.e. S_1).
3. Apply brushlet transform again to the reconstructed IVUS sub-volume.
4. Repeat steps 2 and 3 until the desired level of information is reached.

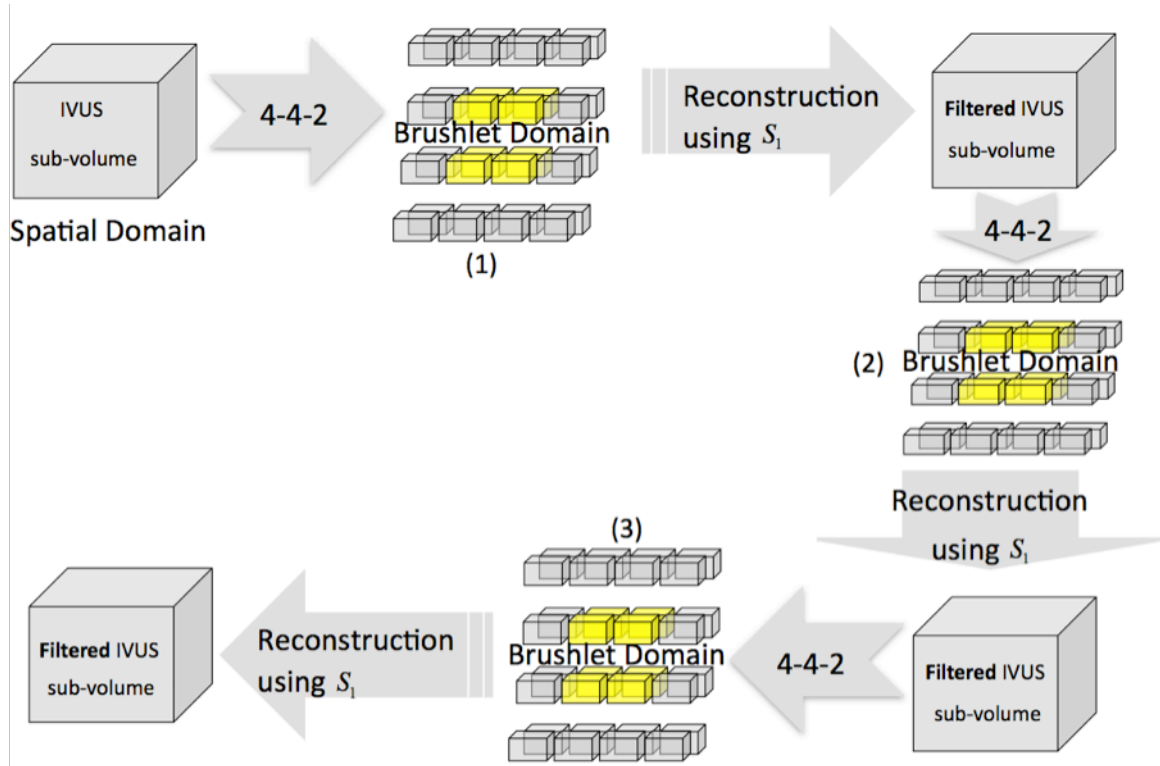


Fig. 6.35. Iterative projections of the innermost spheres, corresponding to low frequency components, using 4x4x2 expansions scheme.

Figure 6.36, illustrates the magnitude of extracted coefficients at each level of decomposition.

Results show that the proposed approach provides deeper observations of cubes preserving low frequency components. In order to make the proposed approach more flexible and to allow even deeper analysis, we modified the algorithm and increased the tiling resolution at each level of decomposition, **Figure 6.37**.

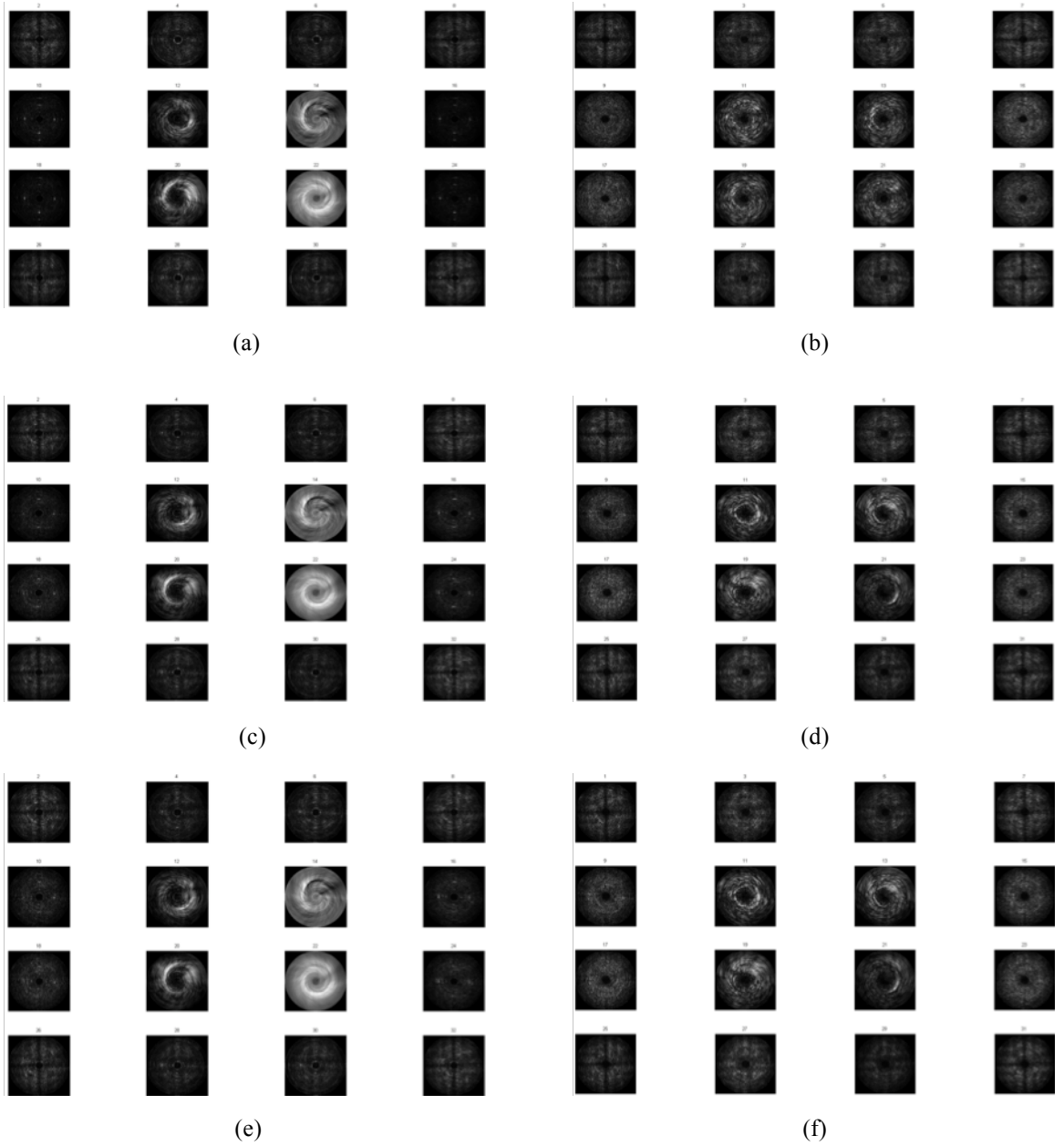


Fig. 6.36. Magnitude of computed brushlet coefficients derived from iterative decomposition of the innermost spheres that preserve low frequency components. Magnitude of coefficients in the first (a) and the second (b) subband after the first decomposition (the first level). Magnitude of coefficients in the first (c) and the second (d) subband after the second decomposition (the second level). Magnitude of coefficients in the first (e) and the second (f) subband after the third decomposition (the third level).

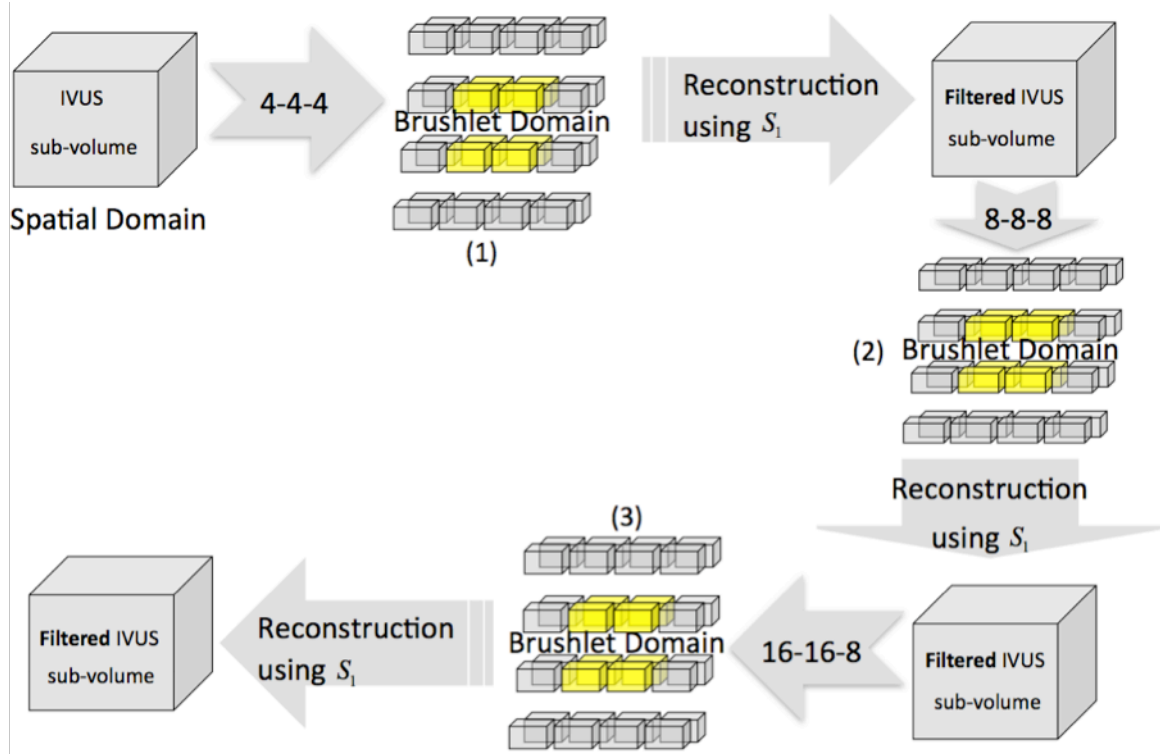


Fig. 6.37. Iterative projections of the innermost spheres, corresponding to low frequency components. Unlike previous approach the resolution of tiling was fixed, here the resolution is increased at each level of decomposition.

Experiment #2

1. Apply brushlet transform to the IVUS sub-volume.
2. Reconstruct the IVUS sub-volume using selected cubes (i.e. rings or spheres) particularly those that contain low frequency components (i.e. S_1).
3. Apply brushlet transform on reconstructed IVUS sub-volume and increase the resolution of tiling in Fourier domain.
4. Repeat steps 2 and 3 until the desired level of information is reached.

We performed abovementioned decomposition/reconstruction technique on sub-volume of IVUS frames and at each level of decomposition we increased the resolution of tiling

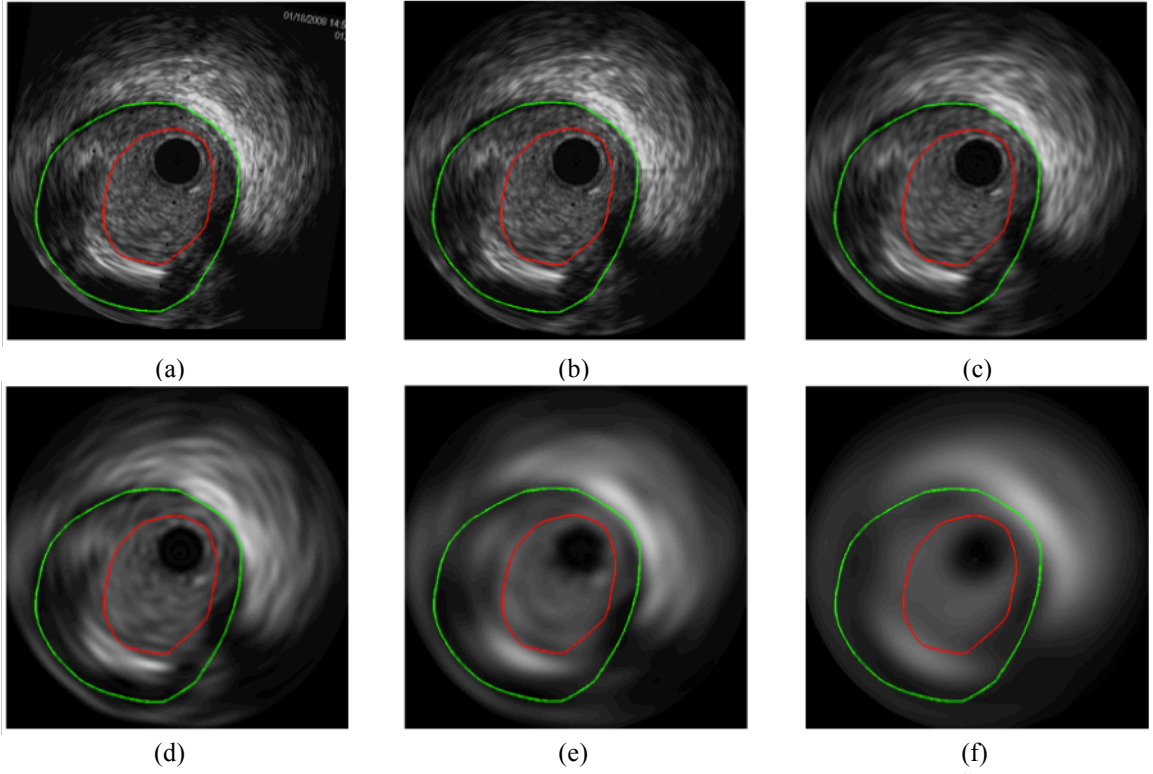


Fig. 6.38. Original IVUS frame (a), reconstructed IVUS frame using coefficients in S_1 in $8 \times 8 \times 2$ (b), $16 \times 16 \times 2$ (c), $32 \times 32 \times 2$ (d), $64 \times 64 \times 2$ (e), and $128 \times 128 \times 2$ (f) expansion schemes.

with power of two along u_x and u_y directions while the resolution along u_z was kept constant. **Figure 6.38** shows the reconstructed IVUS frames at each level of decomposition. Our results show that high frequency components were removed step by step at each level of decomposition since coefficients in S_1 were deployed. Moreover, the IVUS frames become smoother (i.e. contain less speckle) when higher resolution of tiling is applied. The results exhibit potential application of various segmentation methods (i.e. region growing) and/or edge detection algorithms for lumen border detection. We repeated the same experiment but at each level of decomposition we only used coefficients in R_1^1 instead of $R_1^{1,2}(S_1)$. Comparing results in **Figure 6.38** and **Figure 6.39**, we realized that some edges were appeared well when coefficients in R_1^1 were employed in addition to lesser computational complexity.

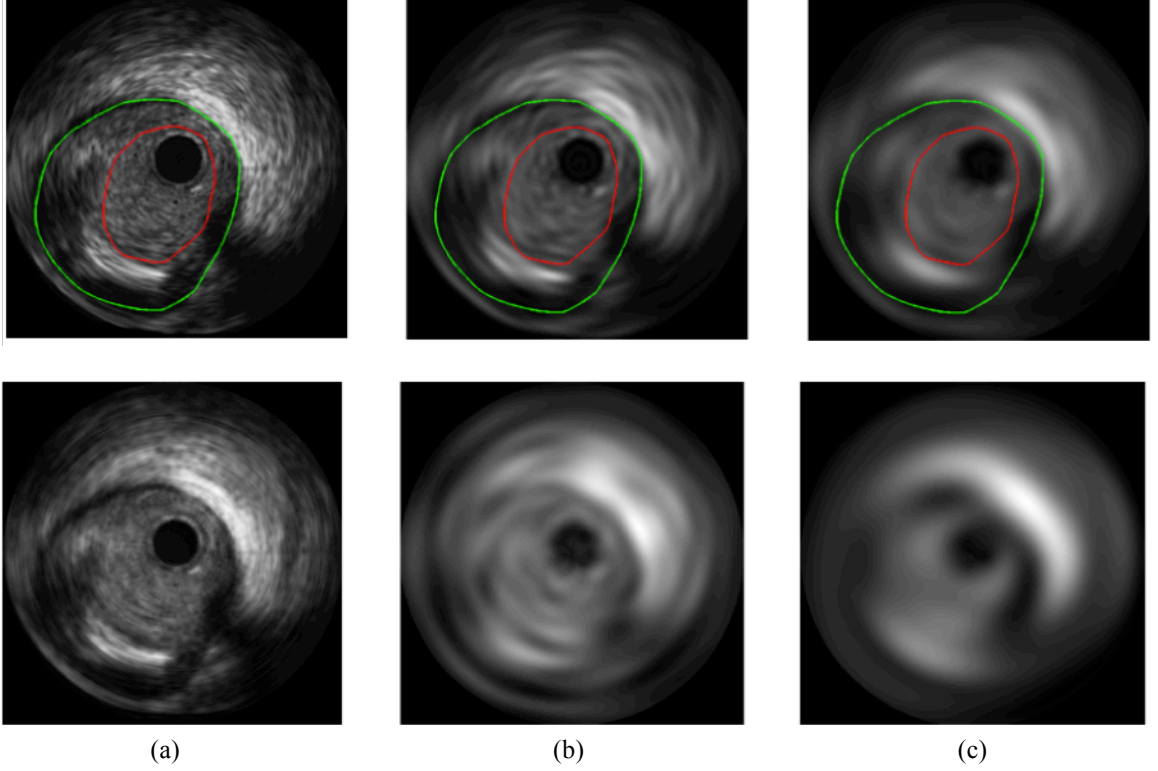


Fig. 6.39. Reconstructed IVUS frame using coefficients in S_1 (top row) and R_1^l (bottom row) in $8 \times 8 \times 2$ (a) $64 \times 64 \times 2$ (b) and $128 \times 128 \times 2$ (c) expansion schemes.

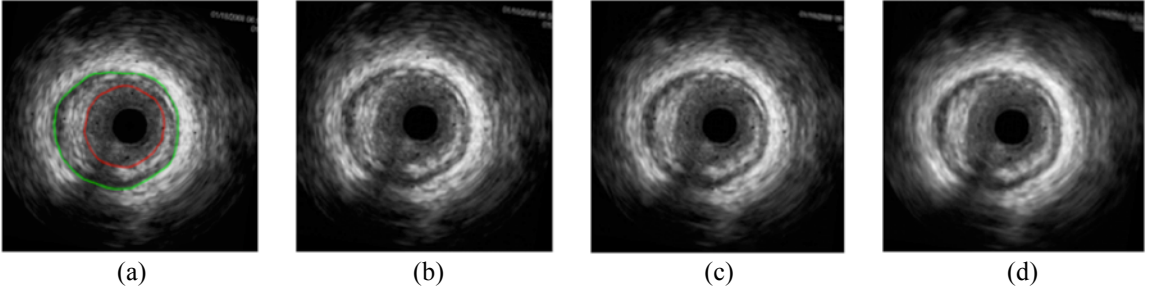


Fig. 6.40. Original IVUS frame (a), reconstructed frame using coefficients in S_1 in $8 \times 8 \times 2$ (b), $8 \times 8 \times 4$ (c) and $8 \times 8 \times 8$ (d) expansion schemes.

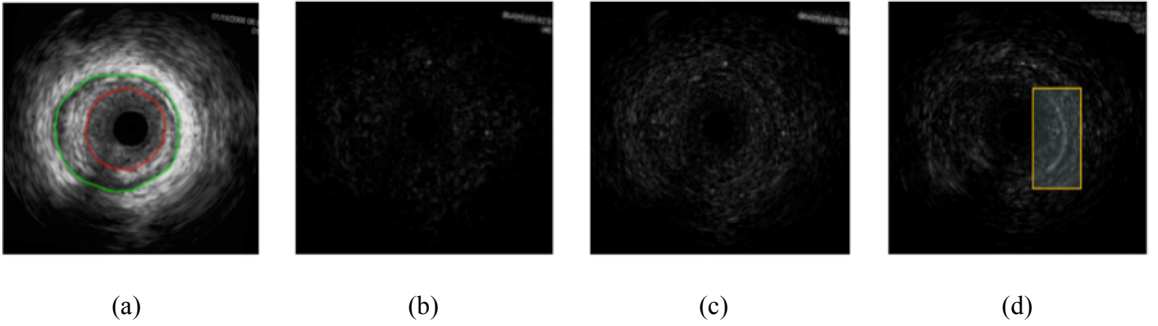


Fig. 6.41. Original IVUS frame (a), reconstructed frame using coefficients in S_2 in $8 \times 8 \times 2$ (b), $8 \times 8 \times 4$ (c) and $8 \times 8 \times 8$ (d) expansion schemes. The highlighted rectangle shows that some border information can be extracted from high frequency cubes (S_2) when u_z is increased.

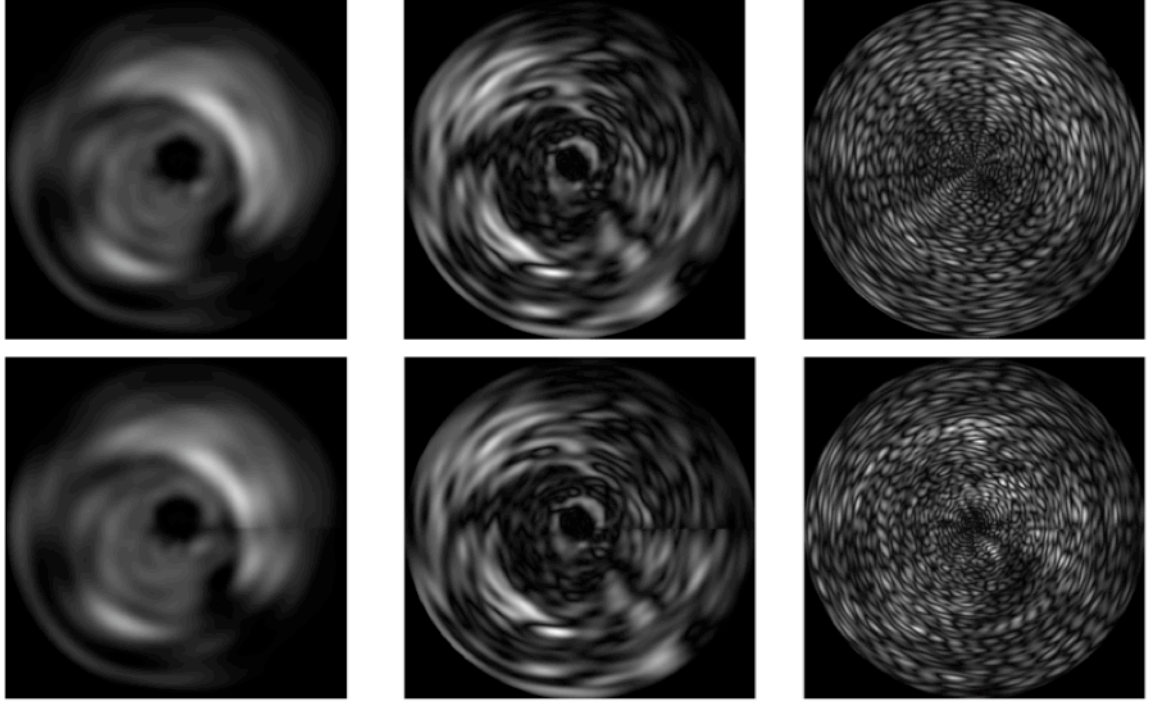


Fig. 6.42. Reconstructed IVUS frames through direct (top row) and iterative (bottom row) decomposition techniques using coefficients in S_1 , S_2 , and S_3 in $64 \times 64 \times 2$ expansion scheme.

Experiment #3

Finally, we studied the effects of tiling resolution along u_z direction in Fourier domain.

Figure 6.40 and **Figure 6.41** demonstrate reconstructed IVUS frames from coefficients in S_1 and S_2 , respectively, while resolution of tiling is increased along pullback direction. As we can see in **Figure 6.40**, when resolution of tiling is increased, reconstructed images become blurred. This could be due to the fact that IVUS frames within sub-volume of analysis were not perfectly registered.

Experiment #4

We also compare resulting reconstructed frames from direct and iterative decomposition schemes, described in *experiment #2*. **Figure 6.42** displays resulting reconstructed IVUS

frames from both techniques. The obvious difference is that the iterative approach provides results with a bit more details. This can be particularly visible in reconstructed images at 360° .

6.7. Summary and Discussion

We performed numbers of experiments in order to extract features as close as possible to DC component and study the effects of different tiling schemes. We presented two iterative methods to tease out features as close as possible to low frequency components. In the first method, we kept the resolution of tiling constant at each level of decomposition while in the second method the resolution was increased along u_x and u_y directions. Our results from both method demonstrated that a large amount of energy was preserved in cubes representing low frequency components and cubes containing high frequency components did not provide any useful features visually. In order to verify energy localization particularly in the innermost cubes, we need to come up with a quantitative approach to compute energy in rings or spheres at each level of decomposition. We also started tiling the Fourier space along u_x and u_y directions using 4×4 cubes and increased the resolution by 32 folds. In all expansion schemes, the innermost cubes provided the most informative features. Furthermore, enhancement techniques, as describe in previous section, could be used to investigate extracted features in cubes representing high frequency components at each level of decomposition.

Increasing the tiling resolution in Fourier space resulting more blurred reconstructed images in spatial domain. Segmentation or edge detection algorithms might be used to detect borders. In this case, detection of vessel wall border is more feasible since adventitia appears as a large and bright region. We selectively chose coefficients in particular cubes and compared resulting grayscale images in brushlet domain with corresponding ones in spatial domain. Some of the results were interesting in a sense that lumen area exhibited less speckles, choosing coefficients in particular cubes, **Figure 6.34(c,f)**. We increased the resolution of tiling along pullback direction and observed that the resulting reconstructed images became more blurred since images within sub-volume of analysis were not perfectly registered.

7. Chapter Seven:

AUTOMATIC DETECTION OF LUMINAL BORDERS IN IVUS IMAGES BY MAGNITUDE-PHASE HISTOGRAMS OF COMPLEX BRUSHLET COEFFICIENTS

In previous chapter, we projected the IVUS sub-volume of grayscale images onto brushlet basis and took advantage of orientation selectivity of expanded volumes in complex transformed domain to either threshold the coefficients or remove high frequency components followed by reconstruction. In this chapter, we look at the analysis from different perspective and study one of the most important characteristics of such analysis that has not been considered by any group before. We will present a technique, which has a great potential to be employed in any complex domain (*i.e.* wavelet, brushlet) to study behavior of computed coefficients and manipulate them.

We present a new framework to delineate lumen borders in intravascular ultrasound (IVUS) volumes of images acquired with a high-frequency Volcano (Rancho Cordova, CA) 45MHz transducer. Through selective projection of IVUS sub-volumes images and their Fourier transforms, tissue-specific backscattered magnitudes and phases identified within brushlet coefficients. We take advantage of such characteristics and construct 2.5-

dimensional (2.5-D) magnitudes-phase histograms of coefficients in the transformed complex brushlet domain that contain distinct peaks corresponding to blood and non-blood regions. We exploit these peaks to mask out coefficients that represent blood regions and ultimately detect the luminal border after spatial regularization employing surface function actives (SFA). We perform our algorithm on both phantom as well as *in vivo* data, acquired with different transducers (40MHz, and 45MHz), and quantify results by comparing them to manually traced borders by an expert. As a complementary study, we evaluate the performance of developed algorithm with two of existing lumen detection techniques. Our results show the potential application of this framework for isolating coherent structures (*i.e.* plaque) from incoherent (*i.e.* blood) ones particularly in IVUS pullbacks and detecting of lumen border.

7.1. A Brief Review on Existing IVUS Lumen Border Detection Algorithms

Often patients with chest pain and high cardiac risk factors undergo PCI procedures. As a result, a catheter is inserted from the femoral artery toward potential sites of coronary occlusions to open up blocked artery with a stent or inflating a balloon. An interventional cardiologist may also deploy an IVUS catheter to acquire cross sectional images of arterial walls and atherosclerotic plaque structures. During such a procedure, hundreds to thousands of IVUS images are recorded. Therefore automatic detection of vessel wall (media-adventitia) and luminal borders has become a subject of study for the following

two reasons. First, one important parameter during angioplasty or stent implantation procedure, is the ratio of lumen to artery cross sectional area for stenosis regions. For instance, the interventional cardiologist uses these measurements to select the appropriate type, length and diameter of a stent. Secondly, vessel walls and lumen contours are required to be traced prior to tissue characterization and plaque RF signals extraction. These have motivates researchers to develop different algorithms that each can be categorized based on its application, domain of analysis, transducer center frequency, dimensionality, and employed technique as listed in **Table 7.1**.

Table 7.1. List of some of existing border detection algorithms in IVUS images and their specifications.

Authors, [Ref.#]	Implementation Technique	Application	Domain of Analysis	Transducer Center Frequency (MHz)
Sonka <i>et al.</i> [127]	2D graph search	Vessel wall and Lumen	Cartesian	30
Shekhar <i>et al.</i> [138]	3D deformable model	Vessel wall and Lumen	Cartesian	30
Plissiti <i>et al.</i> [136]	2D deformable model	Vessel wall and Lumen	Cartesian	30
Cardinal <i>et al.</i> [126]	3D PDF-based fast marching	Vessel wall and Lumen	Polar	20
Unal <i>et al.</i> [128]	2D/3D statistical shape model	Vessel wall and Lumen	Polar	20
Gil <i>et al.</i> [139,140]	2D Probabilistic approach	Vessel wall or Lumen	Cartesian	40
Taki <i>et al.</i> [141]	2D Probabilistic approach	Vessel wall and Lumen	Cartesian	20
Hibi <i>et al.</i> [142]	3D spatio/temporal analysis	Blood speckle reduction	Polar	40
Ballocco <i>et al.</i> [143]	3D spatio/temporal analysis	Blood speckle reduction	Cartesian	30
Katouzian <i>et al.</i> [144]	3D Multiscale Brushlet analysis	Blood speckle reduction	Polar	45
Rotger <i>et al.</i> [145]	3D, Adaboost classifier	Blood detection	Longitudinal Cut	Unknown
O'Malley <i>et al.</i> [146]	3D spatio/temporal/spectral analysis and support vector machine (SVM)	Blood detection	Polar	40
Katouzian <i>et al.</i> [147]	3D Multiscale Brushlet analysis and neural network	Blood detection	Polar	45

As we can see, there are three main approaches: 1) direct detection of border(s), 2) blood speckle reduction as a preprocessing step prior to border detection, and 3) classification of blood versus non-blood regions. For example, authors in [126-128] directly detect vessel wall and lumen borders, employing, fast-marching algorithm with gray level probability density functions (PDFs) of arterial wall structures, heuristic graph search technique on edge sets, and statistical shape models through principle component analysis (PCA), respectively. Authors in [139,140] deployed probabilistic models to detect one of the borders and later refined the results using regularized curvature flow and anisotropic processing technique along with statistical classification methods [148,149]. In a similar approach, Taki *et al.* [141] deployed affine invariant anisotropic filters for preprocessing and used global statistical properties of gray level intensities to detect both borders.

Generally speaking, detection of vessel wall borders is less difficult than lumen borders since the vessel media consists of smooth muscle cells and does not reflect IVUS signals. It therefore appears as a dark region on IVUS images, which can be used as a marker to detect the vessel wall. In contrast, due to high scattering from red blood cells inside the lumen, detection of a luminal border is a more formidable challenge especially when a high-frequency transducer is used. Comparing IVUS ultrasound probes, the lumen border is better depicted in images acquired with a 64-element phased-array 20 MHz transducer in comparison with those acquired with a single-element mechanically rotating 45 MHz transducer. At higher center frequency spatial resolution is improved, at the cost of more scattering from red blood cells inside the lumen. **Figure 6.1** illustrates four distinct cross-sectional grayscale IVUS images acquired with 64-elements phased-array 20MHz,

single-element 30 MHz, 40 MHz, and 45 MHz transducers. As an alternative approach, researchers strived to look at detection of luminal border from different perspective. They either tried to alleviate blood speckle effects [142-144] as a preprocessing step or to detect blood regions through supervised classification methods [145-147].

In any case, clinical applications of automated segmentation methods have seen limited success due to intrinsic (presence of guide wire, presence of calcified plaque, presence of side branch, motion of catheter and heart) and extrinsic (system parameter specifications such as time gain compensation, compression) challenges associated with data acquisition. For example, presence of guide wire, arc of calcified plaques, and side branch significantly affects algorithm performance particularly when deformable models are employed [126,136,138-141,144,147-149]. On the other hand, variability among system specifications or change of acquisition parameters by experts would lead to inconsistency among data sets so that supervised techniques [128,145-147,149], knowledge based methods [127], or those that are rely on statistical properties of gray level intensities [139-141] may not perform efficiently.

7.2. Methodology

7.2.1. Motivations

We design our framework upon what interventional cardiologists often do while tracing the lumen border manually. They usually go back and forth among consecutive frames to be able to visually locate the lumen contour on a single frame. By doing so, blood speckle and plaque embody visually incoherent and coherent spatial patterns, respectively, suggesting a 3-D processing approach. Hence, we design our framework upon multi-scale analysis of textural features, which is the most compatible analysis to human and mammalian vision processing systems due to its conservation of energy in both spatial and frequency domains [113,114]. We will take advantage of the spatial-frequency-localized expansions such as brushlet analysis and their generalization to 3-D to discern the textural patterns on constructed images from backscattered IVUS signals. One of the major advantages of expansion of IVUS sub-volumes onto orthogonal brushlet basis functions is that it is invariant to intensity so that the extracted brushlet coefficients do not depend on intensity but spatial frequency content of IVUS signals. In addition, the brushlet is a well-localized complex valued function in time and frequency domains that is suitable for analyzing the local frequency content of IVUS signals and offers an orthogonal transform of the Fourier coefficients which are Hermitian-symmetric so the phase information might also be used in IVUS image filtering and eventually detection of lumen border.

Our technique was primary developed for images acquired with single-element 45 MHz VOLCANO transducers but later employed for detection of luminal borders in images

obtained with 40 MHz transducers. The IVUS grayscale images were acquired *in vivo* as described in section 3.2.1.

7.2.2. IVUS Signal Modeling in Fourier Domain and Sources

Assumptions

In chapter 6, we reviewed the multiscale brushlet analysis and explained how the phase of brushlet function provides useful information about orientation of the brushlet so we could characterize textures with specific directions, frequencies, and locations. We further described how to project any signal onto brushlet basis indirectly using its Fourier transform, **Eq. 6.3**, which in our case would be the Fourier transform of IVUS signal. We establish our framework by hypothesizing that distinct responses coming from blood and non-blood tissues may be reflected by differences among magnitudes and phases of brushlet coefficient values. Consider the measurements of an IVUS transducer during pullback. In this case, each acquisition line, f , contains information regarding tissues as well as flowing blood and can be represented in transformed domain as follows:

$$\hat{f}_{n,j} = \sum_n \sum_j \alpha_{n,j} e^{-i\omega\varphi_{n,j}} \hat{s} \quad (7.1)$$

where $\varphi_{n,j}$ and $\alpha_{n,j}$ are the resulting phase and amplitude of tissue response \hat{s} to IVUS signal. Using **Eq. 7.1** we rewrite **Eq. 6.3** and obtain:

$$\sum_n \sum_j \alpha_{n,j} e^{-i\omega\varphi_{n,j}} \hat{s} = \sum_n \sum_j \lambda_{n,j} u_{n,j} \quad (7.2)$$

We call two functions s_1 and s_2 disjoint orthogonal if the frequency supports of their Fourier transforms, \hat{s}_1 and \hat{s}_2 , are disjoint. In other words the point-wise product:

$\hat{s}_p \cdot \hat{s}_q = 0, \forall p \neq q, \forall N$. This is a legitimate assumption in our IVUS application because each frequency bin is a function of only and only one tissue's response, which in our case would be blood or non-blood. Since brushlet basis are orthonormal, we can reorganize Eq. 4 in the following form:

$$\lambda_{n,j} = \sum_n \sum_j \left\langle \alpha_{n,j} e^{-i\omega\varphi_{n,j}} \hat{s}_{n,j}, u_{n,j} \right\rangle \quad (7.3)$$

where \langle , \rangle denotes the inner product. Looking at **Eq. 7.3**, we realize that the phase of brushlet functions results in orientation selectivity in transformed space when separable tensor product is used while image phases and amplitudes associated with tissue responses are proportionally preserved in brushlet coefficients. We further hypothesize that the magnitude and phase of brushlet coefficients provide informative features for coherent (non-blood) and incoherent (blood) patterns so we can estimate the lumen border in transformed domain via selection of specific clusters of phases-magnitudes combinations avoiding any thresholding and reconstruction. In the rest of this section we present a classification framework to associate frequency-based clusters of brushlet coefficients with each tissue type (blood or non-blood).

7.2.3. Construction of 2.5-D Magnitude-Phase Histogram in Brushlet Space

Due to homomorphism between the original domain of acquisition (spatial domain) and brushlet space, there is a unique correspondence between a signal and its brushlet transform. Once the IVUS sub-volumes of size (X,Y,Z) are projected onto brushlet basis, we end up with sub-volumes of brushlet coefficients in the transformed domain. As we

described in previous chapter, the coefficients in the innermost cubes, representing the low frequency components, contained the most informative features regarding blood and non-blood textures. The overcomplete representation of brushlet coefficients guaranties a bi-jection within and among each expansion sub-volume and a one-to-one correspondence of the coefficients across sub-spaces of the expansion. Hence, we can sum up the coefficients in the innermost cubes to span 360° of spatially oriented information and construct the complete arterial wall and plaque in transformed domain.

Taking the union of summed coefficients $\hat{F} = \bigcup_{k=1}^{X \times Y} \alpha_k e^{-i\varphi_k}$, we can write:

$$\hat{F}(r, \theta) = \alpha(r, \theta) e^{-i\varphi(r, \theta)}, r = 1, \dots, X, \theta = 1, \dots, Y \quad (7.4)$$

The magnitude and phase associated with each coefficient can be written as:

$$(\alpha(r, \theta), \varphi(r, \theta)) = \left(\left| \hat{F}(r, \theta), \angle \hat{F}(r, \theta) \right| \right) \quad (7.5)$$

A 2.5-D histogram can be constructed for every pair of $(\alpha(r, \theta), \varphi(r, \theta))$ in (α, φ) space as follows. First, we define a mask for (α, φ) :

$$M_{\alpha, \varphi, \Delta_\alpha, \Delta_\varphi}(r, \theta) = \begin{cases} 1 : & \begin{cases} |\ln \alpha(r, \theta) - \ln \alpha| < \frac{\Delta_\alpha}{2} \\ |\varphi(r, \theta) - \varphi| < \frac{\Delta_\varphi}{2} \end{cases} \\ 0 : & o.w. \end{cases} \quad (7.6)$$

We are taking the difference between computed magnitude and phase of brushlet coefficients, $\alpha(r, \theta)$ and $\varphi(r, \theta)$ within $\Delta_\alpha/2$ of α and $\Delta_\varphi/2$ of φ in the histogram, respectively, where Δ_α and Δ_φ are the magnitude and phase resolution widths of the histogram. Then, we can define the histogram as below:

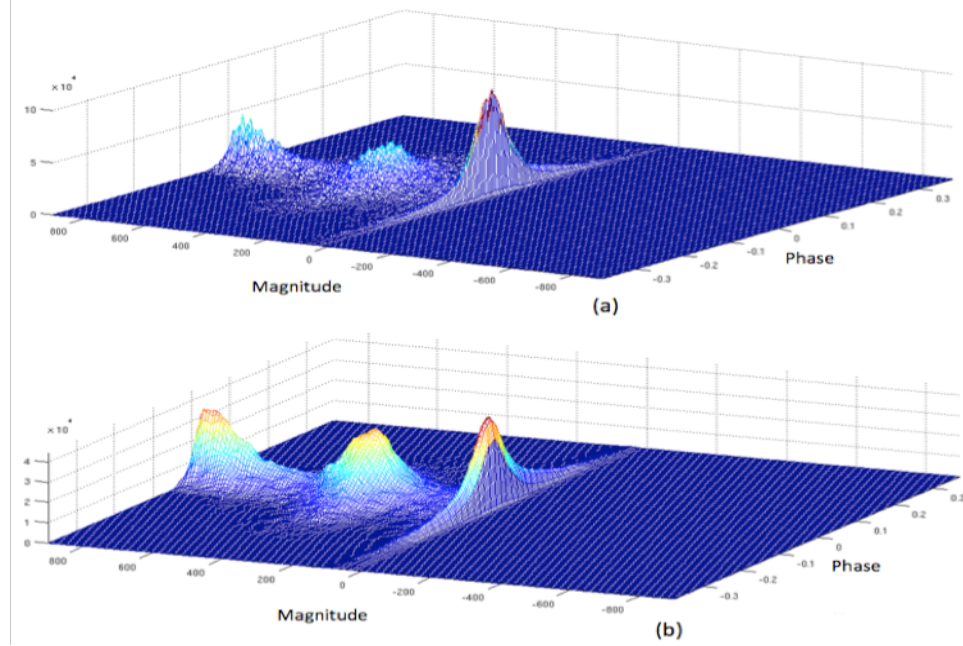


Fig. 7.1. Constructed magnitude-phase 2.5-D histogram from summed coefficients in R_l^1 after projection of in-vitro IVUS sub-volume using $4 \times 4 \times 2$ expansion scheme before (a) and after (b) smoothing. The resolution of both histograms is 200×200 .

$$h(\alpha, \varphi) = \sum_{r, \theta} \left| M_{\alpha, \varphi, \Delta_\alpha, \Delta_\varphi}(r, \theta) \hat{F}(r, \theta) \right|^p \quad (7.7)$$

The parameter p acts similar to the parameter γ in enhancement technique described in Section 6.5.1. As the final step, we will use a 2-D rectangular kernel $K(\alpha, \varphi)$,

$$K(\alpha, \varphi) = \begin{cases} \frac{1}{AD} & , \quad (\alpha, \varphi) \in \left[\frac{-A}{2}, \frac{A}{2} \right] \times \left[\frac{-D}{2}, \frac{D}{2} \right] \\ 0 & , \quad o.w. \end{cases} \quad (7.8)$$

to smooth out the histogram as follows:

$$H(\alpha, \varphi) = [h * K](\alpha, \varphi) \quad (7.9)$$

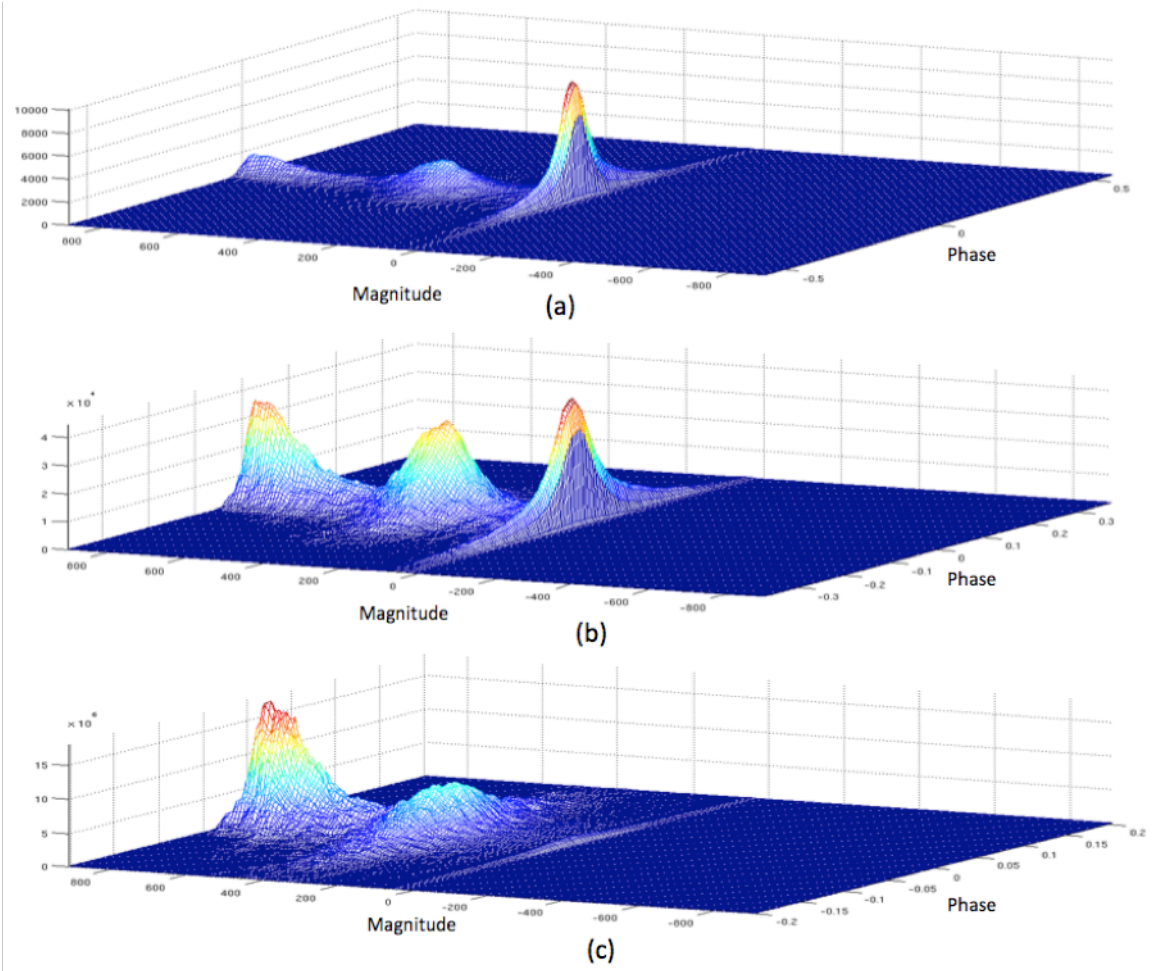


Fig. 7.2. The effects of parameter p on created histogram. $p = 0.5$ (a), $p = 1$ (b), $p = 2$ (c).

where $*$ denotes 2-D convolution. The importance of the smoothing is clear in that it combines all the energy from the estimates in a local region. **Figure 7.1** shows an example histogram before and after smoothing created using summed coefficients in R_1^l derived from expansion of phantom IVUS sub-volume. We are particularly interested in locations of the histogram peaks and the surrounding regions, as these shall be used to generate binary masks to label blood and non-blood regions. **Figure 7.2** also illustrates

the effects of the parameter p on the created histogram. We can suppress or heighten the peaks by choosing the right value for p and improve the segmentation results.

We are particularly interested in locations of the histogram peaks and the surrounding regions, as these shall be used to generate binary masks to label blood and non-blood regions. For this reason, we used manual thresholding to mask out coefficients corresponding to each peak, **Figure 7.3**. The results demonstrate that the peaks provide valuable information regarding blood and non-blood regions, suggesting a technique to automatically retrieve coefficients from each peak and generated a binary mask.

7.2.4. Segmentation of Coefficients and Recovery of Regional Peak Correspondences

In order to localize the histogram peaks, $(\alpha_{peak}, \varphi_{peak})$, we used a K-mean classifier to cluster the data in **Eq. 7.7**. The partitioning algorithm minimizes the sum of point-to-centroid distances, summed over all clusters. We assigned each point to the nearest cluster centroid and updated all centroids iteratively. Once the magnitudes and phases corresponding to the principal Q peaks were found, we computed, Q_* , masks based the following L^2 norm in the histogram space,

$$\forall \{(\alpha_{peak}^l, \varphi_{peak}^l), l = 1, \dots, K\}$$

$$Q_{\alpha_{peak}^*, \varphi_{peak}^*}(r, \theta) = \begin{cases} 1 & , \min_l \left[(\alpha(r, \theta) - \alpha_{peak}^l)^2 + (\varphi(r, \theta) - \varphi_{peak}^l)^2 \right] \\ 0 & , \text{o.w.} \end{cases} \quad (7.10)$$

where **Eq. 7.10** is minimum over all l and K is the number of tissues (classes). Note that the number of classes defined for the K-means classifier may not be necessarily the same as the number of peaks that we observe in the histogram. We expected that the magnitudes and phases of brushlet coefficients would provide some information about tissue types. Hence, $(\alpha_{peak}, \varphi_{peak})$ corresponds to an approximate magnitude-phase for a tissue (class). In **Eq. 7.10**, we tried to identify specific $(\alpha_{peak}, \varphi_{peak})$ among all magnitudes and phases derived from the brushlet coefficients, (α, φ) , and estimated the corresponding regions by masking the coefficients that exhibited the closest magnitude and phase to the approximated one. Once the desirable mask corresponding to blood regions was found (*i.e.*, the one that contains zeros around the surface of the transducer, as illustrated in **Figure 7.3(c)**), spatial regularization (*i.e.* removal of small objects) followed by detection of the most reliable lumen border is requisite.

7.2.5. Spatial Regularization and Detection of Lumen Border via Surface Function Actives (SFA)

Although researchers have introduced novel border detection algorithms in IVUS images challenges associated with this particular problem have not been considered cautiously. The performance of any method, regardless of its implementation technique, could be degraded due to presence of guide wire, appearance of side branch, reflection from surface of the transducer because of impedance mismatch, and presence of arc of calcified plaques. Therefore, regularization plays a crucial role in getting the most

accurate and reliable borders. One of the main advantages of our proposed technique is that we end up with binary images, which are easier to manipulate for spatial regularization. For example, we can get rid of the guide wire by removing small objects and look for objects with 180° or 0° orientation close to the transducer's surface in order to eliminate any possible reflection.

In fact, the major challenges are appearance of side branch, shadows behind guide wire, and presence of eccentric arc of calcified plaques. These are particularly problematic when a deformable model is deployed, leading to leakage or underestimation of the lumen border. In this paper, we employ 1-D evolving curve through surface function actives (SFA) with analytical solution or function basis [150]. SFA not only has great advantages in terms of efficiency and dimensionality reduction but also provides closed form solution, which is a requirement for lumen border, and deals with abovementioned problems. We may choose a 1-D surface function with arbitrary bases functions to represent the luminal border in 2-D polar domain. The proper choice of bases can be incorporated with some prior knowledge such as smoothness of lumen border and its periodicity along lateral direction. Hence, we opt sine and cosine bases and represent the lumen border as follows:

$$g(a_k, b_k, \theta) = a_0/2 + \sum_{k=1}^{M-1} \left(a_k \cos\left(\frac{2k\pi\theta}{N_\theta}\right) + b_k \sin\left(\frac{2k\pi\theta}{N_\theta}\right) \right) \quad (7.11)$$

where N_θ is number of angles that span 360° in Cartesian space or the width of the image in polar domain. The analytical representation of lumen border can be translated into analytical differentiation in downstream analysis, which is beneficial in terms of

computational efficiency. Now the problem is to find the optimal Fourier series coefficients that minimize the segmentation functional. Basically, probabilistic models are used to optimize a cost function, assigning each pixel to a class (blood or non-blood) until convergence is occurred. In such segmentation techniques the gray level intensities or probability density functions corresponding to each class assumed to be distinct and therefore incorporated into the model. As we mentioned in section 7.1, the main drawback of such an approach is the variability among IVUS images. In our proposed framework, the problem becomes simpler since we deal with binary images generated from regional peak correspondences. We find the optimal coefficients in an iterative process as described in **Algorithm I**. Similar approach was also taken by authors in [153].

Algorithm I: Detection of lumen border through 1-D evolving curve g using SFA.

1. Define the number of coefficients M , step size Δt , and threshold value τ .
2. Initialize the curve g by initializing the coefficients a_k, b_k .
3. Set acceptable error ζ .
4. **While** $|\varepsilon| > \zeta$

$$a_0^{t+\Delta t} = a_0^t - 2\Delta t (I(x, y) - \tau)$$

$$\text{a. } a_k^{t+\Delta t} = a_k^t - 2\Delta t (I(x, y) - \tau) \cos\left(\frac{2k\pi\theta}{N_\theta}\right)$$

$$b_k^{t+\Delta t} = b_k^t - 2\Delta t (I(x, y) - \tau) \sin\left(\frac{2k\pi\theta}{N_\theta}\right)$$

$$\text{b. Compute } g^{t+\Delta t}(a_k^{t+\Delta t}, b_k^{t+\Delta t}, \theta).$$

c. Compute $\varepsilon = g^{t+\Delta t} - g^t$.

5. **End.**

Movie 7.1 demonstrates the initialized contour at the center of the transducer, the convergence process, and final detected lumen border after 101 iterations. The smoothness of evolving curve depends on the number of coefficients M and we empirically set $M = 5$ and it worked out well. Since we deal with binary images, the threshold value could be set to $0 < \tau < 1$ as well. Once the contour is found in polar domain it can be transformed and represented in Cartesian space.

7.3. Experimental Results

We processed IVUS sub-volumes of size $512 \times 512 \times 8$ to ensure adequate spatial resolution in the pullback direction (8 slice depth). Higher spatial resolution in this dimension degraded the performance due to the effects of the motion of the catheter and heart. The Fourier domain was tiled using four, four and two cubes in x , y and pullback dimension, respectively each with overcomplete representation. In this case, the brushstroke orientation was $\pm 90^\circ$, $\pm 90^\circ$ and $\pm 180^\circ$ in x , y and pullback direction, respectively. All computations were implemented in MATLAB[®] and executed on an IBM ThinkStation workstation, 64-bit 3 GHz dual Intel Core2Quad Processors with 32 GBs of RAM in Linux platform. The execution time for expansion of each sub-volume onto

brushlet basis and detection of lumen borders through SFA framework was evaluated to be 63ms. 1158 IVUS frames collected from 5 patients and for each frame, an expert manually segmented the lumen border.

7.3.1. Evaluation of Proposed Framework Using Phantom Data

We acquired IVUS frames from phantom cylinder of shrink-wrap material using circulating blood mimicking fluid to study the feasibility of our proposed technique. **Figure 7.3** illustrates an IVUS grayscale image, constructed 2.5-D magnitude-phase histogram, generated binary masks corresponding to each peak, and resulting detected phantom border. Although the histogram exhibited three peaks we only needed to detect two peaks corresponding to coherent (cylinder wall) and incoherent (blood) pattern. Because the binary mask, **Figure 7.3(e)**, generated from the first peak centered at the center of the histogram does not provide any useful information and it represents regions with zero magnitude and phase ($\alpha \approx 0, \varphi \approx 0$) (e.g. catheter, measurement markers).

Previously, we presented a multiscale brushlet based technique to filter IVUS images and characterize blood speckle patterns as a preprocessing step for lumen border detection [11]. In order to validate our framework, we followed the same approach and reconstructed IVUS frame after thresholding the real part of coefficients with threshold value of 0.5 for 2-D and 3-D cases using 4×4 and $4 \times 4 \times 2$ expansion schemes, respectively. Then, we performed our algorithm on coefficients derived from 4×4 expansion scheme in 2-D case. Although the reconstructed results, **Figure 7.4(a,b)**, do not seem to be that much different visually the constructed magnitude-phase histograms,

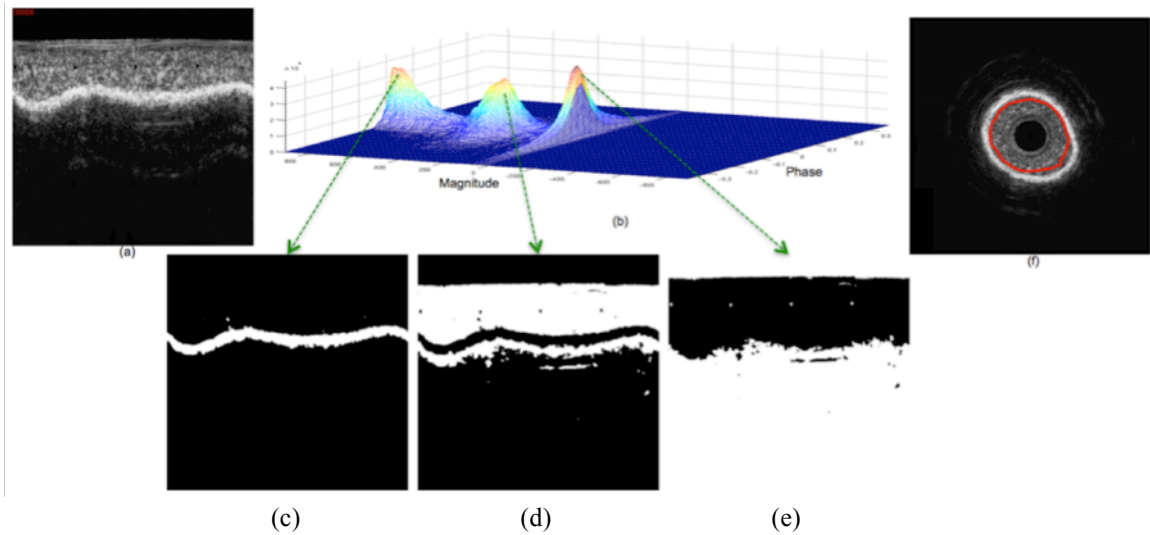


Fig. 7.3. IVUS grayscale image acquired from phantom cylinder of shrink-wrap material with circulating blood mimicking fluid in polar domain (a), constructed 2.5-D magnitude-phase histogram (b), generated binary masks corresponding to each peak (c-e), detected cylinder border (red) imposed on the IVUS grayscale image corresponding to (a) in Cartesian domain (f).

Figure 7.3(b) and **Figure 7.4(c)**, provide more valuable information. We concluded that the 3-D analysis is superior over its 2-D counterpart to isolate coherent versus incoherent patterns since the cylinder border failed to be detected when 2-D analysis was done, **Figure 7.4(d)**.

7.3.2. Evaluation of Proposed Framework Using *In Vivo* Data

7.3.2.1. IVUS Images Acquired With Single-Element 45 MHz Transducer

We evaluated the algorithm performance on 1158 IVUS frames acquired from 5 patients during catheterization procedure. Our datasets consist of small and large arteries with no, mild, and severe stenosis as well as variety of atherosclerotic plaque morphologies (*i.e.* centric, eccentric). **Figure 7.5** illustrates a constructed magnitude-phase histogram for a

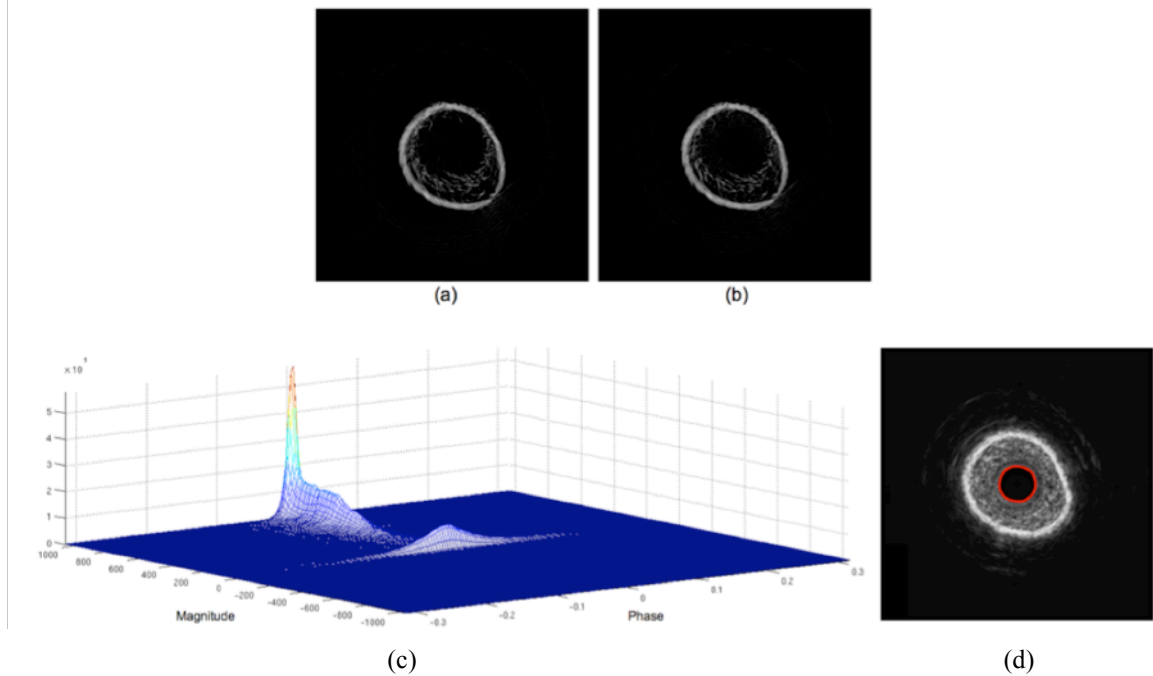


Fig. 7.4. Reconstructed IVUS frame after projection of the frame onto 2-D (a) and 3-D (b) brushlet basis and thresholding the real part of the coefficients, constructed 2.5-D magnitude-phase histogram from coefficients derived from 4x4 expansion scheme in 2-D case (c), and resulting detected cylinder border (d).

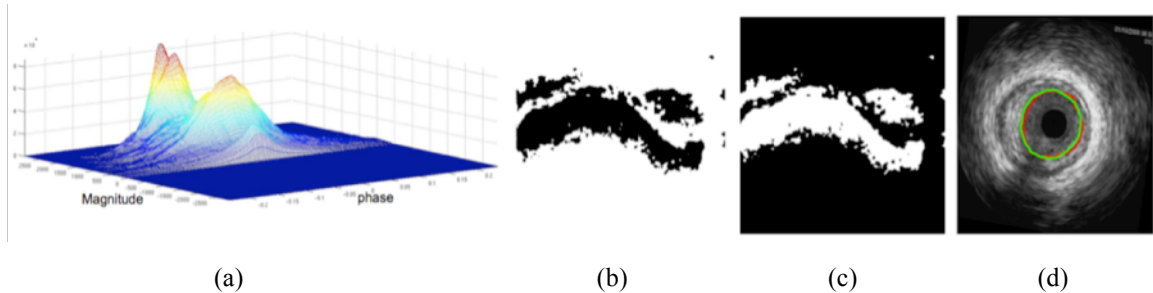


Fig. 7.5. Constructed magnitude-phase histogram (a), generated binary masks (b,c), automated (red) and manual (green) traced borders imposed on original IVUS grayscale image (d).

single IVUS frame, generated binary masks corresponding to blood and non-blood regions, and automated detected luminal border along with manual traced contour by an expert. As we can observe, the peaks are not as well separated as in the case of the phantom data but they still provide good estimates of relative magnitudes and phases for blood and non-blood regions and hence detection of lumen border *in vivo*.

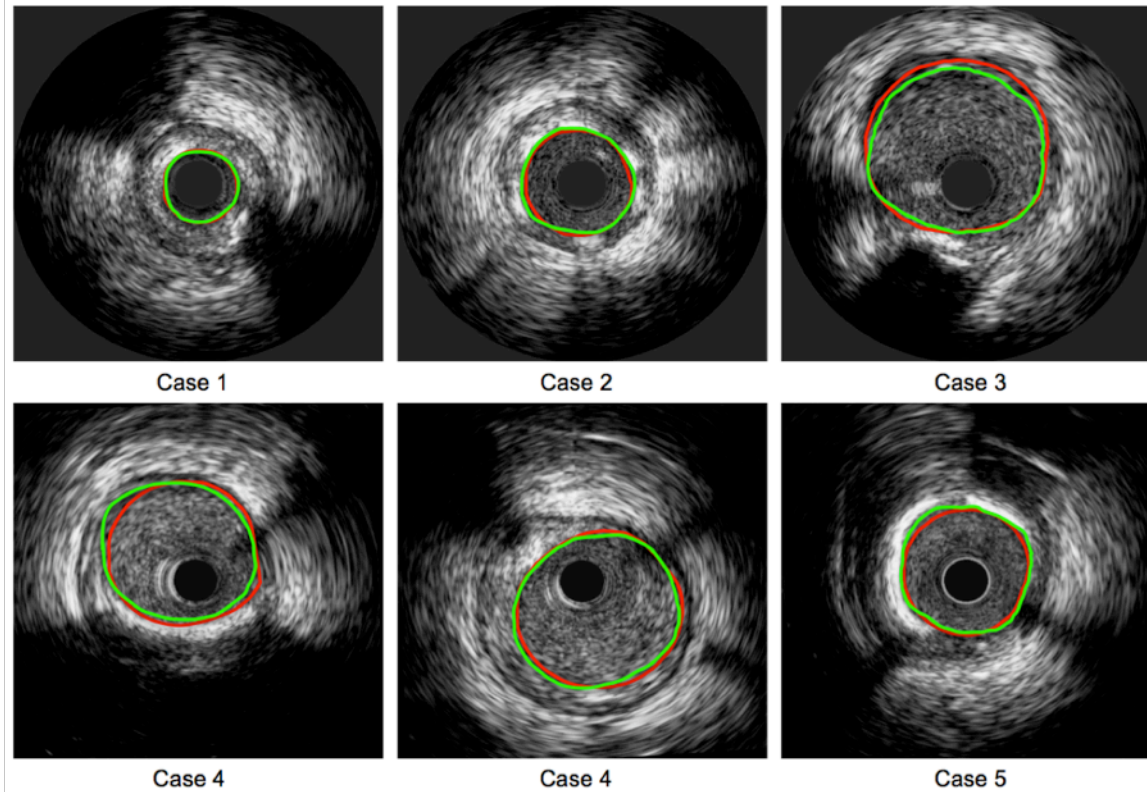


Fig. 7.6. Resulting automated lumen detected border (red) along with manual traced contour (green) imposed on six distinct IVUS frames. The case specifications have been described in **Table 7.2**.

Movie 7.2 demonstrates automated (red) and manual (green) traced borders for a short pullback (Case 6), containing 104 frames. **Figure 7.6** also shows resulting automated lumen border detected contours (red) along with manual traced ones (green) for six frames collected from arteries with distinctive pathological and morphological structures as described in **Table 7.2**. We quantified the results comparing the automated detected borders with manual traced contours by an expert using SFA algorithm. The statistics, true positive (TP), false positive (FP), and root mean square error (RMSE) rates are reported in **Table 7.2**. For each case, the degree of difficulty as well as morphological and pathological specifications was provided too. **Figure 7.7** illustrates the Bland-Altman

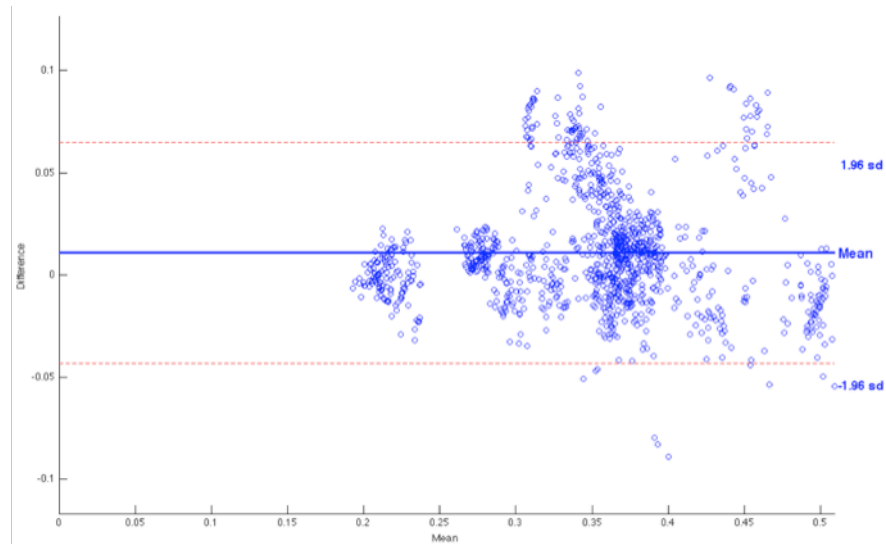


Fig. 7.7. The Bland-Altman plot for lumen areas derived from automated and manual traced borders.

plot and depicts the consistency between lumen areas computed from automated and manual traced borders for all processed IVUS frames (total of 1158 frames).

Table 7.2. Quantification of automated detected borders with corresponding manual ones for images acquired with single-element 45MHz transducers

Case #	Difficulty	Case specification (Number of IVUS frames)	TP (%)	FP (%)	RMSE (mm)
1	High	Registered data. Small centric artery with severe stenosis and calcified plaques (131)	96.7 ± 0.05	3.9 ± 0.01	0.01 ± 0.025
2	Low	Registered data. Case # 1 after stent implantation (94)	95.4 ± 0.03	7.8 ± 0.04	0.005 ± 0.004
3	Medium	Registered data. Large artery with no stenosis (23)	96.5 ± 0.02	7.4 ± 0.06	0.03 ± 0.080
4	High	Registered data. Medium artery with mild stenosis, calcification, and guide wire artifact (500)	91.1 ± 1.00	5.0 ± 0.20	0.03 ± 0.129
5	High	Registered data. Large and medium artery with mild as well as relatively severe stenosis and calcification (306)	89.5 ± 0.03	4.7 ± 0.1	0.04 ± 0.195
6	High	Persistent* and unregistered data. Medium artery with mild stenosis (104)	96.5 ± 0.01	5.0 ± 0.01	0.01 ± 0.021

* Persistency refers to an averaging protocol employed during acquisition resulting relatively blurred images.

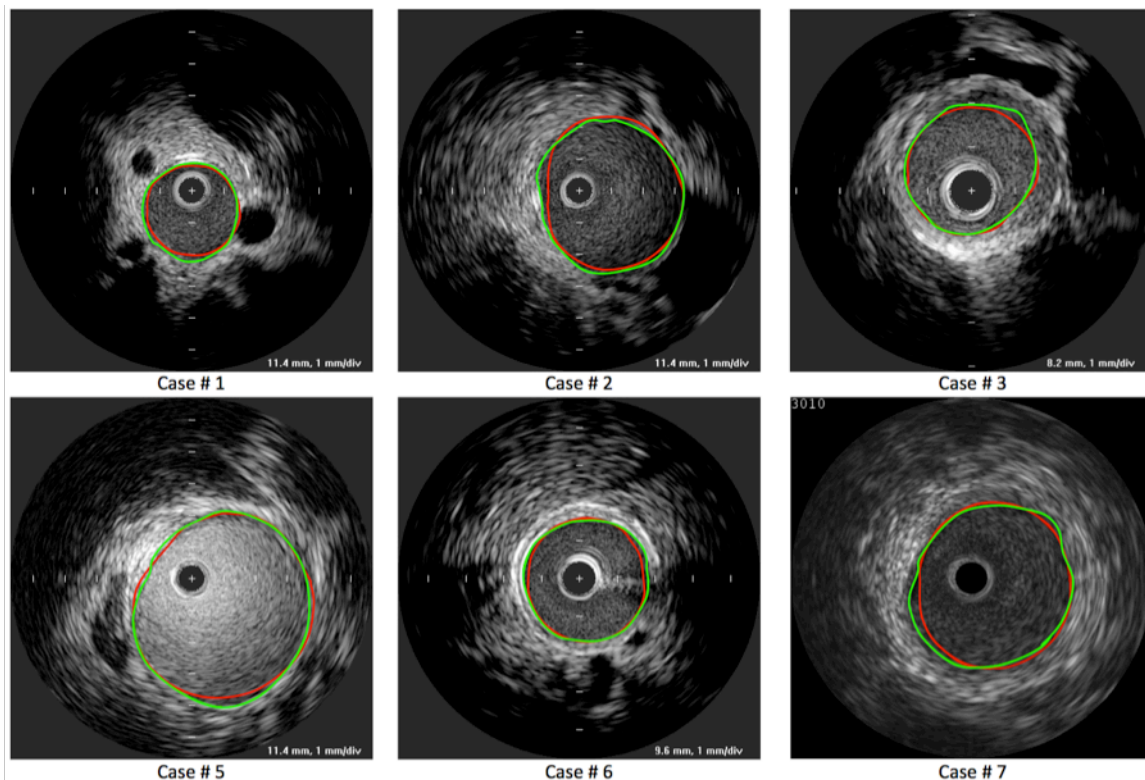


Fig. 7.8. Resulting automated lumen detected border (red) along with manual traced contour (green) imposed on six distinct IVUS images acquired from six patients using single-element 40MHz transducers. The case specifications have been listed in **Table 7.3**.

7.3.2.2. IVUS Images Acquired With Single-Element 40MHz Transducer

In order to further evaluate our proposed algorithm performance, we performed our technique on 320 IVUS images acquired from seven patients using single-element 40MHz transducer. **Figure 7.8** illustrates automated detected contours along with manually traced borders in images collected from six different cases with distinctive pathological and morphological structures as described in **Table 7.3**. As we can see, the overall appearance of images varies case to case. This could be due to dissimilarity among acquisition systems and/or different adjustment of acquisition parameters. For example, the possible effects of TGC parameter could be notable in case #5 and case #7 in **Figure 7.8**.

Table 7.3. Quantification of automated detected borders with corresponding manual ones for images acquired with single-element 40MHz transducers.

Case #	Difficulty	Case specification (Number of IVUS frames)	TP (%)	FP (%)	RMSE (mm)
1	Low	Unregistered data. Small artery with no stenosis (48)	91.74 ± 0.01	0.6 ± 0.01	0.03 ± 0.060
2	Medium	Unregistered data. Small artery with no stenosis (48)	91.93 ± 0.08	1.0 ± 0.12	0.04 ± 0.092
3	Medium	Unregistered data. Medium eccentric artery with stenosis (48)	92.91 ± 0.03	0.1 ± 0.12	0.03 ± 0.023
4	Low	Unregistered data. Medium artery with about 30% stenosis (48)	91.49 ± 0.06	1.2 ± 0.10	0.04 ± 0.176
5	High	Unregistered data. Large artery with no stenosis. The images appear very bright (48)	97.78 ± 0.03	4.45 ± 0.06	0.04 ± 0.081
6	Low	Unregistered data. Small artery with no stenosis (48)	95.20 ± 0.24	0.12 ± 0.00	0.02 ± 0.010
7	High	Unregistered data. Large artery with no significant stenosis (32)	92.80 ± 0.43	0.50 ± 0.00	0.04 ± 0.054

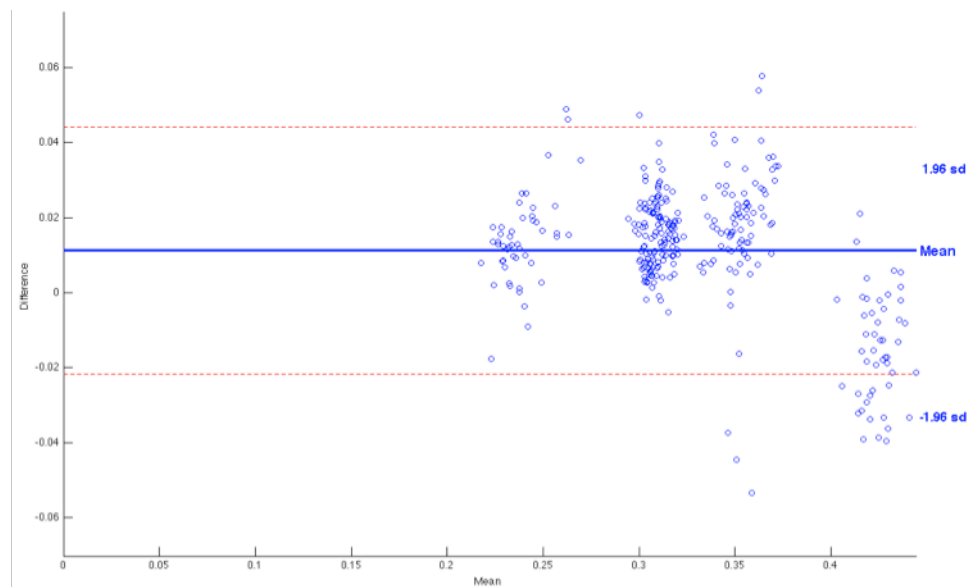


Fig. 7.9. The Bland-Altman plot for lumen areas derived from automated and manual traced borders. The plot is for data acquired with single-element 40MHz transducers.

Figure 7.9 illustrates the Bland-Altman plot and depicts the consistency between lumen areas computed from automated and manual traced borders for all processed IVUS frames (total of 320 frames).

7.3.3. Comparison of Our Proposed Algorithm with Existing Techniques

In order to assess our algorithm (*Method 1*) performance in comparison with existing techniques, we choose two methods introduced in [128,141] to contrast the results. Unal *et. al* [128] (*Method 2*) presented a 2-D algorithm, implemented in polar domain, by building a statistical shape space through principle component analysis (PCA). Once the shape space was built, an initialized contour evolved by minimization of region-based non-parametric probabilistic energy function described in [151]. They estimated the probability distribution inside (ρ_{in}) and outside (ρ_{out}) the lumen using intensity profiles in training dataset. Primarily, this technique was developed for IVUS images acquired with 64-elements phased array 20MHz transducer, **Figure 6.1(a)**. Unlike images acquired with 40MHz and 45MHz transducers, the blood has low echogenicity and lumen appears relatively darker than surrounding plaque in images acquired with 20MHz transducer.

As the second method of comparison, we preprocessed the IVUS images using affine invariant anisotropic filter in combination with hard thresholding and employed geometric deformable model to estimate the lumen border as Taki *et. al* (*Method 3*) suggested in [141]. They applied this technique on IVUS images acquired with 30MHz

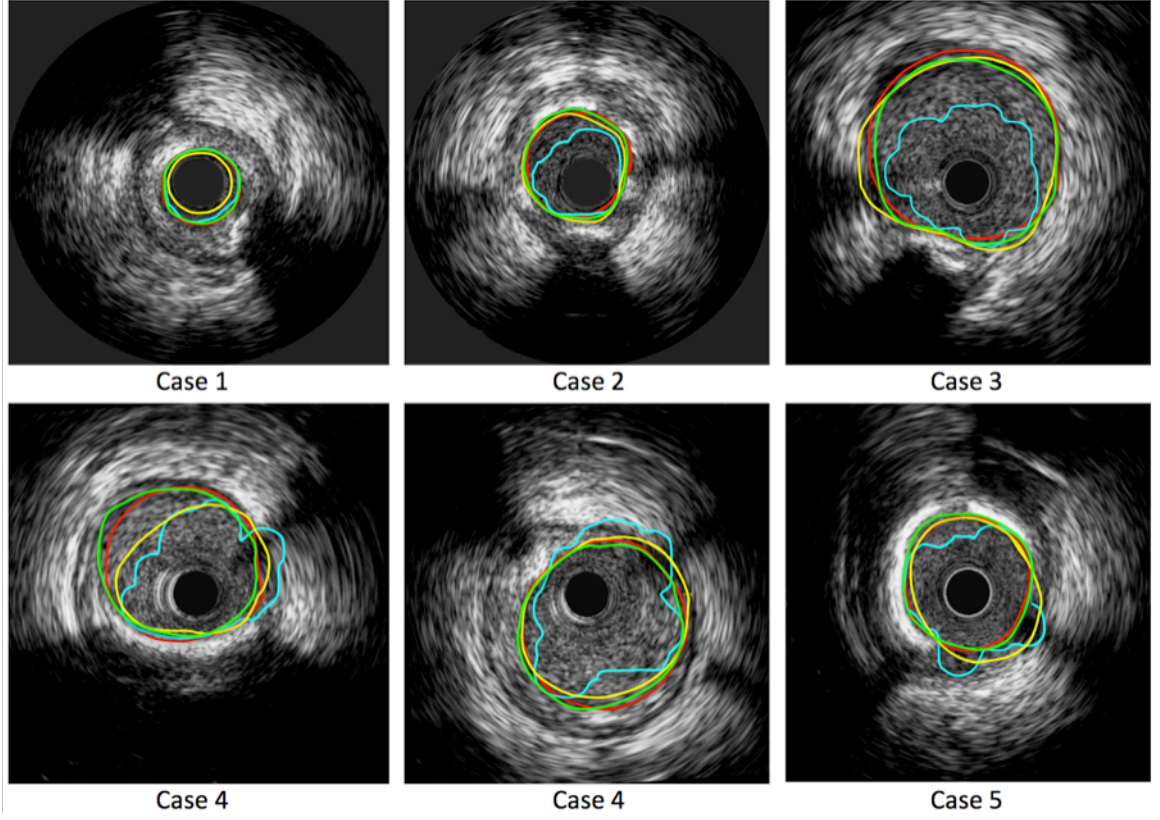


Fig. 7.10. Resulting automated lumen detected border in images acquired with 45MHz single-element transducer through our proposed technique (red), Method 2 (yellow), and Method 3 (cyan), along with manual traced contour (green) imposed on six distinct IVUS images acquired from six patients using single-element 45MHz transducers. The case specifications have been listed in **Table 7.2**.

single-element transducer and highlighted the advantage of despeckling techniques on IVUS images. Authors in [139,140] also took similar approach for IVUS border detection. We implemented this technique, and opted the threshold value for each dataset empirically to achieve the best possible performance.

Figure 7.10 illustrates the automated detected lumen borders in images acquired with 45MHz single-element transducer through our proposed technique (red), Method 2 (yellow) and Method 3 (cyan) along with manually traced borders (green) by an expert. For this experiment, we calculated ρ_{in} and ρ_{out} , **Figure 7.12(c)**, using 30 frames (four frames from case 1, six frames from case 2, two frames from case 3, nine frames from

case 4, six frames from case 5, three frames from case 6) collected from different sections of pullbacks in five cases listed in **Table 7.2**. For the second method of comparison, we observed that a global threshold would not be very well suited for all cases and therefore empirically selected thresholds for each case. **Table 7.4** shows the quantitative results for all three methods and six cases.

Table 7.4. Quantification of automated detected borders through three different methods with corresponding manual ones for images acquired with single-element 45MHz transducers. The first, second, and third outperforming methods have been highlighted with green, orange, and red colors, respectively.

	TP (%)	FP (%)	RMSE (mm)
Case # 1			
Method # 1	96.7 \pm 0.05	3.9 \pm 0.01	0.010 \pm 0.025
Method # 2	97.6 \pm 0.90	38.7 \pm 4.50	0.114 \pm 1.300
Method # 3	93.9 \pm 0.10	2.4 \pm 0.00	0.025 \pm 0.039
Case # 2			
Method # 1	95.4 \pm 0.03	7.8 \pm 0.04	0.005 \pm 0.004
Method # 2	93.4 \pm 0.10	2.1 \pm 0.07	0.031 \pm 0.072
Method # 3	83.2 \pm 0.20	4.5 \pm 0.07	0.073 \pm 0.274
Case # 3			
Method # 1	96.5 \pm 0.02	7.4 \pm 0.06	0.030 \pm 0.080
Method # 2	92.5 \pm 1.10	7.5 \pm 0.10	0.091 \pm 0.466
Method # 3	71.9 \pm 0.20	0.2 \pm 0.03	0.191 \pm 0.506
Case # 4			
Method # 1	91.1 \pm 1.00	5.0 \pm 0.20	0.030 \pm 0.129
Method # 2	83.8 \pm 0.40	5.1 \pm 0.20	0.104 \pm 0.946
Method # 3	80.8 \pm 0.05	9.0 \pm 0.20	0.130 \pm 0.982
Case # 5			
Method # 1	89.5 \pm 0.03	4.7 \pm 0.10	0.040 \pm 0.195
Method # 2	80.3 \pm 1.80	8.3 \pm 0.21	0.145 \pm 0.328
Method # 3	73.1 \pm 1.50	5.6 \pm 0.20	0.166 \pm 1.674
Case # 6			
Method # 1	96.5 \pm 0.01	5.0 \pm 0.01	0.010 \pm 0.021
Method # 2	93.0 \pm 0.20	9.5 \pm 0.20	0.062 \pm 0.363
Method # 3	83.5 \pm 0.40	4.8 \pm 0.08	0.081 \pm 0.370

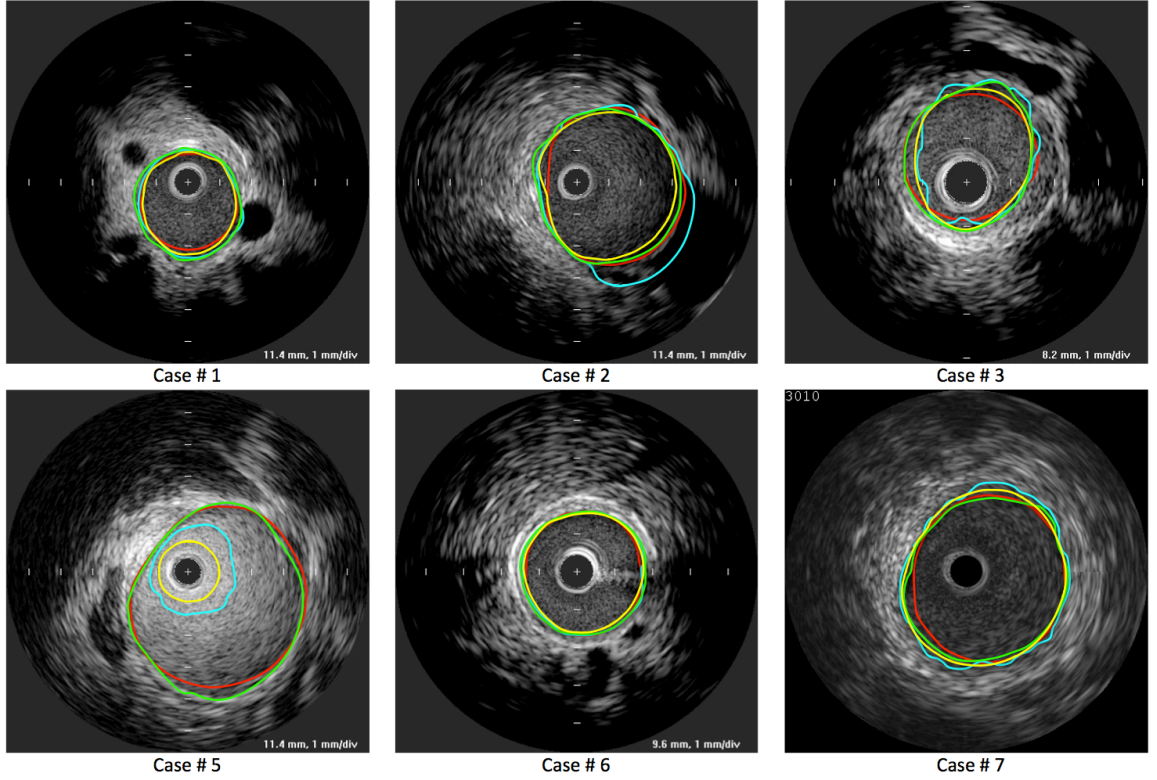


Fig. 7.11. Resulting automated lumen detected border in images acquired with 45MHz single-element transducer through our proposed technique (red), Method 2 (yellow), and Method 3 (cyan), along with manual traced contour (green) imposed on six distinct IVUS images acquired from six patients using single-element 45MHz transducers. The case specifications and quantitative results have been listed in **Table 7.3** and **Table 7.4**, respectively.

We repeated the same experiment using IVUS images acquired with 40MHz transducer as described in **Table 7.3**. For *Method 2*, we computed ρ_{in} and ρ_{out} with two distinct datasets, **Figure 7.12(b)**. In the first dataset we only used the IVUS frames collected from the same cases in **Table 7.3** (*Method 2 (T1)*) whereas in the second dataset we employed the IVUS frames that were not among those cases (*Method 2 (T2)*). Like previous experiment, we selected the threshold empirically for each case in *Method 3*.

Figure 7.11 and **Table 7.5** shows the resulting automated detected borders using each technique in six IVUS frames and quantitative results, respectively.

Table 7.5. Quantification of automated detected borders through three different methods with corresponding manual ones for images acquired with single-element 40MHz transducers. The first, second, third, and forth outperforming methods have been highlighted with green, orange, red, and yellow colors, respectively.

	TP (%)	FP (%)	RMSE (mm)
Case # 1			
Method # 1	91.7 ± 0.01	0.6 ± 0.01	0.030 ± 0.060
Method # 2 (T1)	81.78 ± 0.15	13.3 ± 0.021	0.099 ± 0.186
Method # 2 (T2)	78.7 ± 0.50	10.4 ± 0.32	0.101 ± 0.228
Method # 3	96.4 ± 0.02	1.6 ± 0.04	0.021 ± 0.047
Case # 2			
Method # 1	91.93 ± 0.08	1.0 ± 0.12	0.040 ± 0.092
Method # 2 (T1)	78.28 ± 0.46	13.0 ± 0.14	0.158 ± 0.634
Method # 2 (T2)	78.2 ± 0.46	12.9 ± 0.14	0.158 ± 0.631
Method # 3	98.5 ± 0.01	4.1 ± 0.03	0.035 ± 0.065
Case # 3			
Method # 1	92.9 ± 0.03	0.1 ± 0.12	0.030 ± 0.023
Method # 2 (T1)	83.8 ± 0.14	12.9 ± 0.15	0.125 ± 0.313
Method # 2 (T2)	74.9 ± 3.12	9.7 ± 0.50	0.145 ± 0.961
Method # 3	93.9 ± 0.20	2.3 ± 0.02	0.046 ± 0.135
Case # 4			
Method # 1	91.5 ± 0.06	1.2 ± 0.10	0.040 ± 0.176
Method # 2 (T1)	81.47 ± 0.03	22.3 ± 1.70	0.165 ± 1.271
Method # 2 (T2)	83.3 ± 0.21	24.1 ± 1.86	0.165 ± 1.283
Method # 3	90.0 ± 0.01	1.4 ± 0.01	0.073 ± 0.124
Case # 5			
Method # 1	97.8 ± 0.03	4.4 ± 0.06	0.040 ± 0.081
Method # 2 (T1)	36.2 ± 0.00	0.0 ± 0.00	1.206 ± 0.217
Method # 2 (T2)	51.2 ± 0.00	0.0 ± 0.00	0.980 ± 0.121
Method # 3	58.1 ± 0.10	0.07 ± 0.00	0.231 ± 0.206
Case # 6			
Method # 1	95.2 ± 0.24	0.12 ± 0.00	0.020 ± 0.010
Method # 2 (T1)	92.3 ± 0.00	2.7 ± 0.00	0.04 ± 0.024
Method # 2 (T2)	77.7 ± 4.20	1.9 ± 0.02	0.086 ± 0.958
Method # 3	97.8 ± 0.02	0.2 ± 0.06	0.015 ± 0.078
Case # 7			
Method # 1	92.8 ± 0.43	0.500 ± 0.001	0.040 ± 0.054
Method # 2 (T1)	94.8 ± 0.09	0.12 ± 0.03	0.023 ± 0.016
Method # 2 (T2)	94.3 ± 0.27	1.8 ± 0.52	0.033 ± 0.018
Method # 3	99.9 ± 0.06	3.7 ± 0.03	0.025 ± 0.023

7.4. Conclusion and Discussion

We presented a 3-D segmentation framework for automatic detection of luminal borders through classification of incoherent (blood) and coherent (non-blood) patterns in IVUS grayscale images by constructing the joint magnitude-phase histogram of complex brushlet coefficients. This was possible since brushlet offered orthogonal transformation of Fourier domain so we could sum up the brushlet coefficients derived from Hermitian Fourier coefficients. We studied the feasibility of our proposed framework using both phantom and *in vivo* IVUS data. One of the main advantages of our technique was that the generated binary masks made regularization simpler and therefore detection of lumen border in presence of guide wire and its shadow, side branch, arc of calcified plaque became easier and more accurate. We found SFA segmentation framework more suitable for lumen border detection in comparison with traditional deformable models. We performed our algorithm on 1478 IVUS frames acquired with single-element 45MHz and 40MHz transducers, containing distinctive arteries with variety of pathological and morphological structures, collected from 13 patients.

We achieved promising results on datasets with relatively small (45MHz: Case 1) and large vessels (45MHz: Case 3, Case 5 and 40MHz, Case 5, Case 7), which were of particular interest and demonstrated that our algorithm was reliable, comparing with manual traced borders by an expert and two of existing techniques by Unal *et. al* [128] (*Method 2*) and Taki *et. al* [141] (*Method 3*). The results show that our proposed technique (*Method 1*) is able to reliably detect lumen borders in IVUS images acquired

with both 40MHz and 45MHz transducers. Overall, it outperforms *Method 2* and *Method 3*, keeping in mind that the threshold values in *Method 3* were selected empirically for each case, otherwise, its performance could have been dramatically diminished if a fixed threshold had been deployed. In fact, one of the main limitations associated with PDF- or threshold-based segmentation techniques in IVUS images is that the appearance of images may vary depends on selected parameters during acquisition (*i.e.* TGC), normalization, or reconstruction (*i.e.* non-linear transformation). This leads to variation among intensity profiles derived from inside (ρ_{in}) and outside (ρ_{out}) of luminal area, which is observed among IVUS image dataset acquired with 40 MHz transducer especially Case 5 and Case 7.

In order to better express the challenge inherited with PDF- and threshold-derived segmentation techniques, we calculated the nonparametric probability distribution ρ_{in} and ρ_{out} using Parzen windowing technique also called the kernel density estimator

$\rho(\varsigma) = 1/n\sigma \sum_{i=1}^n K\left(\varsigma - \varsigma_i/\sigma\right)$ where n is the number of pixels inside or outside of lumen

area and $K(p) = \frac{1}{\sqrt{2\pi}} e^{\left(\frac{-p^2}{2}\right)}$ is the Gaussian kernel with heuristically chosen σ (e.g.

$\sigma = 10$). We excluded the intensities resulting from reflection of signals from surface of transducer when calculating ρ_{in} . **Figure 7.12** shows the resulting probability distribution ρ_{in} and ρ_{out} derived from images acquired with 20 MHz, 40 MHz, and 45 MHz transducers. As we can see, the separation between ρ_{in} and ρ_{out} vanishes while transducer center frequency is increased from 20MHz to 45MHz, making segmentation

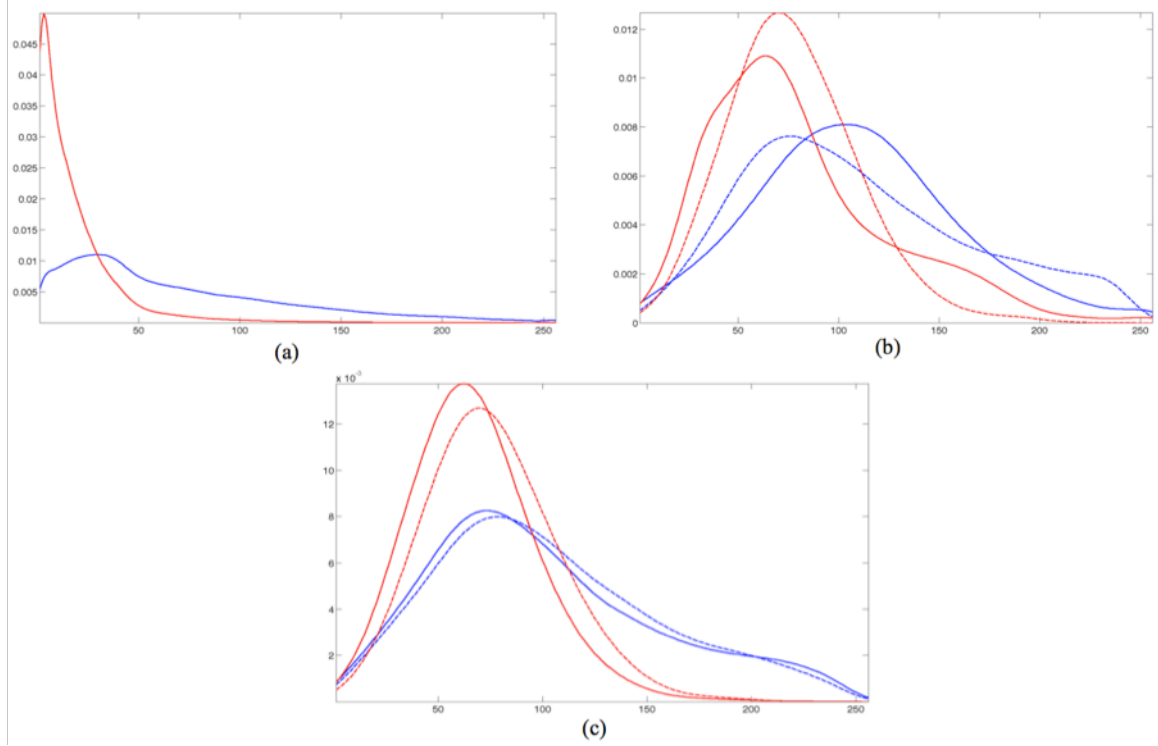


Fig. 7.12. Probability distribution ρ_{in} and ρ_{out} derived from images acquired with 20 MHz (a), 40 MHz (b), and 45 MHz (c) transducers. The probability distributions were computed from two datasets (solid and dashed lines) in images acquired with 40 MHz and 45 MHz transducers.

problem more challenging. This is due to the fact that more scattering from red blood cells emerges as we increase transducer's center frequency. In fact, this explains that why even visual detection of luminal borders in images acquired with 45MHz transducer does not look so easy unless the expert goes back and forth among numbers of frames and look for blood incoherent patterns. As a matter of fact, this is as exactly as what happens when we project sub-volume of analysis onto brushlet basis and look for incoherent (*i.e.* blood) versus coherent (*i.e.* plaque) textures by constructing 2.5-D magnitude-phase histograms. This has also been verified when we compared 2-D and 3-D analysis and observed the advantage of 3-D process in Section 7.3.1. In the same context, we can point to Case 5 in IVUS dataset acquired with 40 MHz transducers, which is a perfect example to observe

the effectiveness of our proposed technique. As we can see in **Figure 7.11** and **Table 7.5**, *Method 2* and *Method 3* fail to detect lumen borders whereas our algorithm performs quite well.

Another shortcoming of *Method 2* is that its performance may vary depending on probability distribution profiles derived from different training datasets. For example, in IVUS dataset acquired with 40 MHz transducers, we utilized two distinct sets (T1 and T2) of probability distributions, **Figure 7.12 (b)**, and consequently got different results, **Table 7.5**.

In brief, the presented technique is advantageous since it can be applied directly on complex brushlet domain and unlike traditional filtering (denoising) methods it does not require thresholding. Nevertheless, we can further improve the results, refine the algorithm, and speed up the computational time, taking into account certain aspects of processing steps.

7.4.1. Registered Versus Unregistered Data

One of the main limitations associated with the proposed framework is misregistration among successive frames within sub-volume of analysis due to heart or catheter motions. This could affect the results in a sense that the lobes corresponding to blood and non-blood regions in 2.5-D magnitude-phase histogram space overlap. In this case, the estimated peaks would not be the true representatives of associated magnitude-phase of tissue types. Our hypothesis is that less registration artifact among frames resulting more

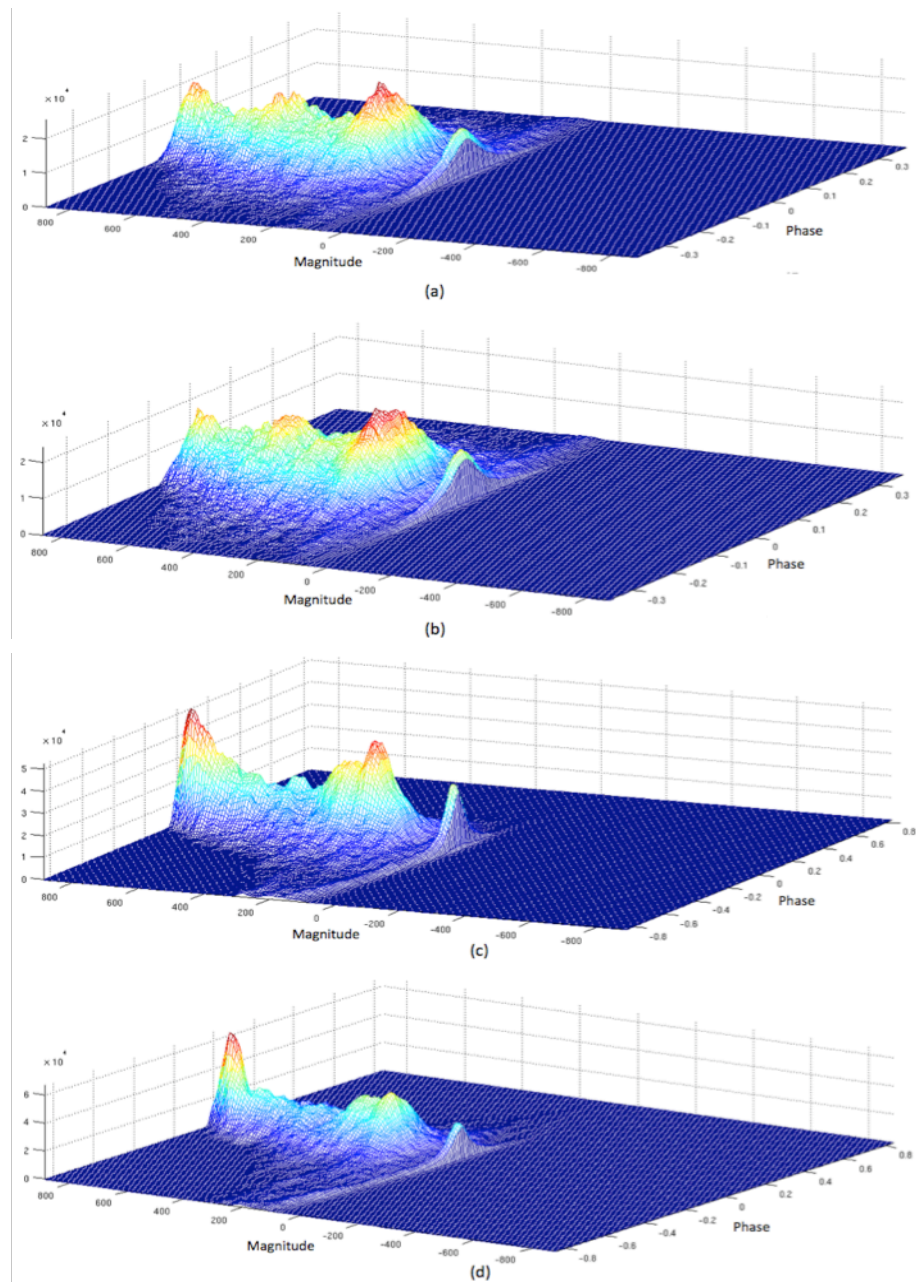


Fig. 7.13. Constructed magnitude-phase histograms for two cases: 1) a frame within stable (consistent) sub-volume of analysis before (a) and after (b) registration, 2) a frame within unstable (inconsistent) sub-volume of analysis before (c) and after (d) registration.

separated lobes. We investigated this issue by constructing the magnitude-phase histograms for a single frame before and after registration. **Figure 7.13** demonstrates

resulting histograms before and after registration for two cases: 1) a frame within stable (consistent) sub-volume of analysis, 2) a frame within unstable (inconsistent) sub-volume of analysis. As we can see, constructed histograms for the frame within consistent pullback are very similar. On the other hand, the histograms are slightly different for the one that is within inconsistent pullback. Perhaps, we could validate the results by comparing both cases, before and after registration, using manually traced borders.

7.4.2. Effects of Tiling Resolution on Constructed Magnitude-Phase Histogram

In Chapter 6, we extensively studied the effects of different tiling schemes, visualized coefficients in various rings or spheres, and reconstructed IVUS sub-volumes accordingly. We pursued the same path and constructed the magnitude-phase histograms using summed coefficients in different rings or spheres to further investigate where the most informative features are located or whether there is sufficient information in cubes representing high frequency components that we were not able to systematically study them through visualization previously. **Figure 7.14** displays the grayscale images of magnitude of summed coefficients in different rings using 4x4x2 and 4x4x4 expansion schemes. **Figure 7.15** also illustrates the corresponding constructed magnitude-phase histograms.

The recent results confirmed our previous observations. We noticed that the most informative features are located in the innermost cubes **Figure 7.14(b,g)** and **Figure**

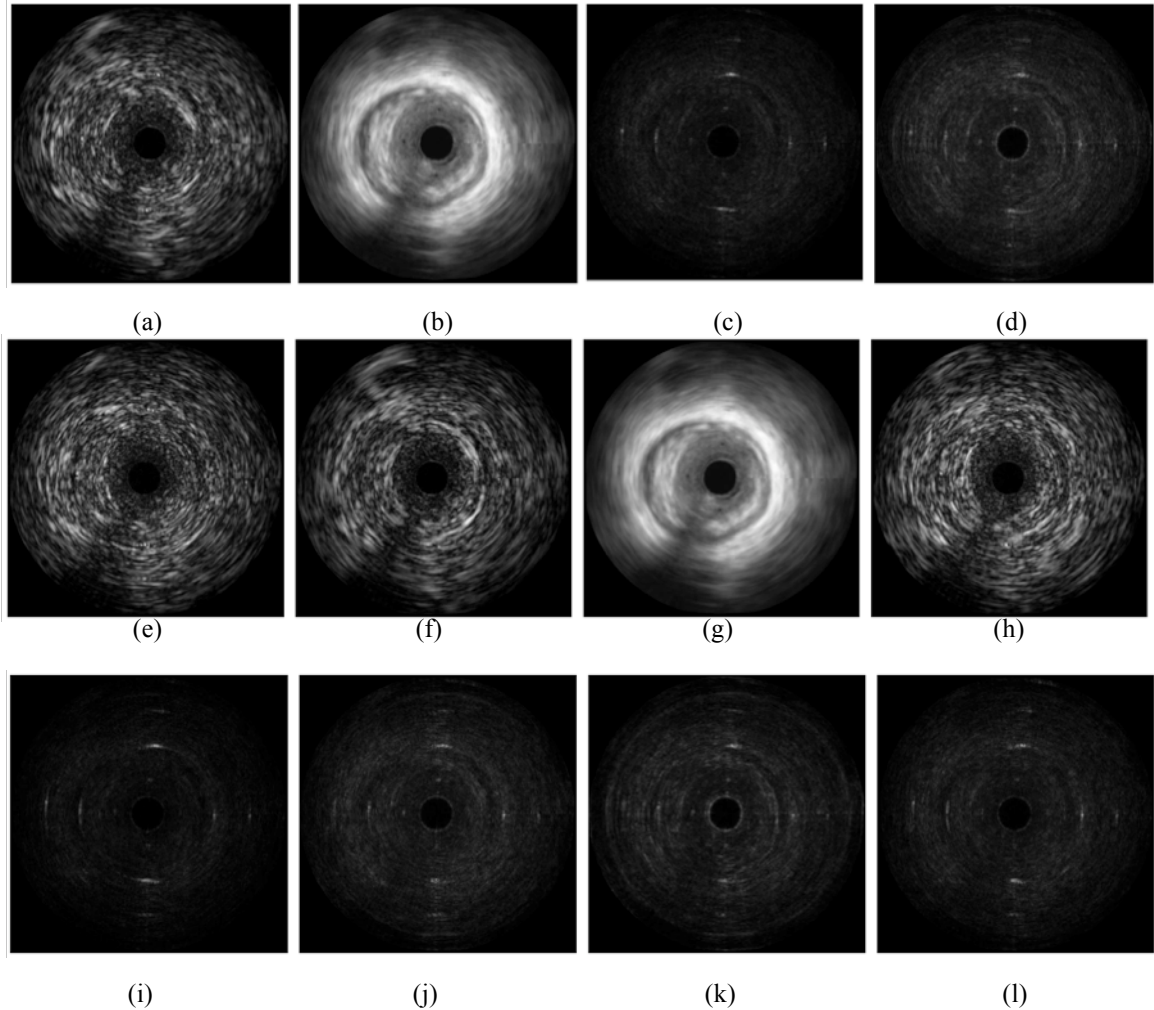


Fig. 7.14. Constructed grayscale images from summed coefficients in R_1^2 (a), R_1^1 (b), R_2^2 (c), R_2^1 (d) using $4 \times 4 \times 2$ expansion scheme and R_1^1 (e), R_1^2 (f), R_1^3 (g), R_1^4 (h), R_2^1 (i), R_2^2 (j), R_2^3 (k), and R_2^4 (l) using $4 \times 4 \times 4$ expansion scheme.

7.15(b,g). As we can see, the lobes are more separated in **Figure 7.15(b,g)** and corresponding histograms contain the majority of energy. Although in Chapter 6 we could not make any firm judgment about rings or spheres representing high frequency components, some of the histograms show separated lobes, **Figure 7.15 (a,c,d,e,i,k)**. This is encouraging since we can also employ the corresponding coefficients in addition to those in the innermost rings or spheres, construct the histograms, and estimate the lumen border. It is worth mentioning that the magnitude-phase histogram approach does not rely

on the overall energy preserved in rings or spheres and only depends on relative magnitudes and phases. Some of the results also confirm that there is not any adequate information in some of the rings or spheres, **Figure 7.15(f,h,j,l)**. We repeated the same experiment and compare the histograms resulting from $8 \times 8 \times 2$ vs. $8 \times 8 \times 4$ and $16 \times 16 \times 2$ vs. $16 \times 16 \times 4$ expansion schemes and the results were similar to those depicted in **Figures 7.14** and **Figure 7.15**.

For all experiments we processed the IVUS sub-volumes containing 8 frames per sub-volume of analysis. We increased the number of frames per blocks and constructed the magnitude-phase histograms to investigate the results. We previously had observed that increasing the number of frames in block of analysis resulting more blurred images after reconstruction especially when there are misregistration among frames. **Figure 7.16** demonstrates constructed histograms for two frames in registered dataset within consistent and inconsistent sub-volume of analysis, respectively. We processed them by choosing 8 frames and 16 frames per block in $4 \times 4 \times 4$ expansion scheme.

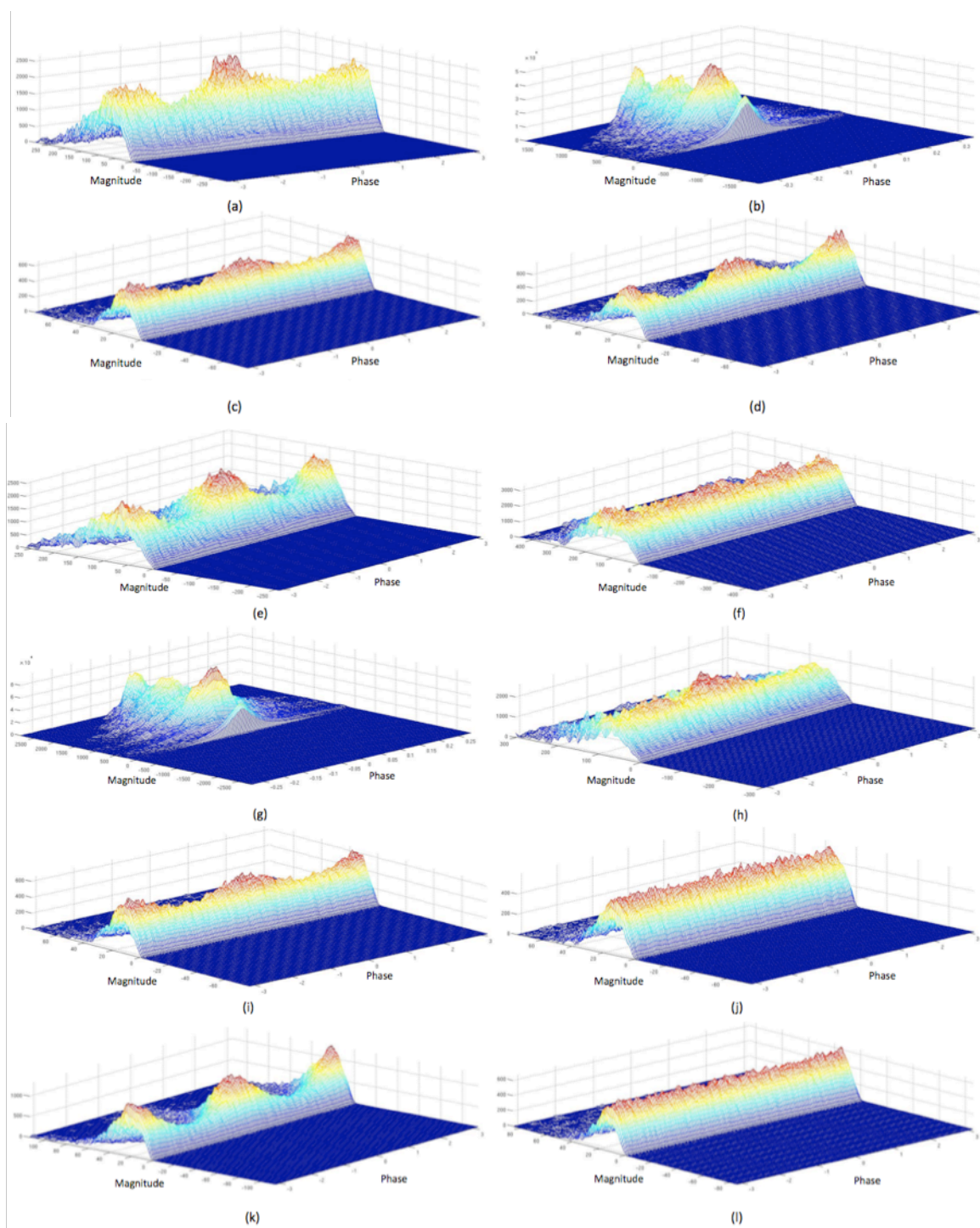


Fig. 7.15. Magnitude-phase histograms constructed from coefficients depicted in **Figure 7.14**.

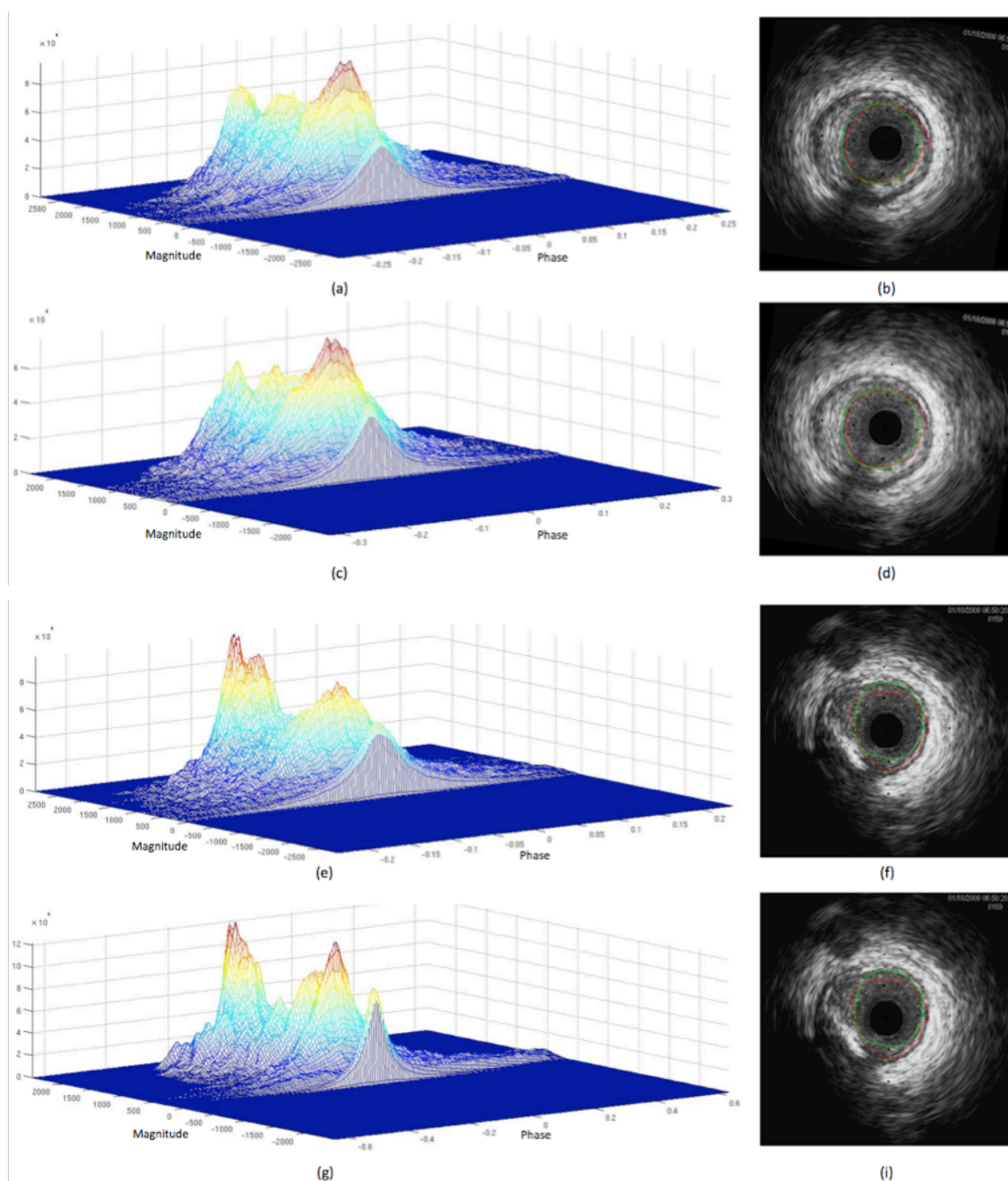


Fig. 7.16. Constructed magnitude-phase histograms from coefficients in S_1 in 4x4x4 expansion scheme for two cases: 1) a frame within stable (consistent) sub-volume of analysis by choosing 8 (a) and 16 (b) frames per block and corresponding detected lumen borders (red) (b,d) along with manually traced borders (green), 2) a frame within unstable (inconsistent) sub-volume of analysis by choosing 8 (a) and 16 (b) frames per block and corresponding detected lumen borders (red) (f,g) along with manually traced borders (green).

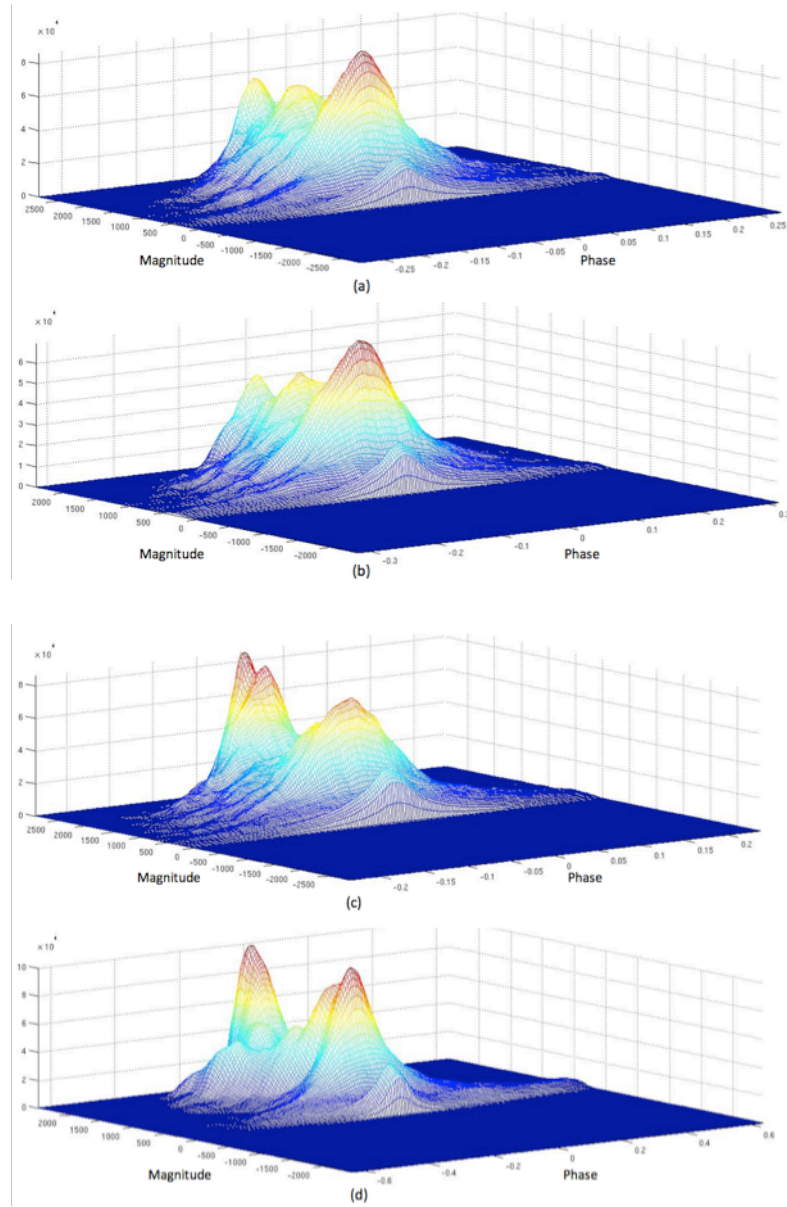


Fig. 7.17. Constructed multiframe magnitude-phase histograms from coefficients in all cubes in S_1 in 4x4x4 expansion scheme for two cases: 1) a frame within stable (consistent) sub-volume of analysis by choosing 8 (a) and 16 (b) frames per block, 2) a frame within unstable (inconsistent) sub-volume of analysis by choosing 8 (a) and 16 (b) frames per block.

7.4.3. Multiple-Frame Magnitude-Phase Histogram

We constructed the magnitude-phase histogram from coefficients corresponding to a single frame. We extended such construction to 3-D and generated the magnitude-phase histograms using all coefficients in cubes within particular rings or spheres. In this case, we can generate a single mask for all frames in block of analysis contrary to the previous method that a mask used to be generated for each frame. This method is advantageous in perfectly registered dataset (sub-volume of analysis) and the speed of segmentation algorithm can be increased. **Figure 7.17** demonstrates the constructed multi-frame magnitude-phase histograms for two cases using 8 and 16 frames per block of analysis in 4x4x4 expansion scheme. The single-frame version of the histograms has been depicted in **Figure 7.16**.

8. Chapter Eight:

SUMMARY, CONCLUSION, AND FUTURE WORK

8.1. Atherosclerotic Plaque Characterization

We described the importance of detection of vulnerable plaques in coronary arteries and concluded that IVUS technology is the predominant imaging modality to date for visualization of arterial wall and its pathological structures, comparing with other comparable imaging techniques. To reach this goal, we investigated realistic challenges from specimen preparation, IVUS data collection toward classification and strived to implement VH algorithm for data collected with single-element 40MHz transducer. However, we observed variations among transducer spectral parameters (*i.e.* bandwidth, center frequency) and extracted features (*i.e.* slope, intercept) that made classification very challenging if not impossible. As an alternative approach we presented an unsupervised multiscale 2-D wavelet-derived approach in combination with ISODATA clustering algorithm to classify tissues into fibrotic, fibro-lipidic, calcified, and no tissue. We then quantify the results employing gold standard histology images and studied numbers of critical factors that had not been considered by any group previously such as effects of flowing blood as well as change of pressure on constructed tissue color maps along with reliability of extracted features in successive frames and classification of tissues in regions behind arc of calcified plaques.

We showed that our algorithm could provide fairly reliable results under various conditions such as pressure changes and presence of arc of calcified. The accuracy of the algorithm was evaluated by an independent histopathologist and reported to be 99.70%, 87.75% and 90.87% for calcified, fibrotic and fibro-lipidic tissues respectively in 83 CSIs collected from 32 hearts *ex vivo*. Our results showed a fine differentiation between fibrotic and fibro-lipidic components, which had been a major challenge in the field.

Indeed the main contribution of our work was that the constructed PH images through our unsupervised approach could be reliably used for building training sets in any supervised classification approach without any manual labeling in the typically highly heterogeneous media of atherosclerotic plaques. Initially, we chose an unsupervised approach to validate the reliability of extracted features, however, extension of algorithm to supervised classification for *in vivo* applications is indispensable. This may also resolve one of the limitations associated with our developed technique, which was direct detection of necrotic core.

8.1.1. Refinement of Proposed Algorithm and Future Work

In Chapter 3, we reviewed existing IVUS-based tissue characterization or vulnerable plaque detection techniques. Although each presented method has its own advantages, in their clinical applications, they have been only partially successful. For example, the challenges associated with RF-based algorithms (*i.e.* [64,69]) have been comprehensively studied in [130]. On the other hand developed textured-based techniques such as [77,87] miss some of the associated factors with vulnerable plaques or the one introduced in

[121] needs to be extended for supervised classification and direct detection of necrotic core tissue. **Table 8.1** demonstrates the existing techniques and their ability to detect factors associated with vulnerable plaques [18,19].

Table 8.1. Existing atherosclerotic tissue characterization algorithms.

	RF-Based Techniques			Texture-Based Techniques		
	IVUS-VH	IVUS-IB	IVE	ECOC	IBH	IVUS-PH
Author (Year)	Nair <i>et. al</i> (2001) [64]	Kawaski <i>et. al</i> (2002) [69]	de Corte <i>et. al</i> (2000) [9]	Escalera <i>et. al</i> (2009) [77]	Taki <i>et. al</i> (2009) [87]	Katouzian <i>et. al</i> (2008) [121]
Fibrotic Cap	Yes (inferred)	Yes (inferred)	N/A	Not Shown	Yes (inferred)	Yes (inferred)
Lipid Core Size	Yes	Yes	Maybe	Not Shown	Maybe	Yes
Percentage of Stenosis	Yes	Yes	Yes	Yes	Yes	Yes
Calcification	Yes	Yes	Maybe	Yes	Yes	Yes
Detection of VP	Yes (inferred)	Yes (inferred)	No	Not Shown	Maybe	Yes (inferred)
Histology Validation	Yes	Yes	Yes	No	Yes	Yes
Tissue Types	Fibrotic Fibrofatty Calcified Necrotic	Fibrotic Lipidic Calcified	Fibrous Fibrofatty Fatty	Fibrotic Soft Plaque Calcified	Fibrotic Calcified Necrotic	Fibrotic Lipidic Calcified No Tissue

As we can see, the existing atherosclerotic tissue characterization techniques that are able to provide tissue color maps [64,69,87,121], have deployed either spectral or textural features for classification. The spectral features are basically derived from early work of Lizzi *et. al* [61,63], who strived to differentiate between benign and malignant tissues in prostate cancer, which were relatively more homogenous comparing with atherosclerotic plaques. They assumed that tissue's spectra have a known autocorrelation function [65] given homogeneity of tissues within windowed backscattered signal. The advantage of spectral-derived technique is that it can provide more details about tissues microstructures given informative, consistent, and reliable features. However, as we presented in Chapter 4, we found large variations among extracted atherosclerotic tissue spectral features particularly when high-frequency transducer (40 MHz up) was used due

to inconsistency among transducer spectral parameters (*i.e.* center frequency, bandwidth), heterogeneity of tissue's windowed signal, non-linear response of tissue's response to ultrasound signal, geometric configuration of scatterers, transducer position and/or beam angle of incidence, *etc.* [130]. On the other hand, texture-based designed techniques fail to detect early versus late necrotic core tissues or dense fibrotic tissues that appear similar to calcified tissues. Hence, we hypothesize that combining both spectral and textural features alleviate inconsistencies while improving detection of tissues. For this purpose, the generated PH images could be used to retrieve signals corresponding to each tissue locally and then spectral features would be computed. At the end, the features vector might be consist of only spectral features or both spectral and textural features.

From classification point of view, we may employ SVM scheme for classification for two main reasons. First, we could classify data that exhibit linear or non-linear behavior in input space so we may be able to take into account tissue's non-linear response to ultrasound signals. Secondly, we not only could generate tissue color maps but also the distance from hyperplanes to each data point in feature space might be used as *confident scaling factor*. This would allow us to incorporate the reliability of classified results into color codes and generate tissue maps (e.g. PH images) with spectrum of colors. Subsequently, an interventional cardiologist can make decisions more confidently.

8.2. Automatic Detection of Luminal Borders In IVUS Images

In this study we explored the applicability of brushlet analysis on IVUS datasets to filter 3-D grayscale IVUS images and detect the lumen borders. We deployed three filtering methods to remove or alleviate the effects of blood speckles prior to lumen border detection. First, we employed similar approach presented in [133] and directly thresholded brushlet coefficients followed by reconstruction. Our hypothesis was that the magnitude or real part of brushlet coefficients corresponding to blood speckles was lower than those of non-blood regions. Secondly, we strived to discover where the most informative features were located and thus developed incremental/decremental expansion and reconstruction algorithms. During such process, we kept the most valuable features, mainly located in cubes/rings/spheres representing low frequency components, and ignored the rest. We looked at the filtered grayscale images constructed from magnitude of brushlet coefficients in transformed domain and also their correspondences after reconstruction in spatial domain. Finally, we developed an algorithm based on estimation and compensation of magnitude as well as phase of ensemble of distinct textures (*i.e.* blood and non-blood in IVUS images) in transformed domain through construction of corresponding 2.5-D magnitude-phase histograms.

Our findings demonstrated that 3-D brushlet analysis had a great potential to isolate coherent patterns (*i.e.* non-blood) from incoherent ones (blood). We visualized brushlet coefficients extensively and observed that they carry out valuable information at different scales, orientations, and frequencies. This was also confirmed through supervised classification of coefficients corresponding to blood versus non-blood regions using neural networks.

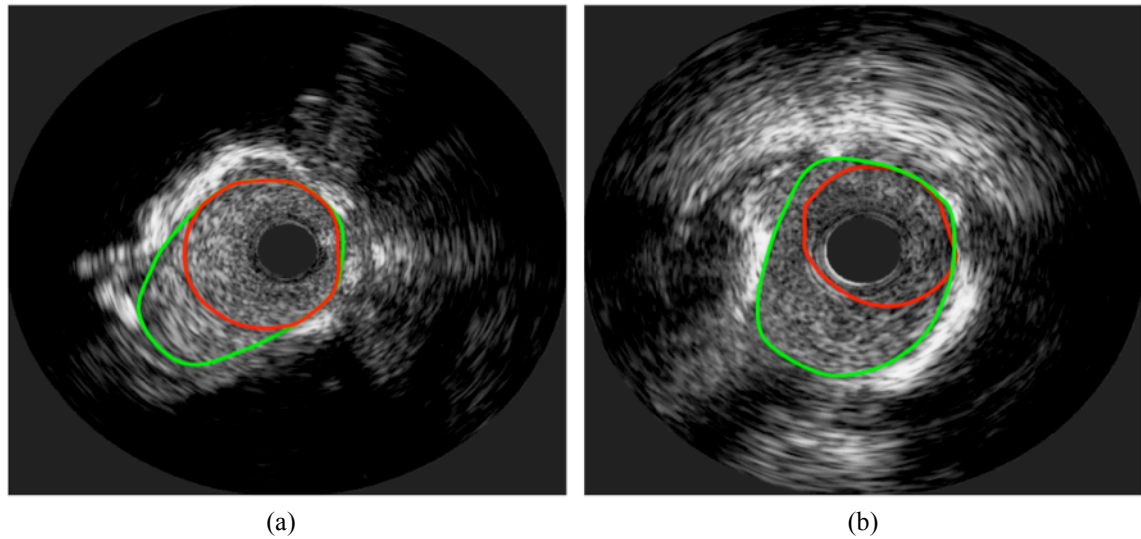


Fig. 8.1. Two examples where the algorithm fails to correctly identify lumen borders. An eccentric artery with deep shadow (a), repetitive reflection of ultrasound signals (ring-down artifact) from surface of transducer's element (b).

The main contribution of this work is classification of brushlet coefficients corresponding to blood and non-blood regions through estimation of peaks of relative magnitudes and phases in constructed 2.5-D magnitude-phase histograms. Once the magnitudes and phases were approximated, we generated binary masks corresponding to blood and non-blood regions in transformed domain and employed the same masks to estimate the lumen borders. Our results showed that the proposed framework performed promising, detecting the lumen border in images acquired with both 40MHz and 45MHz transducers.

Despite encouraging results, there are existing challenges that degrade resulting automated detected borders so further study is required to improve algorithm performance. For example, in some cases, we observed that the lumen borders are underestimated in large arteries with eccentric plaques and deep shadows, **Figure 8.1(a)**. Previously we described that the algorithm removes objects close to transducer surface

with 180° orientation that could be due to reflection of ultrasound signals from transducer's element surface because of impedance mismatch. However, in some cases, the reflection from transducer's element surface (ring-down artifact) could be repetitive, **Figure 8.1(b)**, which calls for more sophisticated regularization.

For future work, we define numbers of projects to explore different aspects of developed methods.

8.2.1. Refinement of Supervised Classification of Blood Versus Non-Blood Regions

In Section 6.4, we confirmed that brushlet coefficients provided valuable information about blood regions so they could be used for supervised classification of blood versus non-blood regions. We achieved encouraging results on datasets with relatively small and large vessels, which were of particular interest. However, there are several items that need to be further studied in order to improve the algorithm performance. For example, we can combine brushlet derived features with statistical (mean, standard deviation, kurtosis, entropy, etc), textural (homogeneity, contrast, energy, correlation, etc) and/or spatial/temporal/spectral features presented in [146]. We can also consider other classification algorithms such as support vector machine (SVM) that is known to be faster and more robust.

We employed two iterative techniques in Section 6.6 in order to extract features as close as possible to low frequency components. We had observed that these features were more informative of those representing high frequency components. In supervised classification approach, this may be verified through a common method of feature selection, known as sequential feature selection. Such techniques have been designed based on an objective function, called the criterion (*i.e.* mean squared error for regression models), which the method seeks to minimize over all feasible feature subsets. The method has two variants: 1) sequential forward selection (SFS), in which features are sequentially added to an empty candidate set until the addition of further features does not decrease the criterion, 2) sequential backward selection (SBS), in which features are sequentially removed from a full candidate set until the removal of further features increase the criterion. In either method, we can verify the localization of the most informative features in an optimum framework.

8.2.2. Quantitative Measurement for Energy Localization in Incremental/Decremental Decomposition Frameworks

Although we visually observed that the most informative features were located in the innermost rings/spheres we needed to verify it in a justifiable basis. Hence, we propose a quantitative measurement technique to calculate the energy at each level of decomposition. In this way, we can investigate that how many percent of the energy in the innermost rings/spheres would be preserve in the innermost rings/spheres after each level of decomposition.

8.2.3. Decreasing Processing Time by Adaptive Selection of Numbers of Frames per Blocks of Analysis

We examined the effects of tiling resolution along pullback direction in Section 6.6.1, experiment # 3. We observed that reconstructed images became blurred due to misalignment among frames when we increased resolution of tiling along pullback direction, **Figure 6.40**. This limits numbers of frames per blocks of analysis and therefore increases processing time. We know that frames acquired close to end of diastolic (ED) phase exhibit more misalignment and most of registration algorithms are designed based on such attribute. Given registered dataset with critical frame numbers (those that present more misalignment), we can increase and decrease numbers of frames per blocks of analysis. For example, in frames that represent consistent and inconsistent pullbacks we can employ 16 and 4 frames per blocks of analysis, respectively. Our hope is to decrease processing time and obtain more reliable results simultaneously.

8.2.4. Dual-Modal Brushlet-Based Lumen Border Detection Technique with Cross Refinement

In Chapter 6 and 7, we demonstrated that brushlet analysis is well suited for delineation of blood pool and confirmed that brushlet coefficients provided valuable information about blood and non-blood regions. We achieved the best results, deploying two distinct techniques: 1) supervised classification of blood regions described in Section 6.4, 2) estimation of relative magnitudes and phases in constructed 2.5-D histogram and

construction of binary masks corresponding to blood and non-blood regions, presented in Chapter 7. Although both techniques provide reasonable results, they have their own advantages and disadvantages. For example, the supervised approach works encouraging and deserves further exploration in large vessels while the histogram-based technique sometimes may not work perfectly due to attenuation of signals in regions far from transducer. On the other hand, the lumen border could be directly detected in masks corresponding to blood regions generated by histogram-based technique with proper regularization, while we needed to threshold the output of the Neural Network to estimate the blood pool and approximate the lumen border with some regularization. Nevertheless, both techniques are common in one thing and it is brushlet space.

Once we come into brushlet space, we can derive required features for either abovementioned algorithm concurrently. Given a trained classifier, we can generate blood maps and binary masks corresponding to blood regions simultaneously. The main question here is *“how to use one of the results to refine the other one?”* or *“how can we come up with some rules to refine both results all at the same time?”* Although refinement of both results simultaneously seems to be more challenging we might be able to use one of them to refine the other one.

Appendix

A. List of Abbreviations

2-D	Two-Dimensional
3-D	Three-Dimensional
ACS	Acute Coronary Artery
AR	Autoregressive
AUC	Area Under Curve
CAD	Coronary Artery Disease
CHD	Coronary Heart Disease
CSI	Cross Section of Interest
CT	Computed Tomography
CTA	Computed Tomography Angiography
DECOC	Discriminant Error Correcting Output Codes
DES	Drug-Eluting Stent
DWF	Discrete Wavelet Frame
DWPF	Discrete Wavelet Packet Frame
DWPT	Discrete Wavelet Packet Transform
EBCT	Electron-Beam Computed Tomography
ECOC	Error Correcting Output Codes
ED	End of Diastolic
EEM	External Elastic Membrane

FDA	Food and Drug Administration
FFT	Fast Fourier Transform
FLDA	Fisher Linear Discriminant Analysis
H&E	Hematoxylin and Eosin
IB	Integrated Backscatter
ICM	Iterative Conditional Mode
ICT	Intracoronary Thermography
IFFT	Inverse Fast Fourier Transform
IVE	Intravascular Elastography
K-NN	K Nearest Neighbor
LAD	Left Anterior Descending
LCX	Left Circumflex
LDL	Low Density Lipoprotein
LMSE	Least Mean Square Error
LV	Left Ventricle
MBF	Mid-Band-Fit
MI	Myocardial Infarction
MRA	Magnetic Resonance Angiography
MRI	Magnetic Resonance Imaging
NIR	Near Infrared
NMC	Nearest Mean Classifier
NURD	Non Uniform Rotational Distortion
OCT	Optical Coherence Tomography

PBS	Phosphate Buffered Saline
PCA	Principle Component Analysis
PCI	Percutaneous Coronary Intervention
PH	Prognosis Histology
PSD	Power Spectral Density
QMF	Quadrature Mirror Filter
RCA	Right Coronary Artery
RF	Radio Frequency
ROC	Receiver-Operating-Characteristic
ROI	Region of Interest
RMSE	Root Mean Square Error
RT3-D	Real-Time Three-Dimensional
SBS	Sequential Backward Search
SFA	Surface Function Active
SFE	Scaling Factor Estimator
SFS	Sequential Forward Search
SNR	Signal-to-Noise Ratio
TCFA	Thin-Cap Fibro Atheroma
TGC	Time Gain Compensation
UCT	Ultrafast Computed Tomography
VH	Virtual Histology
VV	Vasa Vasorum

B. Bibliography

- [1] National Vital Statistics Reports, *National Center for Health Statistics*, Vol. 58, No. 19, 2010.
- [2] A. M. Minino, M. P. Heron, S. L. Murphy, K. D. Kochanek, “Deaths: Final Data for 2004,” Division of Vital Statistics, Vol. 55, No. 19, 2007.
- [3] Heart Disease and Stroke Statistics-2008 Update, *American Heart Association (AHA)*, Dallas, Texas, 2008.
- [4] J. A. Ambrose, M. A. Tannenbaum, D. Alexopoulos, *et al.*, “Angiographic progression of coronary artery disease and the development of myocardial infarction,” *J. Am. Coll. Cardiol.*, Vol. 12, No. 1, pp. 56-62, 1988.
- [5] D. Hackett, G. Davies, A. Maseri, “Pre-existing coronary stenosis in patients with first myocardial infarction are not necessarily severe,” *Eur. Heart J.*, Vol. 9, No. 12, pp. 1317-1323, 1988.
- [6] D. Giroud, J. M. Li, P. Urban, *et al.*, “Relation of the site of acute myocardial infarction to the most severe coronary arterial stenosis at prior angiography,” *Am. J. Cardiol.*, Vol. 69, No. 8, pp. 729-732, 1992.
- [7] R. S. Mitchell, V. Kumar, A. K. Abbas, N. Fausto, “Robbins Basic Pathology,” *Philadelphia: Saunders*, pp. 345. 8th edition, 2007.
- [8] M. Friedman, G. T. Van den Borenkamp, “The pathogenesis of a coronary Thrombus,” *Am. J. Pathol.*, Vol. 48, pp. 19-44, 1966.
- [9] M. Friedman, “The pathogenesis of coronary plaques, thromboses, and hemorrhages: an evaluative review,” *Circulation*, Vol. 52, (suppl. III), pp. III34–III40, 1975.
- [10] E. Falk, “Plaque rupture with severe pre-existing stenosis precipitating coronary thrombosis: characteristics of coronary atherosclerotic plaques underlying fatal occlusive thrombi,” *Br. Heart J.*, Vol. 50, pp. 127-134, 1983.
- [11] M. J. Davies, A. C. Thomas, “Plaque fissuring: the cause of acute myocardial infarction, sudden ischaemic death, and crescendo angina,” *Br. Heart J.*, Vol. 53, pp. 363-373, 1985.
- [12] J. Muller, G. Tofler, P. Stone, “Circadian variation and triggers of onset of acute cardiovascular disease,” *Circulation*, Vol. 79, pp. 733-743, 1989.
- [13] J. E. Muller, G. S. Abela, R. W. Nesto, *et al.*, “Triggers, acute risk factors and vulnerable plaques: the lexicon of a new frontier,” *J. Am. Coll. Cardiol.*, Vol. 23, pp. 809–813, 1994.
- [14] W.C. Little, “Angiographic assessment of the culprit coronary artery lesion before acute myocardial infarction,” *Am. J. Cardiol.*, Vol. 66, pp. 44G-47G, 1990.
- [15] J. E. Muller, G. H. Tofler, “Triggering and hourly variation of onset of arterial thrombosis,” *Ann. Epidemiol.*, Vol. 2, pp. 393-405, 1992.
- [16] E. Falk, “Why do plaques rupture?,” *Circulation*, Vol. 86, pp. III30-III42, 1992.
- [17] P. Libby, “Molecular bases of the acute coronary syndromes,” *Circulation*, Vol. 91, pp. 2844-2850, 1995.
- [18] R. Virmani, A. P. Burke, F. D. Kolodgie, A. Farb, “Pathology of the thin-cap fibroatheroma: A type of vulnerable plaque,” *J. Interven. Cardiol.*, Vol. 16, No. 3, pp. 2672-, 2003.

- [19] M. Naghavi, P. Libby, *et al.* "From Vulnerable Plaque to Vulnerable Patients: A Call for New Definitions and Risk Assessment Strategies: Part I," *Circulation*, Vol. 108, pp. 1664-1672, 2003.
- [20] P. Constantinides, "Plaque fissures in human coronary thrombosis," *J. Atheroscler. Res.*, Vol. 6, pp. 1-17, 1966.
- [21] M. J. Davies, N. Woolf, W. B. Robertson, "Pathology of acute myocardial infarction with particular reference to occlusive coronary thrombi," *Br. Heart J.*, No. 38, pp. 659-664, 1976.
- [22] M. J. Davies, N. Woolf, W. B. Robertson, "The relation of coronary thrombosis to ischaemic myocardial necrosis," *J. Pathol.*, No. 127, pp. 99-110, 1979.
- [23] M. J. Davies, T. Thomas, "The pathological basis and microanatomy of occlusive thrombus formation in human coronary arteries," *Philos. Trans. R. Soc. Lond. B. Biol. Sci.*, No. 294, pp. 225-229, 1981.
- [24] M. J. Davies, A. Thomas, "Thrombosis and acute coronary-artery lesions in sudden cardiac ischemic death," *N. Engl. J. Med.*, No. 310, pp. 1137-1140, 1984.
- [25] M. J. Davies, A. C. Thomas, "Plaque fissuring-the cause of acute myocardial infarction, sudden ischaemic death, and crescendo angina," *Br. Heart J.*, No. 53, pp. 363-373, 1985.
- [26] M. L. Armstrong, M. B. Megan, "Arterial fibrous proteins in cynomolgus monkeys after atherogenic and regression diets," *Circ. Res.*, No. 36, pp. 256-262, 1975.
- [27] D. M. Small, M. G. Bond, D. Waugh, M. Prack, J. K. Sawyer, "Physicochemical and histological changes in the arterial wall of nonhuman primates during progression or regression of atherosclerosis," *J. Clin. Invest.*, No. 73, pp. 1590-1605, 1984.
- [28] J. Schneiderman, R. L. Wilensky, A. Weiss, E. Samouha, L. Muchnik, M. Chen-Zion, M. Ilovitch, E. Golan, A. Blank, M. Flugelman, Y. Rozenman, and R. Virmani, "Diagnosis of thin-cap fibroatheromas by a self-contained intravascular magnetic resonance imaging probe in *ex vivo* human aortas and *in situ* coronary arteries," *J. Amer. Coll. Cardiol.*, vol. 45, pp. 1961-1969, 2005.
- [29] C. Stefanadis, L. Diamantopoulos, C. Vlachopoulos, *et al.*, "Thermal heterogeneity within human atherosclerotic coronary arteries detected in vivo: a new method of detection by application of a special thermography catheter," *Circulation*, No. 99, pp. 1965-1971, 1999.
- [30] C. Stefanadis, L. Diamantopoulos, J. Dernellis, *et al.*, "Heat production of atherosclerotic plaques and inflammation assessed by the acute phase proteins in acute coronary syndromes," *J. Mol. Cell. Cardiol.* No. 32, pp. 43-52, 2000.
- [31] C. Stefanadis, K. Toutouzas, E. Tsiamis, *et al.*: "Increased local temperature in human coronary atherosclerotic plaques: an independent predictor of clinical outcome in patients undergoing a percutaneous coronary intervention," *J. Am. Coll. Cardiol.*, No. 37, pp. 1277-1283, 2001.
- [32] W. Casscells, B. Hathorn, M. David, *et al.* "Thermal detection of cellular infiltrates in living atherosclerotic plaques: possible implications for plaque rupture and thrombosis," *Lancet*, No. 347, pp. 1447-1451, 1996.
- [33] H. Yabushita, B. E. Bouma, S. L. Houser, H. T. Aretz, I. K. Jang, K. H. Schlendorf, C. R. Kauffman, M. Shishkov, D. H. Kang, E. F. Halpern, and G. J. Tearney, "Characterization of human atherosclerosis by optical coherence tomography," *Circulation*, Vol. 106, No. 13, pp. 1640-1645, 2002.

- [34] I. K. Jang, G. J. Tearney, B. MacNeill, M. Takano, F. Moselewski, N. Iftima, M. Shishkov, S. Houser, H. T. Aretz, E. F. Halpern, and B. E. Bouma, "In vivo characterization of coronary atherosclerotic plaque by use of optical coherence tomography," *Circulation*, Vol. 111, No. 12, pp. 1551–1555, 2005.
- [35] E. Grube, U. Gerckens, L. Buellesfeld, and P. J. Fitzgerald, "Images in cardiovascular medicine. Intracoronary imaging with optical coherence tomography: a new high-resolution technology providing striking visualization in the coronary artery," *Circulation*, Vol. 106, No. 18, pp. 2409–2410, 2002.
- [36] T. Kubo, T. Imanishi, S. Takarada, A. Kuroi, S. Ueno, T. Yamano, T. Tanimoto, Y. Matsuo, T. Masho, H. Kitabata, K. Tsuda, Y. Tomobuchi, and T. Akasaka, "Assessment of culprit lesion morphology in acute myocardial infarction: ability of optical coherence tomography compared with intravascular ultrasound and coronary angiography," *J. Am. Coll. Cardiol.*, Vol. 50, No. 10, pp. 933–939, 2007.
- [37] G. J. Tearney, I. K. Jang, and B. E. Bouma, "Optical coherence tomography for imaging the vulnerable plaque," *J. Biomed. Opt.*, Vol. 11, No. 2, 021002, 2006.
- [38] A. I. Kholodnykh, I. Y. Petrova, K. V. Larin, M. Motamedi, and R. O. Esenaliev, "Precision of measurement of tissue optical properties with optical coherence tomography," *Appl. Opt.*, Vol. 42, No. 16, pp. 3027–3037, 2003.
- [39] C. Xu, J. M. Schmitt, S. G. Carlier, R. Virmani, "Characterization of atherosclerosis plaques by measuring both backscattering and attenuation coefficients in optical coherence tomography," *J. Biomedical. Opt.*, Vol. 13, No. 3, 034003, 2008.
- [40] L. A. Cassis, R. A. Lodder, "Near-IR imaging of atheromas in living arterial tissue," *Anal. Chem.*, Vol. 65, pp. 1247–1256, 1993.
- [41] R. J. Dempsey, L. A. Cassis, D. G. Davis, *et al.* "Near-infrared imaging and spectroscopy in stroke research: lipoprotein distribution and disease," *Ann. N. Y. Acad. Sci.*, No. 820, pp. 149–169, 1997.
- [42] T. J. Romer, J. F. Brennan, M. Fitzmaurice, *et al.* "Histopathology of human coronary atherosclerosis by quantifying its chemical composition with Raman spectroscopy," *Circulation*, No. 7, pp. 878–85, 1998.
- [43] W. Jaross, V. Neumeister, P. Lattke, D. Schuh, "Determination of cholesterol in atherosclerotic plaques using near infrared diffuse reflection spectroscopy," *Atherosclerosis*, No. 147, pp. 327–37, 1999.
- [44] J. Wang, Y. Geng, B. Guo, T. Klima, B. N. Lal, J. T. Willerson, W. Casscells, "Near Infrared Spectroscopic Characterization of Human Advanced Atherosclerotic Plaques," *J. Am. Coll. Cardiol.*, Vol. 39, No. 8, pp. 1305–1313, 2002.
- [45] G. Dangas, F. Kuepper, "Restenosis: Repeat Narrowing of a Coronary Artery: Prevention and Treatment," *Circulation*, No. 105, pp. 2586–2587, 2002.
- [46] T. P. Smith, "Atherosclerosis and Restenosis: An Inflammatory Issue," *Radiology*, No. 225, pp. 10–12, 2002.
- [47] J. Rixe, S. Achenbach, D. Ropers, U. Baum, A. Kuettner, U. Ropers, W. Bautz, W. G. Daniel, K. Anders, "Assessment of coronary artery stent restenosis by 64-slice multi-detector computed tomography," *Eur. H. J.*, Vol. 27, No. 21, pp. 2567–2572, 2006.
- [48] O. Fröbert, B. Lagerqvist, J. Carlsson, J. Lindbäck, U. Stenestrand, S. K. James, "Differences in Restenosis Rate With Different Drug-Eluting Stents in Patients With and Without Diabetes Mellitus: A Report From the SCAAR (Swedish Angiography

- and Angioplasty Registry),” *J. Am. Coll. Cardiol.* No. 53, pp. 1660-1667, 2009.
- [49] K. Tanabe, A. Hoyer, P. A. Lemos, *et al.*, “Restenosis rates following bifurcation stenting with sirolimus-eluting stents for de novo narrowings,” *Am. J. Cardiol.*, Vol. 94, No. 1, pp. 115-118, 2004.
- [50] A. V. Oppenheim, R.W. Schaffer, *Discrete-Time Signal Processing*, 2nd edition, Prentice-Hall, 1998.
- [51] T. Hiro, C. Y. Leung, S. De Guzman, V. J. Caiozzo, A. R. Fervid, H. Karimi, R. H. Helfant, J. M. Tobis, “Are soft echoes really soft? Intravascular ultrasound assessment of mechanical properties in human atherosclerotic tissue,” *American Heart J.* vol. 133, pp. 1-7, 1997.
- [52] A. Jeremias, M. L. Kolz, T. S. Ikonen, J. F. Gummert, A. Oshima, M. Hayase, Y. Honda, N. Komiyama, G. J. Berry, R. E. Morris, P. G. Yock, P. J. Fitzgerald, “Feasibility of in vivo intravascular ultrasound tissue characterization in the detection of early vascular transplant rejection,” *Circulation* vol. 100, pp. 2127-2130, 1999.
- [53] J. E. Muller, A. Tawakol, S. Kathiresan, and J. Narula, “New opportunities for identification and reduction of coronary risk: treatment of vulnerable patients, arteries, and plaques,” *J. Am. Coll. Cardiol.*, 47, C2-C6, 2006.
- [54] L. Fellingham, F. Sommer, “Ultrasonic characterization of tissue structure in the in vivo human liver and spleen,” *IEEE Trans. Sonics Ultrason.*, vol. 31, no. 4, pp. 418–428, 1984.
- [55] L. Landini, L. Verrazzani, “Spectral characterization of tissue microstructure by ultrasound: A stochastic approach,” *IEEE Trans. on UFFC.*, vol. 37, no. 5, pp. 448–456, 1990
- [56] M. F. Insana, R. F. Wagner, D. G. Brown, T. J. Hall, “Describing small-scale structure in random media using pulse-echo ultrasound,” *J. Acous. Soc. Ame.* Vo. 87, No. 1, pp.179-192, 1990.
- [57] M. F. Insana, T. J. Hall, “Characterizing the Microstructure of Random Media Using Ultrasound,” *Physics in Med. & Biol.*, Vol. 35, No. 10, pp. 1373-1386, 1990.
- [58] A. Katouzian, S. Sathyanarayana, W. Li, T. Thomas, S. G. Carlier, “Challenges in Tissue Characterization From Backscattered Intravascular Ultrasound Signals,” *Proceeding of SPIE*, 2006.
- [59] W.C.A. Pereira, S. L. Bridal, A. Coron, and P. Laugier, “Singular spectrum analysis applied to backscattered ultrasound signals from *in vitro* human cancellous bone specimens,” *IEEE Trans. Ultrason. Ferroelectr. Freq. Control*, vol. 51, no. 3, pp. 302–312, 2004.
- [60] J. Y. David, S. A. Jones, and D. P. Giddens, “Modern spectral analysis techniques for blood flow velocity and spectral measurements with pulsed doppler ultrasound,” *IEEE Trans. Biomed. Eng.*, vol. 38, no. 6, pp. 589– 596, 1991.
- [61] F. L. Lizzi, M. Ostromogilsky, E. J. Feleppa, M. C. Rorke, and M. M. Yaremko, “Relationship of ultrasonic spectral parameters to features of tissue microstructure,” *IEEE Trans. Ultrason. Ferroelectr. Freq. Control*, vol. UFFC-34, no. 3, pp. 319–329, 1986.
- [62] F. Ossant, M. Lebertre, L. Pourcelot, and F. Patat, “Ultrasonic characterization of maturation of fetal lung microstructure: An animal study,” *Ultrasound Med. Biol.*, vol. 27, no. 2, pp. 157–169, 2001.

- [63] F. L. Lizzi, M. A. Laviola, and D. J. Coleman, "Tissue signature characterization utilizing frequency domain analysis," in *Proc. IEEE Ultrason. Symp.*, pp. 714–719, 1976.
- [64] A. Nair, B. D. Kuban, N. Obuchowski, and D. G. Vince, "Assessing spectral algorithms to predict atherosclerotic plaque composition with normalized and raw intravascular ultrasound data," *Ultrasound Med. Biol.*, vol. 27, no. 10, pp. 1319–1331, 2001.
- [65] F. L. Lizzi, M. Greenebaum, E. J. Feleppa, M. Elbaum, and D. J. Coleman, "Theoretical framework for spectrum analysis in ultrasonic tissue characterization," *J. Acoust. Soc. Amer.*, vol. 73, no. 4, pp. 1366–1373, 1983.
- [66] A. Nair, D. G. Vince, and D. Calvetti, "Blind data calibration of intravascular ultrasound data for automated tissue characterization," in *Proc. IEEE Ultrason. Symp.*, vol. 2, pp. 1126–1129, 2004.
- [67] A. Nair, B. D. Kuban, M. Tuzcu, P. Schoenhagen, S. E. Nissen, and D. G. Vince, "Coronary plaque classification with intravascular ultrasound radiofrequency data analysis," *Circulation*, vol. 106, no. 17, pp. 2200–2206, 2002.
- [68] A. Nair, D. Calvetti, and D. G. Vince, "Regularized autoregressive analysis of intravascular ultrasound backscatter: Improvement in spatial accuracy of tissue maps," *IEEE Trans. Ultrason. Ferroelectr. Freq. Control*, vol. 51, no. 4, pp. 420–431 (2004).
- [69] M. Kawasaki, H. Takatsu, T. Noda, *et al.*, "Noninvasive quantitative tissue characterization and two-dimensional color-coded map of human atherosclerotic lesions using ultrasound integrated backscatter: comparison between histology and integrated backscatter images," *J. Am. Coll. Cardiol.*, vol. 38, no. 2, pp. 486–492, 2002.
- [70] M. Kawasaki, H. Takatsu, T. Noda, *et al.*, "In vivo quantitative tissue characterization of human coronary arterial plaques by use of integrated backscatter intravascular ultrasound and comparison with angioscopic findings," *Circulation*, vol. 105, no. 21, pp. 2487–2492, 2002.
- [71] M. Okubo, M. Kawasaki, Y. Ishihara, *et al.*, "Tissue characterization of coronary plaques: comparison of integrated backscatter intravascular ultrasound with virtual histology intravascular ultrasound," *Circulation Japan*, vol. 72, pp. 1631–1639, 2008.
- [72] J. M. Tobis, J. Mallery, D. Mahon, K. Lehmann, P. Zalesky, J. Griffith, J. Gessert, M. Moriuchi, M. McRae, M. L. Dwyer, "Intravascular ultrasound imaging of human coronary arteries *in vivo*. Analysis of tissue characterization with comparison to *in vitro* histological specimens," *Circulation*, vol. 83, pp. 913–926, 1991.
- [73] K. Gad, M. B. Leon, "Characterization of atherosclerotic lesions by intravascular ultrasound: possible role in unstable coronary syndromes and in interventional therapeutics procedure," *Am. J. Cardiol.* vol. 68, pp. 85B–91B, 1991.
- [74] X. Zhang, C. R. McKay, M. Sonka, "Tissue characterization in intravascular ultrasound images," *IEEE Trans. Med. Imag.*, vol. 17, no. 6, pp. 889–899, 1998.
- [75] K. L. Caballero, O. Pujol, J. Barajas, J. Mauri, P. Radeva, "Assessing *in-vivo* IVUS tissue classification accuracy between normalized image reconstruction and RF analysis," *MICCAI*, pp. 82–89, 2006.

- [76] E. Brunenberg, O. Pujol, B. H. Romeny, P. Radeva, "Automatic IVUS segmentation of atherosclerotic plaque with stop & go snake," *MICCAI*, part 2, pp. 9-16 (2006).
- [77] S. Escalera, O. Pujol, J. Mauri, P. Radeva, "Intravascular Ultrasound Tissue Characterization with Sub-class Error-Correcting Output Codes," *J. Sign. Process. Syst.*, 55(1-3): 35-47, 2009.
- [78] P. Ohanian, R. Dubes, "Performance evaluation for four classes of textural features," *Pattern Recognition*, vol. 25, 819–833, 1992.
- [79] T. Ojala, M. Pietikainen, T. Maenpaa, "Multiresolution gray-scale and rotation invariant texture classification with local binary patterns," *IEEE Transactions on Pattern Analysis and Machine Intelligence*, vol. 24, pp. 971–987, 2002.
- [80] J. G. Daugman, "Uncertainty relation for resolution in space, spatial frequency, and orientation optimized by two-dimensional visual cortical filters," *Journal of the Optical Society of America*, vol. 2(A), pp. 1160–1169, 1985.
- [81] A. C. Bovik, M. Clark, W. S. Geisler, "Multichannel texture analysis using localized spatial filters," *IEEE Transactions on Pattern Analysis and Machine Intelligence*, vol. 12, no. 1, pp. 55–73, 1990.
- [82] T. Hastie, R. Tibshirani, "Classification by pairwise grouping," *NIPS*, vol. 26, pp. 451–471, 1998.
- [83] N. J. Nilsson, "Learning machines", McGraw-Hill, 1965.
- [84] E. Allwein, R. Schapire, Y. Singer, "Reducing multiclass to binary: A unifying approach for margin classifiers," *JMLR*, vol. 1, pp. 113–141, 2002.
- [85] O. Pujol, P. Radeva, J. Vitrià, "Discriminant ECOC: A heuristic method for application dependent design of error correcting output codes," *PAMI*, vol. 28, pp. 1001–1007, 2006.
- [86] J. Friedman, T. Hastie, R. Tibshirani, "Additive logistic regression: A statistical view of boosting," *The annals of statistics*, vol. 38, pp. 337–374, 1998.
- [87] A. Taki, A. Roodaki, O. Pauly, S. Setarehdan, G. Unal, N. Navab, "A new method for characterization of coronary plaque composition via ivus images," *IEEE International Symposium on Biomedical Imaging: From Nano to Macro (ISBI)*, 2009.
- [88] N. Bruining, S. Verheye, and M. Knaapen. Three-dimensional and quantitative analysis of atherosclerotic plaque composition by automated differential echogenicity," *Catheterization and Cardiovascular Interventions*, vol. 70, no.7: pp. 968–978, 2007.
- [89] G.S. Mintz, S.E. Nissen, and W.D. Anderson. American college of cardiology clinical expert consensus document on standards for acquisition, measurement and reporting of intravascular ultrasound studies (ivus): A report of the American college of cardiology task force on clinical expert consensus documents," *Journal of American college of Cardiology*, 37, pp. 1478–1492, 2001.
- [90] K. Tanaka, S. G. Carlier, A. Katouzian, G. Mintz, "Characterization of the Intravascular Ultrasound Radiofrequency Signal within Regions of Acoustic Shadowing Behind Calcium," *J. Am. Coll. Cardiol.*, 49(9 Suppl B): 29B, 2007.
- [91] X. Tang., "Texture information in run length matrices," *IEEE Transactions on Image Processing*, vol. 7, no. 11, pp. 1602–1609.

- [92] F. Kolodgie, H. Gold, A. Burke, D. Fowler, *et al.*: "Intraplaque hemorrhage and progression of coronary atheroma," *New Eng. J. Med.*, vol. 349, pp. 2316–2325, 2003.
- [93] M. Hayden, S. Tyagi, "Vasa vasorum in plaque angiogenesis, metabolic syndrome, type 2 diabetes mellitus, and atheroscleropathy: a malignant transformation," *Cardiovasc. Diabetol* 3, 2004.
- [94] S.M. O'Malley, M. Vavuranakis, R. Metcalfe, C.J. Hartley, M. Naghavi, and I.A. Kakadiaris, "Intravascular ultrasound-based imaging of vasa vasorum for the detection of vulnerable atherosclerotic plaque," in *Proc. Houston Society for Engineering in Medicine and Biology (HSEMB)*, Houston, TX, Feb., 2006.
- [95] A. C. Barger, R. Beeuwkes, L. L. Lainey, K. J. Silverman, "Hypothesis: Vasa Vasorum and Neovascularization of Human Coronary Arteries — A Possible Role in the Pathophysiology of Atherosclerosis," *N. Engl. J. Med.*, Vol. 310, pp. 175–177, 1986.
- [96] M. P. Moore, T. Spencer, D. M. Salter, P. P. Kearney, T. R. D. Shaw, I. R. Starkey, P. J. Fitzgerald, R. Erbel, A. Lange, N. W. McDicken, G. R. Sutherland, and K. A. A. Fox, "Characterization of coronary atherosclerotic morphology by spectral analysis of radiofrequency signal: *In vitro* intravascular ultrasound study with histological and radiological validation," *Heart*, vol. 79, pp. 459–467, 1998.
- [97] R. J. Watson, C. C. McLean, M. P. Moore, T. Spencer, D. M. Salter, T. Anderson, K. A. A. Fox, and W. N. McDicken, "Classification of arterial plaque by spectral analysis of *in vitro* radio frequency intravascular ultrasound data," *Ultrasound Med. Biol.*, vol. 26, no. 1, pp. 73–80, 2000.
- [98] J. F. Granada, D. W. Bradley, H. K. Win, C. L. Alviar, A. Builes, E. I. Lev, R. Barrios, D. G. Schulz, A. E. Raizner, and G. L. Kaluza, "*In vivo* plaque characterization using intravascular ultrasound-virtual histology in a porcine model of complex coronary lesions," *Arterioscler. Thromb. Vasc. Biol.*, vol. 27, no. 2, pp. 387–393, Feb. 2007.
- [99] F. Lizzi, J. Feleppa, M. Astor, and A. Kalisz, "Statistics of ultrasonic spectral parameters for prostate and liver examinations," *IEEE Trans. Ultrason. Ferroelectr. Freq. Control*, vol. 44, no. 4, pp. 935–942, Jul. 1997.
- [100] B. K. Courtney, A. L. Robertson, A. Maehara, J. Luna, K. Kitamura, Y. Morino, R. Achalu, S. Kirti, P. G. Yock, and P. J. Fitzgerald, "Effects on transducer position on backscattered intensity in coronary arteries," *Ultrasound Med. Biol.*, vol. 28, no. 1, pp. 81–91, 2002.
- [101] S. L. Bridal, P. Fornes, P. Bruneval, and G. Berger, "Parametric (integrated backscatter and attenuation) images constructed using backscattered radio frequency signals (25–56 MHz) from human aortae *in vitro*," *Ultrasound Med. Biol.*, vol. 23, no. 2, pp. 215–229, 1997.
- [102] T. Spencer, M. P. Ramo, D. M. Salter, T. Anderson, P. P. Kearney, G. R. Sutherland, K. A. A. Fox, and W. N. McDicken, "Characterisation of atherosclerotic plaque by spectral analysis of intravascular ultrasound: An *in vitro* methodology," *Ultrasound Med. Biol.*, vol. 23, no. 2, pp. 191–203, 1997.
- [103] K. A. Wear, R. F. Wagner, and B. S. Garra, "High resolution ultrasonic backscatter coefficient estimation based on autoregressive spectral estimation using Burg's algorithm," *IEEE Trans. Med. Imag.*, vol. 13, no. 3, pp. 500–507, Sep. 1994.

- [104] T. Baldeweck, P. Laugier, A. Herment, and G. Berger, "Application of autoregressive spectra analysis for ultrasound attenuation estimation: Interest in highly attenuating medium," *IEEE Trans. Ultrason. Ferroelectr. Freq. Control*, vol. 42, no. 1, pp. 99–110, Jan. 1995.
- [105] J. M. Girault, F. Ossant, A. Ouahabi, D. Kouame, and F. Patat, "Timevarying autoregressive spectral estimation for ultrasound attenuation in tissue characterization," *IEEE Trans. Ultrason. Ferroelectr. Freq. Control*, vol. 45, no. 3, pp. 650–659, May 1998.
- [106] F. S. Schlindwein and D. H. Evans, "Selection of the order of autoregressive models for spectral analysis of doppler ultrasound signals," *Ultrasound Med. Biol.*, vol. 16, no. 1, pp. 81–91, 1990.
- [107] A. Boardman, F. S. Schlindwein, A. P. Rocha, and A. Leite, "A study on the optimum order of autoregressive models for heart rate variability," *Physiol. Meas.*, vol. 23, no. 2, pp. 325–336, 2002.
- [108] S. M. Kay and S. L. Marple, "Spectrum analysis—A modern prospective," *Proc. Inst. Elect. Eng.*, vol. 69, no. 11, pp. 1380–1419, 1981.
- [109] G. E. P. Box and G. M. Jenkins, *Time Series Analysis: Forecasting and Control*. San Francisco, CA: Holden-Day, 1970.
- [110] F. L. Lizzi, S. K. Alam, S. Mikaelian, P. Lee, and E. J. Feleppa, "On the statistics of ultrasonic spectral parameters," *Ultrasound Med. Biol.*, vol. 32, no. 11, pp. 1671–1685, 2006.
- [111] M. O'Donnell, D. Bauwens, J. W. Mimbs, and J. G. Miller, "Broadband integrated backscatter: An approach to spatially localized tissue characterization *in vivo*," in *Proc. IEEE Ultrason. Symp.*, 1979, pp. 175–178.
- [112] A. F. Laine, J. Fan, "Frame representation for texture segmentation," *IEEE Trans. Image Proc.*, vol. 5, no. 5, pp. 771–780, 1996.
- [113] R. De Valois, K. De Valois, "Spatial vision", New York, NY: *Oxford University Press*, 1988.
- [114] J. Beck, A. Sutter, R. Ivry, "Spatial frequency channels and perceptual grouping in texture segregation," *Comput. vision, Graph., and Image Proc.*, vol. 37, pp. 299–325, 1987.
- [115] O. Rioul, "A discrete-time multiresolution theory," *IEEE Trans. Sig. Proc.*, vol. 41, no. 8, pp. 2591–2606, Aug. 1993.
- [116] S. G. Mallat, "A theory of multiresolution signal decomposition: The wavelet representation," *IEEE Trans. Patt. Anal. Mach. Intell.*, vol. 11, no. 7, pp. 674–693, 1989.
- [117] I. Daubechies, "Ten lectures on wavelets," Philadelphia: Soc. Ind. Applied Math., 1992.
- [118] M. Unser, "Texture classification and segmentation using wavelet frames," *IEEE Trans. Image Proc.*, vol. 4, no. 11, pp. 1549–1560, November 1995.
- [119] R. R. Coifman, M. V. Wickerhauser, "Entropy-based algorithms for best basis selection," *IEEE Trans. Inform. Theory*, pt. II, vol. 38, no. 2, pp. 713–718, Mar. 1992.
- [120] R. R. Coifman, Y. Meyer, "Orthonormal wave packet bases," *preprint, Yale Univ.*, August 1989.
- [121] A. Katouzian, B. Baseri, E. Konofagou, A. F. Laine, "Texture-Driven Coronary Artery Plaque Characterization Using Wavelet Packet Signatures," *Proceeding of 5th*

- IEEE International Symposium on Biomedical Imaging (ISBI): From Nano to Macro*, pp. 197-200, 2008.
- [122] R. Virmani, F. D. Kolodgie, A. P. Burke, A. Farb, S. M. Schwartz, "Lessons from sudden coronary death: a comprehensive morphological classification scheme for atherosclerotic lesions," *Arterioscler. Thromb. Vasc. Biol.* Vol. 20, no. 5, pp. 1262-1275, 2000.
 - [123] E. Falk, "Pathogenesis of atherosclerosis," *J. Am. Coll. Cardiol.*, vo. 47(8 Suppl.), C7-C12, 2006.
 - [124] K. Fujii, G. S. Mintz, S. G. Carlier, J. R. Costa, M. Kimura, K. Sano, K. Tanaka, R. A. Costa, J. Lui, G. W. Stone, J. W. Moses, M. B. Leon, "Intravascular ultrasound profile analysis of ruptured coronary plaques," *J. Am. Cardiol.*, vol. 98, no. 4, pp. 429-435, 2006.
 - [125] G. S. Mintz, E. Missel, "What is behind the calcium? The relationship between calcium and necrotic core on virtual histology analyses: reply," Letters to the Editor, *European Heart Journal*, vol. 30, pp. 125–126, 2009.
 - [126] M. H. R. Cardinal, J. Meunier, G. Soulez, R. L. Maurice, E. Therasse, G. Cloutier, "Intravascular Ultrasound Image Segmentation: A Three-Dimensional Fast-Marching Method Based on Gray Level Distribution," *IEEE Tran. Med. Imag.*, vol. 25, no. 5, pp. 590-601, May 2006.
 - [127] M. Sonka, X. Zhang, M. Siebes, M. S. Bissing, S. C. DeJong, S. M. Collins, C. R. McKay, "Segmentation of Intravascular Ultrasound Images: A Knowledge-Based Approach," *IEEE Tran. Med. Imag.*, vol. 14, no. 4, pp. 719-732, Dec. 1995.
 - [128] Gozde B. Unal, S. Bucher, S. Carlier, Gregory G. Slabaugh, Tong Fang, K. Tanaka, "Shape-Driven Segmentation of the Arterial Wall in Intravascular Ultrasound Images," *IEEE Tran. Info. Tech. Biomed.*, vol. 12, no. 3, pp. 335-347, 2008.
 - [129] J. D. Klingensmith, R. Shekhar, D. G. Vince, "Evaluation of Three-Dimensional Segmentation Algorithms for the Identification of Luminal and Medial-Adventitia Borders in Intravascular Ultrasound Images," *IEEE. Tran. Med. Imag.*, vol. 19, no. 10, 2000.
 - [130] A. Katouzian, S. Sathyanarayana, B. Baseri, E. E. Konofagou, S. G. Carlier, "Challenges in Atherosclerotic Plaque Characterization with Intravascular Ultrasound (IVUS): From Data Collection to Classification," *IEEE Trans. on Information Technology in Biomedicine*, vol. 12, no. 3, pp. 315-327.
 - [131] F. Meyer and R. R. Coifman, "Brushlets: A tool for directional image analysis and image compression," *Applied and computational harmonic analysis*, vol. 4, pp. 147-187, 1997.
 - [132] P. Ausher, G. Weiss, M. V. Wickerhauser, "Local sine and cosine bases of Coifman and Meyer and the construction of smooth wavelets," in *Wavelets- A tutorial in Theory and Application*, vol. 2, *Wavelet Analysis and its Applications*, C. K. Chui, Ed. San Diego: Academic Press, 1992, pp. 237-256.
 - [133] E. Angelini, A. Laine, S. Takuma, J. Holmes, S. Homma, "LV Volume Quantification via Spatio-Temporal Analysis of Real-Time 3D Echocardiography," *IEEE Trans. Med. Imag.*, Vol. 20, No. 6, pp. 457-469, 2001.
 - [134] D. Mumford, J. Shah, "Optimal Approximation by Piecewise Smooth Functions and Associated Variational Problems," *Communication on Pure and Applied Math.* Vol. 42, pp. 544-685.

- [135] S. Haykin, *Neural Networks: A Comprehensive Foundation*. Upper Saddle River, NJ: Prentice Hall, 1998.
- [136] M. Plissiti, D. Fotiadis, L. Michalis, G. Bozios, "An Automated Methods for Lumen and Media-Adventitia Border Detection in a sequence of IVUS frames," *IEEE Trans. Info. Tech. Biomed.*, Vol. 19, No. 10, pp. 996-1011, 2000.
- [137] M. Rosales, P. Radeva, O. R. Leor, D. Gil, "Modeling of image-catheter motion for 3-D IVUS," *Medi. Imag. Anal.*, Vol. 13, No. 1, pp. 91-104, 2009.
- [138] R. Shekhar, R. M. Cothren, D. G. Vince, S. Chandra, J. D. Thomas, J. F. Cornhill, "Three-Dimensional Segmentation of Luminal and Adventitial Borders in Serial Intravascular Ultrasound Images," *Computerized Med. Imag. and Graphics*, vol. 23, pp. 299-309, 1999.
- [139] D. Gil, P. Radeva, J. Saludes, "Segmentation of artery wall in coronary IVUS images: A probabilistic approach," *15th Int. Conf. Patt. Recog.*, Barcelona, vol. 4, pp. 352-355, 2000.
- [140] D. Gil, A. Hernandez, A. Carol, O. Rodríguez and P. Radeva, "A Deterministic-Static Adventitia Detection in IVUS images," *LNCS-3504, FIMH*, pp. 65-74, 2005.
- [141] A. Taki, Z. Najafi, A. Roodaki, S. K. Setarehdan, R. A. Zoroofi, A. Konig, N. Navab, "Automatic segmentation of calcified plaques and vessel borders in IVUS images," *Int. J. CARS*, vol. 3, pp. 347-354, 2008.
- [142] K. Hibi, A. Takagi, X. Zhang, T. T. Teo, H. N. Boneau, P. G. Yock, P. J. Fitzgerald, "Feasibility of a Novel Blood Reduction Algorithm to Enhance Reproducibility of Ultra-High-Frequency Intravascular Ultrasound Images," *Circulation*, Vol. 102, No. 14, pp. 1657-1663, 2000.
- [143] S. Balocco, O. Basset, C. Cachard, P. Delachartre, "Spatial Anisotropic Diffusion and Local Time Correlation Applied to Segmentation of Vessels in Ultrasound Image Sequences," *IEEE Symp. Ultrasonics*, Vol. 2, pp. 1549-1552, 2003.
- [144] A. Katouzian, E. Angelini, A. Lorsakul, B. Sturm, A. Laine, "Lumen Border Detection of Intravascular Ultrasound via Denoising of Directional Wavelet Representations," *FIMH 2009*, pp. 104 - 113, Nice, France, 2009.
- [145] D. Rotger, P. Radeva, E. F. Nofrerias, J. Mauri, "Blood Detection in IVUS Images for 3D Volume of Lumen Changes Measurement Due to Different Drugs Administration," *CAIP, LNCS 4673*, pp. 285-292, 2007.
- [146] S. M. O'Malley, M. Naghavi, I. A. Kakadiaris, "One-Class Acoustic Characterization Applied to Blood Detection in IVUS," *MICCAI, Part I, LNCS 4791*, pp. 202-209, 2007.
- [147] A. Katouzian, M. A. Selver, E. Angelini, B. Sturm, A. Laine, "Classification of Blood Regions in IVUS Images Using Three Dimensional Brushlet-Derived Features," *EMBC*, pp. 471-474, 2009.
- [148] D. Gil, P. Radeva, J. Mauri, "IVUS segmentation via a regularized curvature flow", XX congreso Annual de la sociedad Espanola de Ingenieria Biomedica, Zaragoza, Nov. 27-29, 2002
- [149] D. Gil, A. Hernandez, O. Rodriguez, J. Mauri and P. Radeva, "Statistical strategy for anisotropic adventitia modeling in IVUS," *IEEE TMI*, vol. 25, No. 6, pp. 768-778, 2006.
- [150] Q. Duan, E. D. Angelini, A. F. Laine, "Surface Function Actives," *J. Vis. Commun. Image R.*, Vol. 20, pp. 478-490, 2009.

- [151] N. Paragios and R. Deriche, "Geodesic active regions and level set methods for supervised texture segmentation," *Int. J. Comput. Vis.*, vol. 46, no. 3, pp. 223–247, 2002.
- [152] J. Suri, K. Chirinjeev, F. Molinari, "Atherosclerosis Disease Mangement," 1st Edition., XIV, 944 p. 282 illus., 182 in color., Hardcover, 2011, ISBN: 978-1-4419-7221-7.
- [153] G. M. Ruiz, M. Rivera, I. A. Kakadiaris, "A probabilistic segmentation method for the identification of luminal borders in intravascular ultrasound images," *IEEE CVPR*, 2008.